UNIVERSITÀ DEGLI STUDI DI PADOVA
Facoltà di Scienze MM.FF.NN.
Dipartimento di Fisica e Astronomia "G. Galilei"

Scuola di Dottorato di Ricerca in Astronomia
Ciclo XXVI

A Multi-wavelength Study of Unidentified Objects in the Second Fermi Gamma-Ray catalogue

Supervisor: Ch.mo Prof. Alberto Franceschini
School director: Ch.mo Prof. G. Piotto

PhD Student: Simona Paiano

Anno Accademico 2014

Contents

Abstract

The research field of the γ-ray astronomy is new and rapidly grown, providing remarkable and promising scientific results. In the last decades, the development of new γ-ray detectors on board satellites as the *AGILE* and the *Fermi* observatories, or groud-based instruments as the *Imaging Atmospheric Cherenkov Technique* telescope MAGIC, lead up to a big increase in the number of discovered γ-ray emitters. Different types of astrophysical sources have been identified as γ-ray emitter classes, of Galactic and extragalactic origin, such as Supernova Remants, Pulsars, Microquasars and Active Galactic Nuclei. Moreover, it has been suggested that γ-ray radiation can be also related to annihilation/decay processes of Dark Matter particles expected in several celestial objects with high DM density as the Galactic Center, the Galaxy clusters, the Dwarf Spheroidal Satellite Galaxies of the Milky Way and finally the clumps of DM overdensities within the DM halo of our Galaxy.

The aim of this PhD Thesis is both searching for γ-ray signals from DM particles and combining the time-progressive all-sky Fermi survey with dedicated pointed observations performed by the Cherenkov telescopes. To perform this purpose, this Thesis work followed two different, but deeply related paths.

The first part of this Thesis has adopted the Second Catalogue of the Fermi Gamma Ray Observatory (2FGL) as the main dataset for searches of new classes of extragalactic sources, DM objects candidates or unexpected high-energy phenomena. The Fermi mission has carried out a survey of the all sky at the γ-ray energies from 30 MeV to 100 GeV, making use of the large area and field of view of the LAT instrument. In the 2FGL catalogue, 1873 points sources are detected: 1297 have been associated as known class of γ-ray emitters, while the remaining 576 objects, the so-called *Unassociated Fermi Objects* (UFO), still lack a plausible identification and offer the best chance to search for DM sources.

The population of the UFOs is the second major component of the γ-ray sky and we selected a

sub-sample of 183 UFOs of high Galactic latitude with $|b| > 20^\circ$ (avoiding the confusion effects in the Galactic plane) with the aim to classify these sources and to determine if, among them, there are new types of AGNs, DM object candidates or unexpected high-energy phenomena. For each UFO of our sample we search for counterparts in optical, X-ray and radio band, in order to determine a possible association with a suitable set of sources of other astronomical catalogs. Then, through new tools based on multiwavelength approaches, we suggest a rather secure classification for most of them.

Our UFO association procedure is primarily based on the use of available X-ray *Swift* satellite data that cover the FERMI error-box (typically of a few arcmins) associated to the γ-ray detection. If an X-ray bright source is revealed within the FERMI error-box and if other sources at different wavelengths (from radio, IR and optical catalogues) are positionally coincident with the X-ray counterpart, we consider them as an unique source associated to the UFO. In addition we perform a dedicated X-ray data analysis for the X-ray counterpart found in order to determine the spectral shape in this energy band. Finally we build the UFO broad-band Spectral Energy Distribution (SED) combining the available measured fluxes at different wavelengths recovered as explained before.

At this point, we perform the characterization of the SED of each our UFO, identifying it as belonging to a class of the main γ-ray emitters. In particular for the *blazar* identification tool, we build a code based on the use of a library of *bona-fide* multi-frequency SED templates of known objects belonging to the four *blazar* categories: High-peaked (HBL), Intermediate-peaked (IBL), Low-peaked BL Lac (LBL), and Flat Spectrum radio Quasar (FSQR). Therefore, through the adoption of these SED template and choosing the one that models the data maximizing the likelihood, this code determines if a given UFO of our sample can be identified as a *blazar* object. In the same time, it provides an estimate of the redshift, still in the absence of spectroscopic observations (that is a well known issue for this kind of sources). From this procedure we obtain a reasonable classification as *blazar* objects for about 50 UFOs of our sample, belonging to all of the classes and with redshifts spanning from 0.2 to 1.5. This tool has been also applied on two well-known *blazars*, 1ES 1011+496 and PG 1553+113, used as *test sources* to prove the efficacy in recognizing AGN sources. Notably, we found results compatible with the real *blazar* class and redshift of the two test sources.

Although in this PhD thesis we study UFOs of high Galactic latitude, the other category of γ-ray emitters that we decided to consider as possible identification was also the class of microquasars. We have been encouraged to pursue this task because, during the procedure of association for some UFOs, we find set of MWL counterparts resulting in a peculiar broad-band SED similar to the those typically observed for microquasar objects. To achieve this interpretation, we built a diagnostic plot superimposing the luminosity data points of four known microquasars. If the SED points of a given UFO are located inside the regions defined by the known microquasar points, we suggest a microquasar identification for the studied object. About 15 UFOs of our sample are turned out to likely be Galactic sources, as microquasars, high galactic latitude Neutron Stars and pulsars. This could be a finding of great interest, given the small number of such objects in the 2FGL catalogue. For this reason, further investigations are ongoing.

We note that for ten objects no X-ray sources in the available *Swift*/XRT data has been found within the *Fermi* error-box and, although we highlight that it might be dependent on the quality of the X-ray observations, they could be considered as the best candidates to perform DM searches. Finally, for the remaining UFOs, we cannot provide a clear identification since we found multiple sets of associations. Further observations, especially in the X-ray and radio bands, will allow us to disentangle this issue.

The second line of investigation of this Thesis is in the field of very high energy (VHE) observations of Fermi sources with Cherenkov telescopes on ground, in particular with the MAGIC telescope, one of the largest IACT stereo systems and situated on the Canarian island La Palma, at 2245 m a.s.l. Such VHE data offer an invaluable astrophysical information on the sources.

In this Thesis a detailed data analysis of the VHE radiation emitted by two HBL *blazars*, PG 1553+113 and 1ES 1011+496, is provided. Both sources have been observed in stereoscopic mode with MAGIC for a total of 12 hours and 21 hours, respectively, in order to perform a complete temporal evolution analysis of the integral flux and a detailed study of the VHE differential energy spectrum.

Futhermore, the MAGIC observations were performed in the framework of dedicated multiwavelength campaigns, and for PG 1553+113 the campaign was planned in collaboration with the WEBT team involving several instruments of the north hemisphere operating at different energy bands.

Simultaneous data, with a good temporal coverage, were collected from radio to VHE regimes, allowing us to sample the whole broad-band SED. The typical doubled bump shape, due to syncrothron and IC mechanisms, is showed by both sources, in agreement with the current Synchrotron Self-Compton *blazar* models. In addition both sources provide a modest (or any) activity in the HE, VHE and radio bands, while a clear variability in the UV and Optical regimes, related to the synchrotron bump frequencies, is present, especially for PG 1553+113. However any evidence of flare episodes have been detected. For this reasons, and thanks to high quality multiwavelength sampling of their SEDs, PG 1553+113 and 1ES 1011+496 were used as *test sources* to verify the efficency of our *blazar* identification tool (explained before) in recognizing AGN sources.

Sommario

Il campo di ricerca dell'astronomia γ é una nuova e fiorente disciplina che, seppure si sia sviluppata recentemente, é cresciuta rapidamente, raggiungendo importanti e promettenti risultati scientifici. Negli ultimi decenni, lo sviluppo di nuovi rilevatori γ a bordo di satelliti come gli osservatori *AGILE* e *FERMI* o di nuovi strumenti di terra come il telescopio *Imaging Atmospheric Cherenkov Technique* (MAGIC), ha portato a un grande incremento del numero di emettitori γ scoperti. Diversi tipi di sorgenti astronomiche sono state identificate come classi di sorgenti γ, di origine Galattica ed extragalattiche, come resti di supernovae, pulsar, microquasar e nuclei galattici attivi. In aggiunta, é stato suggerito che la radiazione γ puó essere relazionata a processi di annichilazione/decadimento di particelle di Materia Oscura attese in oggetti celesti con alta densitá di Materia Oscura come il centro Galattico, gli ammassi di galassie, le galassie sferoidali nane satelliti della nostra Galassia e infine gli agglomerati di sovradensit di Materia Oscura all'interno dell'alone di Materia Oscura della Via Lattea. Quest'ultimi sono suggeriti da svariate simulazioni numeriche all'interno del quadro dei modelli di formazione gerarchica delle strutture cosmiche e sono pensati essere isotropicamente distribuiti nel cielo.

Il progetto a lungo termine di questa tesi di dottorato é la ricerca ad alta energia di segnali γ dovuti al decadimento o all'annichilazione di particelle di Materia Oscura. Abbiamo combinato la survey Fermi, in continuo sviluppo, con dedicate osservazioni ottenute dai telescopi Cherenkov.

Per raggiungere questo scopo, questo lavoro di tesi stato sviluppato seguendo due linee guida, comunque profondamente legate tra loro sia da un punto di vista ideale che programmatico.

La prima parte della tesi ha adottato il Secondo Catalogo del satellite Fermi (2FGL) come il principale dataset per la ricerca di nuove classi di sorgenti extragalattiche, di ipotetici oggetti di Materia Oscura o inaspettati fenomeni di alta energia. La missione Fermi ha prodotto

una survey di tutto il cielo alle energie γ da 30 MeV a 100 GeV, grazie all'uso della grande area di raccolta e del campo di vista dello strumento LAT. Nel catalogo 2FGL, 1873 sorgenti puntiformi sono state osservate: 1297 sono state associate con classi note di emettitori γ, mentre i rimanenti 576 oggetti, chiamati Oggetti Fermi non Associati (UFO), ancora mancano di una plausibile identificazione e offrono, per questo motivo, una delle migliore opportunit per la ricerca di sorgenti di Materia Oscura.
La popolazione degli UFO la seconda pi grande componente di sorgenti del cielo γ e noi abbiamo selezionato un sotto-campione di 183 UFO ad alta latitudine Galattica con $|b| > 20°$ (evitando la confusione all'interno del piano Galattico) con lo scopo di classificare queste sorgenti e determinare se, tra loro, esistono una nuova classe di nuclei galattici attivi, candidati di Materia Oscura e nuovi fenomeni ad alta energia. Per ogni UFO del nostro campione, noi siamo andati in cerca di controparti nell'ottico, nei raggi-X e nel radio, con l'obiettivo di determinare una possibile associazione con un adeguato set di sorgenti appartenenti ad altri cataloghi astronomici. Successivamente, per mezzo di nuovi strumenti che fanno uso di un approccio multibanda, suggeriamo una classificazione abbastanza robusta per molti di loro.

La nostra associazione degli UFO é principalmente basata sull'uso di dati X disponibili dal satellite *Swift* che rientrano all'interno dell'error-box di FERMI (di solito qualche arcominuto) associata alla detezione γ. Se una sorgente X brillante é rivelata all'interno dell'error-box di FERMI e se altre sorgenti a lunghezze d'onda differenti (dati dai cataloghi radio, IR and ottici) sono posizionalmente coincidenti con la controparte X, noi le consideriamo come l'unica sorgente associata all'UFO. In piú per la controparte X trovata abbiamo eseguito un'analisi dedicata dei dati X affinché si possa determinare l'andamento spettrale in questa banda di energia. Infine, costruiamo la Distribuzione Spettrale in Energia (SED) dell'UFO, combinando i flussi misurati disponibili alle diverse lunghezze d'onda ottenuti come spiegato precedentemente.

A questo punto dell'analisi, caratterizziamo la SED di ogni UFO, nel tentativo di associarlo con una classe dei principali emettitori γ. In particolar modo per il tool di identificazione dei *blazar*, abbiamo sviluppato un codice basato sull'uso di librerie di *bona-fide* SED templates multibanda di oggetti noti, appartenenti alle quattro categorie di *blazar*: High-peaked (HBL), Intermediate-peaked (IBL), Low-peaked BL Lac (LBL) e Flat Spectrum radio Quasar (FSQR). Quindi, per mezzo dell'uso di queste SED template, e scegliendo l'unica tra di esse in grado di modellare i dati con la massima probabilit, questo codice determina se un dato UFO puó essere associato ad una particolare classe di *blazar*. Allo stesso tempo, fornisce anche una stima del redshift, anche in assenza di osservazioni spettroscopiche (che é un problema ampiamente noto per questo tipo di sorgenti). Seguendo questa procedura, otteniamo che circa 50 UFO del nostro campione possono essere ragionevolmente classificati come *blazar*, appartenenti a tutte le classi e con redshift che variano da 0.2 a 1.5. Questo tool é stato poi anche testato su due *blazar* ben noti, 1ES 1011+496 and PG 1553+113, usati come sorgenti prova per testarne l'efficienza nel riconoscere AGN: per entrambe abbiamo trovato risultati compatibili con le vere classi di appartenenza e i corrispettivi redshift.

Sebbene in questa tesi di dottorato ci siamo focalizzati su UFO ad alta latitudine Galattica, noi abbiamo deciso di considerare anche un'altra categoria di emettitori γ, cioé quella dei microquasar. Siamo stati incoraggiati a perseguire quest'analisi perché, durante la procedura di associazione di alcuni UFO, sono state trovate delle controparti con delle peculiari SED molto simili a quelle tipicamente osservate nei microquasar. Per consolidare questa interpretazione, abbiamo perció creato un test diagnostico sovrapponendo i punti di luminositá di quattro microquasar noti. Se i punti della SED di un dato UFO sono localizzati all'interno delle regioni definite dai punti dei microquasar noti, noi supportiamo l'ipotesi che l'UFO sia un microquasar. Circa 15 UFO del nostro campione sembrano essere verosimilmente delle sorgenti Galattiche, come i microquasar, Stelle di Neutroni ad elevata latitudine Galattica e pulsar. Questo risultato potrebbe essere di grande interesse, dato l'esiguo numero di tali oggetti nel catalogo 2FGL. Per questo motivo, ulteriori analisi sono in corso.

Facciamo notare che per 10 oggetti nessuna sorgente X, nei dati disponibili di *Swift*/XRT, é stata trovata all'interno dell'error-box di FERMI e, sebbene questo potrebbe essere dovuto al limitato tempo di esposizione delle osservazioni, finora essi possono essere considerati come i migliori candidati per eseguire ricerche di Materia Oscura. Infine, per i restanti UFO, non possiamo fornire nessuna univoca identificazione poiché multiple associazioni sono state trovate. Ulteriori osservazioni, in special modo nella banda X e radio, potrebbero consentire di risolvere questo problema.

Il secondo filone di analisi di questa tesi legato al campo delle osservazioni delle sorgenti Fermi nelle pi energetiche bande di energia, sfruttando i telescopi di terra. In particolare con il telescopio MAGIC, uno dei pi grandi sistemi stereo IACT, situato sull'Isola di La

Palma alle Canaria, a 2245 sul livello del mare. Tali dati ad altissima energia offrono preziose informazioni astrofisiche della sorgente.

In questa Tesi, un'analisi dati dettagliata della radiazione ad alta energia emessa da due *blazar* HBL, PG 1553+113 and 1ES 1011+496, verrá presentata. Entrambe le sorgenti sono state osservate in modalit stereoscopica con MAGIC, rispettivamente per un totale di 12 e 21 ore, con lo scopo di ottenere un completo studio dell'evoluzione temporale del flusso integrato e un'analisi dettagliata dello spettro differenziale ad alta energia.

Inoltre, le osservazioni MAGIC sono state compiute all'interno di una specifica campagna multibanda, e per PG 1553+113 la campagna osservativa fu anche pianificata in collaborazione con il team di WEBT, coinvolgendo diversi strumenti dell'emisfero nord che operano in differenti bande di energia.

Dati simultanei, con una buona copertura temporale, sono stati raccolti dal radio fino al regime di alte energie, consentendo di campionare l'intera SED. Il tipico comportamento spettrale a doppio picco, dovuto alla radiazione di sincrotrone e IC, viene esibita da entrambe le sorgenti, in accordo con gli attuali modelli di Synchrotron Self-Compton dei *blazar*. In piú, entrambe le sorgenti mostrano una minima (o assente) attivitá nelle banda ad alta energia, altissima energia e nella banda radio, mentre una palese variabilitá nell'ultravioletto e nell'ottico, collegato alle frequenze della parte dovuta al sincrotrone, é presente ed in special modo per PG 1553+113. Ad ogni modo, non é stata rivelata nessuna evidenza di episodi di flare. Per questa ragione (illustrate sopra), e grazie all'elevata qualitá delle loro SED, PG 1553+113 e 1ES 1011+496 sono state usate come test per verificare la bontá del tool di identificazione dei *blazar*.

Introduction

0.1 Aim of this Thesis

This PhD Thesis was conceived as a collaboration between the Department of Astronomy and Physics of the Padua University, the MAGIC group of the INFN Padua laboratory and the INAF team in charge for prototyping parts of the Cherenkov Array Telescope (CTA), in the general framework of the γ-ray astronomy. The research field of the γ-ray astronomy is a new and challenging discipline that, in spite of its recent birth, has rapidly grown and already achieved remarkable and promising scientific results. Indeed, in the last decades, the development of new instruments led up to a dramatic increase in the number of discovered γ-ray emitters.

Various different populations of astrophysical sources have been identified as γ-ray emitters, of both galactic and extragalactic origin, such as Supernova Remants, Pulsars and Active Galactic Nuclei. In recent years it has been suggested that γ-ray radiation can be also related to annihilation/decay processes of Dark Matter particles. Several celestial objects, where a high DM particle density is expected, have been considered as good targets to perform DM detection. Among them, the Galactic Center, the Galaxy clusters, the Dwarf Spheroidal Satellite Galaxies of the Milky Way, and, finally, clumps of DM overdensities within the DM halo of our Galaxy. The latter, the so-called *DM sub-halos*, are indicated by several numerical simulations in the framework of the hierarchical structure formation models as potentially detectable gamma-ray sources with a roughly isotropic distribution in the sky.

The long-term motivation of this PhD Thesis is the sky exploration looking for photonic signals from either decaying or annihilating DM particles at high photon energies, by combining the time-progressive all-sky survey by the Fermi space observatory with dedicated pointed observations from ground with Cherenkov telescopes.

Indeed, there are basically two kinds of detecting techniques for γ-ray sources that are sensitive to two different photon energy ranges. In the high energy (HE) regime, photons from 100 MeV to $\sim$ 100 GeV can be only detected by space-borne telescopes, based on tracking-calorimetry instruments, since the Earth's atmosphere is opaque at this energy range. The current generation of γ-ray satellites is representend by the italian detector *AGILE*[1] and by the *Fermi* satellite, launched in 2007 and 2008 respectively, and that constitute the most complete γ-ray source survey so far. Instead the very high energy (VHE) band (100 GeV - 10 TeV) is sampled using groud-based Cherenkov telescopes. These instruments are based on the *Imaging Atmospheric Cherenkov Technique* (IACT) and provide the analysis of astrophysical sources by the detection of UV-blue Cherenkov light emitted by particles of atmospheric showers induced by the interaction of cosmic rays (charged particles, as protons, or very high energy gamma rays) with heavy atmospheric nuclei.

Dark Matter is one of the hottest topics of physics, astrophysics and cosmology of today, and makes one of the major development lines of the next years. Identifying the corresponding electromagnetic signals in the huge energy range from the MeV to the TeV energy domain is considered the premier astrophysical approach to it (as opposed and complementary to the laboratory investigation).

This Thesis work has a final aim to carry out an all-sky search for DM signals at high photon energies. This is a long-range task that is not completed within the Thesis timeframe, but for which we offer a solid starting point for further future investigation. Operationally, our work developed along two parallel lines, however deeply related one with the other both ideally and programmatically. On one side, the DM signal search is performed by us using public all-sky gamma-ray data and looking for unidentified sources that may hide such signals. On the other hand, we complement this blind search with very high energy TeV observations of extragalactic gamma-ray sources for characterizing the most likely population of counterparts of the unidentified objects, the BLAZAR AGNs.

Our first line of investigation has adopted the Second Catalogue of the Fermi Gamma Ray Observatory (2FGL) as the main dataset for searches of new classes of extragalactic sources, DM objects candidates or unexpected high-energy phenomena. Indeed, while two thirds of the about 2000 sources in 2FGL are identified as known sources (*blazars*, pulsars, various kinds of Galactic sources, etc.), about 30% of them still lack an identification (the Unidentified Fermi

---

[1] *Astrorivelatore Gamma ad Immagini LEggero*

Objects, UFO), and offer the obvious best chance to search for DM sources. In this work we selected a suitable high-Galactic latitude sample of UFOs, avoiding the confusion effects in the Galactic plane. This makes our sample of 183 sources, at Galactic latitude $|b| > 20$, a data mine of objects for many of which we suggest a rather secure classification. To get this, we have developed new algorithms able to characterize the Spectral Energy Distribution of the various classes of objects believed as the most likely responsible for the emissions. In particular for the *blazar* identification tool, we build a code based on the use of a library of *bona-fide* multi-frequency SED templates of known objects belonging to the four *blazar* categories: High-peaked (HBL), Intermediate-peaked (IBL), Low-peaked BL Lac(LBL), and Flat Spectrum radio Quasar (FSQR). Therefore, through a multiwavelength approach, this code determines if a given UFO of our sample can be identified as a *blazar* object and in the same time to provide a redshift estimate still in the absence of spectroscopic observations (that are a well known problem for this kind of sources).

For the UFO classification we applied an association procedure, primarily based on the use of X-ray *Swift* satellite data available that cover the FERMI error-box (tipically of a few arcmins) associated to the γ-ray detection. If an X-ray bright source is revealed within the FERMI errorbox and if other sources at different wavelengths (from radio, IR and optical catalogues) are positionally coincident with the X-ray counterpart, we consider them as an unique source associated to the UFO. We hence perform a dedicated X-ray analysis for the X-ray counterpart found and finally build the UFO SED combining the available measured fluxes at different wavelengths recovered as explained before.

Then, we fit the found broad-band UFO SED by the adoption of the built *blazars* SED templates choosing the one that models the data maximizing the likelihood.

From this procedure, indeed we found that many of the UFO sources appear to very likely be *blazars* at an high redshift (like from z=0.4 to z=1). Instead for various other UFOs no typical *blazar* class SED matches their observed broad-band emission. Studying some features of their SED, as the curvature shape of their HE spectrum or the presence of a distinct bump in the IR-Optical band, they are turned out to likely be Galactic sources, as micro-quasars and high galactic latitude neutron stars, in any case a finding of great interest.

At this step, the remaining UFOs, for which no identification was found after applying our classification procedures, could be considered the best DM sub-halos candidates.

Our second line of investigation during the Thesis was in the field of very high energy (VHE) observations of Fermi sources with Cherenkov telescopes on ground, in particular with the MAGIC telescope, one of the largest IACT stereo system and situated on the Canarian island La Palma, at 2245 m a.s.l. Such VHE data offer an invaluable astrophysical information on the sources and in this Thesis the detailed data analysis of the VHE emission from two HBL *blazars*, PG 1553+113 and 1ES 1011+496, is described. Both sources have been observed in stereoscopic mode with MAGIC for a total of XX hours and XX hours respectively, in order to perform a complete temporal evolution analysis of the integral flux and a detailed study of the VHE differential energy spectrum. Moreover the MAGIC observations were performed in the framework of multiwavelength campaigns. As PI of the PG 1553+113 campaign, I have coordinates the multiwavelength observations for this source, in collaboration with the WEBT team and involved several instruments of different energy bands. Very simultanous data, with a good temporal coverage, were collected from radio to VHE regimes, allowing to sample the whole broad-band SED. The typical doubled bump shape, due to syncrothron and IC mechanisms, is exibited by the two sources and modelled with the current Synchrotron Self-Compton *blazar* model.

Both sources show a modest activity in the HE and VHE bands, while a clear variability in the other bands, related to the synchrotron bump frequencies, is present, however without evident flare episode. For this reason, these sources were used as *test objects* to verify the efficancy of our *blazar* identification tool (explained before) in recognizing AGN sources.

In addition, as member of the MAGIC collaboration, I took care the analysis of other observed objects by MAGIC, as the Galactic Center, several *blazars*, and some DM candidates, in particular the low-surface brightness galaxy Segue-1. In addition I have carried out a technical shift during the upgrade of the camera, on the trigger system, and tested the calibration, and several data taking shifts as Shift Leader.

0.2 Outline of the work

This thesis is divided according to the following structure:

In the **Chapter 1** there is an introdution about the gamma-ray astronomy and the main classes of astrophysical objects observed in the γ-ray band. Moreover a brief overview of the mechanisms of γ-ray production and absorption is described, as well as the main $agamma$-ray detection methods.

A description of the *Fermi* satellite and of the second released catalogue of γ-ray sources is presented in **Chapter 2**: here we describe some of the *Fermi* performances and provide a review about the second gamma-ray *Fermi* (2FGL) catalogue, its construction and the main classes of HE emitters identified. Among them the class of the Unidentified Fermi Objects (UFOs) is presented and considered as a new and very important component of the high energy sky since it may hide new class of AGN or Galactic source as well as Dark Matter candidates. In the last part we illustrate the selection criteria, applied to the 2FGL catalogue, to determine the UFO sample used in this PhD Thesis.

In the **Chapter 3** the positional association procedure performed on our sample of UFOs is explained. Starting with the X-ray imaging data, mainly of the *Swift* satellite, and using the entries of several catalogues (in radio, optical and IR band) we determine the best set of multi-frequency counterparts for each UFO of our sample. At this point we built the corresponding broad-band SED, whose data points will be inserted as input into the identification tools described in the Chapter 5.

Chapter 4 is focused on the class of the AGN, the main extragalactic emitters of VHE γ-rays and, in particular, on the *blazar* phenomenology. We describe the principal physic mechanisms associated to the *blazar* emission and the main characteristics of the *blazar* family with particular emphasis on the *blazar sequence*. Then we explain how the library of the multiwavelength averaged SED templates of XX known *blazars* is built. These SED templates are the cornerstone on which our *blazar* identification tool is based.

The **Chapter 5** is divided in two part. The first part is dedicated to the tools for the UFO identification, in particular for the recognition of *blazar* sources among the UFO sample, using the SED templates built in the Chapter 4. We describe the sequential steps necessary to find the best-fitting SED template that matches the SED data points of a given UFOs. To test the efficancy of our identification algorithm we test it on the MWL data, provided from dedicated campaigns described in the Chapter 7, of two well-known *blazar*, 1ES 1011+496 and PG 1553+113. In addition we present another diagnostic plot where the MWL SED of four microquasars are superimposed. It could help us to find these kind of Galactic sources hidden in our UFO sample. In the second part of this Chapter, the main identificatio results for some UFOs of our sample (the same of the Chapter 3) are presented and discussed. In addition, through a color-color diagram based on the ratios of the fluxes in radio, X-ray and γ-ray band, we obtain a cross-check about the validity of our suggested UFO associations.

The **Chapter 6** is addressed to the characterization of two Fermi sources in the VHE band. It is performed in the framework of the MAGIC observations. This chapter starts with a brief introduction about the IAC Technique on the basis of the groud-based telescopes for the indirect detection of the γ-rays. Moreover the whole MAGIC analysis chain is described in every step.

The **Chapter 7** is dedicated to the MAGIC observations of the two high-peaked BL Lac objects PG 1553+113 and 1ES 1011+496.

In the **Chapter 8** the DM physics will be introduced

Finally in the **Chapter 9** the conclusions of this PhD thesis are summarized, related to the UFO identification task and the main results about the characterization of the two *Fermi* HBLs subjected to the dedicated MWL campaigns.

1

Gamma-ray Astronomy

1.1 Gamma-ray astronomy. Generalities

1.1.1 Cosmic Rays and Gamma Rays

The 1912 was a revolutionary year for astrophysics, because the astronomers understand that, beyond the electromagnetic radiation, the Universe has another important messenger to interact with us. In that period the scientists were in front of a dilemma because from the first works performed by E. Rutherford and collaboration the radioactive contribution seemed higher than the predicted natural radiactivity level. A similar conclusion was found by Victor Hess, during his ballon-based experiments where he discovered that a gold-foil electroscope discharged spontaneously, even if they were kept away from natural radioactivity sources [53], and by Domenico Pacini which made a series of measurements to determine the variation in the speed of discharge of an electroscope (and thus the intensity of radiation) while the electroscope was immersed in a box in the sea [47].

In this way the Cosmic Rays (CRs), energetic particles from outer space, were discovered and intensively studied with space-borne and ground based detectors. This led to the birth of new astrophysics disciplines (from Particle to AstroParticle Physics), of new technologies and of the study of previously unknown interaction mechanisms in Physics and Astrophysics (among these the discovery of the so-called *Atmospheric showers* [Rossi+1933][Auger+1939]). Thanks to the works of Millikan and Compton, the extragalactic nature and the composition of the CRs were determined, concluding that the Earth is continuously hit by high energy particles composed mainly by charged particles (as protons (∼90%), heavy nuclei (∼9%) and electrons (∼1%)), by photons (∼0.1%) and by a very marginal fraction of neutrons and neutrinos. The energetic spectrum of the CRs, displayed in Fig 1.1, spans over a very wide energy range covering 13 order of magnitude in energy, from 10^9 to 10^{21} eV, and 32 order of magnitude in flux.

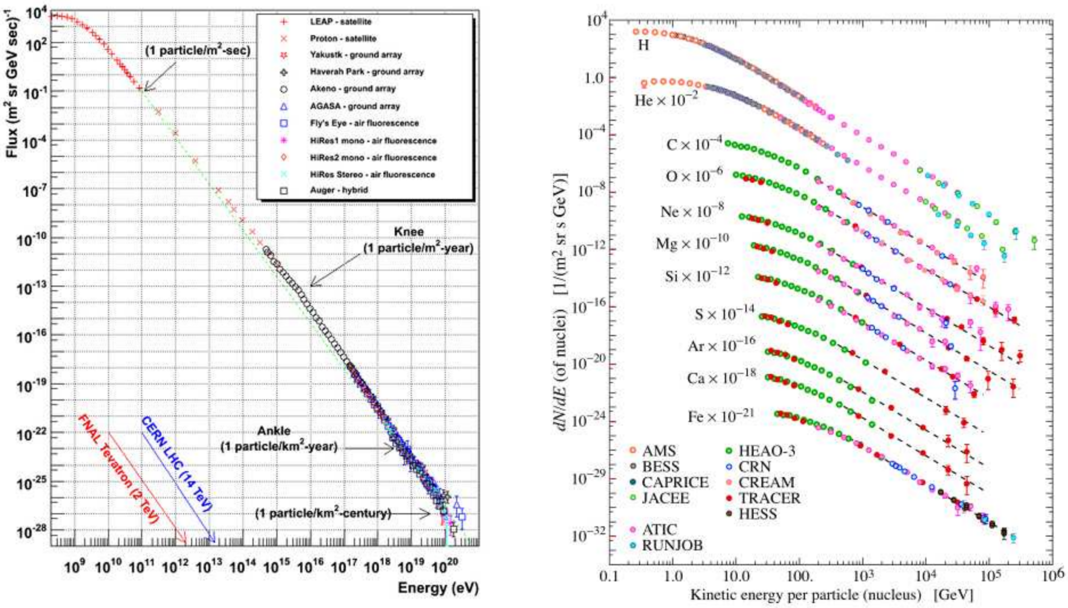

Figure 1.1: The energetic spectrum of cosmic ray as measured by different experiment. *Left*: Figure taken from [62].*Right*: The differential energy spectra of different CR species as a function of the kinetic energy [9].

,

It shows a typical power-law behaviour $N(E)dE \propto E^{\alpha}dE$, with two changes of the spectral index, which has the following values:

- α ∼2.7 up to E ∼$10^{15.5}$ eV (∼100 TeV)
- α ∼3 from E ∼$10^{15.5}$ eV to E ∼10^{18} eV
- α ∼2.6 from E ∼10^{18} eV.

The two regions, where the spectral index changes, are called *knee* at E ∼$10^{15.5}$ eV and *ankle* at E ∼10^{18} eV.

The spreading in energy would suggest a substantially different acceleration mechanism at different energy, however the lack of clear spectral feature implies some kind of universality in the origin of the particles which constitutes the CR population. According to studies about their chemical properties, CRs are divided in two classes: the CR with *galactic* origin, confined in our Galaxy and with energies up to $10^{15.5}$, and CR with *extragalactic* nature beyond the *knee* ($E\,10^{16}$).

Although the charged particles form about 98% of the total cosmic rays, only from the neutral CRs it is possible to extract information about their formation site. This is due to the presence of diffuse magnetic fields that fill the Galactic and intergalactic space and perturb the travel direction of the charged particles. Instead the neutral CRs are not deflected from their initial trajectory and preserve information about their origin and progenitors. Among the neutral CRs there are:

- Neutrons: they have a relatively short lifetime, of about 15 minutes, hence only a small fraction of the primary flux arrives at Earth;

- Neutrinos : unlike the previous particles, they have a very low cross section; hence very extended detector (with huge volumes of interacting material, as the IceCube observatory) are needed to detect and to reduce the signal-to-noise ratio;

- Photons : nevertheless they are a minor fraction of the cosmic radiation, they are more easily detectable and represent ideal messengers of the extreme Universe (in particular the γ-rays). They provide energetic and temporal information about the most powerful astrophysical objects, their acceleration mechanisms and formation sites, and on the propagation effects during the travel along the interstellar or intergalactic medium. The γ-ray emission is related to the acceleration of particles with energies above the TeV range and are located at the highest energy extremity of the electromagnetic spectrum in the energy range between 10^5 and 10^{20} eV (Fig 1.2). Conventionally this range is divided into energy intervals, which are associated with a given detection technique or physical interaction process:

    - *Low Energy* (LE): from 0.51 MeV to 10 MeV. The photons of this energy range are completely absorbed by the Earth atmosphere and therefore they can be observed by space-borne telescopes with scintillators.

- *Medium Energy* (ME): from 10 MeV to 30 MeV. They involve the Compton scattering and can be studied only by space telescopes.
- *High Energy* (HE): from 30 MeV to 100 GeV. These γ-rays can be detected only by calorimeters on board space satellite, as the *AGILE* and *Fermi* satellite, where the pairs production occurs starting from a primary γ-ray.
- *Very High Energy* (VHE): from 100 GeV to 100 TeV. These energetic γ-rays interact with the Earth atmosphere generating electromagnetic shower detectable by Cherenkov ground-based telescopes (for details see Chapter 6).
- *Ultra High Energy* (UHE) and *Extremely High Energy* (EHE): from 100 TeV to 100 EeV. These particles produce very extended atmospheric showers of secondary particles that can be detected by Air Shower Array of detectors (like the AUGER[1].

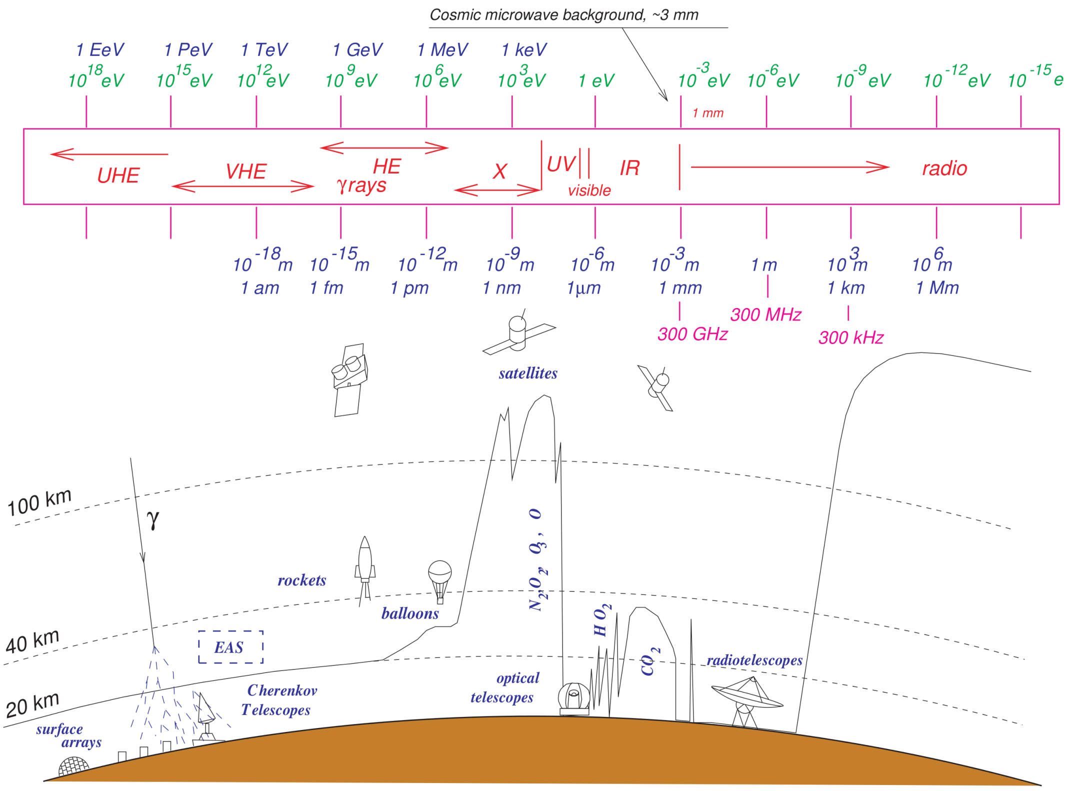

Figure 1.2: Graphical representation of the atmospheric windows for the observation of the Universe [45]. The continuous line indicates the height at which a detector can receive half of the total incoming radiation for every wavelength.

---

[1] http://www.auger.org/) observatory

Production of Gamma Rays

The γ-ray photons are associated to the most violent processes of the Universe and are produced by particles accelerated to very high energies. Hence the search for astronomical sources emitting γ-rays is closely linked to the study of regions of the sky in which hadrons or/and leptons of high energy.

In the following, we present a brief description of the main *non-thermal*[2] interaction processes of VHE photon production:

- *Synchrotron emission*

  When a relativistic charged particle (for example an electron of mass m_e) travels in a magnetic field, it undergoes an acceleration due to the Lorentz's force, spiraling around the lines of the magnetic field and emitting beamed radiation with frequency:

  $$\nu_s = \frac{eB}{\gamma m_e c} \tag{1.1}$$

  and a power described by:

  $$P = \frac{2e^2}{3c^3}\gamma^2 \frac{e^2 B^2}{m_e^2 c^2} v^2 sin^2 \alpha \tag{1.2}$$

  where $\gamma = (1/\sqrt{1-(\frac{v^2}{c^2})})$ and α is the angle between the velocity vector and the magnetic field. A generic spectrum of synchroton emission by relativistic electrons, displayed in Fig 1.3, is a continuum spectrum that increases following a power law up to a characteristic frequency $\nu_c = \frac{3}{2}\gamma^2 \frac{eB}{2\pi m_e}$ where the emitted power is maximum. For higher frequencies the spectrum follows a power law function $I(\nu)d\nu \propto \nu^{\alpha} = \nu^{(1-s)/2}$ where the spectral index α is linked to the energy distribution index s of the electrons.

- *Bremsstrahlung*

  The Bremsstrahlung emission is electromagnetic radiation produced by interaction of free charged particles (e.g. electrons) with the electrostatic field created by ions and atomic nuclei of an ionized gas. When the electrons interact with the electrostatic field, they are subjected to an acceleration, change their trajectory and can lose energy by radiation. The amplitude of the emitted radiation is proportional to this acceleration and the typical emission spectrum (Fig 1.4) is flat up to a cut-off frequency above which

---

[2] Unlike *thermal* processes where the radiation is emitted by thermal motion of charged particles in matter.

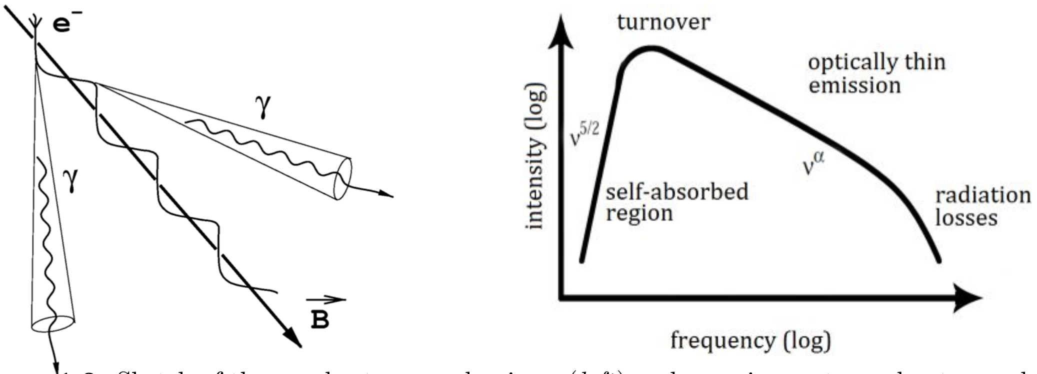

Figure 1.3: Sketch of the synchrotron mechanismc (*left*) and generic spectrum due to synchrotron emission (*right*).

the emission falls steeply. At lower frequencies a process of *self-absorption* occurs.

Bremsstrahlung is one of the most important emission processes in astrophysical enviroments containing ionized plasma. It is responsible for radio emission (the case of nebulae), or X-ray emission in the accretion disc of AGNs, but if the electrons are relativistic and have energies of few TeV the spectrum can achieve the gamma frequencies.

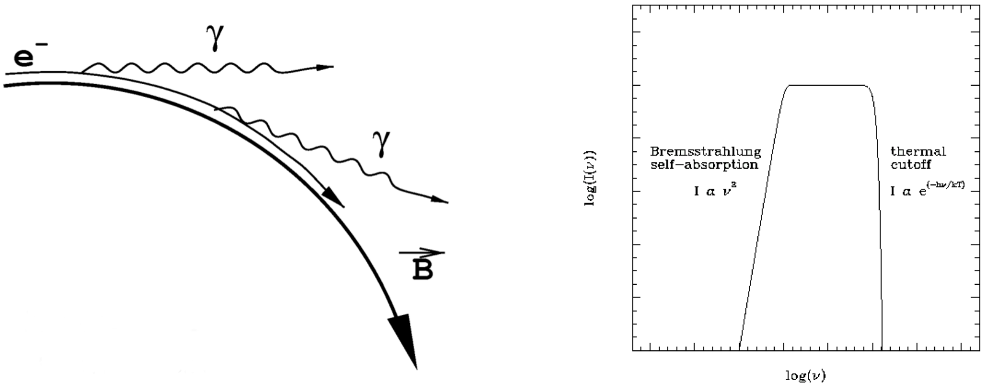

Figure 1.4: Sketch of the Bremsstrahlung mechanismc (*left*) and generic continuous spectrum due to Bremsstrahlung emission (*right*).

- *Inverse Compton (IC) scattering* When ultra-relativistic electrons scatter on low energy photons, part of their kinetic energy can be trasferred to these seed photons resulting in a production of VHE photons. The resulted energy of a photon, with initial energy

ϵ, and the corresponding change in wavelength are expressed as:

$$\epsilon_s = \frac{\epsilon}{1 - \frac{\epsilon}{m_e c^2}(1 - cos\theta)} \tag{1.3}$$

$$\lambda_s - \lambda = \lambda_c(1 - cos\theta) \tag{1.4}$$

where $\lambda_c \equiv \frac{\hbar}{m_e c}$ is the Compton wavelength and θ indicates the scattering direction.

The energy loss of the electron is given by:

$$\frac{dE}{dt} = \frac{4}{3}\sigma U_{rad}\beta^2\gamma^2 \tag{1.5}$$

where U_{rad} is the energy density of the radiation field and σ is the scattering cross section that, as a function of the energy ratio between the photons and electrons, can be expressed as:

$$\sigma \begin{cases} \simeq \sigma_T\big(1 - 2x + \frac{26x^2}{5} + ...\big) & \text{if} \quad x = \frac{h\nu}{m_e c^2} \ll 1 \quad \text{(Thomson regime)} \\ = \sigma_{KN} = \frac{3}{8}\sigma_T x^{-1}(ln2x + \frac{1}{1}) & \text{if} \quad x\frac{h\nu}{m_e c^2} \gg 1 \quad \text{(Klein-Nishina regime)} \end{cases} \tag{1.6}$$

where $\sigma_T = \frac{8\pi r_o^2}{3}$ is the Thompson cross section and r_o the electron radius.

The emitted radiation is a continuum spectrum with a maximum at the energy $E \sim 4\gamma^2 E_0$, that in case of γ-ray emission from astrophysical object peaks in the GeV-TeV range. The γ-ray spectrum is well described by a power law with spectral index α depending on the slope (Γ) of the accelerated electron distribution and on the energetic regime:

$$\alpha \begin{cases} = \frac{(\Gamma+1)}{2} & \text{if} \quad x = \frac{h\nu}{m_e c^2} \ll 1 \quad \text{(Thomson regime)} \\ = (\Gamma + 1) & \text{if} \quad x\frac{h\nu}{m_e c^2} \gg 1 \quad \text{(Klein-Nishina regime)} \end{cases} \tag{1.7}$$

- *Syncrhrotron self-Compton (SSC)*

This process occurs when in a magnetized region the electron and radiation densities are high enough to permit that the electrons emit synchrotron radiation, fill the region with photons and scatter on the same produced photons increasing their frequencies by IC up to γ-ray energies. The final spectrum shows a typical doubled bump shape, as in Fig 1.5, spanning from the radio to the GeV-TeV regime.

- *Fermi acceleration*

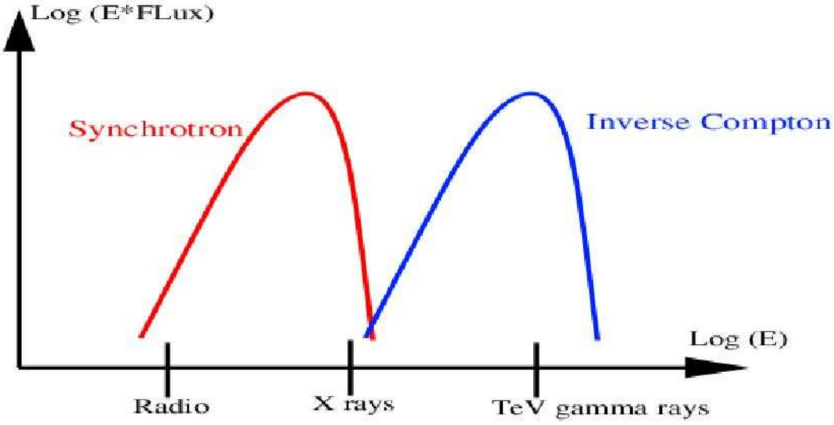

Figure 1.5: Typical doublep bump shape (in the plot log EF(E) versus E) of emission due to Syncrhrotron self-Compton process.

In 1950 Enrico Fermi proposed a new process of particle acceleration to explain the high energies observed for the cosmic rays. It is mostly related to cyclic reflection of charged particles by shock waves. They undergo an acceleration when being repeatedly reflected and, while crossing the shock front, the particle fractional energy gain would be of the order of the shock-front velocity reaching the observed energies in the CR spectrum.

This is thought to be the primary mechanism by which particles gain non-thermal energies in astrophysical shock waves. It plays a very important role in many astrophysical models, mainly of shocks including solar flares and supernova remnants.

- *Pion decay*

Charged and uncharged pions can be produced by inelastic scatterings between relativistic protons of sufficient energy[3] with nuclei of the interstellar medium:

$$pp \rightarrow pp\pi^{+}\pi^{-}\pi^{0} \tag{1.8}$$

They can subsequently decay according to the following decay channels:

---

[3] The minimum kinetic energy of a proton to produce pions is $E_{th} = \frac{2m_{\pi}c^{2}(1+m_{\pi})}{4m_{p}}$

$$
\begin{aligned}
&\pi^+ \to \mu^+ \nu_\mu \qquad \mu^+ \to e^+ \nu_\mu \overline{\nu_e} \\
&\pi^- \to \mu^- \overline{\nu_\mu} \qquad \mu^- \to e^- \nu_e \overline{\nu_\mu} \\
&\pi^0 \to \gamma\gamma
\end{aligned}
\tag{1.9}
$$

where the charged pions decay into muons and neutrinos by weak interaction and with a life-time of ~2.6×10^{-8}, whereas the neutral pions decay electromagnetically into two γ-rays.

The photon energy depends on the pion velocity ($v = \beta c$) and can be expressed as:

$$E_\gamma = \gamma m_{\pi^o}(1 + \beta cos\theta_\gamma) \tag{1.10}$$

where θ_γ is the angle between the pion velocity and the emission direction of the photon. The resulted spectum follows a power law with a spectral index α ~-2.5.

The γ-rays produced by pions decay are called *of hadron origin* to distinguish them from the γ-rays with electromagnetic nature.

- *Annihilation e^+e^-*

High energy electrons can be interact with positron to annihilate into γ photons:

$$e^+e^- \to \gamma\gamma \tag{1.11}$$

This can occur in a plasma where the positrons annihilate with cold electrons. The energy of the γ photons depends on the electron energy but it will be exactly the same for both photons. Assuming that the gamma photons are produced by annihilation of rest particles, their energy will be $m_e c^2/2$ and they will be emitted with an angle of 180°.

- *Dark Matter Annihilation and Decay*

Many observational evidences suggest that about 23% of the Universe is composed by non-baryonic matter, called Dark Matter (DM). In particle physics there are many theories beyond the Standard Model, i.e. Supersymmetric models and Extra-dimensional theories, that provide particles with suitable characteristics for being good DM particle candidates. In such models these DM candidates are self-annihilating particles into stardard particles and γ-ray photons. The typical DM annihilation γ-ray spectrum is predicted to be continuous, universal and characterized by some spectral features, like a cut-off and a spectral hardening, depending on the mass of the DM particle. Some details about this process will be discussed in the Chapter 8.

To summarize, the domination of one process over another depends on the energy range and on environments where the process occurs. In general the main processes involved in the astrophysical sources are neutral pion-decays, IC scatterings and SSC mechanisms.

Gamma-Ray Absorption

1.2 Classes of Gamma-ray emitters

In this section we briefly describe the main characteristics of the most important classes of galactic and extragalactic γ-ray emitters. Thanks to the rapidly development of γ-ray detectors, on-board satellites or as groud-based telescopes, the number of γ-ray sources is considerably increased, as shown in the skymaps displayed in Fig 1.6, counting almost 2000 objects in HE band and 124 in VHE. As said before, the γ-ray emission is due to non-thermal processes that involve the presence of intense magnetic fields and mechanisms of particle acceleration. In general the γ-ray emission from galactic sources is detected up to higher energies with respect to the extragalactic sources.Indeed the energy range of emission is determined by the size of the sources, the strength of its magnetic field and the possible absorption effects of γ-rays that occur during the path from the source to the observer. Since the EBL attenuation is a function of the distance, the extragalactic sources are more affected by this absorption, as opposed to tha Galactic objects for which it is negligible.

1.2.1 Galactic sources

The study of γ-ray emitters within our Galaxy is a very important task because most of them are detected as extended objects and it is possible to investigate, in addition to their emission, also their morphology. The galactic sources are divided in extened sources, where the emission is thought depending on the conditions of the surrounding enviroment, and point-like sources with the emitted radiation associated to the formation of jets and relativistic particles flows.

The main counterpart classes of these Galactic VHE sources are:

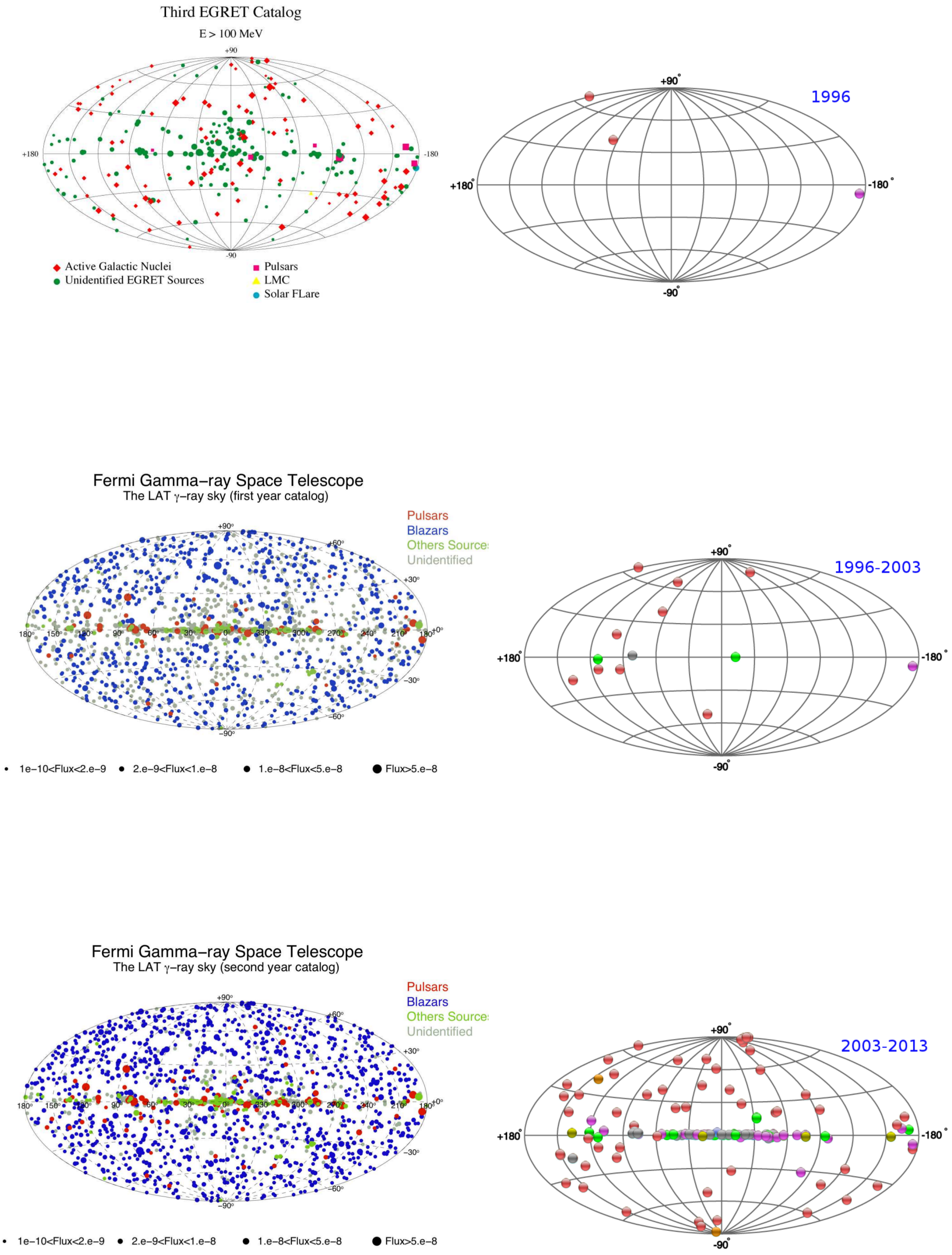

Figure 1.6: HE and VHE sky evolution. On the left side the sky map of the number of γ-ray sources in HE band, from the last EGRET catalogue (*top*) to the second *Fermi* catalogue. On the right side the increasing of the VHE sources from the first detection until today where more than hundred objects have been detected.

Pulsars

Pulsars are neutron stars that, with a radius of about 10 km and a mass of ∼1.4 $M_\odot$, are one of the most dense objects of the Universe. They are characterized by a very high rotational velocity (with rotational periods of the order of a few milliseconds/seconds) and by a strong magnetic field up to $\sim 10^{13}$-10^{15} G. These objects present an intense wind of relativistic particles that, interacting with the magnetic fields, are accelerated and emit synchrotron and IC radiation, from the radio to γ-ray band. The emission is collimated along the axis of the magnetic field which is thought misaligned with the pulsar rotation axis to take into account the pulsed signal observed in a number of such objects (Fig 1.8).

According to the emission model, the predicted γ-ray spectrum follows a power law with an exponential cut-off above a few GeV if the primary γ-rays are produced close to the magnetic poles and a strong absorption due to the magnetic field is expected (*polar-cap model* ([22],[23]), otherwise the cut-off is located at energies above 100 GeV if the γ-ray production occurs in a region far from the star (*outer-gap model* [51]). It is important to note that the class of pulsars is the most populous in the HE band among the galactic γ-ray sources.

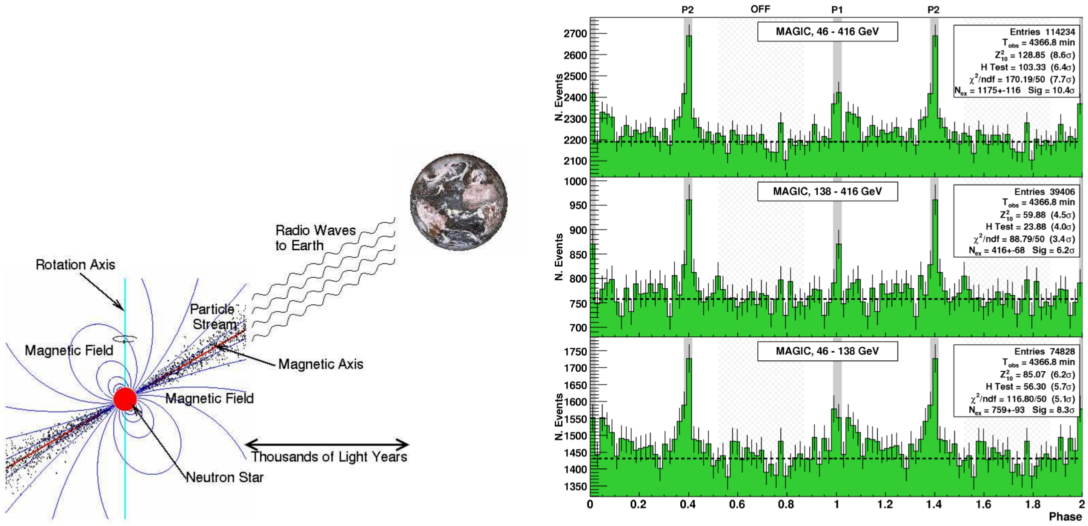

Figure 1.7: *Left*:A sketch of the model of a pulsar as a magnetised rotating neutron star in which magnetic and rotational axis are misaligned. *Right*: The γ-ray pulsed signal from the Crab Pulsar, for three ranges of estimated energies (from 40 GeV to 400 GeV), taken from [8].

Supernova Remnants (SNRs)

When a massive star ($\geq$12-30M$_\odot$) exhausts its fuel of light elements, as hydrogen and helium, which support the thermonuclear reaction, it undergoes a fast collapse by gravitational pressure which is no longer balanced by the thermal pressure. In the core of the star, mainly composed by Fe and Ni, the gravitational pressure begins to be counteracted by the neutron degeneracy pressure. As said above, neutrons should decay in about 15 minutes, but in this case the Fermi level is completely filled and for this reason there is no energy gain in the neutron decay. During the collapse of the core, a huge amount of energy is released in the form of neutrinos and heat. It results in a violent and brilliant explosion called supernova (SN) [45] where the surrounding envelope is blown away at speeds in excess of 15000 km s^{-1}, leaving as a result a compact Neutron Star (the core remnant).

A SNR is the structure resulting from this explosion. It consists of material ejected by the explosion and is bounded by an expanding shock wave. It interacts, as shocks, with the interstellar medium. SNRs are considered as good site for acceleration of galactic cosmic rays by successive collisions with the magnetized medium and by the Fermi mechanism. The resulted broad-band spectrum is thought being the superimposition of several synchrotron and IC spectra generated by different electron populations. In addition to the electrons, also the hadron particles contribute substantially to the γ-ray spectrum, especially in the VHE band, through *pp* interactions with the molecular clouds surrounding the SN progenitor. To discriminate between the hadronic and leptonic contribution is very difficult and this argument is still under debate.

Binary systems and Microquasars

X-ray binary systems (XRB) are generally constituted by a compact object and a companion star. The compact object can be a white dwarf (WD), a Neutron Star (NS) and a Black Hole (BH). XRB are usually classified as Low Mass X-ray Binaries (LMXB) and High Mass X-ray Binaries (HMXB): the former are characterised by a high mass companion star (higher than the compact object mass), while the former by a low mass companion star (often lower than $\sim$ 1 M$_\odot$). In LMXBs, usually the companion star has evolved towards the red-giant branch, filling its Roche-lobe, while in HMXB strong stel-

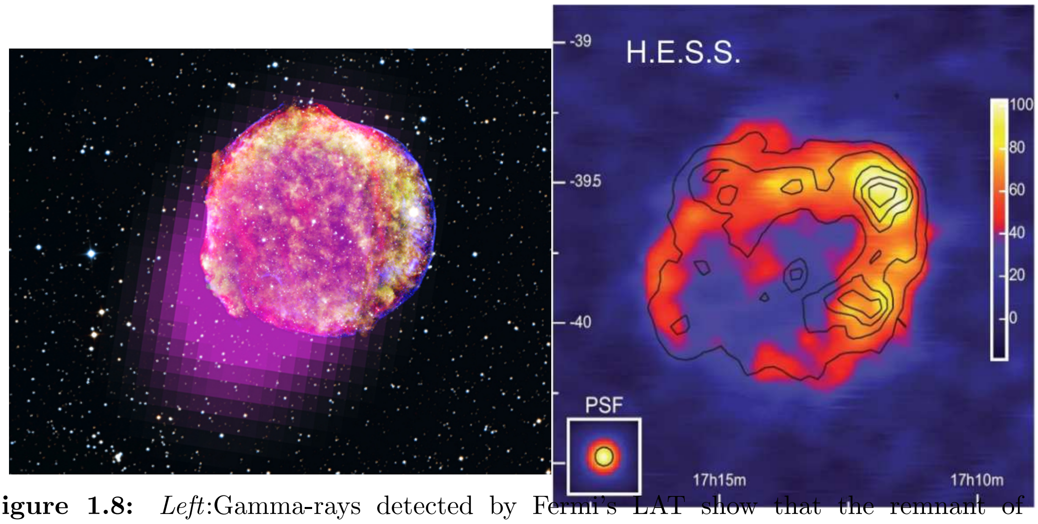

Figure 1.8: *Left*:Gamma-rays detected by Fermi's LAT show that the remnant of Tycho's supernova shines in the highest-energy form of light. This portrait of the shattered star includes gamma rays (magenta), X-rays (yellow, green, and blue), infrared (red) and optical data. (Credit: Gamma ray, NASA/DOE/Fermi LAT Collaboration; X-ray, NASA/CXC/SAO; Infrared, NASA/JPL-Caltech; Optical, MPIA, Calar Alto, O. Krause et al. and DSS). *Right*: HESS image of the SNR RX J1713.7-3946 at energies above 190 GeV with the ASCA (X-ray 1-3 keV) contours superposed [34].

lar winds are not negligible. In both cases, material from the companion star is driven towards the Roche lobe of the compact object. Therefore X-ray emission is produced as the gravitational potential energy of the accreting material is released in form of high energy photons. At specific accretion rate and in the proximity of the compact object, the energy of the accreting material is higher than that necessary to escape from the system and, for this reason, it is common to observe two relativistic jets ejected by the innermost regions. The jets are leaded along the rotation axis of the disc and their emission is mainly produced by sinchrotron emission and inverse compton scattering. Accreting X-ray systems where jets are clearly detected are called *microquasars* as they resemble the same physical properties identified in extragalactic quasars. They were proposed to be GeV-TeV emitters because the jets contain relativistic particles emitting VHE photons by IC scatter. Furthermore, in HMXB, interactions between relativistic winds produced by the accreting compact object and the accreting flow from the companion star are also expected to produce the observed VHE emission.

Pulsar Wind Nebula (PWNe)

A Neutron Star surroundend by a nebula is called *Pulsar Wind Nebulae*, and consists

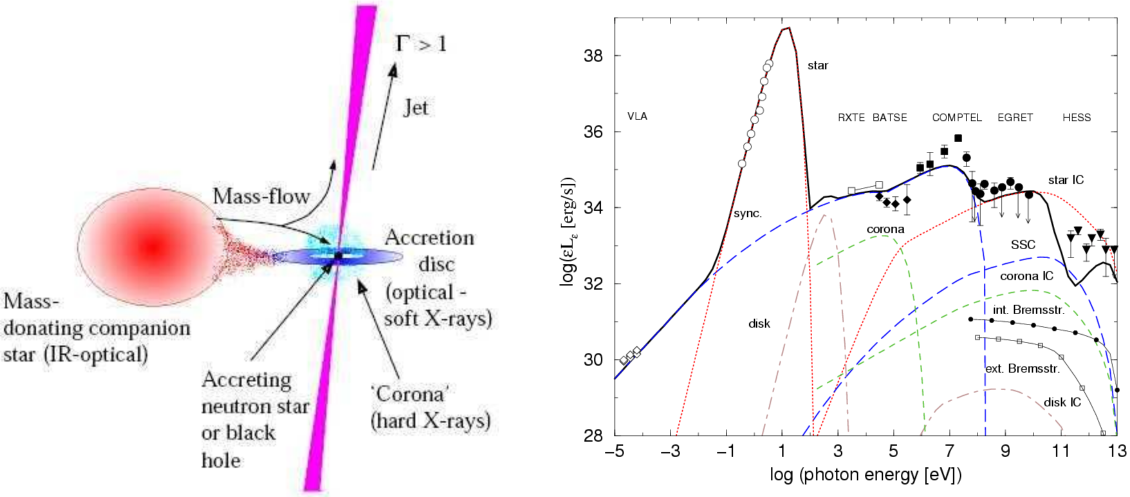

Figure 1.9: *Left*: A schematic model of a microquasar powered by a compact object through mass accretion from a companion star. *Right*: Spectral Energy Distribution of the microquasar LS 5039; (the observations were not taken simultaneously). Image taken from [48].

of bubbles of relativistic particles and magnetic fields created when the ultrarelativistic wind from the pulsar interacts with its local environment. Th emitted spectrum is composed by synchrotron radiation which extends up to X-ray emission and at higher energies by IC emission of electrons scattering on the background radiation. The Crab Nebula (Fig 1.10) is the most common and studied PWN, used as standard candle in the field of the γ-ray astrophysics for the calibration of the space and ground-based detectors.

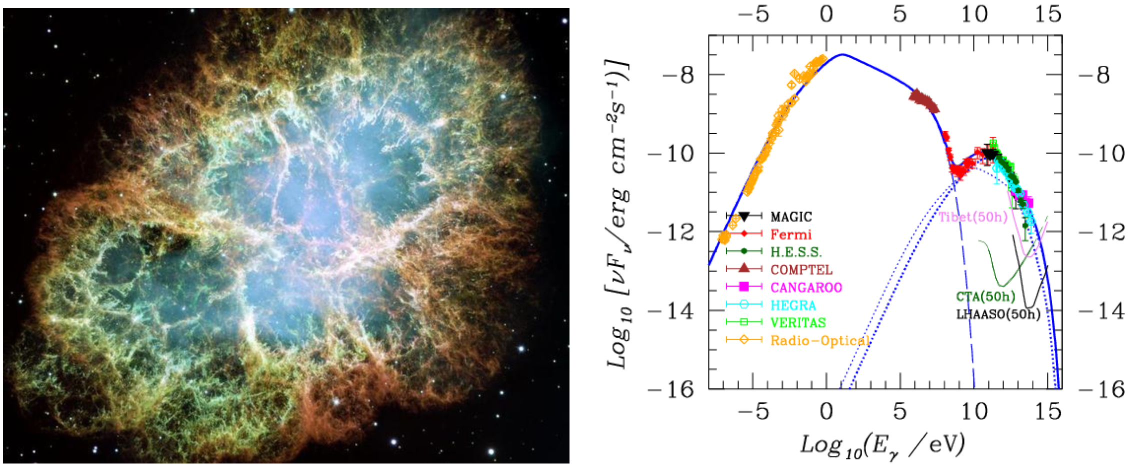

Figure 1.10: *Left*. *Right*: Spectrum fitted to the stationary component of radiation from Crab Nebula. The solid line shows the total spectrum. The dashed and the dotted lines represent the synchrotron and the inverse-Compton emissions, respectively. (Figure taken from [37]).

1.2.2 Extragalactic sources

There are basically two classes of extragalactic sources that emit in the γ-ray band:

Active Galactic Nuclei (AGN) and *blazars*

It is currently accepted that about 1% of the galaxies host an active supermassive black hole at their center. With respect to the remaining host galaxy, this central region is characterized by a very intense and highly variable non-thermal emission.

Most of the AGNs detected in the γ-ray regime are *blazars*. They are radio-loud AGNs characterized by a compact radio core, extreme variability (in amplitude and timescale) at all frequencies and high optical and radio polarization. In the unification scheme (4.1.1), all of these properties are interpreted as a result of the large relativistic beaming of the jet radiation when the jet axis is close to the line of sight. The emission of blazars is dominated by the non-thermal continuum of the jet, with SED extending from radio to γ-rays and showing double bump shape typical of the SSC mechanism.

The Chapter 4 of this PhD Thesis is mostly focused on this kind of γ-ray sources where a description of the different subclasses of AGN, their phenomenology, physics and modeling is provided.

Gamma-ray Bursts (GRBs)

The last category of γ-ray emitter is the Gamma Ray Burst class. These objects have been detected for the first time in the late 60^s [36]. They are transient events which show a duration ranging from a fraction of second (*short* GRBs) up to few hundreds of seconds (*long* GRBs), characterized by an intense and impulsive emission of soft γ-rays (<MeV), where an huge quantity of released power, of the order of 10^{48-53} erg/s, is involved. In the time interval when a GRB occurs, it became the most luminous γ-ray source of the whole sky. The γ-ray emission is usually followed by a subsequent *afterglow* emission from the X-ray to the radio energies observed for several days or weeks.

Their isotropic distribution in the sky, (as shown in Fig 1.11) suggested an extragalactic origin for these objects. This was confirmed from measurments of their redshift, finding z between 0.0085 and 6.7.

Although already detected in the HE regime, no GRB emission has been detected in the

VHE domain, despite several intensive follow-up observations of GRB alerts are continually performed by the ground-based telescopes triggered by X-ray and HE monitoring.

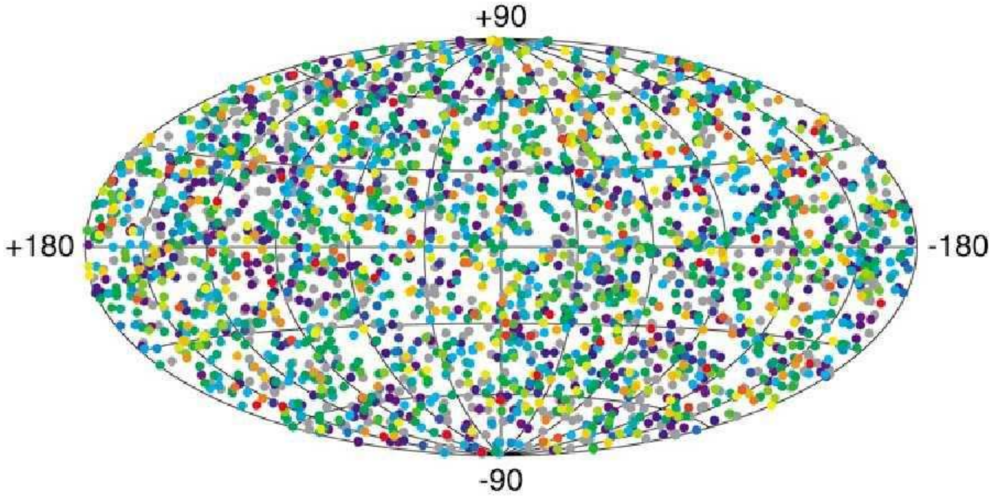

Figure 1.11: Distribution of the 2704 GRBs detected by the BATSE observatory from 1991 to 2000 [61].

1.2.3 Exotic sources: Dark Matter (DM) objects

In the ΛCDM cosmological scenario about 80% of the matter of our Universe is believed to be constituted by cold, neutral, non-baryonic, weak-interacting stable particles [56]. Among the huge plethora of DM candidates, the best motivated ones are related to the Super Symmetrical and Extra Dimensional extensions of the Standard Model of particle Physics [15] that provide self-annihilating DM particles into γ-ray photons and/or standard particles.

Since the expected gamma-ray flux from DM annihilation is proportional to the square of the density of DM, the best search targets are those astrophysical objects where high DM concentration is expected. Among them, the most probable ones are the Galaxy Clusters, the Galactic Center, the dwarf Speroidal Satellite Galaxies of the Milky Way and the overdensity clumps (so-called *DM sub-halos*) of the no-smooth DM halo of the our Galaxy.

These exotic sources, and in particular the DM sub-halos, will be described in Chapter 8 of this PhD thesis, where also an overview about the theory of γ-ray emission from DM annihilation will be presented.

1.3 Detection of gamma-rays

In this Section the main experiments and instruments for the γ-ray detection will be described. Since the γ-ray spectrum spans several orders of magnitude in flux and energy, only one type of instruments would be constrictive to have a complete picture of the phenomenon. Moreover, due to their relatively high energy, γ-ray photons cannot be focused using telescopes formed by a classical reflector surface, as done for example in the optical and radio energies, but using an instrument that is much more similar to a particle detector. There are two kinds of γ-ray detectors: the *space-borne* satellites, mainly required to sample the electromagnetic spectrum from the MeV energies up to a few GeV that is completely absorbed by the Earth atmosphere, and the *groud-based* telescopes that thanks to their bigger collected area are able to detect the γ-ray emission above 50 GeV.

Direct detection and Space-borne telescopes

For energy up to few hundred of GeV, the detection can be done in a *direct way* using the so-called pair-conversion telescopes, on space-borne satellite.

These detectors consist of a *converter* where a γ-ray photons can interact with matter, producing an e^+e pairs. The created pairs are then detected by a *tracer*, composed by several producer modules, where their direction and local energy loss are estimated making possible the reconstruction of the primary γ-ray incoming direction. Finally e^+e can start a particles cascade within a *calorimetry* module in order to estimate the energy of the incoming γ-ray photon.

For this kind of instruments, the observable energy range depends on the depth of the calorimeter and on the collected area. With a typical collected area of $\sim$1 m^2, they are able to detect photons with energies of the order of a few GeV because for higher energies the γ-ray flux rapidly decreases under the instrument sensitivity. Moreover thanks to their big *field of view*, of the order of some steradians, they can perform scans of the whole sky in a few hours.

The first γ-ray observations, carried out from space, were performed since the beginning of 60^s and among the most important instruments of the past, we can remember the *SAS-II* and *COS-B* missions and the *Compton Gamma ray Observatory* (CGRO) [30] with onboad the *Oriented Scintillation Spectrometer Experiment* (OSSE), the *Imaging Compton Telescope*

(COMPTEL) and the *Energetic Gamma Ray Experiment Telescope* (EGRET). The current generation of space-based γ-ray instruments is represented by two observatories: the *Astro-rilevatore Gamma a Immagini Leggero* (AGILE) [58] and the *Fermi* telescopes. The main characteristics of the latter and the second catalogue of γ-ray sources released from the *Fermi* collaboration are presented in Chapter 2.

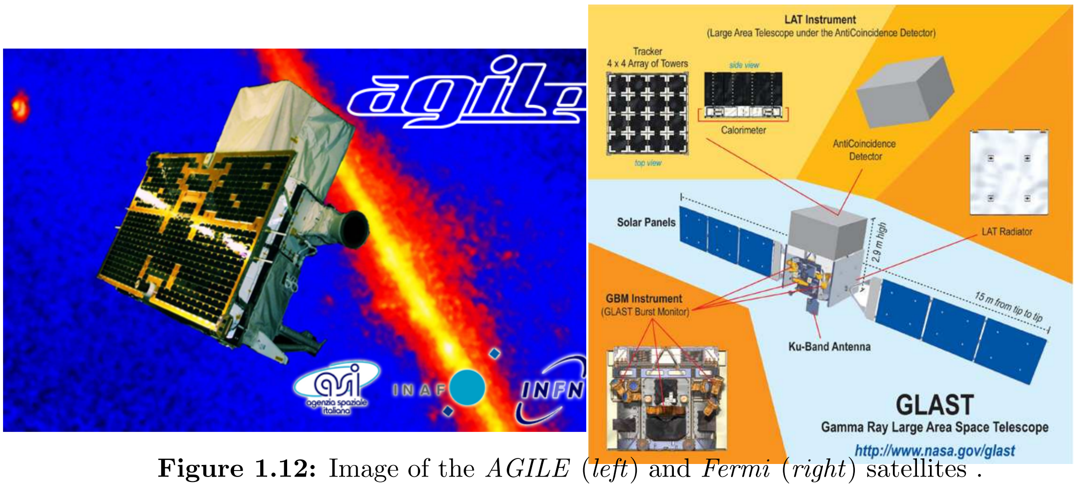

Figure 1.12: Image of the *AGILE* (*left*) and *Fermi* (*right*) satellites .

Indirect detection and Ground-based telescopes

For energies above $\sim$ hundreds of GeV, the direct detection of the γ-ray photons is hampered because the space-based instruments are not able to reconstruct the incoming direction and the energy of the primary γ-ray. At such a high energy, groud-based telescopes, based on a *indirect methods* of detection, are used. Moreover, being constructed on the groud, it possible to have larger collected area detectors combined with long exposure times for the observations.

There are two different types of instruments:

The Imaging Atmospheric Cherenkov Telescopes (IACTs):

These telescopes detect γ-ray photons with energies between 100 GeV - 10 TeV through the IAC Technique. This technique is based on the detection of UV-blue Cherenkov photons emitted by very fast charged particles of atmospheric showers initiated by the interaction of cosmic rays (charged particles, as protons, or very high energy γ-rays) with heavy atmospheric nuclei. Cherenkov photons, produced by each shower, are reflected and form an image in the focus plane. These images are then recorded and analyzed. The γ-ray signal is discriminated from that due to charged particles (the main source

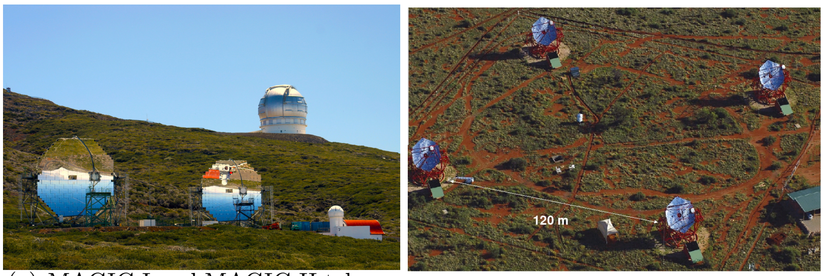

(a) MAGIC-I and MAGIC-II telescope in stereo system.

(b) HESS Telescope Array.

(c) VERITAS Telescope Array.

Figure 1.13: A overview of the main groud-based Cherenkov telescopes.

of background), and its energy and incoming direction can be estimated.

Thanks to the bigger mirror dishes, and consequently to a larger collected area, these telescopes have a better sensitivity in the VHE regime with respect to the satellites, but unlike the latter, their smaller field of view allows to observe only one object for each pointing.

The current generation of IACTs comprises three important experiments: the *High Energy Stereoscopic System* (HESS), an array of four 10 meter diameter telescopes installed in Namibia, the *Very Energetic Radiation Imaging Telescope Array System* (VERITAS), an array of four 12 meter optical reflectors in Arizona, and the *Major Atmospheric Gamma-ray Imaging Cherenkov* (MAGIC) telescope, a stereo system of two 17 m diamater telescopes located at the Roque de los Muchachos Observatory on the Canary Island of La Palma. For latter the performances and the main steps of the data analysis chain will be described in the Chapter 6.

The extensive air shower arrays (EAS array):

The extensive air shower arrays are a number of several scintillation detectors or water Cherenkov detectors distribuited over a large area of several km^2. They directly detect the secondary particles of an EAS that reach the observatory altitude. A typical

(a) Surface Detector Stations of AUGER. (b) ARGO experiment in Tibet

(c) MILAGRO Gamma-Ray Observatory

Figure 1.14: A overview of the most important EAS array.

air shower detector has an effective field-of-view of 2 sr and operates nearly 100% of the time. Among these important experiments there are the *AUGER* observatory in Argentina, the *Milagro* experiment situated in New Mexico and *ARGO-YBJ* in Tibet.

2

The Fermi mission and the second gamma-ray catalog

2.1 The Fermi instruments and design

The first all-sky survey in the energy band above 50 MeV was performed by the EGRET instrument on board the *Compton Gamma-Ray Observatory*, with the aim to explore the high energy sky and perform observations of gamma-ray emitters. Its heir is the *Fermi* satellite, formerly called *Gamma-ray Large Area Space Telescope*, built thanks to an international collaboration with contributions from space agencies (NASA and United States Department of Energy), high-energy particle physics institutes and universities in the United States, Italy, France, Japan and Sweden. It was successfully launched by NASA in June 2008 on a Delta II Heavy launch vehicle into an elliptical near-Earth orbit, at a height of 565 km off the surface of the Earth. It is also designed to scan the whole sky in the *scanning* mode, which can provide in about 3 hours an uniform all-sky map in the energy range from below 20 MeV to more than 300 GeV.

The main scientific aims of this satellite are:

- to explore the most extreme objects in the Universe and to create an all-sky catalog of high energy sources, providing information about their localization in the sky and spectra from 20 MeV to 50 GeV;

- to understand the mechanisms of particle acceleration operating in main astronomical gamma-ray emitters, particularly in active galactic nuclei, pulsars, pulsar wind nebula and supernovae remnants;
- to study the black hole accretion physics;
- to determine the nature of the unidentified γ-ray sources and the origins of the diffuse emission revealed by EGRET;
- to probe and identify the nature of the Dark Matter from γ-ray observations;
- and finally to study the most powerful explosions in the Universe, better known as Gamma-Ray Bursts.

In order to achive these objectives, the *Fermi* telescope is equipped with two instruments (Fig 2.1-*left*): the *Gamma-ray Burst Monitor* (GBM) and the *Large Area Telescope* (LAT).

The GBM consists of 12 thallium-activated sodium iodide scintillation counters and two bismuth germanate scintillation counters that cover the energy ranges from 8 keV to 1 MeV and from 200 keV to 40 MeV, respectiverly. They are designed to detect transient sources and Gamma-ray Bursts, to estimate their location in sky and to alert the astronomical community to perform follow-up observations at other wavelengths, sending an instant alert to the astronomical community.

The LAT instrument is an imaging, wide field-of-view, pair-convertion telescope, sensitive to γ-rays of energy between 100 MeV and 300 GeV, with an effective area of 9500 cm^2 and a field of view of 2.5 sr (at 1 GeV). It is designed to estimate the directions, the energies and the times of arrival of γ-rays, which are converted into an e^+ e^- pair and generate electromagnetic cascades inside the telescope detector. Moreover it makes use of an on-board event processing to reject the background contamination triggered by cosmic-ray particles, maximizing the number of events associated to γ-rays. These information are then trasmitted to the ground.

As shown in Fig 2.1-*right*, the LAT consists of three detector subsystems: a precision converter-tracker, a calorimeter and a segmented anti-coincidence detector. The *tracker* is formed by 16 planes interleaved with position-sensitive detectors of high-Z material (tungsten) and divided in two sections with notable differences in performance, especially with respect

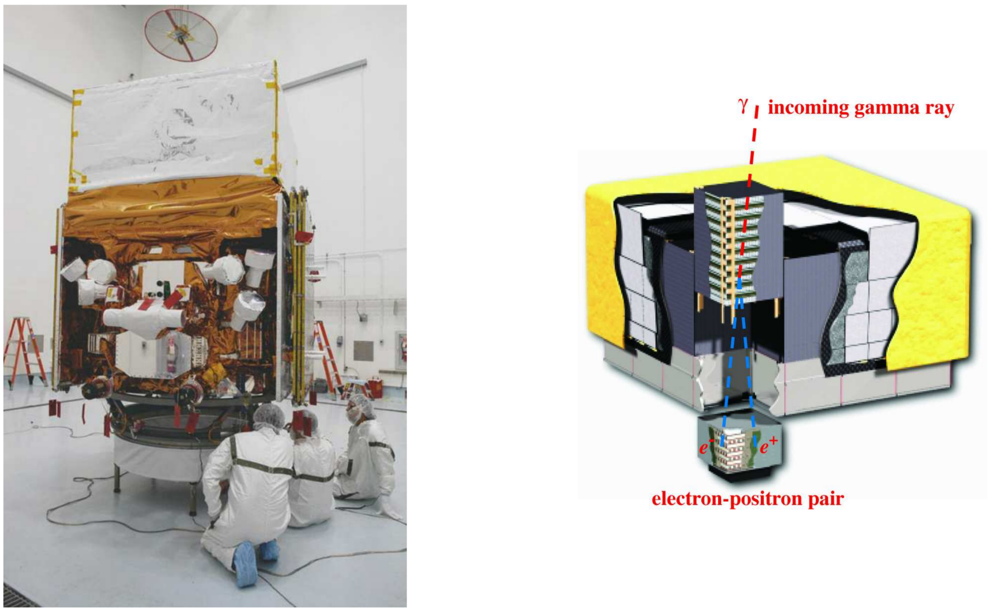

Figure 2.1: *Left*: A picture of the *Fermi Gamma-Ray Space Telescope*. Photo credit: NASA/Kim Shiflett. Picture adopted from [43].*Right*:Schematic view of the Large Area Telescope, adopted from [11]..

to the PSF and background contamination: the *thin*, or *front*, section composed by the first 12 paired layers and farthest from the calorimeter, and the the *thick*, or *back*, section formed by 6 layers with thicker tungsten converter[1]. In there the incident γ-rays can be converted into electron-positron pairs and the tracks of these charged particles are recorded and used at a later stage to reconstruct the incoming direction of the primary γ-ray. Connected to the tracker, a *CsI(Ti) crystal 3D imaging calorimeter* permits to measure the energy released by the γ-ray photons into the electromagnetic particle shower generated by the e^+ e^- pair and to image the development of the shower profile. In this way a first important background discrimination is provided. Moreover an energy leakage corrections is applied, especially for energies of the showers greater than a few GeV in which leakage might be stronger, allowing an enhancement of the energy resolution. Both the tracker modules and the calorimeter are enclosed in the *Anticoincident detector* (ACD) with an active area of about 8.3 m^2 divided in 89 individual sections that surround the top and four sides of the LAT. The ACD is the main instrument for the charged-particle rejection, with an efficiency over 99.7%, where the gamma-rays cross freely its thin plastic scintillator tiles while the cosmic rays produce a flash

---

[1] The tracker is divides into two distinct instruments to satisfy the need to balance two basic (and somewhat conflicting) requirements: simultaneously obtaining good angular resolution and a large conversion probability.

of light and hence are recognizable and rejected. A more detailed description about the structure of the LAT components can be found in [11], [33] and [5].

Thereafter, the data collected by the Tracker, Calorimeter, and ACD subsystems are carried to the Data Acquisition System (DAQ). Through an onboard multi-event triggering process, running in parallel different filter algorithms, it selects and records the most likely γ-ray candidate events reducing the number of events that will be trasmitted on the ground. In addition to the hadronic-induced showers recognized as background events, there is another source of noise, the so-called *ghost events*. In other words, the remnants of electronic signals from particles that traversed the LAT a few μs before the particle that triggered the event. Such events complicate the analysis and event reconstructions, deteriorating the performance of the instrument especially at the lower energies. Moreover the LAT performs a rapidly onboard science analysis in order to search for transient sources.

ight data. They affect all of the subsystems, significantly complicate the event reconstruction and analysis,and can cause serious errors in event classification:

2.1.1 Performance of the Fermi-LAT

In this section we summarise the performance of the LAT instrument (Table 2.1). The main ingredients that determine the LAT performance are the hardware design, the algorithm for the event reconstruction and the method of discrimination between the γ-ray signal and the background events. Thanks to the Instrument Response Functions (IRFs), generated by full detector Monte Carlo simulations of γ-rays and calibrated in beam tests and updated via on-orbit measurements, the key performance parameters are described as function of photon energy, incidence angle and conversion point within the instrument.

We present the plots of three main parameters: the effective area, the PSF, and the energy resolution. We show and compare the performance plots of IRF versions *P7SOURCE_V6*, used to construct the second Fermi source catalog (2FGL), and the latest version *P7REP_SOURCE_V15* which corresponds to the currently status of the instrument and analysis.

The effective area is a measure of the efficiency of the LAT for detecting γ-rays. The parameters that mainly influence the effective collecting area are the cross section of the LAT and the efficiency for identifying the incident γ-rays, related respectively to the inclination

Performance parameter	**Value or Range**
Energy range	20 MeV - 300 MeV
Field of View	2.4 sr
Event Readout time (dead time)	26.5μs
Effective Area at normal incidence	9500 cm^2
Energy resolution (equivalent Gaussian σ)	
100 MeV - 1 GeV (on axis)	9%-15%
1 GeV - 10 GeV (on axis)	8%-9%
10 GeV - 300 GeV (on axis)	8.5%-18%
Single Photon angular resolution (on axis, $\theta_{68\%}$)	
100 MeV	3.5°
1 GeV	0.6°
$>$ 10 GeV	<0.15°
on axis, 95% containment radius	$< 3\times\ \theta_{68\%}$

Table 2.1: Key LAT instrument parameters and estimated performance.

angle and energy of the incoming photon. In Fig 2.2 we plot the effective area as function of the energy and the incidence angle (for a given energy of 10 GeV) for the front and back sections of the LAT separately and for the two IRF versions considered.

In Fig 2.3 the LAT energy resolution is shown and it represent the error on the reconstructed energy with respect to the true energy of an incoming γ-ray photon. It remains approximately constant in the energy band ranging from 1 GeV to 100 GeV, while shows a worsening and a strong energy-dependency at lower and higher frequencies.

Another key performance parameter is the PSF. Its value is determined by the containment radius of the incoming γ-ray distribution and its profile, especially at lower energies, is affected by multiple scatterings that hamper the track reconstruction. It is important to note that this parameter is crucial for the localization and the estimate of the positional error ellipse of the sources detected by Fermi. The 68% and 95% angular containment radii of the PSF, as function of the energy, derived using the in-flight data for the IRF version *P7SOURCE_V6* (*Left*) and *P7REP_SOURCE_V15* are shown in Fig 2.4. From them we can see that the angular resolution is rather poor. This has to be taken into account during the analysis of a given γ-ray source because it can lead to contaminations due to the Galactic gamma diffuse emission and the nearby source emissions.

Moreover the very large values of the PSF, and consequently of the positional errors of the detected sources, with respect to the PSF values of telescopes operating at lower frequencies, constituites a strong limitation, especially during the process of association and identification

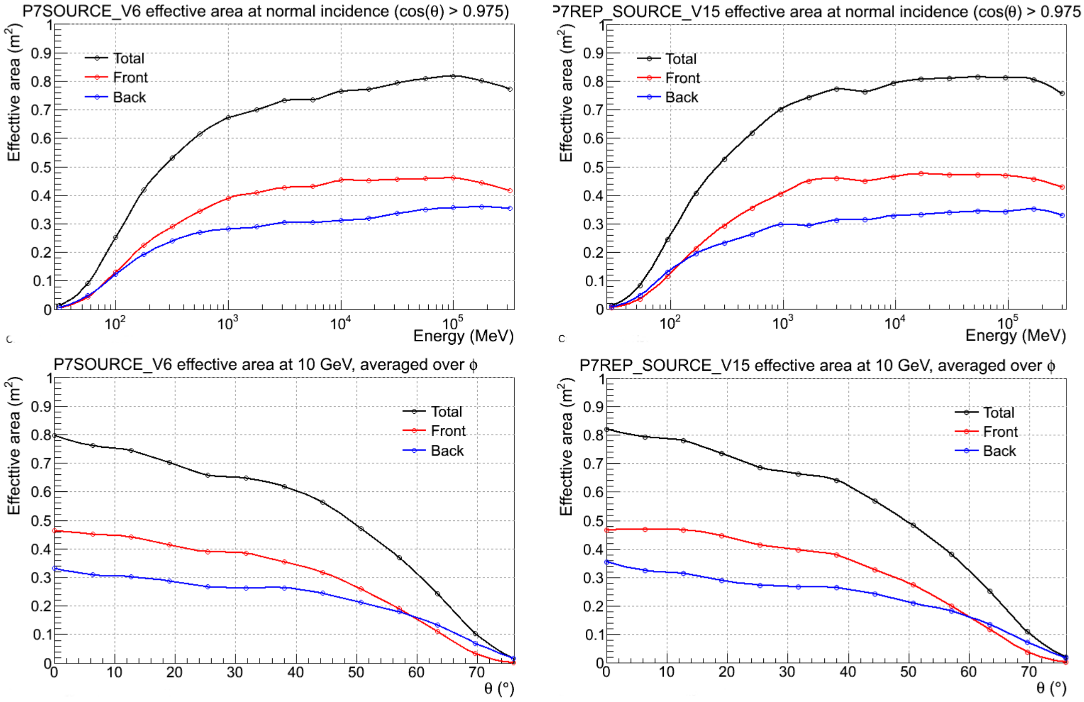

Figure 2.2: The effective area as function of the energy (*Upper panels*) and of the incidence angle at 10 GeV (*Bottom panels*), for the IRF version *P7SOURCE_V6* (*Left*) and *P7REP_SOURCE_V15* (*Right*).

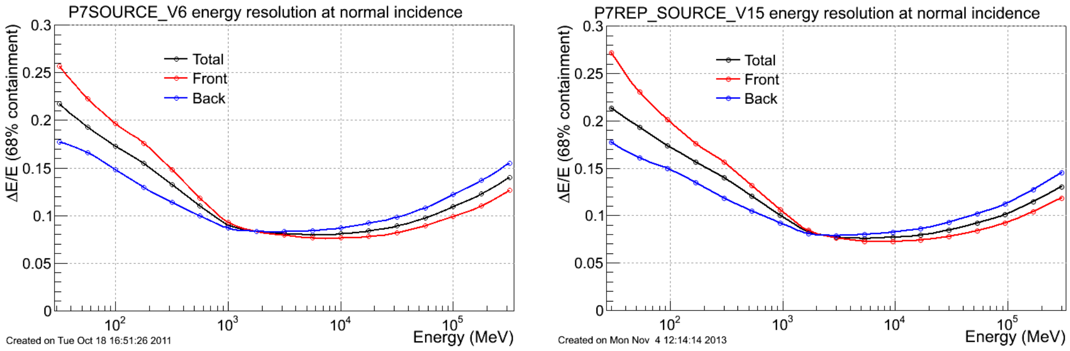

Figure 2.3: Energy resolution (68% containment of the reconstructed incoming photon energy) as function od the energy for normallu incident photon and for the IRF version *P7SOURCE_V6* (*Left*) and *P7REP_SOURCE_V15* (*Right*).

of the γ-ray sources detected by *Fermi* satellite.

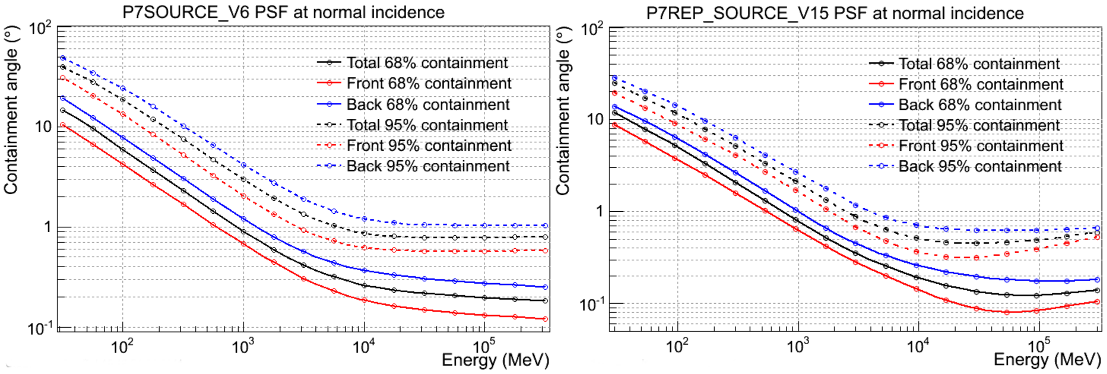

Figure 2.4: 68% and 95% containment angle of the PSF for normal incidence photons and for the IRF version *P7SOURCE_V6* (*Left*) and *P7REP_SOURCE_V15* (*Right*).

2.2 The second Fermi gamma-ray source catalog (2FGL)

One of the purposes of the *Fermi* mission is to accomplish an all-sky survey of the high energy sky and to build a complete catalogue of γ-ray sources. Since the launch of the satellite, two main catalogs of point-like γ-ray sources have been released together with other several catalogs dedicated to the different classes of γ-ray emitters (i.e. pulsars, AGNs, and GRBs). In this Section we briefly present the second catalog of high energy γ-ray sources detected by the LAT instrument on board of the *Fermi* satellite based on the first two years of observations, whcih started on 2008 August 4 [46]. As for the first catalog, but with many improvements, the procedure used to build the 2FGL catalog is mainly based on three steps: the detection, the localization and the estimation of the detection significance of the sources. Building such a catalogue crucially needs the use a model of diffuse γ-ray intensity of the sky, generated by the interactions between the cosmic rays and the interstellar gas and photons: it should take into account the Milky way emission, that represents the brightest and structured foreground, and the unresolved and isotropic emission due to extragalactic gamma emitters. In order to characterize the detected sources the IRFs, based on the Pass 7 event selections, are used and the resulting spectra, for point-like and extended sources, are fitted with different spectral shapes, in addition to the simple power law fitting function.

2.2.1 Construction of the Catalog: Detection, Localization and Significance

In order to detect and insert a γ-ray source in the catalog, an iterating procedure is involved. First of all, the potential point sources, the so-called *seeds*, are found and identified. This step is repeated several times to find and include new seeds. Then a full all-sky optimization of the model of the γ-ray sky is performed. The all-sky dataset is divided in 1728 circular regions and each region is then analysed taking into account the diffuse emission, the point-like sources and the 12 spatially extended sources detected previously (in the first catalogue) by the LAT, and the new seeds found in the preceding step. Each circular region is optimized independently and the optimization procedure is iterated several times. This procedure allows a refinement of the previously estimated positions and of the evaluation of the detection significance for the single sources. Based on the type of the object, the spectra of every source are modeled with different spectral shapes (described below), and every seed is characterized by two versions of the likelihood TS [41]: the TS_{band} measuring the spectral-shape indipendent measure from indipendent fits of the fluxes in different energy bands, and the TS_{model} which is the result of the fit to the spectral model. The difference between the two TS is used to decide to switch from a power law to another spectral shape. Moreover seeds with $\mathrm{TS}_{band} < 10$ are rejected. After the optimization, only the seeds with $\mathrm{TS}_{model} > 10$ survives and the last step of the detection phase is the creation of a residual TS map, where $\mathrm{TS} = 2\ (\log L(\mathrm{source})\text{-}\log L(\mathrm{no\_source}))$ and L is the likelihood of the data given the model with or without source present at a given position on the sky. From this map, divided in about 3.1M points, clusters of such pixels with $\mathrm{TS} > 10$ are recognized and represent a source candidate. The position of a presumed source is the centroid of the pixels, weighted by TS. The positional uncertainty for each source was estimated by examining the shape of the log likelihood function, fitting the distribution to the expected quadratic form in the angular deviations from the best-fit position. A measure of the quality of this fit is the mean square deviation of the log likelihood with respect to the fit on a circle of radius corresponding to two standard deviations. In the catalog the elliptical parameters including the fit position and the fit quality are tabuled. Finally for the catalog, the significances, the fluxes and the spectral parameters are evaluated using the public LAT analysis tools. The sky is divided in 933 Regions of Interest (RoI) in order to maximaze the likelihood function ($\log(L)$) varying half a dozen sources near the center of the RoI. Hence the significance is define as $\mathrm{TS} = 2\Delta\ \log L$ and gives the estimate of how a given source emerges from the background. A threshold of $\mathrm{TS} > 25$ is applied to all sources that corrisponds to a significance of 4σ evaluated from the χ^2 distribution with 4 degrees of freedom (position and spectral parameters).

2.2.2 Spectral Fitting Shapes and Flux Determination

The use of a power law (PL) model to fit the spectral shapes of the gamma-ray sources, as made in the first *Fermi* catalogue, is not always a good spectral representation because it may provide an overestimate of the flux especially at the lower energies.

In the second catalogue, the *Fermi* collaboration, used a spectral fitting that can deviate from the PL increasing of one the number of free parameters of the fitting function. Below, we present the different spectral models used for the various kinds of sources.

The simplest function used to fit the majority of the sources detected by the *Fermi* satellite is the PL, espressed as:

$$\frac{dN}{dE} = K \frac{E}{E_0}^{-\Gamma} \tag{2.1}$$

The parameter Γ is the spectral slope, reported in the catalog as `Spectral_Index`. K is the normalization factor, labelled as `Flux_Density`, defined as the differential flux at the refence energy $E_0 = E_p$, where E_p (`Pivot_Energy`) is the energy at which the relative uncertainty on the differential flux K is minimal and varies for each source.

For all of the known pulsars with significant γ-ray pulsations detected by LAT, an exponentially cutoff PL, i.e. the product of a PL and an exponential, is adopted:

$$\frac{dN}{dE} = K \frac{E}{E_0}^{-\Gamma} e^{-\frac{E-E_0}{E_c}} \tag{2.2}$$

where E_0 and E_{cut}, that is the cutoff energy, are the free parameters.

Many bright sources, mainly AGNs, are not well represented by a simple PL and the so-called LogParabola function is instead used. It is defined as:

$$\frac{dN}{dE} = K \frac{E}{E_0}^{-\alpha-\beta \cdot log(E/E_0)} \tag{2.3}$$

where α is the spectral index and β is the curvature factor that is always found positive (hence spectra curved downward) for all of the sources with curved spectrum. The switch from PL to LogParabola function is based on the value of a curvature parameter defined as $\mathrm{TS}_{curve} = 2$ (log$L$(LogParabola)-log$L$(PL)). If $\mathrm{TS}_{curve} > 16$ (that implies a significance of 4σ for the curvature) the source spectrum is fitted by a LogParabola. In any case, for consistency with the first *Fermi* catalog, 2FGL reports, for all of the sources, the spectral index of the best PL fit, labelled as `PowerLaw_Index`.

In the 2FGL catalogue the source photon flux over the full band (1 - 100 GeV) and in five energy bands (100-300 MeV; 0.3-1 GeV; 1-3 GeV; 3-10 GeV; 10-100 GeV) is reported. In addition the energy flux in 100 MeV - 100 GeV is provided. In the five bands, the fluxes are reported as measurements or as 2σ upper limits, in case of very weak source with TS<10 or relative uncertainty on th flux $\Delta F_i/F_i > 0.5$ in a given band. The fluxes are obtained by freezing the spectral index to that obtained in the fit over the full range and adjusting the normalization in each spectral band. For the curved spectra, the spectral index in a single energy band is set to the local spectral slope at the logarithmic mid-point of the band. In order to evaluate the agreement between the proposed spectral shape and the band fluxes, a spectral fit quality indicator, the `Curvature_Index`, is defined:

$$C_{syst} = \sum_i \frac{(F_i - F_i^{fit})^2}{\sigma_i^2 + (f_i^{rel} F_i^{fit})^2} \tag{2.4}$$

where i runs over all bands, f_i^{rel} is related to the systematic uncertainty on the effective area and F_i^{fit} is the predicted flux in the i-th band from the spectral fit to the full band.

2.2.3 Variability

The study of the flux variability is a important task in the field of the γ-ray astronomy. Flux variability on long timescales is a common feature of the γ-ray emitters and it is useful to understand the physical processes occuring inside them and to determine their nature. The monthly light curve over the full energy range, from 100 MeV to 100 GeV, of all of the 2FGL sources are available in the *Fermi* Science Support Center. The first 11 time bins correspond to the 1FGL catalogue lightcurves. As in the case of the flux determination, upper limits of the flux are given when a source is too faint to be detected in a single time bin. In order to evaluate the level of variability of a given γ source, the parameter called `Variability_index` is defined from the value of the likelihood in the null hypothesis (where the source flux is constant across the two years of obsevations and is associated to a flat lightcurve), and the value under the alternate hypothesis where the flux in each time bin is estimated:

$$TS_{var} = 2\sum_i [logL_i(F_i) - logL_i(F_{const})] = 2\sum_i V_i^2 \tag{2.5}$$

where L_i is the likelihood related to the individual time bands. Values of TS_{var} >41.6 indicates there is a less than 1% chance of being a steady source.

2.2.4 Associations and classes of gamma-ray emitters

In 2FGL catalog, 1873 sources has been detected and listed with the designation `2FGL JHHMM.m+DDMM` and with the corrisponding proprierties including the position in the sky and the error ellipse, the fluxes in different energy bands, the curvarture and variability index, and the astronomical class (in Fig 2.5 two tables taken from Nolan+2012 that illustrate the information provided for each source and their description).

In total 15 classes of sources are designed to categorize the 2FGL sources. They are displayed in Tab 2.2 with the number of sources for each class and acronym used in the catalogue. In Fig 2.6 taken from [46], the full skymap shows the localization of the different classes of sources. In the catalog, the *Fermi* collaboration makes a distinction between identified and associated sources: the class designator is given in lowercase letters if the source has an association based on a close positional correspondence with objects belonging to catalogs of other wavelenghts, it is instead given in capital if the source is identified through the characterization of the finite angular extent (especially for galactic sources, studying their morphology) or the measurements of correlated variability at other wavelengths. In particular, for the pulsars and the high-mass binaries, the periodic variability was investigated. For all of the pulsars identified in the catalogue, the pulsed γ-ray emission has a probability that the periodicity occurs by chance of less than 10^{-6}. On the other hand, for AGNs, known as variable objects, the γ-ray variations have been matched with changes in emission seen at the other wavelengths.

The automatic association procedure is similar to that used to build the previous *Fermi* catalogues and the *EGRET* catalogue, described in details in [42], [3] and [46]. It is based on a Bayesian approach that estimates the probability that a given counterpart association is real, comparing the positional coincidence of possible counterparts with 2FGL sources againts the expected number of chance coincidences. The posterior probability P_{ik} that a source i of a given catalog is really associated with the LAT source k is espressed as:

$$P_{ik} = (1 + \frac{1 - P_{prior}}{P_{prior}} 2\pi\sigma_k a_k b_k e^{\Delta_k})^{-1} \tag{2.6}$$

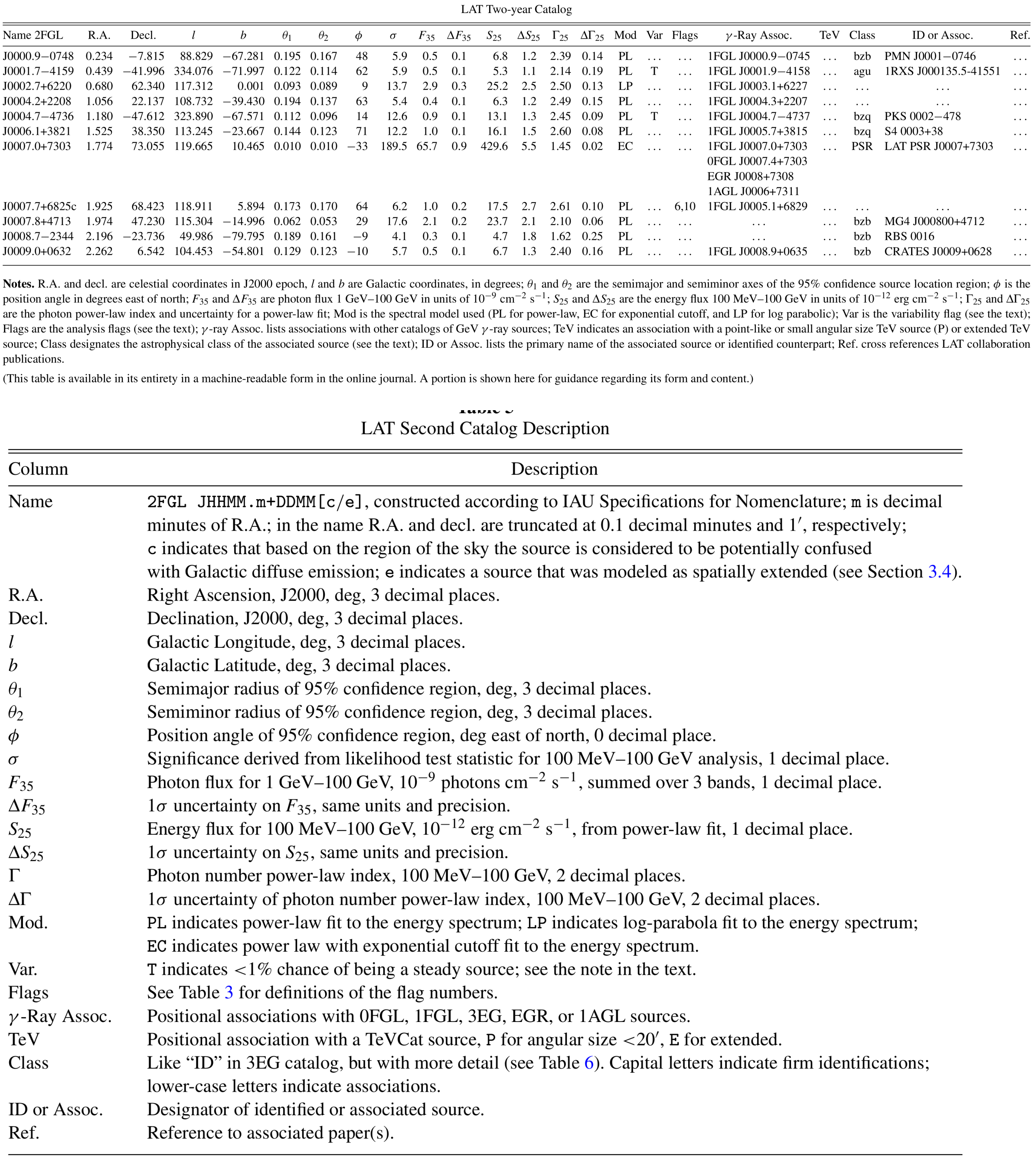

LAT Two-year Catalog

Name 2FGL	R.A.	Decl.	l	b	θ_1	θ_2	ϕ	σ	F_{35}	ΔF_{35}	S_{25}	ΔS_{25}	Γ_{25}	$\Delta\Gamma_{25}$	Mod	Var	Flags	γ-Ray Assoc.	TeV	Class	ID or Assoc.	Ref.
J0000.9−0748	0.234	−7.815	88.829	−67.281	0.195	0.167	48	5.9	0.5	0.1	6.8	1.2	2.39	0.14	PL	…	…	1FGL J0000.9−0745	…	bzb	PMN J0001−0746	…
J0001.7−4159	0.439	−41.996	334.076	−71.997	0.122	0.114	62	5.9	0.5	0.1	5.3	1.1	2.14	0.19	PL	T	…	1FGL J0001.9−4158	…	agu	1RXS J000135.5-41551	…
J0002.7+6220	0.680	62.340	117.312	0.001	0.093	0.089	9	13.7	2.9	0.3	25.2	2.5	2.50	0.13	LP	…	…	1FGL J0003.1+6227	…	…	…	…
J0004.2+2208	1.056	22.137	108.732	−39.430	0.194	0.137	63	5.4	0.4	0.1	6.3	1.2	2.49	0.15	PL	…	…	1FGL J0004.3+2207	…	…	…	…
J0004.7−4736	1.180	−47.612	323.890	−67.571	0.112	0.096	14	12.6	0.9	0.1	13.1	1.3	2.45	0.09	PL	T	…	1FGL J0004.7−4737	…	bzq	PKS 0002−478	…
J0006.1+3821	1.525	38.350	113.245	−23.667	0.144	0.123	71	12.2	1.0	0.1	16.1	1.5	2.60	0.08	PL	…	…	1FGL J0005.7+3815	…	bzq	S4 0003+38	…
J0007.0+7303	1.774	73.055	119.665	10.465	0.010	0.010	−33	189.5	65.7	0.9	429.6	5.5	1.45	0.02	EC	…	…	1FGL J0007.0+7303 0FGL J0007.4+7303 EGR J0008+7308 1AGL J0006+7311	…	PSR	LAT PSR J0007+7303	…
J0007.7+6825c	1.925	68.423	118.911	5.894	0.173	0.170	64	6.2	1.0	0.2	17.5	2.7	2.61	0.10	PL	…	6,10	1FGL J0005.1+6829	…	…	…	…
J0007.8+4713	1.974	47.230	115.304	−14.996	0.062	0.053	29	17.6	2.1	0.2	23.7	2.1	2.10	0.06	PL	…	…	…	…	bzb	MG4 J000800+4712	…
J0008.7−2344	2.196	−23.736	49.986	−79.795	0.189	0.161	−9	4.1	0.3	0.1	4.7	1.8	1.62	0.25	PL	…	…	…	…	bzb	RBS 0016	…
J0009.0+0632	2.262	6.542	104.453	−54.801	0.129	0.123	−10	5.7	0.5	0.1	6.7	1.3	2.40	0.16	PL	…	…	1FGL J0008.9+0635	…	bzb	CRATES J0009+0628	…

Notes. R.A. and decl. are celestial coordinates in J2000 epoch, l and b are Galactic coordinates, in degrees; θ_1 and θ_2 are the semimajor and semiminor axes of the 95% confidence source location region; ϕ is the position angle in degrees east of north; F_{35} and ΔF_{35} are photon flux 1 GeV–100 GeV in units of 10^{-9} cm^{-2} s^{-1}; S_{25} and ΔS_{25} are the energy flux 100 MeV–100 GeV in units of 10^{-12} erg cm^{-2} s^{-1}; Γ_{25} and $\Delta\Gamma_{25}$ are the photon power-law index and uncertainty for a power-law fit; Mod is the spectral model used (PL for power-law, EC for exponential cutoff, and LP for log parabolic); Var is the variability flag (see the text); Flags are the analysis flags (see the text); γ-ray Assoc. lists associations with other catalogs of GeV γ-ray sources; TeV indicates an association with a point-like or small angular size TeV source (P) or extended TeV source; Class designates the astrophysical class of the associated source (see the text); ID or Assoc. lists the primary name of the associated source or identified counterpart; Ref. cross references LAT collaboration publications.

(This table is available in its entirety in a machine-readable form in the online journal. A portion is shown here for guidance regarding its form and content.)

LAT Second Catalog Description

Column	Description
Name	`2FGL JHHMM.m+DDMM[c/e]`, constructed according to IAU Specifications for Nomenclature; `m` is decimal minutes of R.A.; in the name R.A. and decl. are truncated at 0.1 decimal minutes and 1′, respectively; `c` indicates that based on the region of the sky the source is considered to be potentially confused with Galactic diffuse emission; `e` indicates a source that was modeled as spatially extended (see Section 3.4).
R.A.	Right Ascension, J2000, deg, 3 decimal places.
Decl.	Declination, J2000, deg, 3 decimal places.
l	Galactic Longitude, deg, 3 decimal places.
b	Galactic Latitude, deg, 3 decimal places.
θ_1	Semimajor radius of 95% confidence region, deg, 3 decimal places.
θ_2	Semiminor radius of 95% confidence region, deg, 3 decimal places.
ϕ	Position angle of 95% confidence region, deg east of north, 0 decimal place.
σ	Significance derived from likelihood test statistic for 100 MeV–100 GeV analysis, 1 decimal place.
F_{35}	Photon flux for 1 GeV–100 GeV, 10^{-9} photons cm^{-2} s^{-1}, summed over 3 bands, 1 decimal place.
ΔF_{35}	1σ uncertainty on F_{35}, same units and precision.
S_{25}	Energy flux for 100 MeV–100 GeV, 10^{-12} erg cm^{-2} s^{-1}, from power-law fit, 1 decimal place.
ΔS_{25}	1σ uncertainty on S_{25}, same units and precision.
Γ	Photon number power-law index, 100 MeV–100 GeV, 2 decimal places.
$\Delta\Gamma$	1σ uncertainty of photon number power-law index, 100 MeV–100 GeV, 2 decimal places.
Mod.	`PL` indicates power-law fit to the energy spectrum; `LP` indicates log-parabola fit to the energy spectrum; `EC` indicates power law with exponential cutoff fit to the energy spectrum.
Var.	`T` indicates <1% chance of being a steady source; see the note in the text.
Flags	See Table 3 for definitions of the flag numbers.
γ-Ray Assoc.	Positional associations with 0FGL, 1FGL, 3EG, EGR, or 1AGL sources.
TeV	Positional association with a TeVCat source, `P` for angular size <20′, `E` for extended.
Class	Like "ID" in 3EG catalog, but with more detail (see Table 6). Capital letters indicate firm identifications; lower-case letters indicate associations.
ID or Assoc.	Designator of identified or associated source.
Ref.	Reference to associated paper(s).

Figure 2.5: *Upper panel*: Part of the second *Fermi* catalogue (2FGL) with information for each of the 1873 sources reported. *Bottom panel*: Table with the descriptions of each column of the 2FGL catalogue. (Both figure taken from [46])

Class	**Designator**	**N. of sources**
Pulsar	PSR	108
Pulsar Wind Nebulae	PWN	3
Supernova Remnant	SNR	68
Globular cluster	GLC	11
High-mass binary	HMB	4
Nova	NOV	1
BL Lac type of *blazar*	BZB	436
FSRQ type of *blazar*	BZQ	370
Non-*blazar* active galaxy	AGN	11
Radio galaxy	RDG	12
Seyfert galaxy	SEY	6
Active galaxy of uncertain type	AGU	257
Normal galaxy (or part)	GAL	6
Starburt galaxy	SBG	4
Unassociated object (UFO)	-	576

Table 2.2: The different classes of γ-ray objects reported in the 2FGL catalogue. In the second column the corresponding designation, in the third column the number of sources assigned to each class.

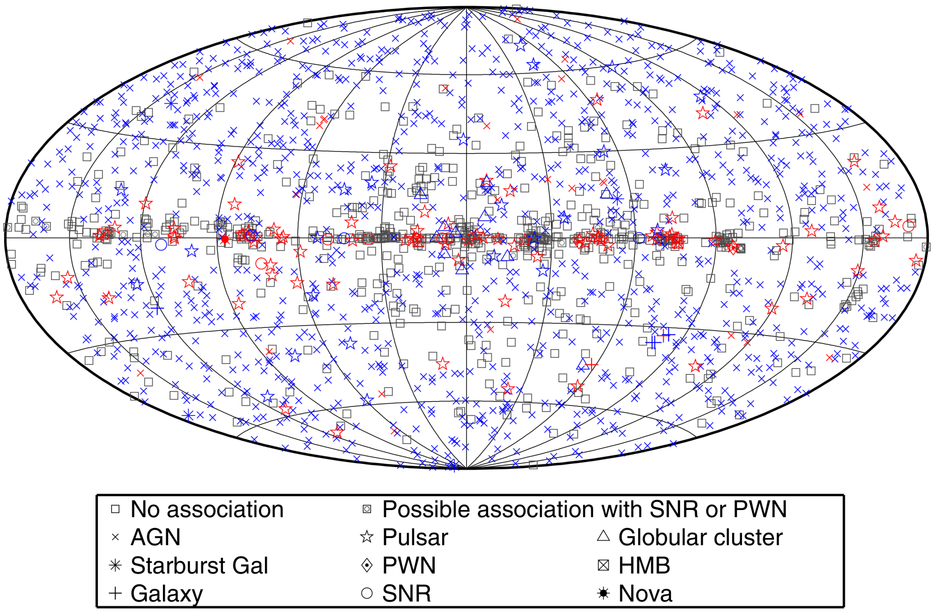

Figure 2.6: Full sky map showing 2FGL sources by source class. Identified sources are shown with re symbol, associated ones in blue.. Taken from [46].

where P_{prior} is the prior probability that the counterpart i is detected by LAT[2]. The *Fermi* collaboration rejects associations with a posterior probability less than 80% which means that each association has a 20% chance probability to be a sporious association. a_k and b_k are the axes of the error ellipse at 1σ (it is smaller than the semi-axes at 95% confidence of a factor 2.45), σ_k is the local counterpart density around the the LAT source k and Δ_k is defined as $\Delta_k = \frac{r^2}{2}(\frac{cos^2(\phi-\phi_k)}{a_k^2} + \frac{sin^2(\phi-\phi_k)}{b_k^2})$, with ϕ and r the position angle and the angular separation between the LAT source k and the counterpart i, respectively, and ϕ_k the position angle of the LAT error ellipse. If it is not possible to apply this procedure, for example in case where the positional error-box of the counterpart is larger of the LAT semimajor axis[3], the association is provided when the angular distance between the counterpart and the LAT source satisfies the following relation:

$$\Delta < d_x = \sqrt{\theta^2_{x\_Countpart} + \theta^2_{x\_2FGL}} \tag{2.7}$$

with θ^2 as the positional error axis of the x% confidence.

The list of the catalogs at other wavelengths and of the potential counterpart candidates used in the automatic association procedure is shown in Fig 2.7, taken from [46]. Among these catalogs, there are catalogs of well-known and identified γ-ray emitters in order to determine the astronomical class for each 2FGL source, catalogs of GeV and TeV sources with the aim to confirm the previous detection in the HE band, and finally catalogs of surveys of other frequencies that permit to find the multiwavelength counterparts and reveal their nature.

Most of the 2FGL sources are associated with AGNs. Among them there are blazars (the most populous class with the largest number of objects including FSRQs and BL-Lac objects), radio galaxies, Seyfert galaxies (four as narrow-line Seyfert 1, a new class of γ-ray AGNs), and active galaxies of uncertain type (about 14%). All of the 2FGL AGNs also emit in the X-ray and radio band with a radio emission larger than the average flux of the other AGNs included in the multiwavelength counterpart catalogs considered by the *Fermi* collaboration. For the AGN class there is a dedicated *Fermi* catalogue (the so-called 2LAC catalogue, [4]) containing a more numerous sample and based on a different association procedure. Seven normal galaxies are found as γ-ray emitters, the Large and Small Magellanic Clouds, M31

---

[2] The prior probability P_{prior} is assigned so that the expected number of false associations that have prior probabilities above the threshold P_{th} is given by $N_{false} = \sum_{P_{ik}>P_{th}}(1 - P_{ik})$.

[3] This happens mainly for the other γ-ray catalogs, including the 1FGL.

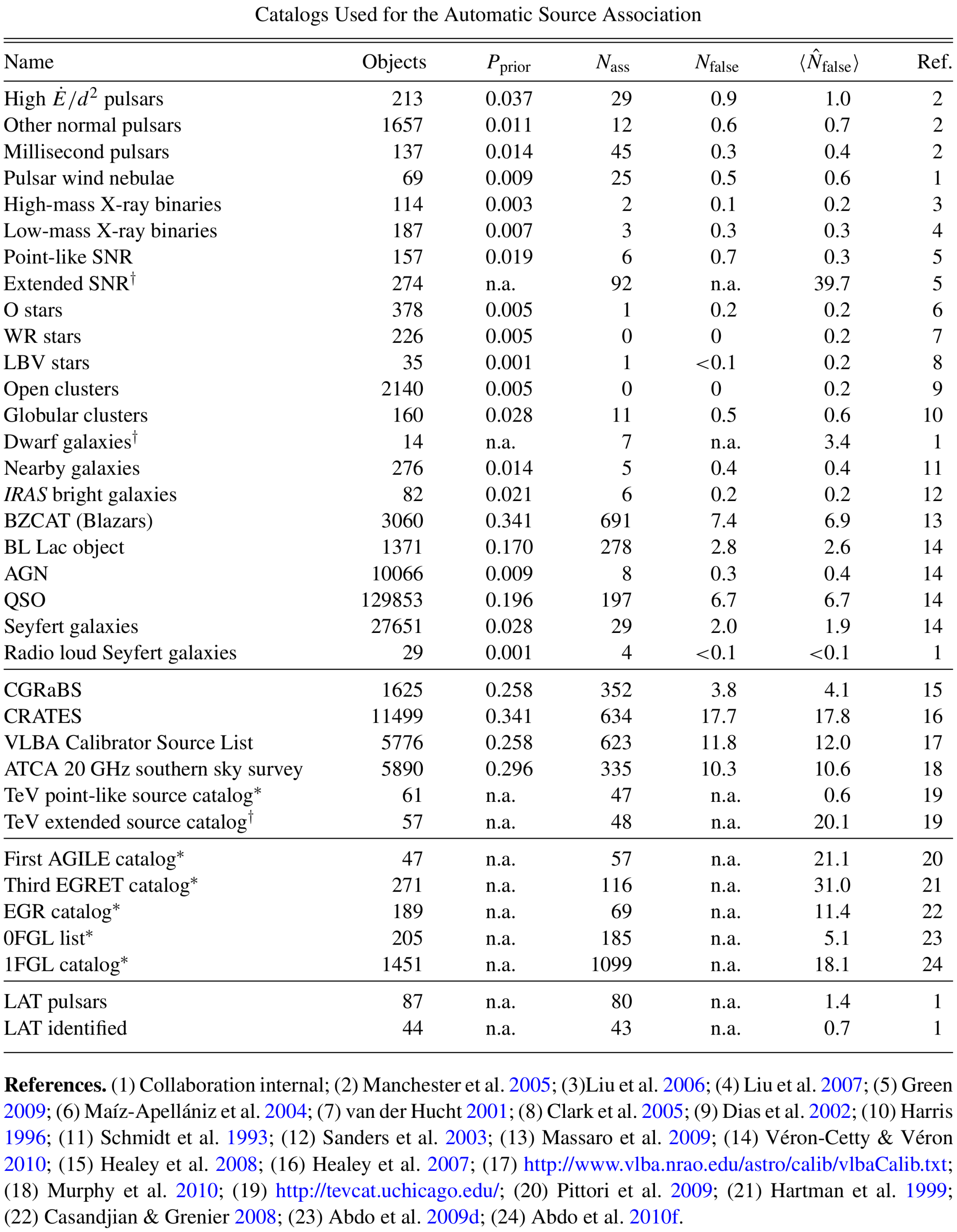

Catalogs Used for the Automatic Source Association

Name	Objects	$P_{\rm prior}$	$N_{\rm ass}$	$N_{\rm false}$	$\langle \hat{N}_{\rm false} \rangle$	Ref.
High $\dot{E}/d^2$ pulsars	213	0.037	29	0.9	1.0	2
Other normal pulsars	1657	0.011	12	0.6	0.7	2
Millisecond pulsars	137	0.014	45	0.3	0.4	2
Pulsar wind nebulae	69	0.009	25	0.5	0.6	1
High-mass X-ray binaries	114	0.003	2	0.1	0.2	3
Low-mass X-ray binaries	187	0.007	3	0.3	0.3	4
Point-like SNR	157	0.019	6	0.7	0.3	5
Extended SNR†	274	n.a.	92	n.a.	39.7	5
O stars	378	0.005	1	0.2	0.2	6
WR stars	226	0.005	0	0	0.2	7
LBV stars	35	0.001	1	<0.1	0.2	8
Open clusters	2140	0.005	0	0	0.2	9
Globular clusters	160	0.028	11	0.5	0.6	10
Dwarf galaxies†	14	n.a.	7	n.a.	3.4	1
Nearby galaxies	276	0.014	5	0.4	0.4	11
IRAS bright galaxies	82	0.021	6	0.2	0.2	12
BZCAT (Blazars)	3060	0.341	691	7.4	6.9	13
BL Lac object	1371	0.170	278	2.8	2.6	14
AGN	10066	0.009	8	0.3	0.4	14
QSO	129853	0.196	197	6.7	6.7	14
Seyfert galaxies	27651	0.028	29	2.0	1.9	14
Radio loud Seyfert galaxies	29	0.001	4	<0.1	<0.1	1
CGRaBS	1625	0.258	352	3.8	4.1	15
CRATES	11499	0.341	634	17.7	17.8	16
VLBA Calibrator Source List	5776	0.258	623	11.8	12.0	17
ATCA 20 GHz southern sky survey	5890	0.296	335	10.3	10.6	18
TeV point-like source catalog*	61	n.a.	47	n.a.	0.6	19
TeV extended source catalog†	57	n.a.	48	n.a.	20.1	19
First AGILE catalog*	47	n.a.	57	n.a.	21.1	20
Third EGRET catalog*	271	n.a.	116	n.a.	31.0	21
EGR catalog*	189	n.a.	69	n.a.	11.4	22
0FGL list*	205	n.a.	185	n.a.	5.1	23
1FGL catalog*	1451	n.a.	1099	n.a.	18.1	24
LAT pulsars	87	n.a.	80	n.a.	1.4	1
LAT identified	44	n.a.	43	n.a.	0.7	1

References. (1) Collaboration internal; (2) Manchester et al. 2005; (3)Liu et al. 2006; (4) Liu et al. 2007; (5) Green 2009; (6) Maíz-Apellániz et al. 2004; (7) van der Hucht 2001; (8) Clark et al. 2005; (9) Dias et al. 2002; (10) Harris 1996; (11) Schmidt et al. 1993; (12) Sanders et al. 2003; (13) Massaro et al. 2009; (14) Véron-Cetty & Véron 2010; (15) Healey et al. 2008; (16) Healey et al. 2007; (17) http://www.vlba.nrao.edu/astro/calib/vlbaCalib.txt; (18) Murphy et al. 2010; (19) http://tevcat.uchicago.edu/; (20) Pittori et al. 2009; (21) Hartman et al. 1999; (22) Casandjian & Grenier 2008; (23) Abdo et al. 2009d; (24) Abdo et al. 2010f.

Figure 2.7: List of the multiwavelength catalog used in the *Fermi* automatic association, as reported in [46]..

and four starburst galaxies.

Among the 2FGL Galactic sources, 108 objects have been associated with pulsars (87 have a firm identification through the pulsation studies). 21 of them belong to the class of the millisecond pulsars: two do not have counterparts in the 1FGL catalog and the others were discovered thanks to radio observations of unassociated 1FGL sources. In the catalogue, every 2FGL pulsar has associated the own PWN, but more intriguing are the three 2FGL sources cataloged as PWN without no pulsar so far identified. Four 2FGL sources, identified thanks to their orbital modulation, are high mass X-ray binary systems: LSI +61 303 [1], 1FGL J1019.0-5856 [17], LS 5039 [2] and Cygnus X-3. No low mass X-ray binary have been associated with 2FGL sources. 11 LAT sources are associated with globular cluster and finally the last class considered is the SNR class composed by point-like sources but also by a sufficient number of extended sources, with an angular diameter >20', potentially resolved by the LAT. There are two special objects, 2FGL J1045.0-5941 associated with η-*Carinae*, and 2FGL J2030.7+4417 with the O-type star *HD 195592*: both are not included in any category of sources previous listed.

2.2.5 The Unassociated *Fermi* objects (UFO)

The class of unassociated LAT sources, the most populated in the 2FGL catalogue, will be described in this section. About one third (575) of the sources detected by the Fermi satellite are unidentified/unassociated, either due to the lack of counterparts or because there are many possible associations at the other wavelengths and the identification is ambiguous.

The full sky map of all of the catalogued sources is shown in Fig 2.8. It compares the distribution of the associated (dots) and unassociated sources (large symbols) detected by *Fermi*. The majority of the UFOs are along the Galactic plane that is a particularly crowded region of the sky, not only in the γ-ray band but also at other wavelengths and it is affected by significant interstellar obscuration that hides possible optical counterparts. Moreover the UFO density decreases with increasing Galactic latitude showing an asymmetry in their distribution above and below the Galactic plane. As shown in Fig 2.9, the UFO distribution decreases steeper at positive latitudes. The *Fermi* collaboration explains this fact as an higher completeness of the north emispheres of the counterpart catalogs used in the automatic association procedure rather than an intrinsic feature of the UFO population.

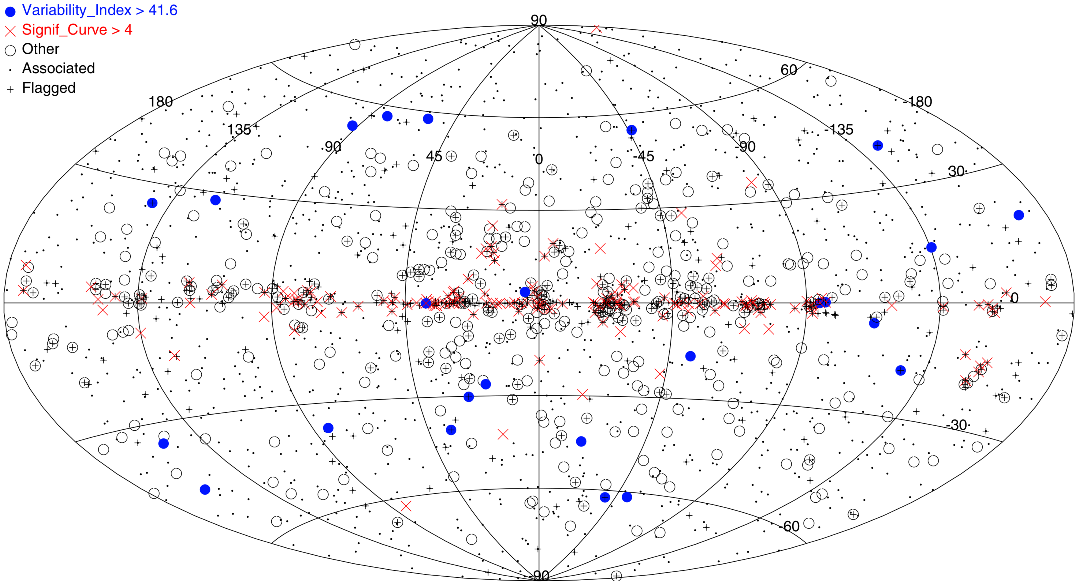

Figure 2.8: Sky distribution of associated (dots) and unassociated (large symbols) sources of the 2FGL catalog. Adapted by [46].

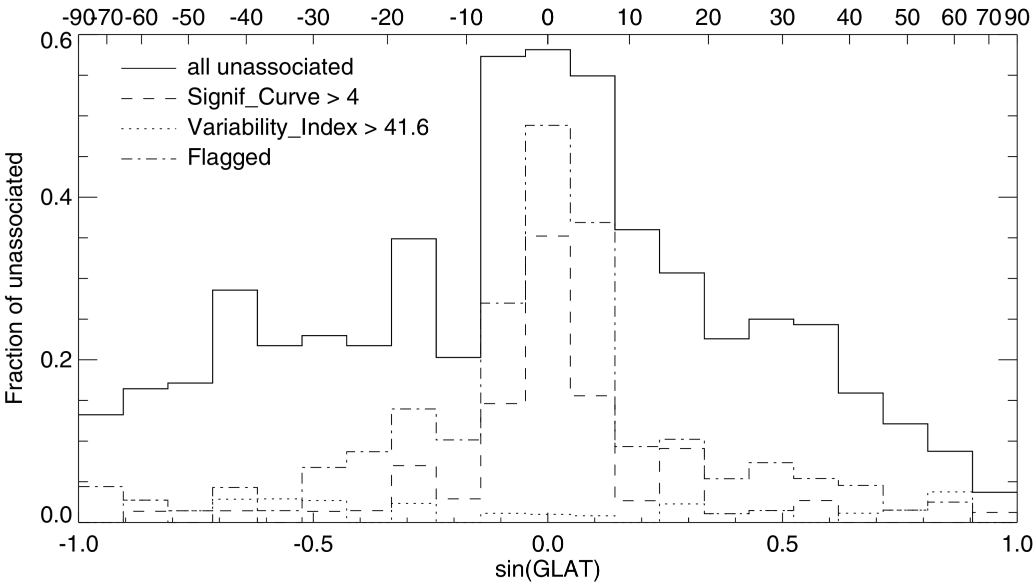

Figure 2.9: Latitude distribution of 2FGL unassociated sources [46]..

Class of sources	**N. of sources**	**N. of sources** $\lvert b\rvert < 10°$	**N. of sources** $\lvert b\rvert > 10°$	**N. of sources** $\lvert b\rvert > 20°$
AGN	11	1	10	9
AGU	257	66	191	138
BZB	436	17	419	351
BZQ	370	19	351	298
GLC	11	10	0	1
GAL	6	0	6	6
HMB	4	4	0	0
NOV	1	1	0	0
RDG	12	1	11	5
SBG	4	0	4	3
SEY	6	0	6	4
SNR	10	10	0	0
SPP	58	58	0	0
PSR	108	64	44	26
PWN	3	3	0	0
UFO	576	304	272	183
All	1873	559	1314	1024

Table 2.3: Number of the 2FGL sources assigned to each catalogue class and for different cuts in Galactic latitude b.

Another feature is that the fraction of UFOs with curved spectra is about 28%, higher than the 16% of the associated sources, and they are located mainly at low Galactic latitudes, forming clusters along the Galactic plane as shown from their spatial distribution. This suggests that a part of UFOs at low latitudes may be local emission maxima of the diffuse Galactic emission, not adequately modeled, rather than true gamma-ray emitters.

2.2.6 The Catalog Statistics

In this section, we provide a statistic study of the 2FGL catalog, useful also to select a good sample of 2FGL UFOs to study in this PhD work.

In Tab 2.3, in the first column, we summarise the number of associated 2FGL sources for each class of γ-ray emitters. In the other columns we list the number of sources that survived to different cuts in Galactic latitude b. For $|b|$ <10° we consider the region of the Galactic plane populated mainly by Galactic sources. Not surprisingly the extragalactic sources, especially AGNs of known types, are located outside the Galactic plane for $|b|$ >10°, but about 41% of the pulsars survive to this cut. Extending the interval for $|b|$ >20° , the number of pulsar drops to 25%. Hence the probability, that among the UFOs located at high Galactic latitudes there are pulsars, decreases in favor of the extragalactic sources.

The behaviour of the UFOs confirms the trend found by the *Fermi* collaboration, indeed as seen in the latitude distribution plot of Fig2.10 the most of unassociated sources lies in the Galactic region at lower latitues.

DA FINIRE....

2.3 **Our Selected Sample of UFOs**

A major surprise of the Fermi mission is the large number of unidentified sources among the 1873 objects detected in the 2nd Fermi catalogue (2FGL): indeed, for as many as 576 sources no plausible identifications have yet been found. This makes an important component of the high-energy sky, and may hide new classes of AGNs, Dark-Matter (DM) candidates, or even unexpected high-energy phenomena.

In this PhD thesis, we have embarked on a systematic campaign of UFO identification, involving all of the available public information and multiwavelength data, on an UFO sample selected appling the following basic selection criteria to the Fermi 2FGL catalogue:

1. No association in the 2FGL and no association in other gamma-ray catalogs (EGRET and AGILE catalogs) and catalogs at other wavelengths considered by the Fermi collaboration;

2. To be far from the Galactic plane, with a Galactic latitude $|b|$ >20°. Many UFOs are in the Galactic plane, but we exclude this region because it is very crowded and confused, and the *Fermi* procedure hardly converges towards correct associations.Furthermore, in this way we have a higher probability to select extragalactic sources and Galactic dark matter substructures that show a Galactic latitude distribution more homogeneous (Diemand,Kuhlen+2008).

An additional possible criterion to be considered is the Fermi 2FGL variability index on a 2-years baseline *Fermi* observations, which allows to perform DM candidate searches. Indeed the γ-ray emission from DM objects is expected to be constant during time and hence to select only not-variable UFOs increases the probability of finding DM objects in our sample. Actually only a few of the high-Galactic latitude UFOs are detected to be significantly non-

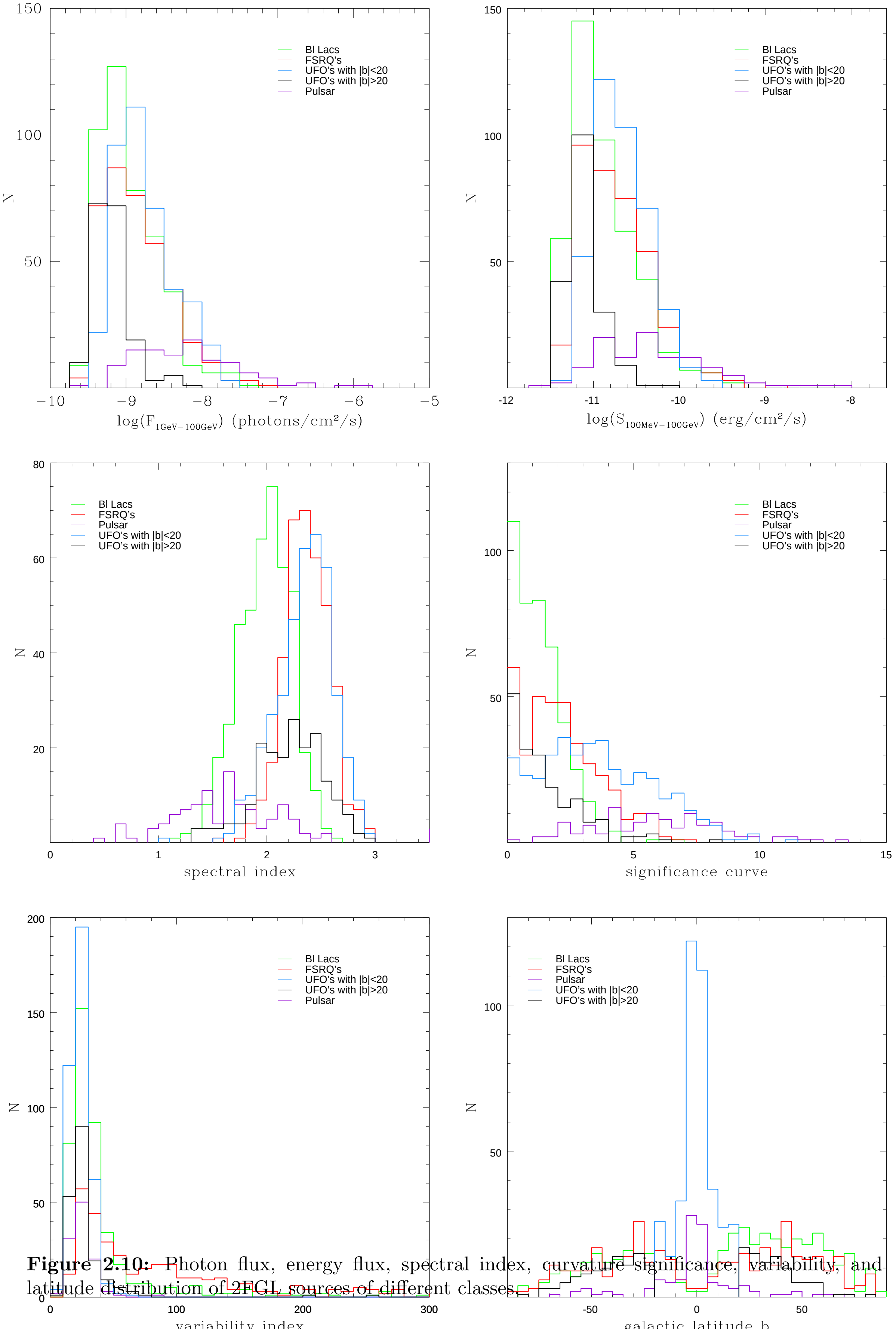

Figure 2.10: Photon flux, energy flux, spectral index, curvature significance, variability, and latitude distribution of 2FGL sources of different classes.

Figure 2.11: Redshift distribution of 2FGL *blazar* of different classes (FSRQ and BL Lac objects).

variable, so we do not further consider this criterion and we decide to attempt an identification also for these 13 sources.

The effects of this selection on the UFO population and on the different source classes are summarized in the last column of Tab 2.3 and finally our reference UFO sample is then made of 183 UFO sources.

At this point for each UFO of our sample it is essential to search for counterparts in X-ray, optical, IR and radio wavelenghts, to determine a possible positional association with a canonical astrophysical object. This work was performed for all of the 183 UFOs and the results are described in Chapter 3 dedicated to the association procedure and the determination of their broad-band SED. At the later stage, described in Chapter 5, through a new multiwavelength method based on physical parameters of their multiwavelength SED, we could estimate the probability that a given UFO is a conventinal *blazar*, a Galactic sources or belongs to a new class of γ-ray sources.

3
UFO positional associations

3.1 Multi-wavelength associations

About one third of the sources reported in the second catalog of the Fermi satellite are unassociated either due to the lack of counterparts or because there are many possible association. This population of unassociated γ-ray sources is the second major component of the γ-ray sky[1] and investigating their nature is a crucial task in the field of the high energy astrophysics. Indeed they may hide high-energy and high-redshift blazars, important for the study of the extragalactic background light and its imprint in the blazars γ-ray spectra, new classes of AGNs, i.e. the so-called extreme *blazars* [19], Dark Matter candidates objects [63] [Massaro et al 2013a], or even unexpected high-energy phenomena (e.g. the recent detection of four Novae at γ-ray band, [16]).

An association method based only on a positional correlation with a known object is not enough due to the very large *Fermi* error-boxes that typically ranging from XX to XX arcmin (for a fraction of UFOs the error box exceed this limit and can reach up to ∼10 arcmins). Instead a multiwavelength approach using datasets of X-ray, optical, IR and radio source, with smaller positional error respect to the *Fermi* error boxes, may help to solve this issue and determine a set of likely counterparts for a given UFO.

In this PhD work, using all of the available public information of different multi-frequency

---

[1] The major component of the γ-ray is the blazar-like AGN class.

catalogs, we carried out a systematic association campaign of a selected sample of 183 objects among the 2FGL UFOs, chosen according to the following selection criteria:

- No association in the 2FGL and no association in other gamma-ray catalogs (EGRET and AGILE catalogs) and catalogs at the other wavelengths considered by the Fermi collaboration;

- To be far from the galactic plane, with a galactic latitude $|b| > 20$ (many UFOs are in the galactic plane, but we exclude this region because it is very crowded and confused and because in this way we have a higher probability to select extragalactic sources)

Following previous works in literature ([57], [**?**], and Takahashi+2012), the first step of our UFO association procudure is primarily based on the analysis of all of the public *Swift*/XRT X-ray imaging data. This choice is supported by several factors: the X-ray surveys provide a good coverage of the *Fermi* error-box, give us information about an energy range close to the *Fermi* γ-ray band, and the error radius of the position in the X-ray band is of the order of a few arcseconds. Moreover most of the classes of sources detected by *Fermi* are X-ray emitters and hence it is confident searching for likely counterparts in this energy regime.

Furthermore, also the radio band is of fundamental importance for our identification work: indeed finding a suited radio conterpart allows a likely identification, especially for the blazar class since all blazar discovered so far have been identified as radio emitters.

This chapter is structured as follows. We firstly describe the association procedure based on positianal coincidence of objects of different catalogs and the construction of the SEDs for our UFO sample, starting from the results obtained by the *Swift* data analysis (if available) or searching for good candidates in the X-ray and radio catalogues. In the next Section the association results for each UFO are presented: we show the sky map that covers the whole Fermi error-box, the close-up sky map (or more than one in case of multiple associations) of the X-ray source detected during our *Swift* data analysis and the built multiwavelength SED. In detail we discuss the analysis of 11 UFOs particularly interesting or with specific issues.

3.1.1 *Swift*/XRT data analysis and Fermi source associations

The X-ray mission *Swift* [29] is a a multi-frequency observatory launched on 20th November 2004, dedicated to the high-energy astrophysics and mainly to the observation of the gamma-ray bursts (GRBs). It consists of three coaligned instruments designed to work together to observe in the gamma-ray, X-ray, ultraviolet, and optical wavebands: the Burst Alert Telescope (BAT, 15-150 keV), the X-ray Telescope (XRT, 0.2-10 keV) and the Ultraviolet/Optical Telescope (UVOT, 170-650 nm). The XRT telescope on-board the *Swift* satellite, thanks to its high mobility, rapid-response and sensitivity to localize sources, has been systematically used during the recents years, and is still being used, to provide X-ray follow up for most of UFO sources and to allow the discovery of new serendipitous X-ray sources that may be good candidates as UFO counterparts.

So far, among 183 UFOs selected, only ∼130 have dedicated *Swift* observations and in our XRT analysis we only analysed the PC[2] mode data. We have studied the XRT data through the UK Swift Science Data Centre XRT analysis tool [**?**][3] that allows the creation of X-ray images, positions, spectra and light curves of any object in the Swift XRT field of view [26], [32]. For each UFO we fill the UK Build Swift-XRT products form inserting the name of the source or the corrisponding coordinates reported in the 2FGL catalogue. The first step is to produce a single XRT image in FITS format merging all avaiable data. This is necessary, in particular, for sources which are too faint to be found in a single snapshot but it is not recommended for highly variable sources. To avoid this risk, and not to have wrong results, we checked if a given X-ray source is variable looking at its light curve (provided automatically) and we verified that the majority of UFOs is affected by this problem.

We obtain 3 images in different energy bands, 0.3-10 keV, 0.3-1.5 keV and 1.5-10 keV. An example of XRT skymap obtained is shown in Fig 3.3. For our scope, we decide to use the 0.3-10 keV energy band and by means of the visualization tool `ds9` we checked if X-ray sources (*green circles*) are inside the Fermi error-box (*yellow ellipse*) of a given UFO source. In the same sky map we also display the X-ray sources of the 1SXPS Swift XRT Point Source Catalogue [27] as white crosses and the radio sources of the catalogs NRAO VLA Sky Survey (NVSS) and Sydney University Molonglo Sky Survey (SUMSS), (plotted as *cyan circles or ellipses* respectively).

Since every X-ray source within the Fermi error box can be considered as possible UFO counterparts, for each of these we determine the position, the corresponding error and the

---

[2] Photon-counting mode: PC mode is the more traditional frame transfer operation of an X-ray CCD. It retains full imaging and spectroscopic resolution, but the time resolution is only 2.5 seconds. The instrument is operated in this mode only at very low fluxes (useful below 1 mCrab).

[3] http://www.swift.ac.uk/user_objects/

X-ray spectrum. In order to get the best position in the XRT astrometric frame and the best accuracy on the position, in the software form we use the XRT coordinates found inspecting the images previously created and we use the option *Try to centroid?* with a search radius of 1 arcmin on the source[4]. If the X-ray source is too faint the centroid algorithm may not find the source: in this case we exclude this option in the creation of the spectrum.

Two types of position can be produced: the so-called *unenhanced position*, estimated using only a PSF fit, and the *enhanced position* [32] where the absolute astrometry is corrected using field stars in the UVOT telescope, where the systematic uncertainty is then decreased to 1.4" (90% confidence), if compared to the 3.5" systematic for the unenhanced positions, in which the astrometry is determined from the star trackers. Moreover for both of these kind of positions, bad column and pile-up corrections are applied.

For each X-ray source detected we perform an interactive analysis of all of the available data in order to extract the energy spectrum in the 0.3-10 keV X-ray band. The output spectral files are downloaded and the data are then modeled and fitted using the XSPEC software (version 12.8.1g) [10] of the HEASOFT ftool package. The spectral data are managed in different ways according to the number of total counts; if the source shows less than 25 counts we provide an estimate of the flux calculated by the Mission Count Rate Simulator WebPIMMS[5], using a power law model with spectral index 2. Otherwise with more than 25 total counts we use an unbinned analysis applying the Cash statistic. For bright source with at least 100 counts, we binned (with the ftool grppha) the spectra in order to collect at least 20 counts per bin.

Once the X-ray counterpart list inside the Fermi error-box is defined, the next step is to search for counterparts of these sources in radio, infrared and optical bands, with the aim to determine a possible positional association with a canonical astrophysical object. For each candidate we perform a search in the main astronomical catalogs and surveys around the XRT enhanced position (or unenhanced position if the former is not available) with a search radius equal to the found 90% confidence error radius (*green circle* as example in Fig 3.3). The results are displayed in the close-up images (i.e. Fig 3.3) where on the XRT sky map we superimpose entries from the radio catalogs NRAO VLA Sky Survey (NVSS) and

---

[4] This option is normally recommended since the position in the XRT coordinate frame may slightly from the object position in other frames (the XRT has an astrometric uncertainty of 3.5" to 90% confidence).

[5] http://heasarc.gsfc.nasa.gov/Tools/w3pimms.html

Sydney University Molonglo Sky Survey (SUMSS), (plotted as *cyan circle or ellipses*), from the Wide-field Infrared Survey Explorer [20] catalogue (*blue crosses*) and the Two Micron All Sky Survey (2MASS) catalogue [55] (*green diamonts*) in the near and mid-infrared band, and finally from the United States Naval Observatory star catalogue (USNO-B1.0) [44] and Sloan Digital Sky Survey (SDSS) catalogue [7] [6] (*magenta crosses*) in the optical regime. As a further check on the goodness of the XRT position estimates, we superimpose the positions of the X-ray sources belonging to the 1SXPS Swift XRT Point Source Catalogue (1SXPS) [27] and the Seven year Swift-XRT point source catalog (1SWXRT) [24], with their error-boxes: we can note that each XRT position, found with our procedure, is pretty compatible with the cataloged positions of 1SXPS and 1SWXRT (if this does not happen, the results will be described in detail in the next section). For display purpose, in the close-up images we display only the 1SXPS source position with *white crosses.* Combining all information, the sources of the different multi-frequency catalogs inside the XRT error radius, and positionally coincident with each other, can be considered the same object observed at different wavelengths and individualized as a good candidate set of counterparts for a given UFO. It is important to note that for a certain UFO, more than one set of counterparts can be identified.

Finally the multiwavelenght dataset of these selected sources can be related in order to create the SED for each UFO. We combine the MWL data through the SED Builder tool of the ASI ASDC database [60] and the SEDs (i.e. Fig 3.4) have been built using the gamma-ray fluxes listed in the 2FGL catalog and the data fluxes of the catalogues above mentioned to the search of counterparts (NVSS data at 1.4 GHz and SUMSS data at 843 MHz, the WISE fluxes at 3.4, 4.6, 12, and 22 μm, the 2MASS fluxes in J-, H- and K$_s$-bands and the optical data of USNO B1.0 catalogue in B-R-I bands and of the SDSS catalogue in u-g-r-i-z filters). Finally we also insert also the *Swift*-XRT flux data previously calculated (*light green points*) or the flux estimated with WebPIMMs if the total counts are not statistically sufficient (*orange point*). Both of the kind of plotted data are corrected for Galactic absorption. If avalaible we display also the flux data points reported by [**?**] (*black points*); these are considered as a cross-check of our analysis but they will not be considered in the further diagnostic work.

3.1.2 Associations without *Swift*/XRT data

So far about 25% of our selected UFOs have not been observed by XRT telescope or are still not included in one of the sky regions pointed by *Swift* in the past. Despite this, the XRT follow-up observations of unidentified fermi objects is on-going and probably the missing UFOs can be observed in the future. Furthermore new observations of already pointed UFOs will be performed and they can help us in the case of marginal or no detection.

In case of UFOs without *Swift* observations, we try to select possible counterparts searching cataloged X-ray or radio sources within the *Fermi* error-box. We focus mainly on the ROSAT catalogues and on NVSS or SUMSS radio sources with a flux greater than 10 mJy. For each found source, a further search for infrared and optical sources is performed using the positional error boxes reported in the ROSAT or radio catalogs. These are much larger than the XRT error radius spanning from 0.3 to 1 armin and for most of the sources having a unique association in the IR and optical bands is not possible.

Since the information in the X-ray band is crucial (especially for our multiwavelength diagnostic algorithm discussed in Chapter 5) and this is a first attempt to identificate UFOs without dedicated *Swift* observations, for these sources we show the results only if we find an unambiguous and reasonable set of candidate counterparts.

3.2 **Results**

In this Section we present the results of our positional association precedure performed for 183 UFOs of our selected sample. They are listed in order of Right Ascension (RA). For each UFO we provide the values of the detection significance and *semi major axis* reported in the 2FGL catalogue, and, in case of available *Swift*/XRT data, the main information about the XRT data analysis as the exposure time, the number of X-ray sources found within the *Fermi* error-box, and the corresponding estimated count rate, with emphasis on those proposed as possible X-ray counterparts. For each UFO, we also display the XRT sky map of the whole region covering the *Fermi* error ellipse and the close-up XRT map of each X-ray counterparts proposed superimposing the position of the other objects found at the other wavelengths (radio, IR and optical band).

3.2.1 2FGL J0102.2+0943

This UFO shows a detection significance of 5.5σ and an error-box of 7.8' in the 2FGL catalogue. Two observations are performed by *Swift*/XRT for a total exposure time of 3991 sec.

Using the XRT imaging analysis tool of UK Swift Science Data Centre, in the XRT sky map (Fig 3.1-*left*) only one faint X-ray source is detected within the 2FGL J0102.2+0943 error-box (*yellow ellipse*), with (RA,DEC)=(01 02 17.15, 09 44 11.16)[6] and a 90% positional error radius of 4.5". The estimated count rate is $(2.624\times10^{-3} \pm 8.314\times10^{-4})$ cts/s (95.2% total) for a total of 11 counts.

Superimposing the catalogues of the other wavelengths (Fig 3.1-*right*) we find a positional coincidence with the radio source NVSS 010217+094407 (*cyan circle*), the IR source 2MASS 01021713+0944098 (*green diamond*) and the optical SDSS10 1237678833220911130 (*magenta cross*). Another IR source seems positionally within the XRT error-box, but we do not consider it because the coincidence is very marginal and the corresponding optical source is outside the region.

Through the SED Builder tool of the ASI ASDC Data Center we build the multifrequency SED (in Fig 3.2) combining the fluxes of the proposed set of counterparts and including also the unabsorbed X-ray flux (estimated by WebPIMMs using a power law model with a photon index of 2) and the XRT flux data from [**?**].

---

[6] This XRT position is corrected by UVOT field astrometry

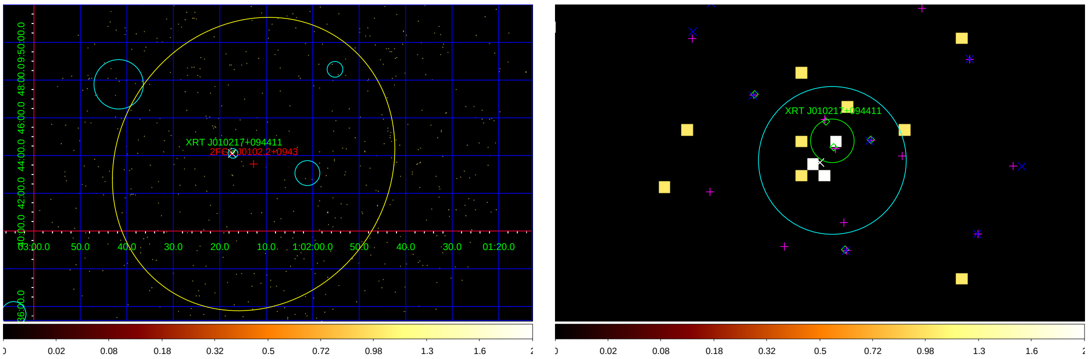

Figure 3.1: *Left*:*Swift*/XRT images of the UFO 2FGL J0102.2+0943 created using the online data analysis tool of UK Swift Science Data Centre. The red cross is the 2FGL J0102.2+0943 the yellow ellipse the 95% error region of 2FGL catalog. The XRT source detected in this work is displayed as a green circle. The cyan circles show the error circles of the NVSS radio sources and the white crosses are *Swift*/XRT objects of the 1SXPS Swift XRT Point Source Catalogue (Evans+2014). Right: Close-up of XRT J010217+094411 skymap. The white cross is the position of the XRT source in the 1SXPS catalog. The blue and magenta crosses are the positions of WISE and SDSS objects and the green diamonds corresponds to 2MASS sources.

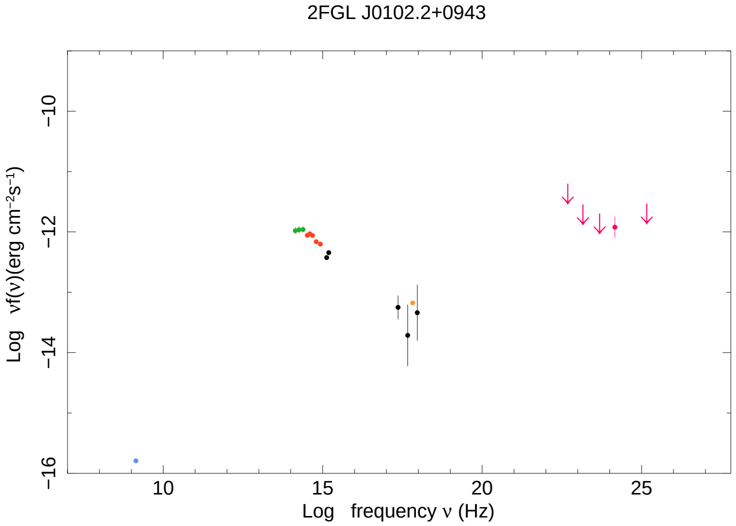

Figure 3.2: Broadband SED of the UFO 2FGL J0102.2+0943 created using the SED Builder tool of the ASI ASDC Data Centre. We combine NVSS radio data (light blue point), WISE and 2MASS IR data (violet and green points), SDSS optical data (red points) with the HE γ-ray data (magenta points) from the 2FGL catalog. The X-ray flux (orange point) is estimated by the WebPIMMS tool of the Nasa's HEASARC in the energy range 0.5-5keV. The flux data taken from [**?**] are shown as black points.

3.2.2 2FGL J0116.6-6153

In the 2FGL catalogue this object is found with a detection significance of 5.5 σ and the *semi major axis 95* is 6'. Two *Swift*-XRT observations are available for a total of 3276 sec. Through the online data analysis of UK Swift Science Data Centre and following the procedure described in the previous section, we can provide the X-ray image for 2FGL J0116.6-6153, shown in Fig 3.3-*left* . Within the Fermi error-box (yellow ellipse) we detect only one X-ray source (RA,DEC) = (01 16 19.24, -61 53 40.2) with a 90% error radius of 5.7 arcsec on the XRT position enhanced by UVOT field astrometry. The estimated net count rate is $(6.424{\times}10^{-3} \pm 1.432{\times}10^{-3})$ cts/s (95.7% total). We propose this object to be the most likely counterpart of 2FGL J0116.6-6153.

The radio source SUMSS J011619-615343 (*cyan ellipse*) appears to be the radio counterpart of XRT J011619-615340. Moreover from the Fig 3.3-*right* the IR sources WISE J011619-615343 (*blue cross*) and 2MASS 01161959-6153434 (*green diamond*) with the optical source USNOB U0281-0014602 (*magenta cross*) are spatially coincident with the X-ray position.

The multiwavelength SED (Fig 3.4) is built combining all available flux data of this set of counterparts through the SED Builder tool of the ASI ASDC Data Center. Since we have not a statistically sufficient number of counts, the X-ray flux is estimated using the WebPIMMS tool in the energy range 0.5-5 keV and assuming a power law model with photon index of 2.

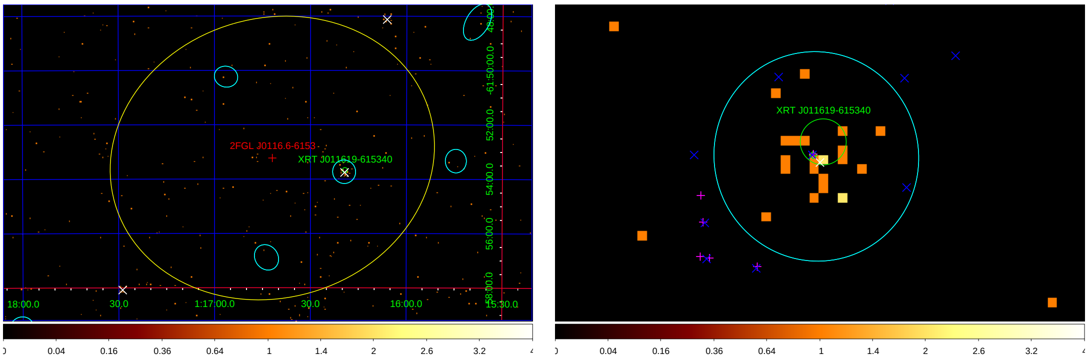

Figure 3.3: *Left*:*Swift*/XRT images of the UFO 2FGL J0116.6-6153 created using the online data analysis tool of UK Swift Science Data Centre. The red cross is the 2FGL J0116.6-6153 position and the yellow ellipse the 95% error region of 2FGL catalog. The XRT source detected in this work is displayed as a green circle. The cyan ellipses show the error ellipses of the SUMSS radio sources and the with crosses are *Swift*/XRT objects of the 1SXPS Swift XRT Point Source Catalogue (Evans+2014). Right: Close-up of XRT J011619-615340 skymap. The white cross is the position of the XRT source in the 1SXPS catalog. The blue and magenta crosses are the positions of WISE and USNO objects and the green diamond corresponds to 2MASS source.

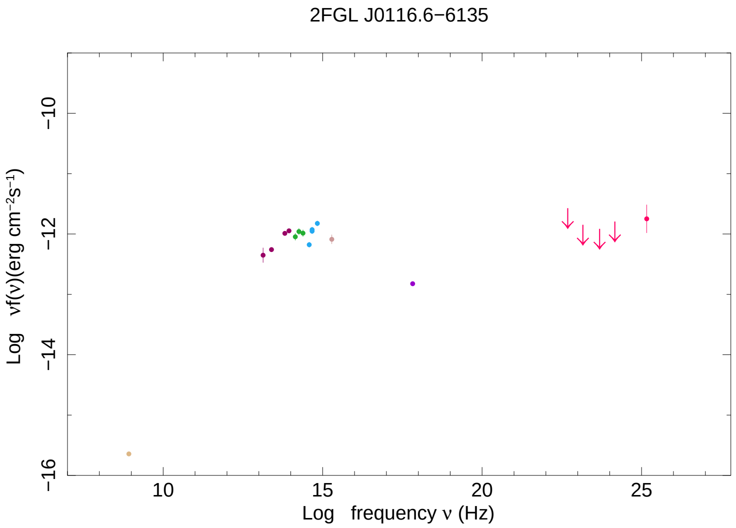

Figure 3.4: Broadband SED of the UFO 2FGL J0116.6-6153 created using the SED Builder tool of the ASI ASDC Data Centre. We combine SUMSS radio data (beige point), WISE and 2MASS IR data (violet and green points), USNOB1.0 optical data (blue points) with the HE γ-ray data (red points) from the 2FGL catalog. The X-ray flux (orange point) is estimated by the WebPIMMS tool of the Nasa's HEASARC in the energy range 0.5-5keV.

3.2.3 2FGL J0129.4+2618

This source shows a very big *semi major axis 95* of 19'.8 and it is reported in the Fermi catalog with a significance of 4.9σ. No *Swift*/XRT observations are available. Producing a sky map with radius of 30' (Fig.3.5) centered in the 2FGL J0129.4+2618 position (*violet circle*), we can note an isolate X-ray source (XMMSLD5 J012939+260258) reported in the XMMSL1D5[7] catalogue (*blue circle*) at the distance of 15'.8 and a very bright NVSS radio source (1.7 Jy) at the distance of 16'.9 (red circles) which is associated to the source 4C+25.06. Although both sources are not outside the *Fermi* error-box of 2FGL J0129.4+2618, we determine two sets of associations considering these sources as the likely counterparts for 2FGL J0129.4+2618. Looking at the corresponding catalogues, we have that the X-ray source XMMSLD5 J012939+260258 and the radio source 4C+25.06 have a positional error radius of 14.2" and 7.5", respectively. For both sources we construct the MWL SED centered on their respective positions, using a search radius equal to their positional error radius. The resulting SED are shown in Fig 3.6.

---

[7] XMM-Newton Slew Survey Full Source Catalog

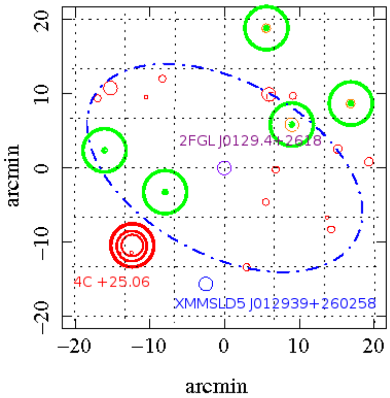

Figure 3.5: Skymap of 2FGL J0129.4+2618 created by the ASDC Sky Explorer tool. In the center of the figure we have the position of 2FGL J0129.4+2618 (violet circle) with the corrisponding error ellipse (blue dashed line). We superimpose the default catalogs of different energy bands provided by the ASI ASDC database: the radio sources are in red, the X-ray sources in blue, the optical sources in green and finally the IR ones in yellow. Note that the size of the circles is not the positional error but it is proportional to the object flux.

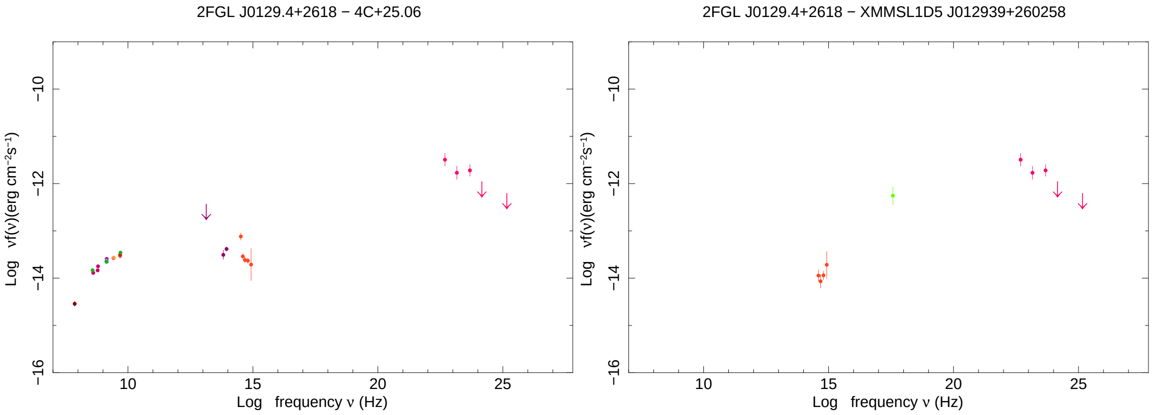

Figure 3.6: Broadband SED of the UFO 2FGL J0129.4+2618 created using the SED Builder tool of the ASI ASDC Data Centre and considering 4C+25.06 (*left*) or XMMSLD5 J012939+260258 (*right*) as possible counterpart. We combine the NVSS radio data (light blue point), the WISE and 2MASS IR data (violet and green points), the SDSS optical data (red points) and the XMM X-ray data (light green point) with the HE γ-ray data (magenta points) from the 2FGL catalog.

3.2.4 2FGL J0143.6-5844

In the 2FGL catalogue, this source is listed with a detection significance of 14.2σ and a *semi major axis* of 3.6'. The object was observed by *Swift*/XRT three times pointing to the coordinates of the 1FGL J0143.9-5845 and collecting 4348 seconds of good exposure time. The XRT skymap resulted from the image analysis is in Fig 3.7-*left* and three X-ray sources are detected within the *Fermi* error-box (*yellow ellipse*). We consider the brightest one, XRT J014347-584551, as likely X-ray counterpart for 2FGL J0143.6-5844. It is a very bright X-ray source with a count rate of (3.765×10^{-1} ± 9.337×10^{-1}) cts/s (99.4% total). The XRT enhanced position is (RA,DEC)=(01 43 47.57, -58 45 51.6) with the error radius of 1.9". In Fig 3.7-*right* we find that the radio source SUMSS J014347-584550 is spatially coincident, together with the infrared sources WISE J014347-584551 and 2MASS 01434742-5845514, and the optical object USNOA2.0 U0300_00524092 located within the XRT error radius. The broad-band SED built joining the fluxes of the likely counterparts is show in Fig 3.8. The light green points are the X-ray data calculated from our dedicated XRT analysis and the black points taken from [**?**].

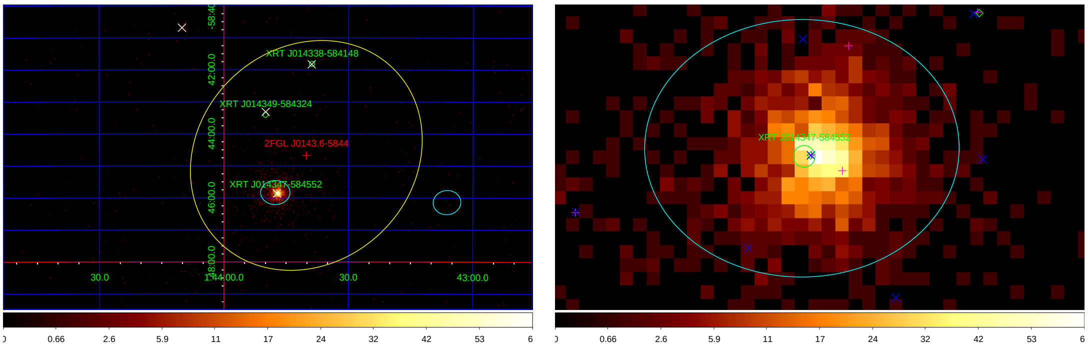

Figure 3.7: *Left*:*Swift*/XRT images of the UFO 2FGL J0143.6-5844 created using the online data analysis tool of UK Swift Science Data Centre. The red cross is the 2FGL J0143.6-5844 position and the yellow ellipse the 95% error region of 2FGL catalog. The XRT sources detected in this work are displayed as green circles with radius equal to the XRT error radius. The cyan ellipses show the error ellipses of the SUMSS radio sources and the with crosses are *Swift*/XRT objects of the 1SXPS catalog. Right: Close-up of XRT 014347-584551 skymap. The white cross is the position of the XRT source in the 1SXPS catalog. The blue and magenta crosses are the positions of WISE and USNO objects and the green diamonds correspond to 2MASS sources.

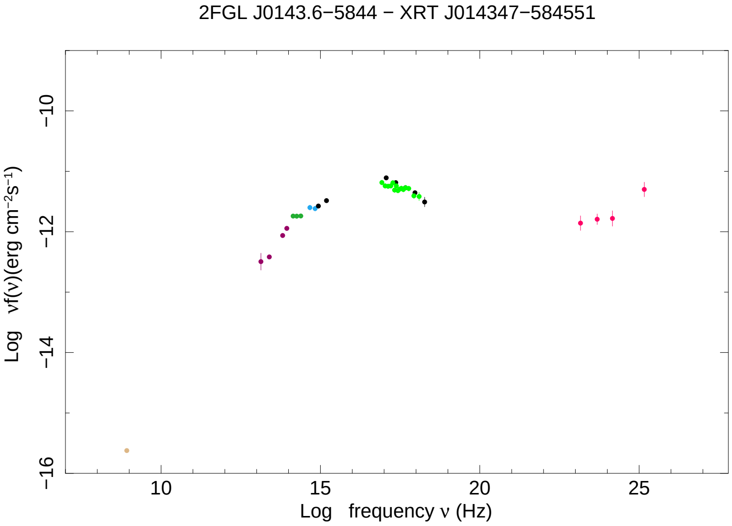

Figure 3.8: Broadband SED of the UFO 2FGL J0143.6-5844 created using the SED Builder tool of the ASI ASDC Data Centre. We combine SUMSS radio data (beige point), WISE and 2MASS IR data (violet and green points), USNOA2.0 optical data (light blue points) with the HE γ-ray data (red points) from the 2FGL catalog. The X-ray flux (light green point) is given from our *Swift*/XRT analysis.

3.2.5 2FGL J0227.7+2249

In the Fermi catalogue this object is classified as a variable source (*Fermi* variability index[8] = 66.4) with an error box of 7.2' and a detection significance of 6.5'. *Swift*/XRT pointed 2FGL J0227.7+2249 in 2012 for a total of 3629 seconds. The resulting XRT sky map from the image analysis is shown in Fig 3.9-*left* and only one X-ray source is detected within the Fermi error-box (*yellow ellipse*) with (RA,DEC)=(02 27 44.43, 22 48 37.9) and error radius of 5.2". Its count rate is $(1.751\times10^{-3} \pm 7.296\times10^{-4})$ cts/s (90.7 % total) hence we have not a significant number of counts to perform the XRT analysis. We estimate the X-ray flux by the WebPIMMs tool in the 0.5-5 keV band and adopting a powerlaw of spectral photon index of 2.

The close-up image centered in the XRT J022744+224837 position is in Fig 3.9-*right* and in the error radius of this X-ray source we can see the radio object NVSS J022744+224834, the IR source WISE J022744+224834 and the optical source SDSS10 1237670960548807265. The MWL SED built with this set of counterparts is shown in Fig 3.10 where the X-ray data (*orange point*) is the unabsorbed estimated flux from WebPIMMs.

---

[8] We remember that the variability index in the 2FGL catalog is the sum of 2*Log(Likelihood) comparison between the flux fitted in 24 time segments and a flat lightcurve over the full 2-year catalog interval. A value greater than 41.64 indicates there is a less than 1% chance of being a steady source. See (2FGLpaper) for details.

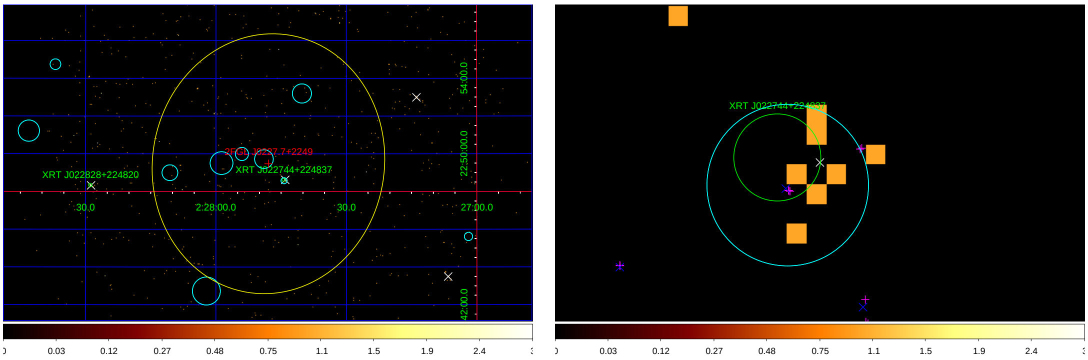

Figure 3.9: *Left*:*Swift*/XRT images of the UFO 2FGL J0227.7+2249 created using the online data analysis tool of UK Swift Science Data Centre. The red cross is the 2FGL J0227.7+2249 position and the yellow ellipse the 95% error region of 2FGL catalog. The XRT sources detected in this work are displayed as green circles with radius equal to the XRT error radius. The cyan circles show the error box of the NVSS radio sources and the with crosses are *Swift*/XRT objects of the 1SXPS catalog. Right: Close-up of XRT 022744+224837 skymap. The white cross is the position of the XRT source in the 1SXPS catalog. The blue and magenta crosses are the positions of WISE and SDSS objects and the green diamonds correspond to 2MASS sources.

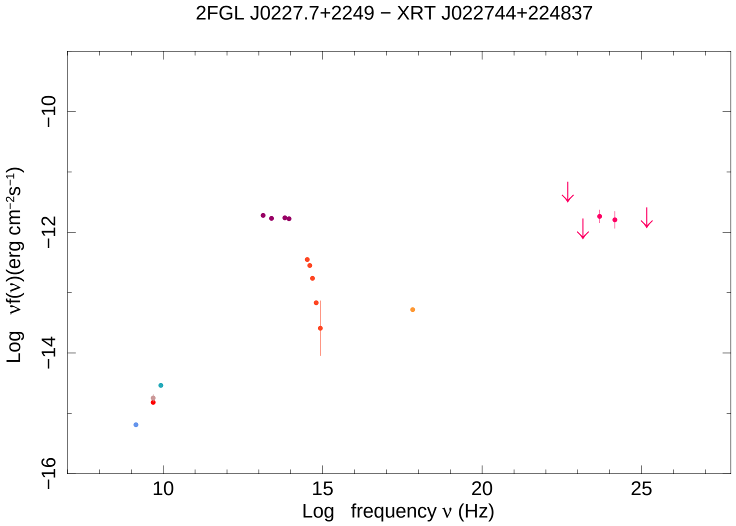

Figure 3.10: Broadband SED of the UFO 2FGL J0227.7+2249 created using the SED Builder tool of the ASI ASDC Data Centre. We combine NVSS radio data (blue point), IR WISE data (violet and green points), SDSS optical data (red points) with the HE γ-ray data (magenta points) from the 2FGL catalog. The X-ray flux (orange point) is estimated by the WebPIMMS tool of the Nasa's HEASARC in the energy range 0.5-5keV.

3.2.6 2FGL J0338.2+1306

This gamma object is a 2FGL source with detection significance of 5.8 σ and an error-box of 6.6'. It was observed by *Swift*/XRT on 4th July 2012 with a exposure time of 3344 sec. The resulting XRT skymap is in Fig.3.14-*right*. We can find two X-ray sources in the XRT skymap, but only the brightest one, XRT J033829+130216, is within the Fermi error-box (*yellow ellipse*). Therefore we decide to suggest it as the most likely X-ray counterpart. From the image analysis, the XRT positional error for this source is 2.1" and its count rate is $(7.160\times10^{-2} \pm 4.653\times10^{-3})$ cts/s (98.9 % total) with 242 total counts found. Using an appropriate absorbed model, the integral flux in the energy range 0.3–10 keV is 4.1319×10^{-12} ergs cm^{-2} s^{-1}.

Looking the close-up image in Fig 3.14-*left*, we can see that the radio source NVSS J033829+130215, the infrared sources WISE J033829+130215 and 2MASS 03382926+1302151, and the optical USNOB 1030-0045117 are spatially coincident with the X-ray counterpart. The multifrequency SED of 2FGL J0338.2+1306, combining the data points of these objects, is in Fig 3.12. We include also the X-ray data provided by our XRT analysis (*light green points*).

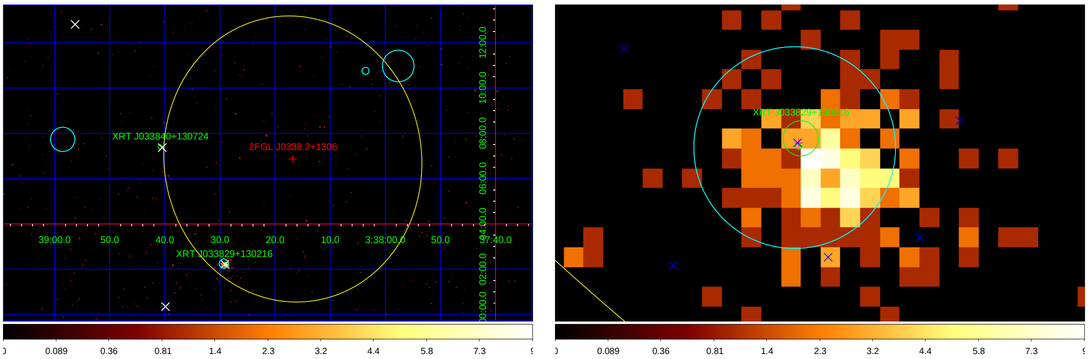

Figure 3.11: *Left*:*Swift*/XRT images of the UFO 2FGL J0338.2+1306 created using the online data analysis tool of UK Swift Science Data Centre. The red cross is the 2FGL J0338.2+1306 position and the yellow ellipse the 95% error region of 2FGL catalog. The XRT sources detected in this work are displayed as green circles with radius equal to the XRT error radius. The cyan ellipses show the error circles of the NVSS radio sources and the white crosses are the*Swift*/XRT objects of the 1SXPS catalog. Right: Close-up of XRT J033829+130216 skymap. The white cross is the position of the XRT source in the 1SXPS catalogue. The blue and magenta crosses are the positions of WISE and USNO objects and the green diamonds correspond to 2MASS sources.

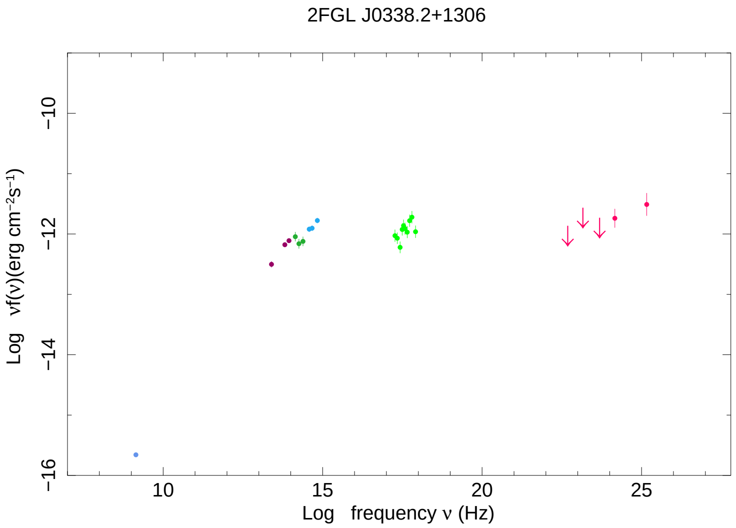

Figure 3.12: Broadband SED of the UFO 2FGL J0338.2+1306 created using the SED Builder tool of the ASI ASDC Data Centre. We combine NVSS radio data (blue point), WISE and 2MASS IR data (violet and green points), USNO B1.0 optical data (light blue points) with the HE γ-ray data (red points) from the 2FGL catalog. The X-ray flux points (light green points) are obtained from our *Swift*/XRT analysis.

3.2.7 2FGL J0458.4+0654

In the 2FGL catalofue this object is reported with a significance of 5.5σ and an error box of 9'. Three Swift/XRT pointings are available, the first one of 2860 sec on 3rd April 2012, the others of about 1800 sec made on 4th April 2012 and 8th April 2012. The XRT sky maps, performed using the ASDC XRT data analysis tool[9], related to each observation are displayed in Fig.3.13. The only X-ray source detected in the all of the three frames is the source with (RA,DEC)=(04 58 02.5, 06 50 14.0) reported also in the RASS catalogue as 1RXS J045802.4+065023. We can note that in the three observations the detected X-ray source shows a variability as summarised in table of Fig 3.13 where the estimated count rate of each observation is reported. Moreover we calculated the X-ray energy spectrum using the XRT data of the 4th April 2012 observation, because it shows the highest count rate, although the exposure time is the smallest of the three observations. We provide the XRT sky map of the 2FGL J0458.4+0654 *Fermi* region joining all the three observations (Fig 3.14-*Left*). Within the UFO error ellipse we found the mentioned XRT source labelled as XRT J045802+065013, and other X-ray sources of the 1SXPS catalogue (*white crosses*). In any case, we decide to propose XRT J045802+065013 as the likely X-ray source because it is the brighest in the X-ray energy band.

---

[9] In this case we use the Online XRT data analysis tool of the ASDC database to have the sinlge sky map of each observation

In Fig 3.14-*Right*, the close-up image of XRT J045802+065013 with superimposed the sources of other catalogues: the IR sources WISE J045802+065014 and 2MASS 04580276+0650141, and the optical source USNOB1 0097-00967-1 are spatially coincident with the X-ray object proposed. No radio source, spatially coincident, was found.

The broad-band SED corresponding to this set of associations is displayed in Fig 3.15.

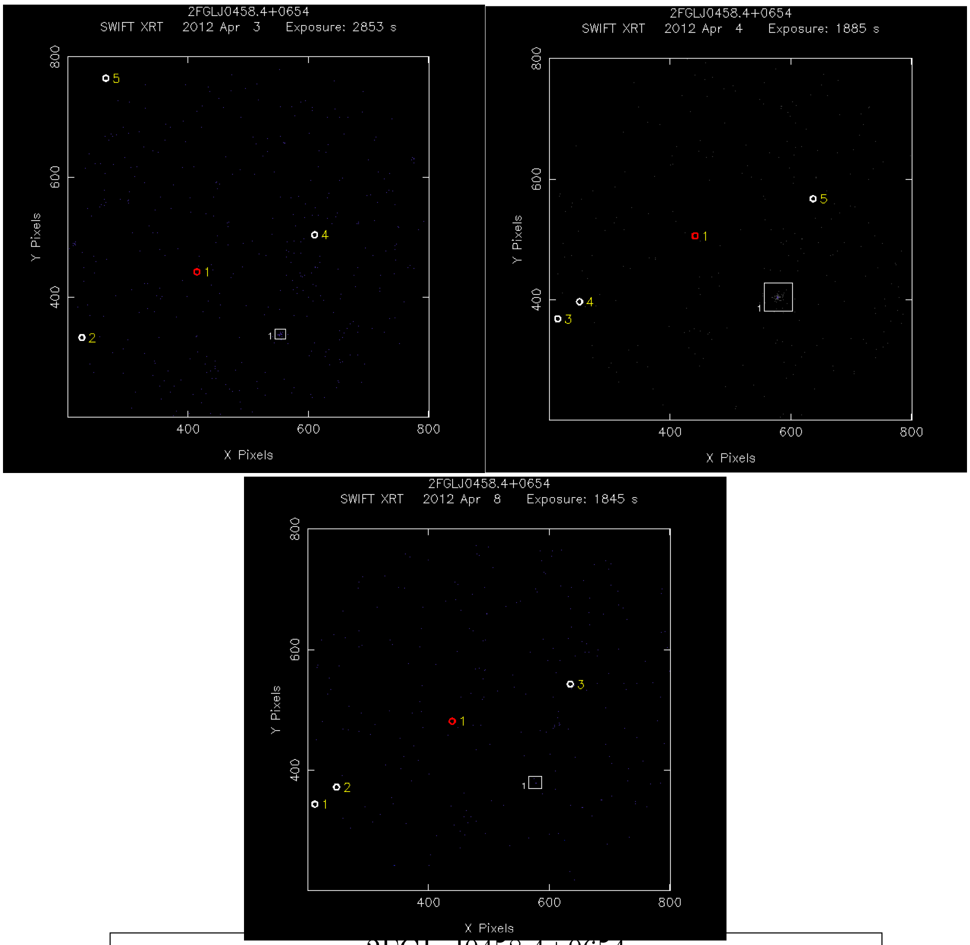

2FGL J0458.4+0654		
Date	Count Rate (cts)	(RA,DEC)
3 April 2012	0.0164 ± 0.0028	(04 58 02.4, 06 50 10.3)
4 April 2012	0.0598 ± 0.0061	(04 58 02.5, 06 50 13.9)
8 April 2012	0.0073 ± 0.0023	(04 58 02.5, 06 50 14.6)

Figure 3.13: *Swift*/XRT images of the UFO 2FGL J0458.4+0654 created using the online data analysis tool of the ASI ASDC Data Centre, for the three observations performend on 3rd April 2012, 4th April 2012 and 8th April 2012. The red circle is the 2FGL J0458.4+0654 position and the white circles the NVSS radio sources. The box corresponds to the detected XRT source with a significance 3σ.

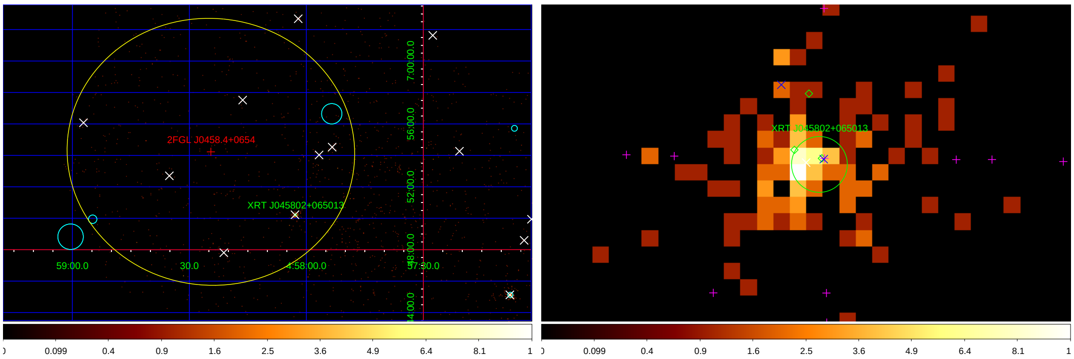

Figure 3.14: *Left*:*Swift*/XRT images of the UFO 2FGL J0458.4+0654 created using the online data analysis tool of UK Swift Science Data Centre. The red cross is the 2FGL J0458.4+0654 position and the yellow ellipse the 95% error region of 2FGL catalog. The XRT sources detected in this work are displayed as green circles with radius equal to the XRT error radius. The cyan ellipses show the error circles of the NVSS radio sources and the white crosses are the*Swift*/XRT objects of the 1SXPS catalog. Right: Close-up of XRT J045802+065013 skymap. The white cross is the position of the XRT source in the 1SXPS catalogue. The blue and magenta crosses are the positions of WISE and USNO objects and the green diamonds correspond to 2MASS sources.

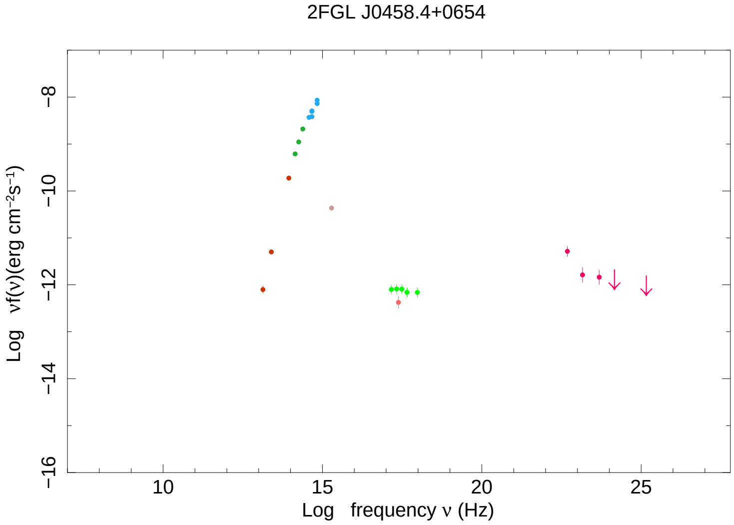

Figure 3.15: Broadband SED of the UFO 2FGL J0458.4+0654 created using the SED Builder tool of the ASI ASDC Data Centre. We combine NVSS radio data (blue point), WISE and 2MASS IR data (violet and green points), USNO B1.0 optical data (light blue points) with the HE γ-ray data (red points) from the 2FGL catalog. The X-ray flux points (light green points) are obtained from the *Swift*/XRT analysis.

3.2.8 2FGL J1038.2-2423

This gamma emitter is reported in the 2FGL catalogue with a *semi major axis* of 9.6' and 5.9σ of detection. It was observed by *Swift*/XRT in 2012 for 4585 sec. The XRT sky map is shown in Fig 3.16 and four X-ray sources are detected inside the Fermi error-box, but we consider the two brightest objects as the likely X-ray counterparts for 2FGL J1038.2-2423. These sources have a sufficient number of X-ray counts to extract their spectrum. In Table 3.16 we report the XRT position, the positional error and the count rate found for the two XRT counterparts proposed and the list of the objects found at other wavelengths spatially coincident with their XRT position. In Fig 3.17 and Fig 3.18 the XRT close-up images for XRT J103754-242546 and XRT J103748-242841 with the respective MWL SED built with the flux data points of their set of associations, including the X-ray spectrum determined by our dedicated analysis.

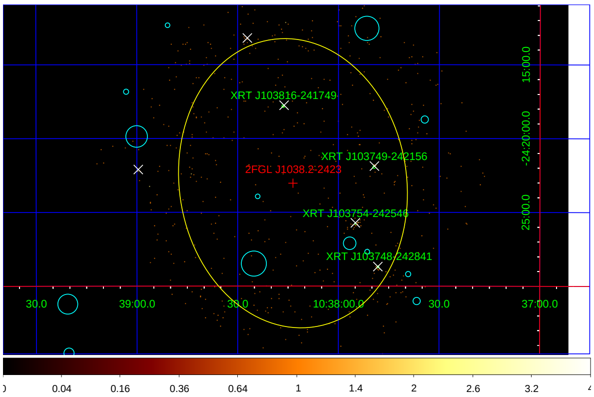

2FGL J1038.2-2423 XRT counterparts	
XRT J103754-242546	
(RA,DEC), eP	(10 37 54.97, -24 25 46.0), 2.5"
Count Rate (cts/s)	(8.504e-03 +/- 1.397e-03) (95.1 % total)
Infrared	WISE J103754-242544
Infrared	2MASS 10375493-2425446
Optical	USNOB1.0 0655-0249305
XRT J103748-242841	
(RA,DEC), eP	(10 37 48.20, -24 28 41.9), 3.8"
Count Rate (cts/s)	(5.121e-03 +/- 1.091e-03) (93.9 % total)
Infrared	WISE J103748-242845
Infrared	2MASS 10374809-2428456
Optical	USNOB1.0 0655-0249283

Figure 3.16: *Swift*/XRT images of the UFO 2FGL J1038.2-2423 created using the online data analysis tool of UK Swift Science Data Centre. The red cross is the 2FGL J1038.2-2423 position and the yellow ellipse the 95% error region of 2FGL catalog. The XRT sources detected in this work are displayed as green circles. The cyan ellipses show the error circles of the NVSS radio sources and the white crosses are *Swift*/XRT objects of the 1SXPS Swift XRT Point Source Catalogue (Evans+2014).

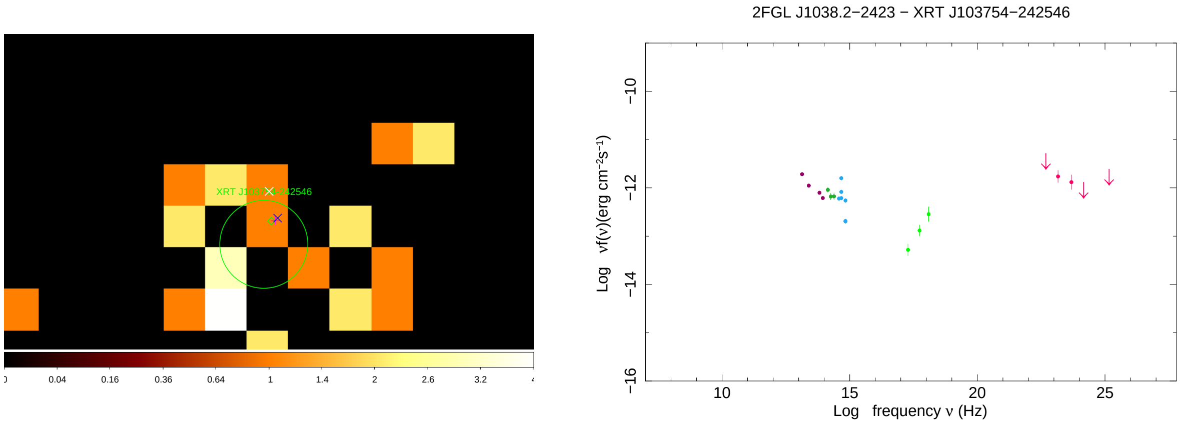

Figure 3.17: *Left*: Close-up of XRT J103754-242546 skymap. The white cross is the position of the XRT source in the 1SXPS catalog. The blue and magenta crosses are the positions of WISE and USNOB1.0 objects and the green diamonds corresponds to 2MASS sources. *Right*: Broadband SED for the UFO 2FGL J1038.2-2423 created using the SED Builder tool of the ASI ASDC Data Centre. We combine the WISE IR data (violet points), the 2MASS IR data (green points), the USNOB1.0 optical data (light blue points) with the HE γ-ray data (magenta points) from the 2FGL catalog. The X-ray flux points (light green points) are from the *Swift*-XRT data analysis of performed this work.

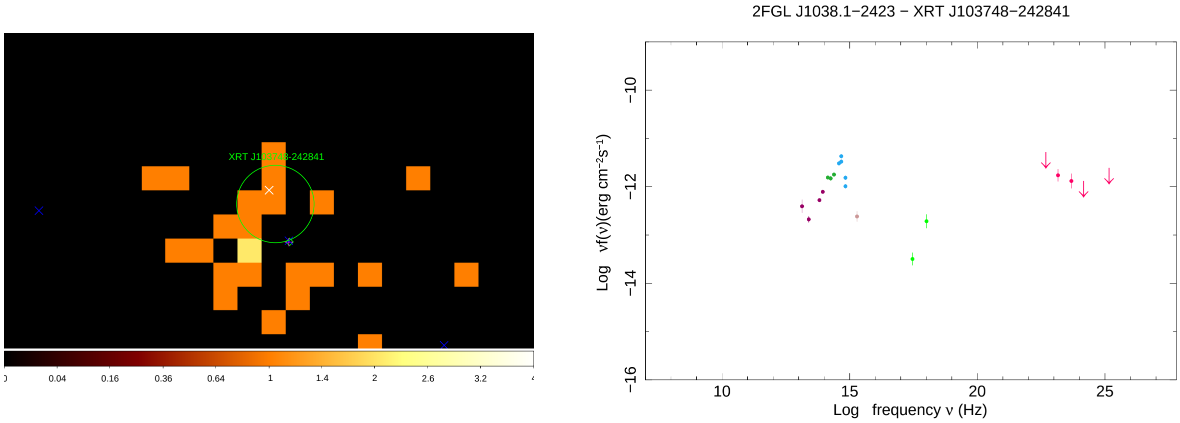

Figure 3.18: *Left*:Close-up of XRT J103748-242841 skymap. The white cross is the position of the XRT source in the 1SXPS catalog. The blue and magenta crosses are the positions of WISE and USNOB1.0 objects and the green diamonds corresponds to 2MASS sources. *Right*: Broadband SED for the UFO 2FGL J1038.2-2423 created using the SED Builder tool of the ASI ASDC Data Centre. We combine the WISE and 2MASS IR data (violet and green points), the USNOB1.0 optical data (light blue points) with the HE γ-ray data (magenta points) from the 2FGL catalog. The X-ray flux points (light green points) are from the *Swift*-XRT data analysis performed in this work.

3.2.9 2FGL J1410.4+7411

In the second Fermi catalog 2FGL J1410.4+7411 has a 9.8σ significance and a *semi major axis* of 4.8'. There are many short *Swift*/XRT observations for a total exposure time of $\sim$ 3000 sec, but looking at the obtained XRT skymap any X-ray source is detected. Moreover the 1SXPS sources, superimposed in the sky map, are all out of the UFO error ellipse (Fig 3.19). For this reason we cannot create a set of MWL counterpart.

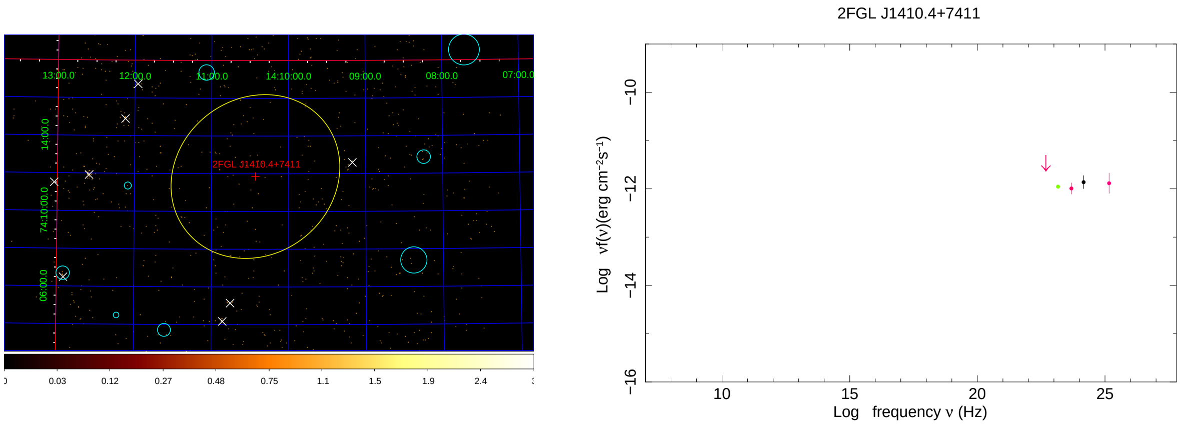

Figure 3.19: *Left*:*Swift*/XRT images of the UFO 2FGL J1410.4+7411 created using the online data analysis tool of UK Swift Science Data Centre. The red cross is the 2FGL J1410.4+7411 position and the yellow ellipse the 95% error region of 2FGL catalog. The XRT sources detected in this work are displayed as green circles. The cyan ellipses show the error circles of the NVSS radio sources and the white crosses are *Swift*/XRT objects of the 1SXPS Swift XRT Point Source Catalogue (Evans+2014). *Right*: Broadband SED for the UFO 2FGL J1410.4+7411 created using the SED Builder tool of the ASI ASDC Data Centre.

3.2.10 2FGL J1511.8-0513

The UFO 2FGL J1511.8-0513 is recorded in the *Fermi* catalogue with a detection significance of 7.8σ and a *semi major axis* of 4.8'. Pointing the position reported in the 1FGL, *Swift*/XRT observed the 2FGL J1511.8-0513 sky region in 2010 for a total time of 4160 sec. The XRT data analysis was performed by the UK XRT analysis tool and the resulting sky map is shown in Fig 3.20. Within the *Fermi* error-box we found two X-ray sources. Although they have a different brightness in the X-ray band (1369 counts for the brightest and 31 counts for the other one), we decide to consider both of them as possible X-ray counterparts and to determine two distinct set of associations. In the corresponding table of Fig 3.20 we report the name of the source, the position in the sky with the related positional error radius, the estimated count rate and the sources at the other wavelengths (IR and optical) found within the X-ray error-box. The positional coincidences, between the X-ray counterparts and the other objects, can be seen in the close-up images shown in the Fig 3.21-*left* and Fig 3.22-*left*.

Finally for each set of counterparts, the broad-band SED was built joining all flux data points (Fig 3.21-*right* and Fig 3.22-*right*).

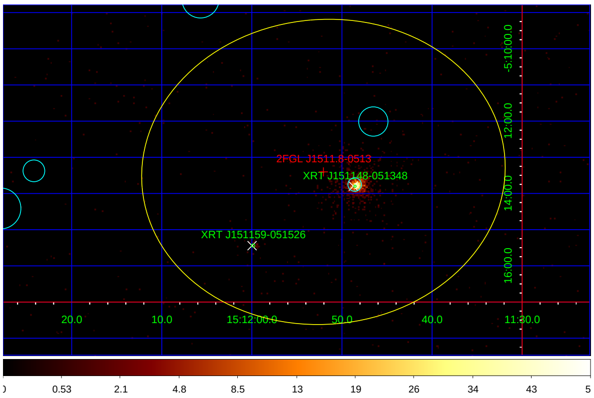

2FGL J1511.8-0513 XRT counterparts	
XRT J151148-051348	
(RA,DEC), eP	(15 11 48.55, -05 13 48.0), 1.9"
Count Rate (cts/s)	$3.422\times10^{-01} \pm 9.309\times10^{-03}$ (99.4 % total)
Radio	NVSS J151148-051345
Infrared	WISE J151148-051346
Infrared	2MASS 15114857-0513467
Optical	USNOB1.0 0847-0269314
XRT J151159-051526	
(RA,DEC), eP	(15 11 59.86, -05 15 26.3), 2.7"
Count Rate (cts/s)	$3.900\times10^{-03} \pm 1.345\times10^{-03}$ (52.3 % total)
Infrared	WISE J151159-051524

Figure 3.20: *Swift*/XRT images of the UFO 2FGL J1511.8-0513 created using the online data analysis tool of UK Swift Science Data Centre. The red cross is the 2FGL J1511.8-0513 position and the yellow ellipse the 95% error region of 2FGL catalog. The XRT sources detected in this work are displayed as green circles. The cyan ellipses show the error circles of the NVSS radio sources and the white crosses are *Swift*/XRT objects of the 1SXPS Swift XRT Point Source Catalogue (Evans+2014).

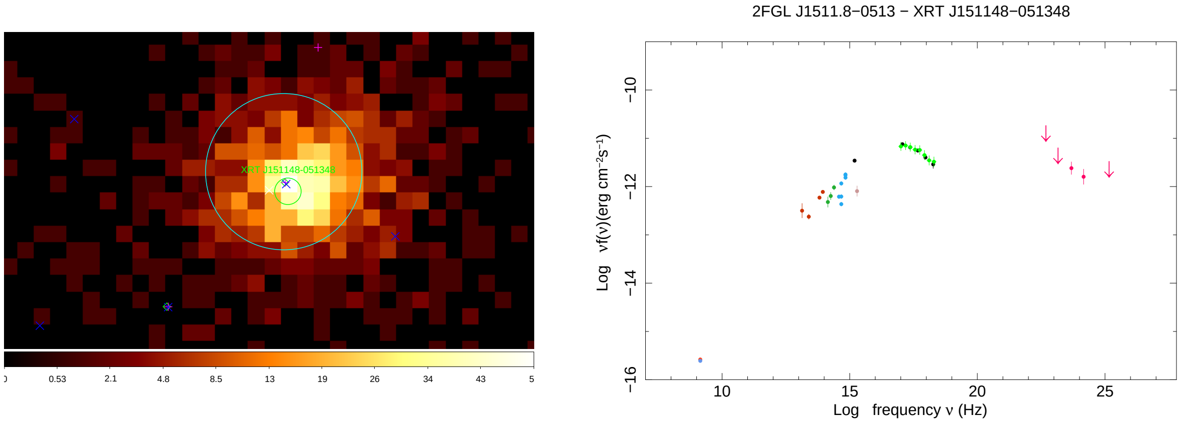

Figure 3.21: *Left*: Close-up of XRT J151148-051348 skymap. The white cross is the position of the XRT source in the 1SXPS catalog. The blue and magenta crosses are the positions of WISE and USNOB1.0 objects and the green diamonds corresponds to 2MASS sources. *Right*: Broadband SED for the UFO UFO 2FGL J1511.8-0513 created using the SED Builder tool of the ASI ASDC Data Centre. We combine the WISE IR data (violet points), the 2MASS IR data (green points), the USNOB1.0 optical data (light blue points) with the HE γ-ray data (magenta points) from the 2FGL catalog. The X-ray flux points (light green points) are from the *Swift*-XRT data analysis of performed this work.

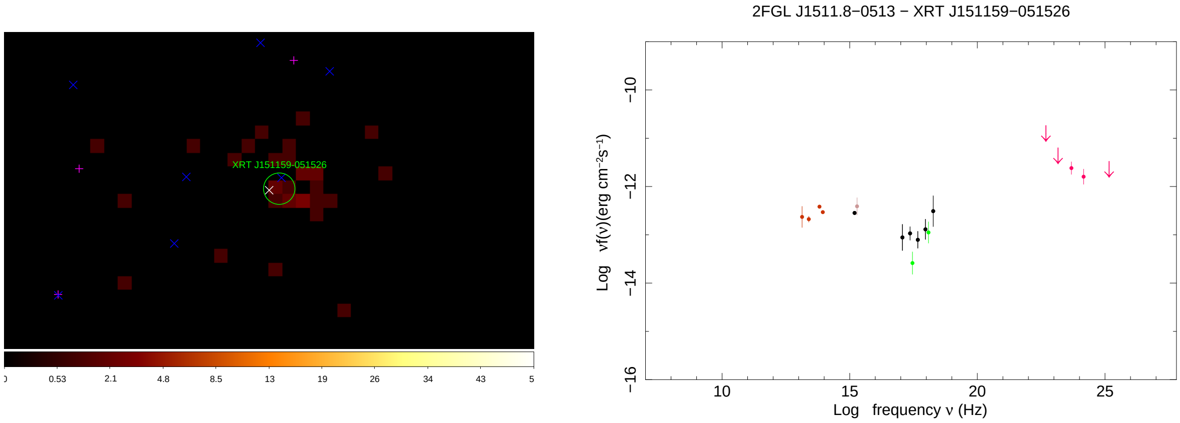

Figure 3.22: *Left*:Close-up of XRT J151159-051526 skymap. The white cross is the position of the XRT source in the 1SXPS catalog. The blue and magenta crosses are the positions of WISE and USNOB1.0 objects and the green diamonds corresponds to 2MASS sources. *Right*: Broadband SED for the UFO 2FGL J1511.8-0513 created using the SED Builder tool of the ASI ASDC Data Centre. We combine the WISE and 2MASS IR data (violet and green points), the USNOB1.0 optical data (light blue points) with the HE γ-ray data (magenta points) from the 2FGL catalog. The X-ray flux points (light green points) are from the *Swift*-XRT data analysis performed in this work.

3.2.11 2FGL J1544.5-1126

In the second Fermi catalog 2FGL J1544.5-1126 is reported with a detection significance of 5.79σ and a *semi major axis 95%* of 8.4'. *Swift*/XRT did not observe it directly, but pointed the source 1RXS J154439.4-112820 which is the brightest X-ray source within the 2FGL J1544.5-1126 error-box. We suggest it as the likely X-ray counterpart. From the XRT data with an exposure time of 13350 seconds the XRT sky map has been created (Fig 3.23-*left*) and the X-ray source, labelled as XRT J154439-112804, has an associated error-box of 1.7" (much less than the error-box provided by ROSAT). In the close-up image (Fig 3.23-*right*) we can see that the IR object WISE J154439-112804 and the optical source USNOB1.0 0785-0287377 are positionally coincident and hence we consider them as unique source associable to 2FGL J1544.5-1126. The estimated XRT J154439-112804 count rate is $(7.003\times10^{-2} \pm 2.311\times10^{-3})$ cts/s (98.3 % total) and the integral 0.3-10 keV flux is 4.4394×10^{-12} ergs cm^{-2} s^{-1}. The obtained differential spectrum, deabsorbed for Galactic extiction, is plotted in the multiwavelength SED of Fig 3.24 (*light green points*) together with the XRT spectrum taken from [**?**] (*black points*) and the data points of the other associated sources.

For the honour of completeness, we would like to mention that in the 2FGL J1544.5-1126 error-box (*yellow ellipse*) there are other six very faint X-ray sources belonging to the 1SXPS catalogue. For each of them, the position and the positional error-box was determined through a dedicated imaging analysis. However for most of them, the straightforward determination was not possible and then we used the catalogue position. The close-up sky map of these X-ray sources are displayed in Fig 3.25 where we superimposed the entries from the others catalogues in radio, IR and optical bands. The possibility to associate them to 2FGL J1544.5-1126 will be discussed in the Sec 5.2.11.

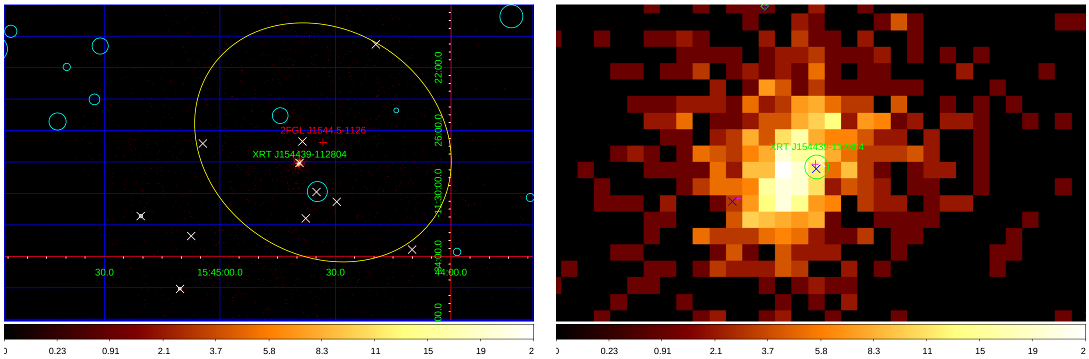

Figure 3.23: *Left*:*Swift*/XRT images of the UFO 2FGL J1544.5-1126 created using the online data analysis tool of UK Swift Science Data Centre. The red cross is the 2FGL J1544.5-1126 position and the yellow ellipse the 95% error region of 2FGL catalog. The XRT sources detected in this work are displayed as green circles with radius equal to the XRT error radius. The cyan ellipses show the error circles of the NVSS radio sources and the white crosses are the*Swift*/XRT objects of the 1SXPS catalog. Right: Close-up of XRT J154439-112804 skymap. The white cross is the position of the XRT source in the 1SXPS catalog. The blue and magenta crosses are the positions of WISE and USNO objects and the green diamonds correspond to 2MASS sources.

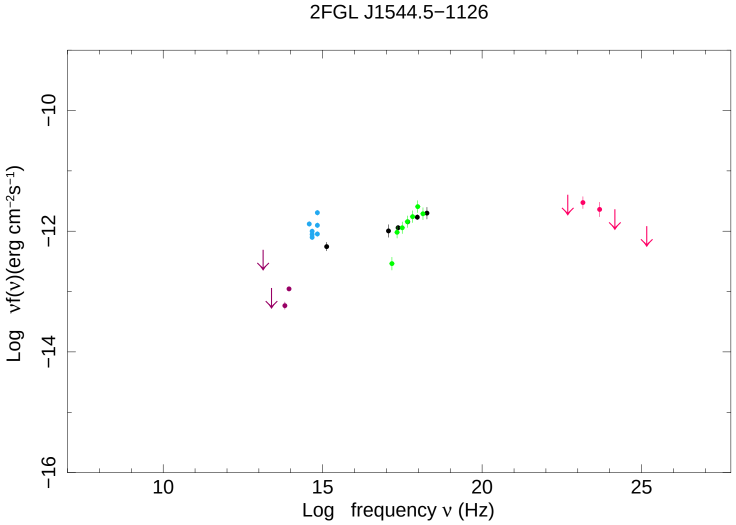

Figure 3.24: Broadband SED of the UFO 2FGL J1544.5-1126 created using the SED Builder tool of the ASI ASDC Data Centre. We combine NVSS radio data (blue point), WISE and 2MASS IR data (violet and green points), USNO B1.0 optical data (light blue points) with the HE γ-ray data (red points) from the 2FGL catalog. The X-ray flux given from our *Swift*/XRT analysis are the light green points, while the data taken form [**?**] in black.

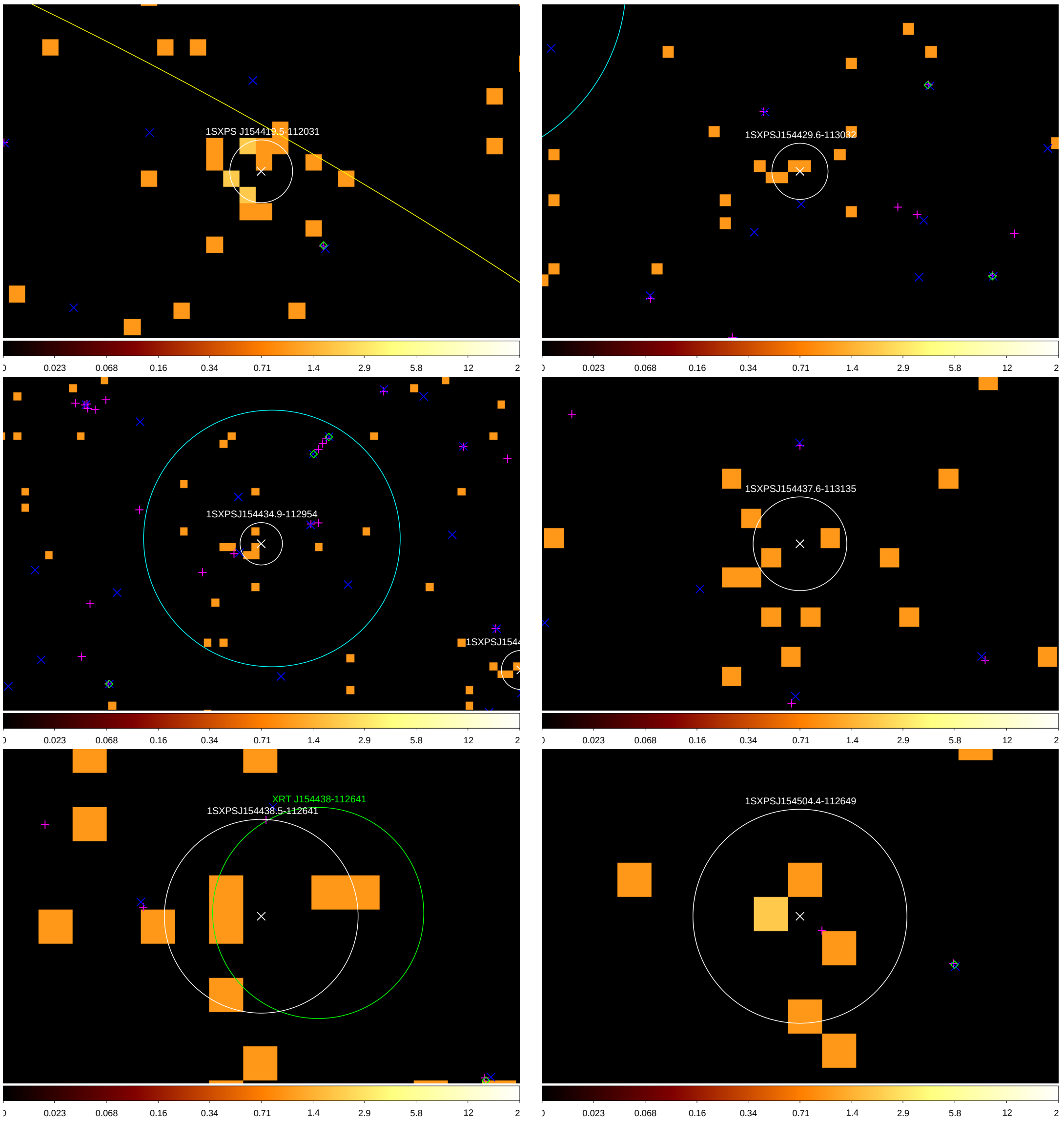

Figure 3.25: Close-up sky maps of the X-ray sources of the 1SXPS catalogue within the 2FGL J1544.5-1126 error-box. The white circle is the position of the XRT source as taken from 1SXPS catalogue. The green circle is the position estimated through our dedicated XRT imaging analysis. The blue and magenta crosses are the positions of WISE and USNO objects and the green diamonds correspond to 2MASS sources.

3.2.12 2FGL J1614.8+4703

2FGL J1614.8+4703 is a very faint gamma-ray emitter cataloged in the 2FGL catalogue with a detection significance of 4.59σ and a rather big Fermi error box *semi major axis* of 13.8'. There are not *Swift*/XRT pointings dedicated to this source, but the observations of the IR source 2MASX J16154117+47111 of 4990 sec cover part of the 2FGL J1614.8+4703 error-box as we can see in Fig 3.26-*left.* Only the X-ray source XRT J161541+471110 is detected and we suggest it as likely X-ray counterpart. We can note that superimposing the 1SXPS catalogue and searching inside a radius of 30', only the object spatially coincident with XRT J161541+47111 is found and no other 1SXPS sources appears in the skymap, supporting our choice. The close up image around XRT J161541+47111 position is in Fig 3.26-*right* where within the XRT positional error of 4.8" we find the IR objects WISE and 2MASS, and the optical object SDSS10 (labelled as SDSS10 588007004192637004) . For the latter we have the optical spectrum performed by the SDSS survey[10] that suggests for it a quasar nature with a redshift of 0.19 (Fig 3.27-*right*).

The MWL SED for 2FGL J1614.8+4703 is displayed in Fig 3.27-*left* joining all flux data of the proposed counterparts. The light green points indicate the X-ray spectrum estimated through the analysis of the XRT J161541+471110 data. For it we find a count rate (6.761×10^{-3} $\pm1.186\times10^{-3}$) cts/s (96.4 % total) and a integral flux between 0.3 to 10 keV of 2.6344×10^{-12} ergs cm^{-2} s^{-1}).

---

[10] http://skyserver.sdss3.org/dr10/en/tools/chart/navi.aspx

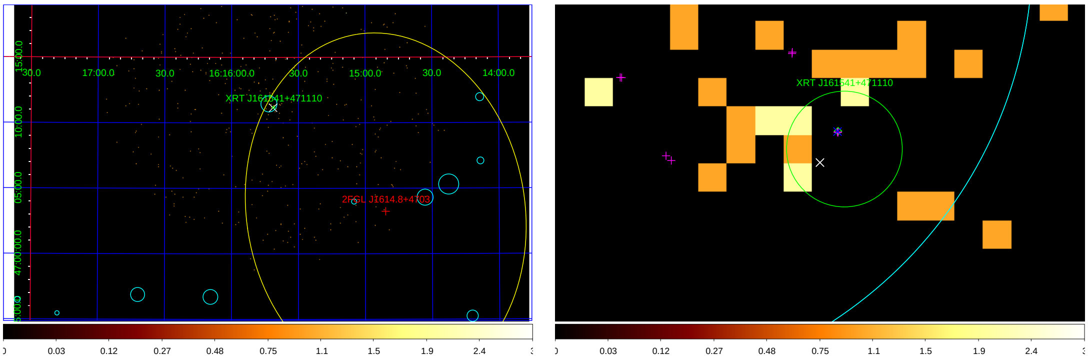

Figure 3.26: *Left*:*Swift*/XRT images of the UFO 2FGL J1614.8+4703 created using the online data analysis tool of UK Swift Science Data Centre. The red cross is the 2FGL J1614.8+4703 position and the yellow ellipse is the 95% error region of 2FGL catalog. The XRT sources detected in this work are displayed as green circles with radius equal to the XRT error radius. The cyan circles show the error circles of the NVSS radio sources and the white crosses are the*Swift*/XRT objects of the 1SXPS catalog. Right: Close-up of XRT J161541+471110 skymap. The white cross is the position of the XRT source in the 1SXPS catalog. The blue and magenta crosses are the positions of WISE and SDSS objects and the green diamonds correspond to 2MASS sources.

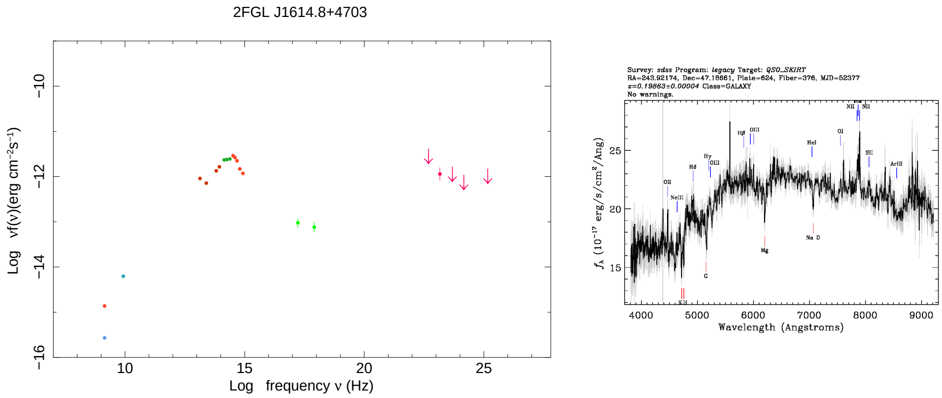

Figure 3.27: *Left*: Broadband SED for the UFO 2FGL J1614.8+4703 created using the SED Builder tool of the ASI ASDC Data Centre. We combine the WISE IR data (violet points), the 2MASS IR data (green points), the SDSS10 optical data (red points) with the HE γ-ray data (magenta points) from the 2FGL catalog. The X-ray flux points (light green points) are from the *Swift*-XRT data analysis of performed this work. *Right*:XXXX

4

BLAZAR AGNs and the Definition of a BLAZAR SED Template Set

4.1 Active Galactic Nuclei

In about 1% of the galaxies of the Universe, a substantial fraction of their energy release is not attributed to the normal galaxy processes from stars, dust, interstellar gas, and their interactions, but it is generated by a compact region located in the center of the galaxy. A such radiation is highly variable and characterized by a non-thermal origin, spanning the whole electromagnetic spetrum from radio to γ-ray energies.

These sources form the class of the *Active Galactic Nuclei* (AGN) where the emission of the very bright nucleus, with bolometric luminosity of $\sim 10^{42}$-$\sim 10^{48}$ erg s^{-1} ($\sim 10^{12}$-$\sim 10^{15}$ $L_{\odot}$) [12, 38, 50], is explained as gravitational energy released by accretion of gas into the BH. The gas, subjected to the gravitational field induced by the BH and not in a stable orbit around it, moves by free-fall towards the compact object. If the amount of gas is consistent and locally reaches the thermodinamic equilibrium, it is possible to form an accretion disc which is a powerful engine to dissipate energy via viscous torques and able to carry out the angular momentum of the material from the inner regions to the outer regions of the disc. The temperature T of the accretion disc depends on the accretion rate and the mass of the BH, and, in general, in the inner region it reaches up to 10^5 K. Such a high temperature of the disc produces strong UV and X-ray emission. The efficiency of the process, defined as the ratio of the energy released in the emission and the rest mass of the accreting material, can reach up to 10%.

Part of the power can be radiated at lower energies mainly due to absoprtion effects and re-emission processes (i.e. scattering) involving dust and gas around the central regions. For a given spin and BH mass, in particular accreting conditions (especially when viscous forces are negligible), the velocity of the accreting material is higher than the escape velocity. For this reason, part of the accreted material can be expelled outwards in highly collimated jets of plasma orthogonal to the disk plane of the AGN and propagating for kpc or Mpc. The formation and chemical composition of the jets are still matter of debate, nevertheless they significantly contribute to the emitting power and affect the shape of the emission spectrum.

AGN are classified in radio-loud and radio-quiet, according to their radio emission. The dicotomy between the two classes is strongly driven by the existence of jets, as they are characterised by radio emission. This is one of the observational features, togheter with the optical spectrum, behind the phenomenological classification of the AGN described in the next section.

4.1.1 AGN taxonomy and the Unified Model of AGNs

In literature, AGN can be hardly grouped in specific classes characterised by their features. Many of them have been instead empirically classified on the basis of their observational properties.

A first attempt of classification [59] was based on the morphology of the optical spectum, investigating the width of the emission lines, and on the intensity and geometry of the radio emission.

Regarding the properties in the optical band, the AGN spectra show prominent emission lines arising from gas which is more likely photoionised by a non-stellar continuum source. As we can see in Fig4.1 there are two different types of emission lines in according to their widths:

- The broad lines (Doopler widths of thousand of km s^{-1}) associated to permitted and semi-forbidden transitions; They are produced in the so-called Broad-Line Region (BLR) at ∼1 pc from the central engine and their high velocities are due to the galactic potential;

- The narrow lines (Doppler width of hundreds of km s^{-1}) produced only by forbidden transitions in the Narrow-Line Region located at ~10-1000 pc within the potential of the SMBH;

Once that these two distinct emission regions and their optical lines associated, the AGNs were classified as *Type-1 galaxies*, if they exhibit broad and narrow lines and hence reveals also the BLR, or *Type-2 galaxies*, if only narrow lines of the NRL are shown.

Another observational criteria used for AGN classification is the presence of radio emission, introducing the parameter of *Radio-loudness* (R) defined as the ratio of the radio (5 GHz) and optical (B band) fluxes. Using the threshold R = 10 [35], the objects were divided in two categories: the *Radio-quiet* and the *Radio-loud galaxies.*

The **Radio-quiet** galaxies do not show an important radio emission and are further subdivided in *Seyfert galaxies* and *Quasars.* The former are AGNs hosted into spiral galaxies with lower bolometric luminosity, with respect to the whole class of the AGNs, while for the quasars the host galaxy is usually elliptical.

The **Radio-loud** galaxies constitute 10-20% of the whole AGN population and characterized by the presence of jets of matter expelled from the central engine and extending on scales of the order of Mpc [14] (not present in the radio-quiet sources). Based on their morphology, described in terms of *extended* (spatially resolved) and *compact core* (unresolved) components, the radio-loud sources are subdivided in various categories.

In the case of extended radio sources, where the radio emission is originated in two radio *lobes*, two populations are distinguishable (Fig 4.2): the *Faranoff-Riley Class I* (FR I) sources, that have the brighest radio regions close to the core and low luminosity lobes connected to the central region by two continuos jets, and the *Faranoff-Riley Class II* (FR II) objects, the most powerful lobe dominated AGNs with only one jet connecting one lobe with the central core.

Another small fraction of radio-loud AGNs is formed by the *blazars* that appears compact and point-like objects and they are interpreted as radiogalaxies with the jet closely aligned with the line of sight. They are sub-divided in *Radio quasars*, hosted into elliptical galaxies and with clear broad lines in their optical spectrum, and *BL Lac objects* characterized by a flat radio spectrum, by very weak or absence of emission lines and by variable flux at all

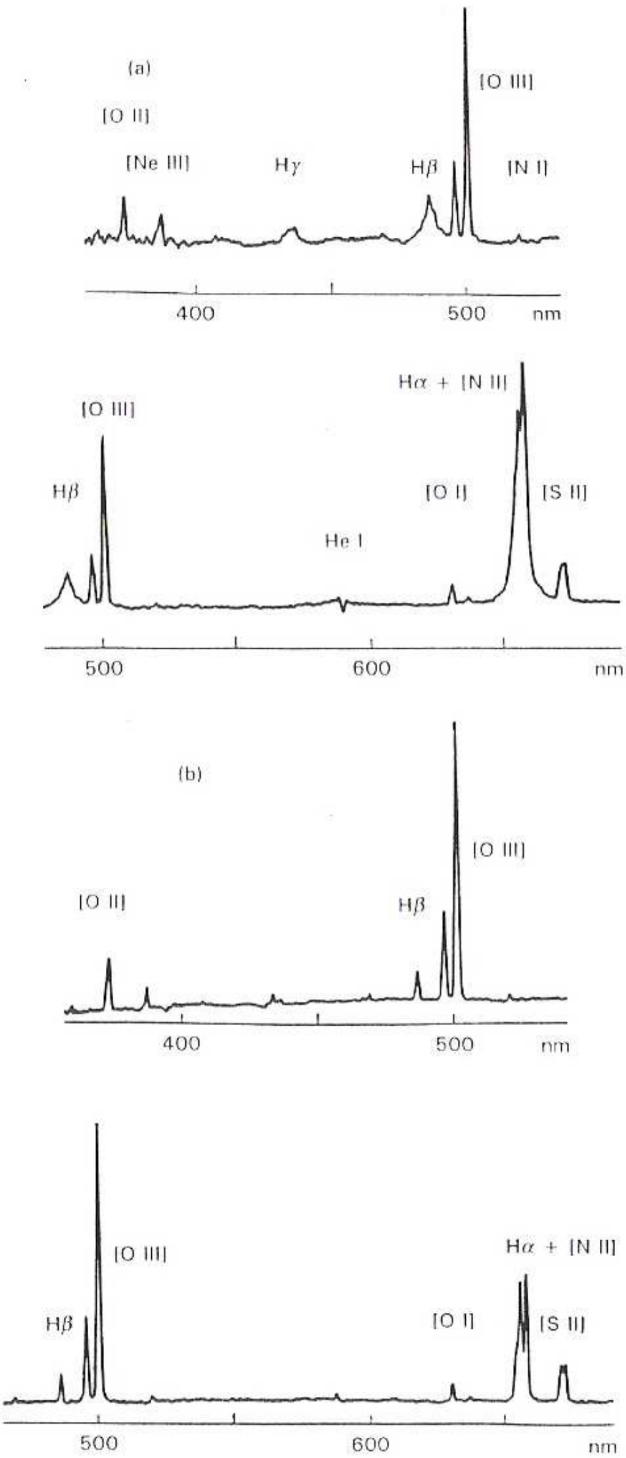

Figure 4.1: Optical spectrum of the AGN type-1 NGC 3227 (*upper panel*), and AGN type-2 Mrk1157.

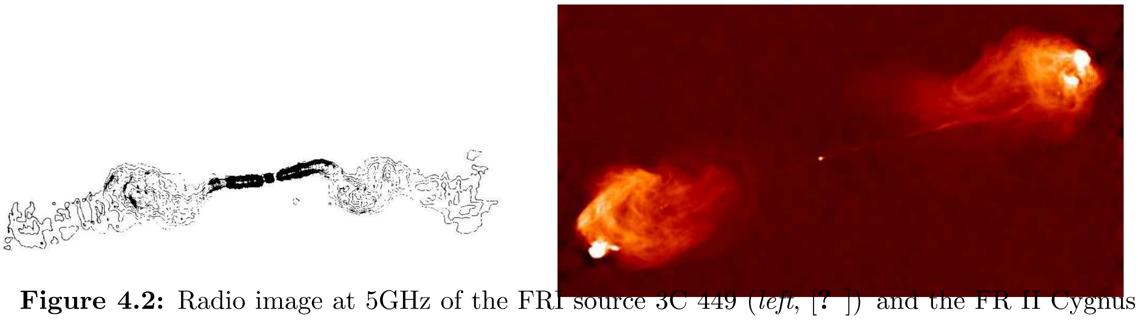

Figure 4.2: Radio image at 5GHz of the FRI source 3C 449 (*left*, [?]) and the FR II Cygnus A (*right*, credits:VLA/J.Conway and P. Blanco).

wavelength. The class of the *blazar* AGN and the main physicical processes related to this kind of objects, are described in Sec 4.2.

Despite the numerous classes of AGNs (as shown in Fig 4.3), according to their observational spectral features, it has been possible to unify all of these sources within a simple scheme, the so-called *The AGN unified model* [59]. The basic idea is the assumption that all of the apparently classes of AGN can be considered as a single class of objects observed at different inclination angles with respect to the line of sight. This model is well illustrated in Fig 4.4-*left* and permits to explain the different observational features in terms of the different viewing angles to the sources.

4.1.2 The AGN central kiloparsec

Thanks to spectroscopical observations, many theories were suggested to describe the region within the central kiloparsec that is the core of the AGN activity. It is supposed to be a region highly ionized by an intense and very bright central source responsible for the continuous radiation and emission lines.

According to the sketch of Fig 4.4-*right*, at the center of the AGN structure there is a *Super-Massive Black Hole* (SMBH) surrounded by a thin accretion disc of infalling gas. The accretion flow of matter, through viscous or turbolent torques, trasforms its kinetic energy into thermal radiation. The total observed power, emitted by the disc as UV/X radiation, can be described as superposition of several black body spectra emitted in a number of anulus of the accretion disc, each one emitted with a specific effective temperature. Disc emission is then dependent on the BH mass, accretion rate and the properties of the accretion disk. The

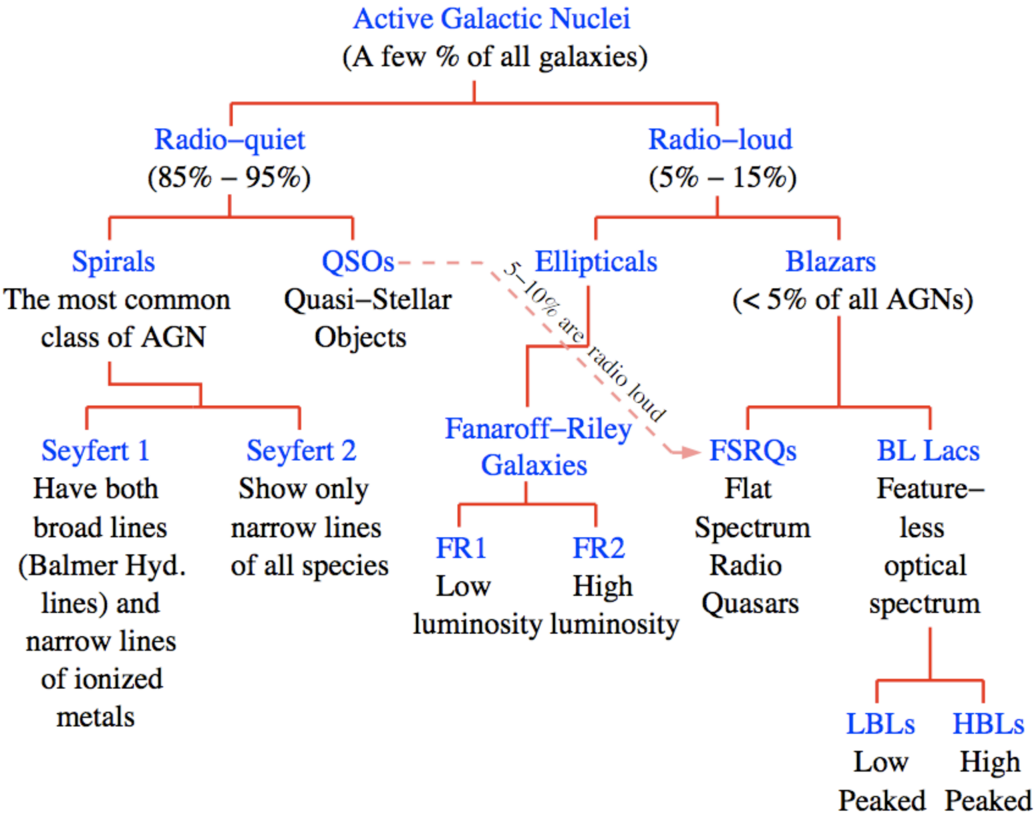

Figure 4.3: AGN classification diagram from [39] and based on [59]

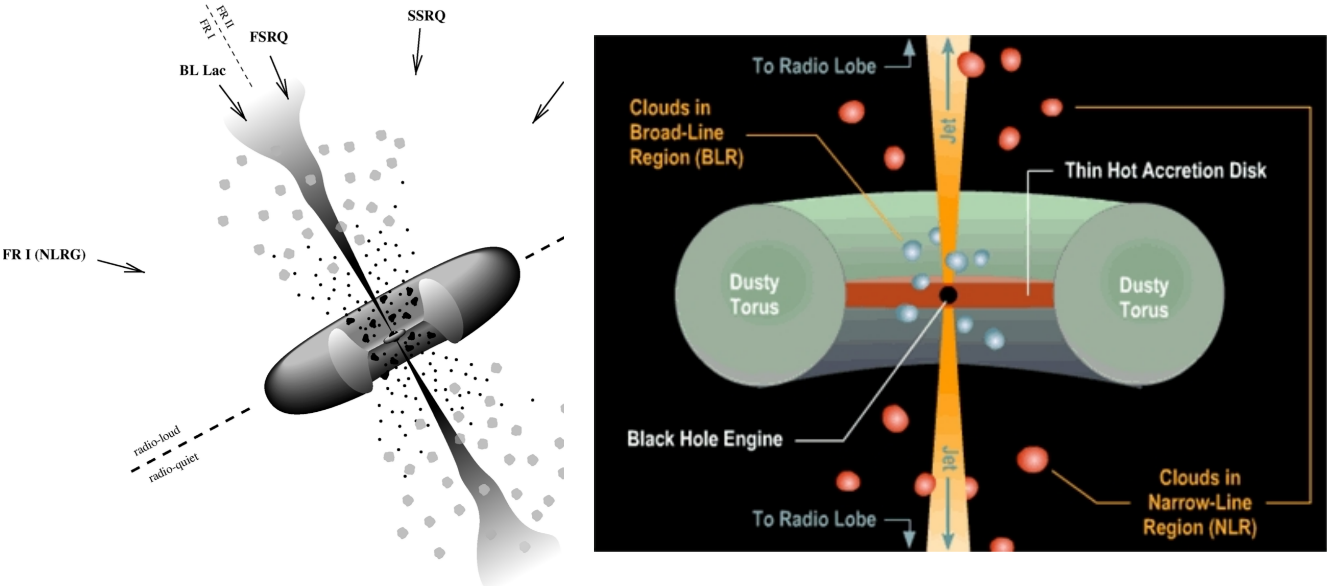

Figure 4.4: *Left*: Sketch of the unified model for the AGNs [372Conr+]. *Right*: Scheme of the currently accepted model of the AGN central kiloparsec indicanting the individual components and emission regions..

accretion rate can be espressed as:

$$\dot{M}_{acc} = \frac{dm}{dt} = \frac{L}{Qc^2} \rightarrow L_{acc} = Q\dot{M}_{acc}c^2 \tag{4.1}$$

where Q denote the accretion efficiency. This simple situation is complicated from severals factors. First of all, accretion can be stopped by the Eddington luminosity, defined as the luminosity at which the gravitational pressure on the accretion flow is balanced by the ram-pressure. This luminosity is defined for homegenous and spherical accretion. It is directly proportional to the BH mass:

$$L_{edd} = \frac{4\pi G M m_p c}{\sigma_T} = 1.3 \times 10^{38} \frac{M}{M_\odot} \qquad \text{erg s}^{-1} \tag{4.2}$$

with m_p is the proton mass, σ_T the Thompson cross section and G the gravitation constant. The second aspect concerns the properties of the accretion disk: if the accretion disk is optically thick, we have the regime of *Efficient Accretion* with $\dot{M}_{acc} > 0.01\dot{M}_{edd}$ and characterized by high value of efficiency and luminosity (this is the case for the FSRQs); viceversa the optically thin disks show *Inefficient Accretion* with $\dot{M}_{acc} < 0.01\dot{M}_{edd}$ and lower efficiency and luminosity (mainly this situation is associated to the BL Lac objects).

Embedded in the gravitational potential field of the central engine, at a distance of 0.1-1 pc, a hot and photoionized shell of gas clouds originates the *Broad-Line Region*. This is the place of the formation of the broad emission lines observed in the optical band and broadened by Doppler effects due to the motion of the clouds.

At 1-10 pc, a region of toroidal shape, composed of gas and dusty clouds, surrounds the BLR and the accretion disk. This *Molecular Torus* absorbes the primary UV-X radiation generated by the innermost part of the AGN, reprocessing it as IR band emission. In the unified model the orientation of the molecular torus determines the possibility to observe the BLR (and explain the different AGN types): if the torus symmetry axis is along the line of sight the broad emission lines of the BLR can be detected, otherwise if it is orthogonal the absorption is maximum and the BLR is hidden.

Outside this torus, AGNs show activity from the *Narrow-Line Region*, an extended clumpy region composed by slow moving ionized matter located at ∼100 pc and that can be spatially resolved for the closest galaxies. It emits the narrower lines of the optical spectrum of an AGN, with respect to the BLR lines.

Finally, only in the radio-loud population, two collimated jets are produced close to the SMBH and, perpendicularly to the plane od the disc, can extend in opposite directions for several kiloparsecs connecting the central nucleus to two radio lobes. The jets consist of relativistic plasma embedded in strong magnetic fields, responsable for emission spanning from radio to γ-ray frequencies. This emission is mainly due to synchrotron processes and Inverse Compton (IC) scattering. It is important to note that the only component of an AGN able to produce gamma-rays are the relativistic jets and the largest fraction of AGNs emitting in the gamma-ray bands are blazars.

4.2 Physics of BLAZARs

Blazars are a subclass of radio-loud AGNs and represent the most numerous population of extragalactic gamma-ray emitters among the AGNs and for this reason we focus our attention on this category of sources. From the unified model, they are radio-loud AGNs with the relativistic jet axis that is closely aligned with the line of sight of the observer. The main properties of this class of objects are the presence of a compact radio core, with radio-loudness $R > 10$ and a flat or inverted radio spectrum, high and fast variability in amplitude and timescale at all frequencies, any or very weak emission lines in the optical band, and high degree of radio and optical polarization. All these properties are interpreted as a result of the large relativistic beaming of the jet radiation spanning the whole electromagnetic spectrum and generated by non-thermal processes inside the jets.

4.2.1 Spectral Energy Distribution of BLAZARs

Blazars emit non-thermal radiation produced within the jets at all frequencies and their SED (espressed as νF_ν versus the frequency ν) is characterized by a strong variability (more intense at the higher energies) and by the typical doubled-humped structure with two broad peaks. In general the first bump is located typically in the infrared to X-ray region, and is interpreted as due to synchroton emission by electrons spiraling along the lines of force of the magnetic field. Instead the second peak is placed at higher frequencies, between the X-ray and the VHE energies, and many models have been suggested to explain this emission. The most popular models are the so-called *Synchroton-Self Compton* (SC) scenario, where the emission is produced by inverse Compton scattering of photons generated by the same electron population responsable for the synchrotron emission, and the *External Compton* model, where the soft photons come from an external electromagnetic field. Other theories, the hadronic models, suggest that the particles involved in the radiative processes are protons, finding a better agreement with the observational data.

In according to their SED and in particular to the properties of the optical spectrum, Blazars are divided in sub-classes:

- **Flat Spectrum Radio Quasars (FSRQ)**: Blazars with a strong non-thermal continuum and presence of emission lines in the opical regime (related to the BLR and the NLR). They show the highest bolometric luminosity ($L \sim 10^{48}$ erg cm^{-2} s^{-1}) and their two peaks are located in the IR and HE (~1 MeV) regime respectively. The Optically Violent Variables quasars (OVVs) belong to this class of objects.
- **BL Lac objects**: Blazars with feature-less optical spectrum or with very weak emission lines. They are the less powerful objects ($L \sim 10^{42}$ erg cm^{-2} s^{-1}) of the blazar class and the peaks of the emission are located at higher energies: the first peak in the UV-soft X-ray band, the second one near the TeV region. Based on the peak positions of their SED, the BL-Lac are further sub-divided in:
  - **Low-peaked BL-Lacs (LBL)**: when the synchrotron peak spanning from ~10 to ~10 Hz;
  - **Intermediate-peaked BL-Lacs (IBL)**: when the synchrotron peak ranging from ~10 to ~10 Hz;
  - **High-peaked BL-Lacs (HBL)**: when the synchrotron peak is located above ~10 Hz;

Another important feature of the blazars, that is reflected directly on their SED, is the variability. It affects the flux level at all frequencies and can cause variations of the peak frequencies and the spectral slopes (in general an hardening of the spectrum follows a flux increasing). Studies of the blazar variability are very important to infer the size, the location and the physical parameters of the emission region. Correlated flux variability at different wavelengths indicates a common region of emission, and an upper limit of its dimension can be determined by the causality relation:

$$R < ct\frac{\delta}{(1+z)} \tag{4.3}$$

with δ is the Doppler factor of the source and t is the variability timescale.

4.2.2 The BLAZAR Sequence

In 1998 Fossati and collaborators attempted a first systematic exploration of the properties of the blazars studying the SEDs of a selected sample of such objects [28]. They constructed averaged broad-band SEDs binning the objects according to their radio luminosity, irrespective of their classification. The result is shown in Fig 4.5-*left*, the so-called *Blazar Sequence*, where a well defined trend is found between the overall spectral shape of the variuos SEDs and the apparent bolometric luminosity. It allows us to make the following considerations:

- The SEDs follow a systematic regularity where the FSRQs are in the upper part of the sequence with higher radio luminosity and lower peak frequencies, while the BL-Lacs occupy the lower extremity peaking at higher energies and with fainter radio luminosities;
- The peak frequencies increase as the radio power decreases;
- The peak frequencies of the two bumps are correlated;
- The *Compton dominance*, defined as the ratio of the peak of the Compton to the synchrotron peak luminosities, increase as the bolometric luminosity increaseases: for the FSRQs the bolometric luminosity is dominated by the high energy bump, while for the BL-Lacs there is equality between the two peaks;
- The different sub-classes of the BL-Lacs represents the different section of the blazar sequence, according to the radio luminosity, suggesting a continuous spectral sequence within the blazar family rather than separate spectral classes;

In a recent work, the blazar sequence was updated including data from the first three months γ-ray observations by the FERMI satellite (Fig 4.5-*right*).

4.3 **Definition of a BLAZAR SED template set**

Finding a regularity in the celestial objects belonging to a same astronomical class, but with different physical properties, is one of the main goal of astronomers.

For the radio-loud AGNs, the blazar sequence is a useful tool to find evidence the continuous spectral sequence within the blazar family and to represent them as a single population,

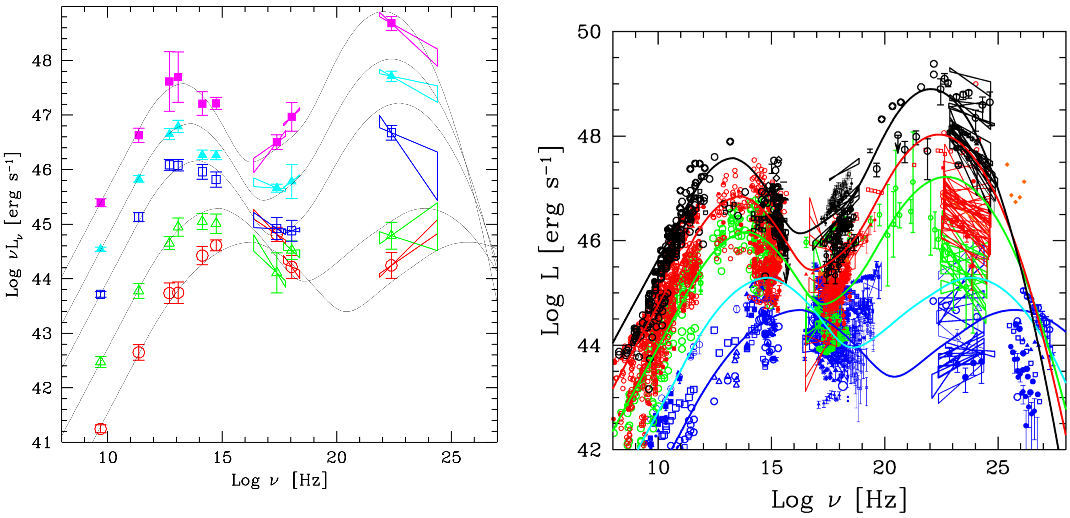

Figure 4.5: *Left*:The blazar sequence from Fossati+1998. The continuos black lines are the SED fits as reported in [25]. *Right*: The update blazar sequence divided into bins of different γ-ray luminosities in the [0.1-10 GeV] taken from [31].

that appears different from object to object, but has instead the same basic jet structure (Maraschi+1994, Cavaliere+2002).

Many important results were predected thanks to the blazar sequence as the detection of many blazars in the frequency range sampled by the Fermi satellite and the discovery of BL-Lacs at TeV energies proposed by [18]. Moreover the parametric averaged SEDs built by Donato+2001 are still used as blazar prototypes to fit empirically the data points of known blazars of unclassified sources that show a doubled-bump shape in their spectra [63].

Given the undoubted utility, the blazar sequence is a good starting point to shed light on the phenomenology of the blazars. In this Section we explain one of the reasons that led us to undertake the work performed in this PhD thesis. We start from the basic idea of the blazar sequence and build new blazar SEDs using the most recent data of blazars collected by the new generation telescopes as for example the Fermi satellite.

4.3.1 Motivations

Starting from the works of [28] and [25], the idea is to build broad-band SEDs that represent the different class of blazars. We decide to use all of them available archivial multi-frequency data, in particular including the data of the current generation of gamma-ray telescopes. In this way we are able to study the higher energy part of the electromagnetic spectrum that so far was precluded due to an insufficient sensitivity of the instruments and, once an *updated* *blazar sequence*is obtained, it will be possible to understand if the well defined trend found in the previous works is still confirmed.

Moreover the built SEDs can be a useful tool for the classification of the Unidentified Fermi Objects and their presumed counterparts (see the work presented in Chapter 5 of this Thesis). Considering them as a library of templates, we can search the curve that is more consistent with the data of a given UFO and to infer about its nature.

4.3.2 Sample of known BLAZARs

In order to build the blazar SED templates we select a sample of well-known blazars of different classes. We use all of the *blazars* belonging to the TeVCat database (http://tevcat.uchicago.edu/) plus 11 identified[1] FSRQs of the 2FGL catalogue which we have knowledge of the redshift, except for PG 1553+113. For this source, although the distance is unknown, we use a redshift of 0.4 in according to the work of [21] and [49]. The reason to use PG 1553+113 is because so far it is thought to be the most distant HBL object and until April 2012, before its first and unique VHE flare, it was considered as an extragalactic standard candle in the VHE band. Moreover PG 1553+113 shows an moderate activity at all frequencies which makes it a good candidate to build a average SED not affected by the variability.

The list of the used blazars, 23 HBLs, 3 IBL, 4 LBL and 13 FSRQs, is in Table 4.1 where we indicate the name, the blazar class, the belonging catalogue and their redshift.

4.3.3 BLAZAR Datasets

We use the ASI ASDC Database and the SED Builder tool in order to collect all archivial data for every blazar selected in our sample,. For each source we create a data file containing the luminosities versus the emission frequency according to the corresponding redshift of the object. The data points range from the radio to the HE frequencies and the complete list of the data catalogs used is in *http://tools.asdc.asi.it/SED/docs/SED_catalogs_reference.html.*

An example of SEDs adopted in this work are shown in Fig 4.6.

4.3.4 Creation of the SED templates

Once that the whole archive dataset is collected, the next step is to determine an average SED for each blazar. At first, we divide the data in equally spaced frequency bins and for every bin we calculate the average of the logarithms of the luminosities (of all of data

---

[1] usiamo solo gli identificati e non gli associati

Source Name	AGN Class	Catalog	Redshift
3C 279	FSRQ	2FGL	0.5362
PKS 1510-08	FSRQ	2FGL	0.36
PKS B1424-418	FSRQ	2FGL	1.522
PKS 1622-29	FSRQ	2FGL	0.815
CGRaBS J2345-1555	FSRQ	2FGL	0.621
PKS 0420-01	FSRQ	2FGL	0.9161
PKS 1502+106	FSRQ	2FGL	1.839
3C 454.3	FSRQ	2FGL	0.859
NRA 0512	FSRQ	2FGL	1.66
3C 345	FSRQ	2FGL	0.593
4C +49-22	FSRQ	2FGL	0.334
S 41030+61	FSRQ	2FGL	1.4
PKS 0537-441	FSRQ	2FGL	0.894
BLLacertae	LBL	TeVCat	0.0069
Ap Lib	LBL	TeVCat	0.049
1ES 1215+303	LBL	TeVCat	0.13
S 50716+714	LBL	TeVCat	0.31
3C 66A	IBL	TeVCat	0.444
WComae	IBL	TeVCat	0.102
1ES 1440+122	IBL	TeVCat	0.16
1ES 0033+595	HBL	TeVCat	0.086
1ES 0414+009	HBL	TeVCat	0.287
1ES 0502+675	HBL	TeVCat	0.341
1ES 0647+250	HBL	TeVCat	0.45
1ES 0806+524	HBL	TeVCat	0.138
1ES 1011+496	HBL	TeVCat	0.212
1ES 1218+304	HBL	TeVCat	0.182
1ES 1727+502	HBL	TeVCat	0.055
1ES 1741+196	HBL	TeVCat	0.083
1ES 1959+650	HBL	TeVCat	0.048
1ES 2344+514	HBL	TeVCat	0.044
1RXS J064847.8+151626	HBL	TeVCat	0.179
H 1426+428	HBL	TeVCat	0.129
H 2356-309	HBL	TeVCat	0.165
Markarian180	HBL	TeVCat	0.045
Markarian501	HBL	TeVCat	0.034
PG 1553+113	HBL	TeVCat	0.4*
PKS 0301-243	HBL	TeVCat	0.26
PKS 0447-439	HBL	TeVCat	0.2
PKS 2005-489	HBL	TeVCat	0.071
PKS 2155-304	HBL	TeVCat	0.116
RBS 0413	HBL	TeVCat	0.19
RGB J0710	HBL	TeVCat	0.125

Table 4.1: List of the blazars that form the sample used for the SED template library. HBL, IBL and LBL are High, Intermediate and Low-peaked BL Lacs respectively, FSRQ denotes Flat Spectrum Radio Quasar. The redshift labelled by * (of PG 1553+113) is not officially recognized.

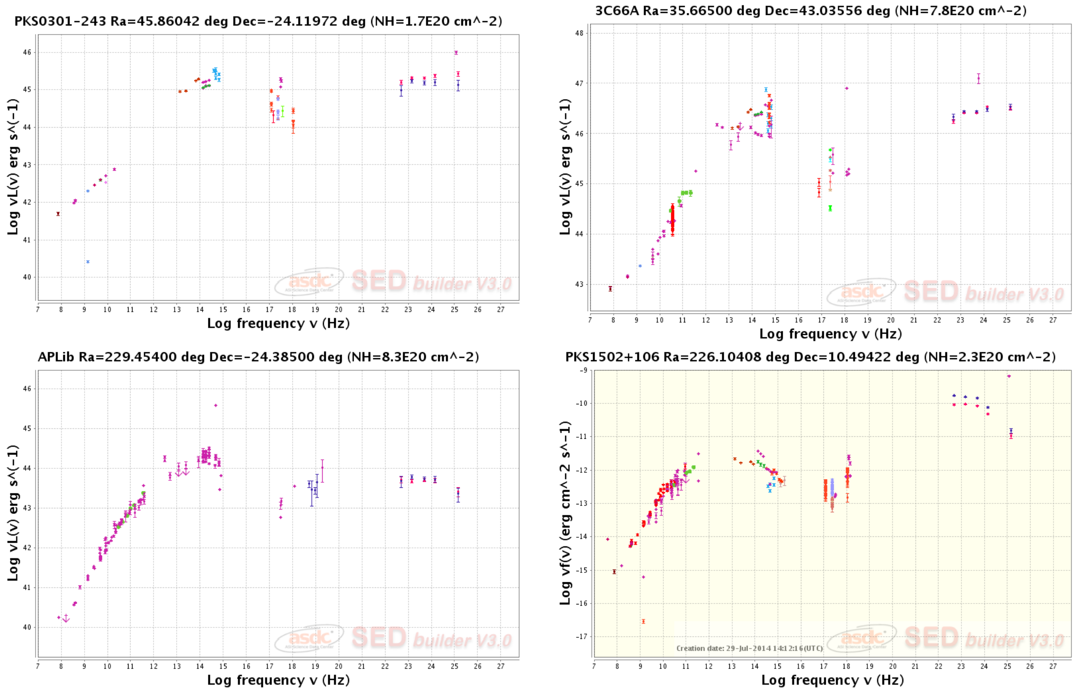

Figure 4.6: Dataset of four blazars used in the SED template library: PKS 0301 is an HBL, 3C66A a IBL, ApLib is a LBL, and PKS 1502+106 is a FSRQ. (The *blazar* SEDs are espressed as νF_ν versus the frequency ν).

including in each frequency bin). Then we estimate the best fit curve through a simple analytic parametrization of the SED with a double power-law with exponential convergence function, given by the following expression:

$$L(\nu) = l_1(\nu) + l_2(\nu) \tag{4.4}$$

with

$$\begin{aligned} log l_1(\nu) &= A + log(\frac{\nu}{\nu_1})(1-\alpha) + log[e^{-\frac{1}{2\sigma_1^2} log(1+\frac{\nu}{\nu_1})^2}] \\ log l_2(\nu) &= B + log(\frac{\nu}{\nu_2})(1-\alpha) + log[e^{-\frac{1}{2\sigma_2^2} log(1+\frac{\nu}{\nu_2})^2}] \end{aligned} \tag{4.5}$$

The parametric function has 7 free parameters: A and B related to ... , α , ν_{1-2} and σ_{1-2}...

The resulting fitting curves for the average SEDs of the blazars are shown in Fig 4.7.

We deliberately decided to adopt a simple analytic function to fit the average SEDs, without imposing any particular model of *blazars* (as for example the SSC model). In this way, we were able to fit the whole broad-band dataset and, in particular, the radio band which

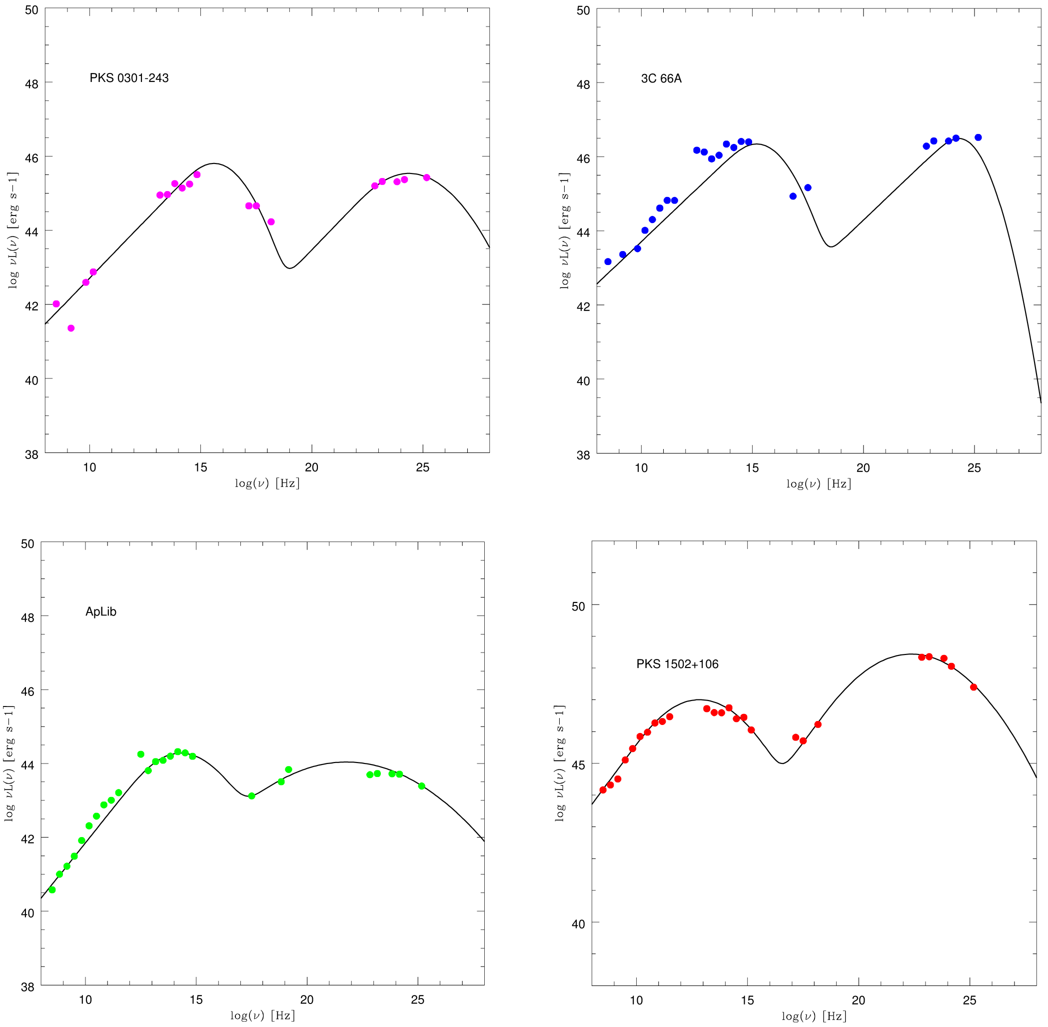

Figure 4.7: Analytical fit with a double power-law with exponential convergence function for the average SEDs of the four blazars shown in Fig 4.6.

is not easily explained by the blazar models. Moreover, unlikely the work of [28] and [**?**], **we did not average together the SEDs of different sources**. Instead we only averaged all the SED data points of each single source, obtaining only one corresponding SED template. This turns out to be a library of 43 averaged SEDs.

4.3.5 Results

In this last section, in Fig 4.8, we show the SED templates built as explained before, for the four classes of blazars: HBL, IBL and LBL objects, and FSRQ.

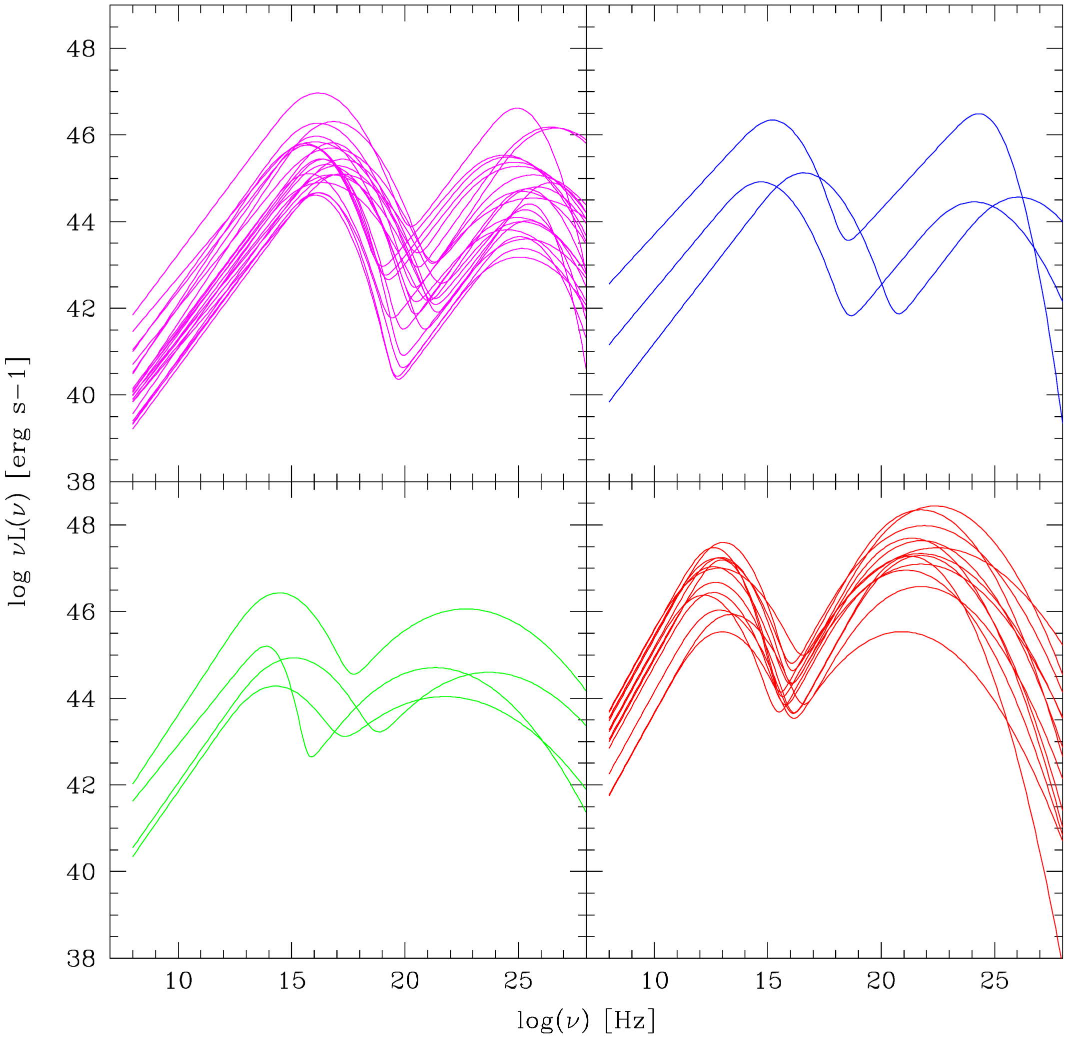

Figure 4.8: Analytical fit with a double power-law with exponential convergence function for the average SEDs of the objects of our *blazar* sample divided in the four classes of *blazars*: HBLs (*magenta*, IBLs (*blue*, LBLs (*green*, FSRQs (*red*).

In order to compare the results found with the blazar sequence, we superimpose all of SED templates in the same plot (Fig 4.9).

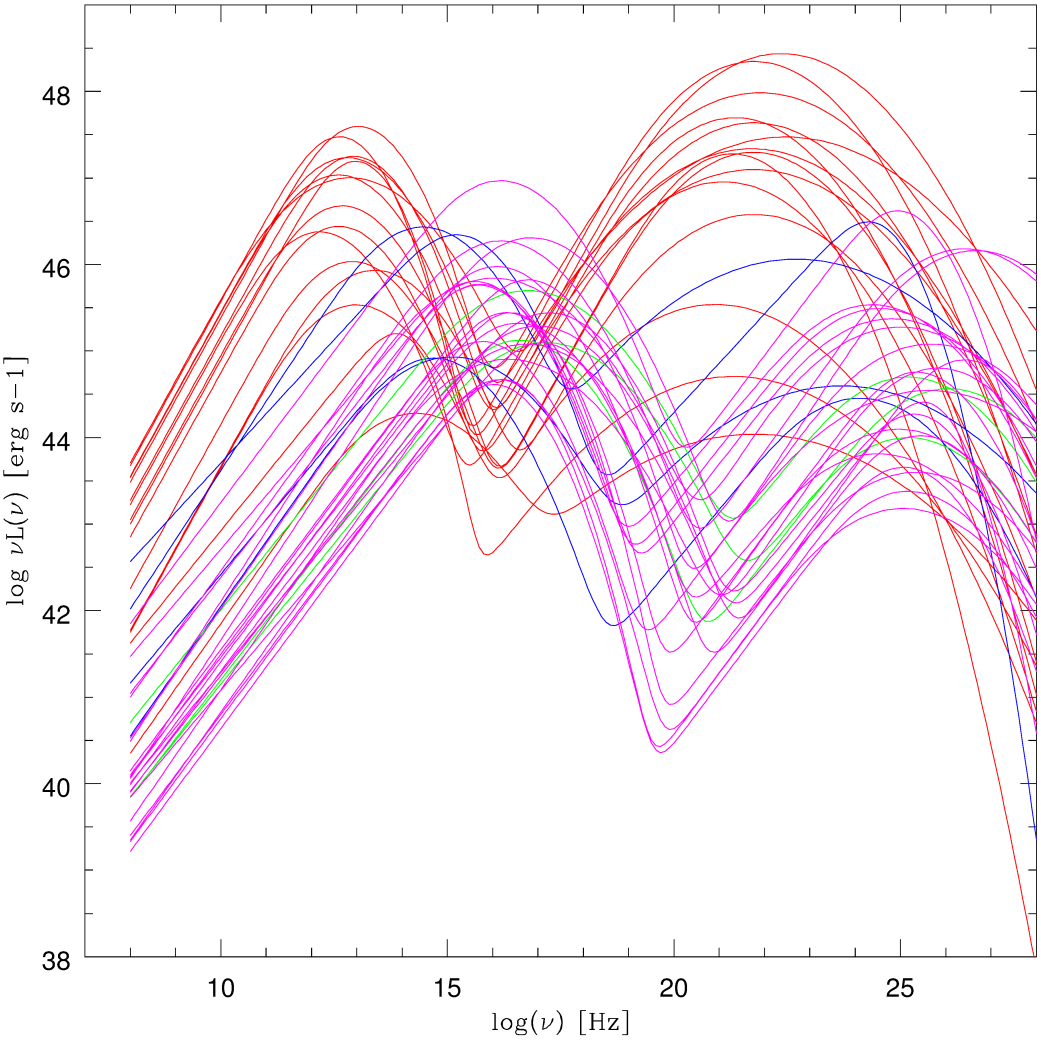

Figure 4.9: Analytical fit with a double power-law with exponential convergence function for the average SEDs of the objects of our *blazar* sample divided in the four classes of *blazars*: HBLs (*magenta*, IBLs (*blue*, LBLs (*green*, FSRQs (*red*).

We can see that the plot, although it is pretty confused especially for the LBL and IBL classes, shows the general behaviour found by [25]: the FSRQs (red curves) occupy the higher luminosity extreme of the sequence with the frequency peaks at lower energies with respect to the BL-Lacs SEDs. In anyway, it is importat to stress that the division in these four classes is purely arbitary, empirically determined and subject to continuous changes, especially with the increase of data in the GeV band.

Finally we are aware that some improvements can be made. In the future we can expand the number of *blazars* used and create a more complete set of SED templates, especially for the LBL and IBL classes, and we can include the data of the TeV band, if the blazar is detected at the VHE energies. In addition we can use MWL data of a given source collected simultaneously to build SED templates that corrispond to different activity states to take account of the variability.

5

UFO Identifications and Characterization

5.1 The UFO Identification

In Chapter 3, we described the UFO association procedure adopted in this PhD Thesis. It is primarily based on the use of the available *Swift* X-ray data covering the *Fermi* error-box associated to the γ-ray source corresponding to every UFO. In this way, for every γ-ray source we are able to associate objects inside the *Fermi error-box* detected at other wavelengths and create a set of most likely associations.

This association method has been applied to the sample of 183 UFOs selected according to the criteria explained in the Sec 2.3. Once the set of associations is obtained for a given UFO, and the corresponding SEDs are built, the next step is the source identification. This means understanding whether the resulted SED is compatible with the typical SED of a canonical astrophysical object or is generated by a new class of GeV-TeV sources.

To achieve this task, it is natural to firstly consider the classes of sources already detected by the *Fermi* satellite and recognized as γ-ray emitters for which the physical processes of γ-ray production are known. Hence, to shed light onto the possible nature of a given UFO, we developed some multiwavelength tools able to provide a first identification, mainly regarding to the class of *blazar* sources (Sec **??**), microquasars (Sec **??**) and pulsars (Sec 5.1.4).

The ultimate goal is to propose an identification for the largest number of UFO sources of our sample. This permits to discern *blazar*-like objects, especially at high redshift, and galactic sources, as pulsars and micro-quasars, among the UFOs.

One of our final aims, after having compiled a list of UFOs without obvious X-ray and/or radio or optical associations inside the corresponding *Fermi* error-box, is to consider if these unidentified sources might reveal some good Dark Matter candidates.

Finally the identified objects could be proposed as targets for multi-wavelength observational campaign, in particular for observations with the current IACT telescopes and, in the future, with the next generation Cherenkov Telescope Array that, with its increased sensibility, is the suitable instrument to further investigate such γ-ray emitting objects.

5.1.1 A tool for *blazar* Identification and Characterization

In order to identify an UFO and its multi-wavelength counterparts as a typical, previously unknown, *blazar*, we have developed a new tool based on the use of a library of *bona-fide* AGN SED templates. The code [1] evaluates the affinity of a given broad-band UFO SED with a *blazar* SED of our library.

In the first step, as described in the Chapter 4, we have created a set of SED templates of known objects belonging to the four *blazar* classes: High-peaked (HBL), Intermediate-peaked (IBL), and Low-peaked (LBL) BL Lac objects, as well as the Flat Spectrum Radio Quasars (FSRQ). Every observed AGN SED has been fitted with the simple analytic spectral form defined in the Eq. 4.5 and parametrized by seven free parameters.

Once the SED template library has been build, the UFO classification tool requires the following steps to be performed.

1. We start by considering the plots of luminosity versus frequency reported in Fig. 5.7 for all of the four blazar categories and including all SEDs of all sources in each category. The units in these plots are, along the y-axis, the logarithm of the $\nu L(\nu)$ luminosity in *erg/sec*, and, along the x-axis, the logarithm of photon frequency ν in *Hz*.

2. Then, using the observed multiwavelenght fluxes ($F_i(\nu_i)$) of a given UFO candidate counterpart, we convert them into luminosities ($\nu_i L_i(\nu_i)$) as above by considering a suited grid of redshifts z spanning from the value of 0.05 to 2.0. Then we overplot the obtained luminosity data points on the SED templates of each *blazar* class.

---

[1] The numerical code for the *blazar* identification tool is written for the package SuperMongo for ease of graphical comparison between the photometric data and the SED templates.

3. For the same UFO object and every redshift of the grid, we calculate a quantity that we named the *Minimum Average Distance* (MAD), defined as

$$MAD = |\sum_i (\chi_j)| \qquad \text{where} \qquad \chi_j = \sum_j (\frac{\log L_i(\nu_i) - \log l_j(\nu_i)}{0.5 \log l_j(\nu_i)}) \tag{5.1}$$

   where i is running over all photometric data-points for that UFO, j is an index marking the SEDs of each BLAZAR template in the template set and $l_j(\nu_i)$ is the luminosity of the j-*th* SED template interpolated at the frequency ν_i. MAD is a first measure of how far is the UFO SED, for a given assumed redshift of the grid, with respect to the SEDs of the *blazar* template set.

4. The second quantity that we use to estimate the *affinity* of the UFO SED with those of a blazar class (and for a given assumed UFO's redshift in the grid) is a modified χ^2. Then, every redshift of the grid and with respect to every SED of the *blazar* template set, the parameter χ^2_{min} is calculated as

$$\chi^2_j = \sum_i (\frac{(\log L_i(\nu_i) - \log l_j(\nu_i))^2}{(0.1 \log l_j(\nu_i))^2}) \tag{5.2}$$

   with the same meaning of the various quantities as defined in point 3 above. The minimum of this quantity offers a measure of how close is that j-*th* SED template to the observational UFO SED for a given assumed redshift for the UFO in the grid.

5. The best-guess redshift and spectral class, for a given UFO and its counterparts, are chosen according to the best combination between the minimum values of the MAD and χ^2_{min} parameters.

As an example, the output of this procedure is shown in Fig 5.8. Looking at that plot, we see how the values of MAD and χ^2_{min} guide our choice of the best-fitting SED template allowing the identification of the most likely *blazar* class for a given UFO. In particular the minumim MAD estimates the distance of the assued UFO luminosity data points from the distribution determined by the SED template set. Consequently it provides a first hint about the *blazar* class and the source redshift. Instead the χ^2_{min} value is more closely related to the spectral shapes for both of the UFO and the templates and, in particular, to the slopes of the rising and descending part of the two broad bumps of the UFO SED. Hence, it evaluates the degree of similarity with the typical doubled-bump shape of a *blazar* SED and offers a rough quantification of the likelihood that the UFO SED can be interpreted as emission due to a *blazar* object.

At the same time, our *blazar* identification procedure offers a fairly precise method of estimating the redshift for the UFO, in cases in which the agreement between the observational and template SEDs are good. The validity of our method will be discussed later by considering applications to some well known objects.

5.1.2 Test of the *blazar* identification tool on two known blazars

In order to test the efficacy in recognizing AGN sources from the *blazar* identification tool described in the previous section, we decide to apply it on the MWL dataset of two well-known *blazar* objects: PG 1551+113 and 1ES 1011+496. We consider these two *blazars* as two UFO sources with unknown *blazar* class and redshift, and we run the algorithm using the simultaneous MWL dataset collected during two dedicated MWL campaigns planned for the two sources. The details about these two observational campaigns are explained in the section 7.1.7 and 7.2.6 of the Chapter 7. According to the procedure described above, starting with the flux data points of the two known sources, we determine the different datasets, varying the luminosity as a function of the redshift, we construct the diagnostic plots (Fig5.1, Fig5.2), by the adoption of the *blazar* SED templates.

- **Results for PG 1553+113**

  To apply the *blazar* identification tool on PG 1553+113, we use the flux data collected during the extensive 2013 MWL campaign. The data are pretty simultaneous and spanning from radio to VHE band. Regarding the VHE data, we decide to use the observed data, no-corrected by EBL effect mainly because the redshift for this source is still unknown. Once the tool has worked its results out, for every redshift and every SED template we obtain the values of the two fitting parameters MAD and χ^2_{min}. In the corresponding table of Fig 5.1 the best MAD and χ^2_{min} values, referred to the best fit SED template, are reported for every *blazar* class with the estimated redshift.

  The minimum value of χ^2_{min} is associated to a SED template of the HBL class (*black curve*), suggesting that PG 1553+113 is an HBL object with a redshift of 0.5. The other larger values indicate that there is not compatibility between the source dataset and the SED templates of the other *blazar* types. Indeed this source is cataloged as an HBL *blazar* with unknown redshift but with lower limit pointing to ∼0.40.

It is important to note that the corresponding high value of the MAD is not in contrast with the classification of PG 1553+113. Since this source is the brightest and distant HBL *blazar*, it is expected being located in the upper edge of the distribution drawn by the SED templates.

- **Results for 1ES 1011+496**

  The second *test-source* to verify the *blazar* identification tool is 1ES 1011+496 and we use the simultaneous multi-wavelength data provided by the 2012 observational campaign. As for PG 1553+113, we construct the diagnostic plots through the AGN SED templates (shown in Fig 5.2) and the corresponding table with the MAD and χ^2_{min} values referring to the best fit SED templates for each *blazar* class. The minimum χ^2_{min} corresponds to the HBL class, but unlike the previous case, we observe a degeneracy as we found two best-fitting SED template candidates. The first one modelled the 1ES 1011+496 luminosity points with assumed redshift of 0.2, providing a χ^2_{min} ∼0.15, while the second one, with χ^2_{min} ∼0.11, corresponds to a redshift of 0.6. At this point the MAD parameter is decisive for the choice among these two solutions since it determines the distance of the luminosity points from the centroid of the distribution drawn by the SED templates. A lower MAD value indicates that, for the assumed redshift, the source SED luminosity is closer to the average of the SED distribution for the template set. Hence with a MAD=0.78, our tool suggests an HBL SED template as best-fitting curve (*magenta line*) for 1ES 1011+496, identifying the object as an HBL at $z \sim 0.2$. This is in agreement with the real *blazar* classification and redshift ($z = 0.212$) of this source.

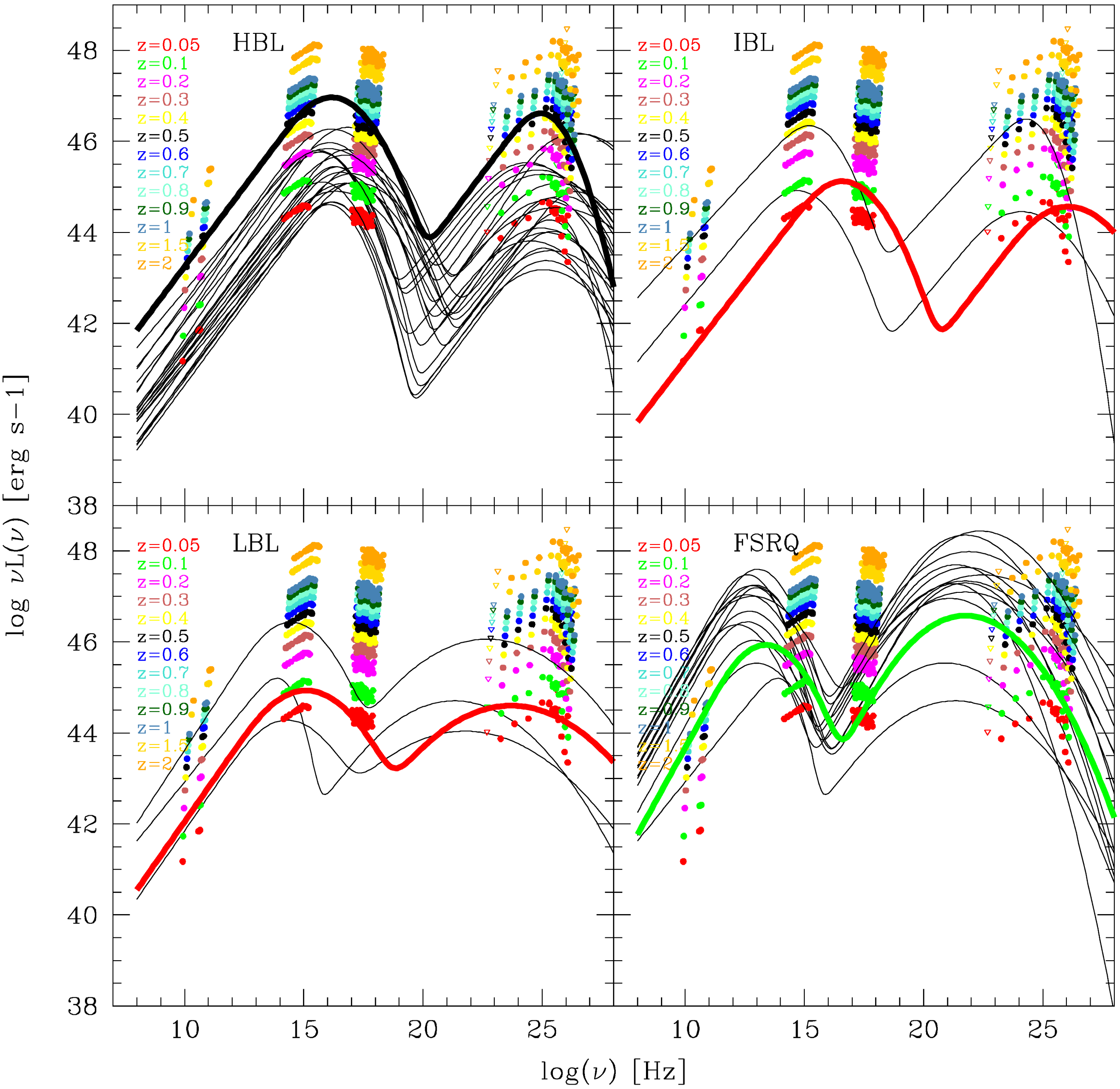

Blazar class	MAD	χ^2_{min}	z
HBL	4.01	0.11	0.5
IBL	1.22	0.76	0.05
LBL	0.10	0.51	0.05
FSRQ	1.56	1.56	0.1

Figure 5.1: Spectral luminosity points of PG 1553+113 for different assumed redshift (from 0.05 to 2.0), compared to the *blazar* SED templates. The latter are built from archive data of known *blazars* for the four classes: HBL, IBL, LBL and FSRQ. The written values of MAD and χ^2_{min} written in the table are referred to the best fit SED template of each class (*bold colored line*). The color of the selected SED template indicates the estimated redshift with our tool. For PG 1553+113 the best-guess identification is an HBL at z ∼0.5.

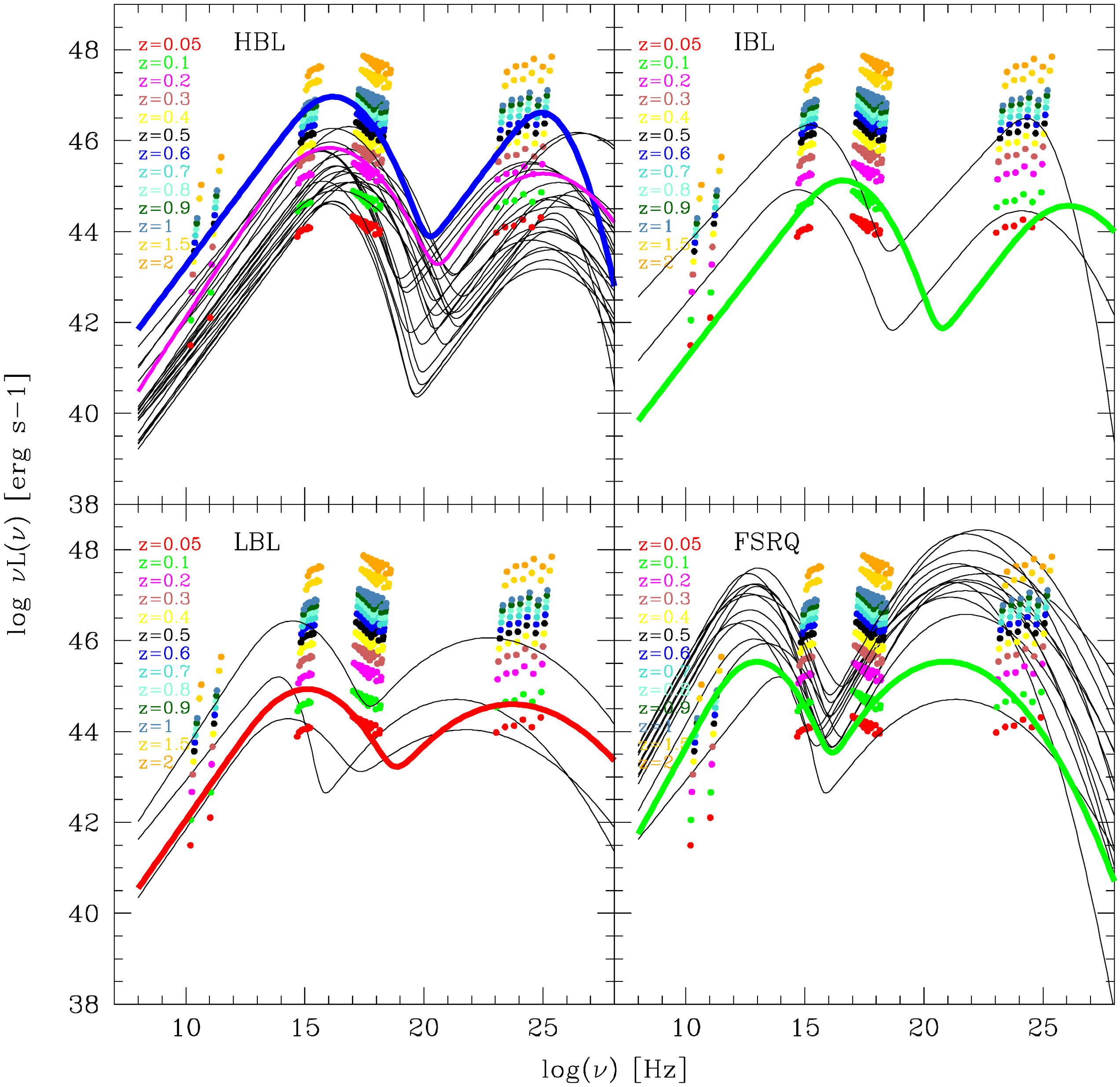

Blazar class	MAD	χ^2_{min}	z
HBL	0.78 (2.63)	0.15 (0.11)	0.2 (0.6)
IBL	0.2	0.37	0.1
LBL	0.3	0.48	0.05
FSRQ	1.55	0.89	0.1

Figure 5.2: The same diagnostic plot of Fig.5.1 for 1ES 1011+496. For 1ES 1011+496 the best-guess identification is an HBL at z ∼0.2 (*magenta line*).

5.1.3 Identification of Microquasar Candidates

We highlight that, although in this PhD thesis we study UFOs of high Galactic latitude, another category of γ-ray emitters that we decided to consider as possible identification is the class of microquasars. We have been encouraged to pursue this task because, during the procedure of association for some UFOs, we find set of MWL counterparts resulting in a peculiar broad-band SED similar to the those typical for microquasar objects.

In the second Fermi catalogue, there are only four microquasars located along the Galactic plane: LS I+61 303 (2FGL J0240.5+6113), LS 5039 (2FGL J1826.3-1450), Cyg X-3 (2FGL J2032.1+4049) and 2FGL J1019.0-5856, but only two of them are characterized from a SED spanning from radio to the *Fermi* energy range. In addition another microquasar, Cyg X-1, was detected at HE regime, but it is cataloged only in the first *Fermi* catalogue and disappears in the 2FGL. All of them are the so-called high mass X-ray binaries (HMXRB) as they are binary systems formed by a compact object, a black hole or neutron star, and by a companion star of higher mass.

In order to develop a tool to identify this kind of objects among UFOs of our sample and given the small number of known objects at the HE range, we build a diagnostic plot superimposing the broad-band SEDs of some microquasars (Fig 5.3) . As prototypes of the microquasar class, we select four objects: Cygnus X-1 (*black points*), LSI +61 303 (*cyan points*), LS 5039 (*blue points*) and SS 433 (*red*). They have the most sampled SEDs, spanning from the radio to the HE band, among the objects included in the microquasar class. In this way, we locate the region of the space $Log\ \nu F(\nu)\ vs\ \nu$ occupied by the data points of the selected microquasars and which characterizes their emission. In addition, we have a tool that allows to compare the emission of the companion star (the bump in the IR-optical regime) with the emission of high energy.

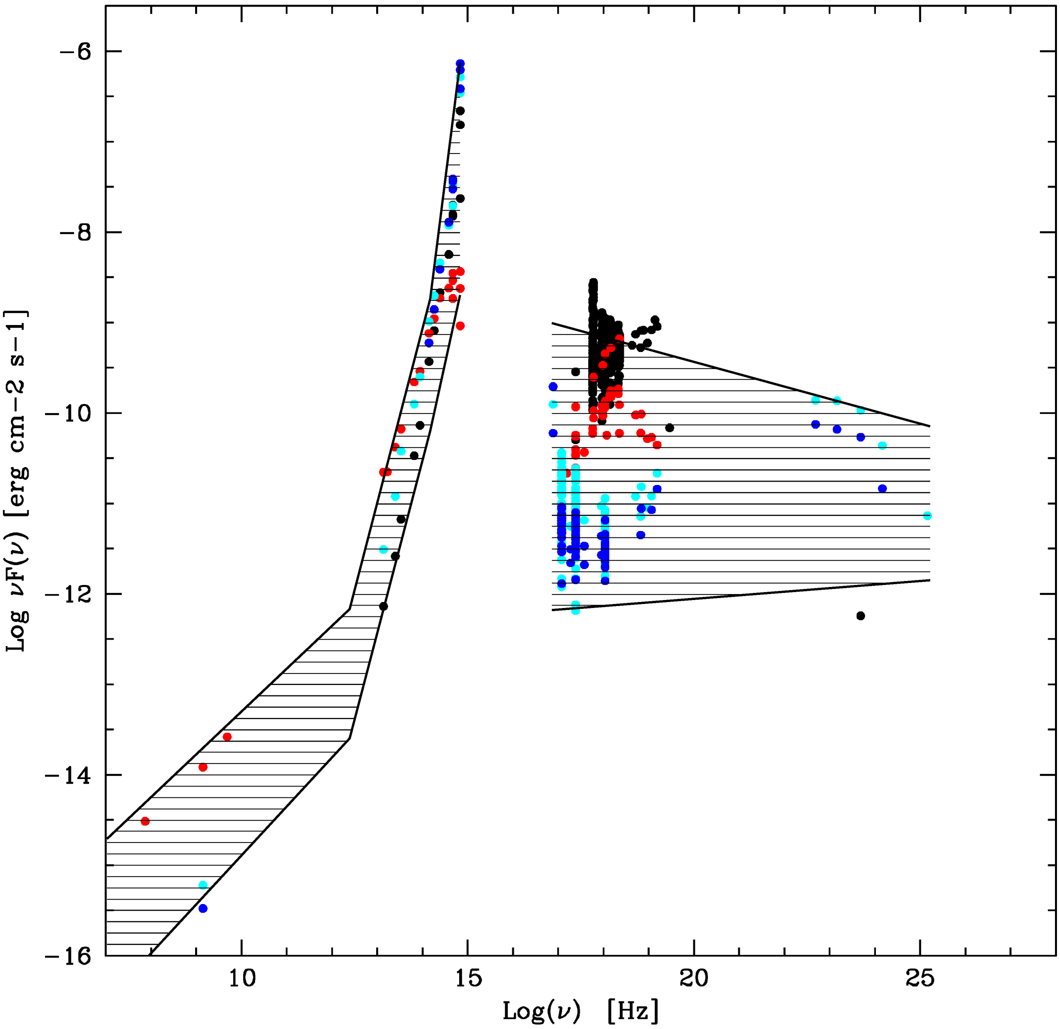

Figure 5.3: .

5.1.4 Identification of Pulsar Candidates

5.2 UFO Identification: the Results

In this section we present our proposals of identification for the 11 UFOs of the our selected sample. For each UFO we consider the set of the most likely multiwavelength counterparts found in Chap 3 and hence we adopt the different identification tools to classify them.

5.2.1 2FGL J0102.2+0943

From the 2FGL catalogue we have a detection significance of 5.5σ and a *semi major axis* of 7.8' for 2FGL J0102.2+0943. About 4 ks of XRT observations has been performed for this source and we propose a counterpart set described in Sec 3.2.1. Starting with the corresponding multiwavelength flux points, we run the code for the *blazar* identification to construct the diagnostic plots and the table with the MAD and χ^2_{min} values of the best-fitting SED template of every *blazar* class, displayed in Fig 5.4. The template with the minimum χ^2_{min} corresponds to an LBL SED. It fits the source luminosity data points with assumed a redshift of 0.5. We then suggest that 2FGL J0102.2+0943 could be an LBL object with $z \sim 0.5$.

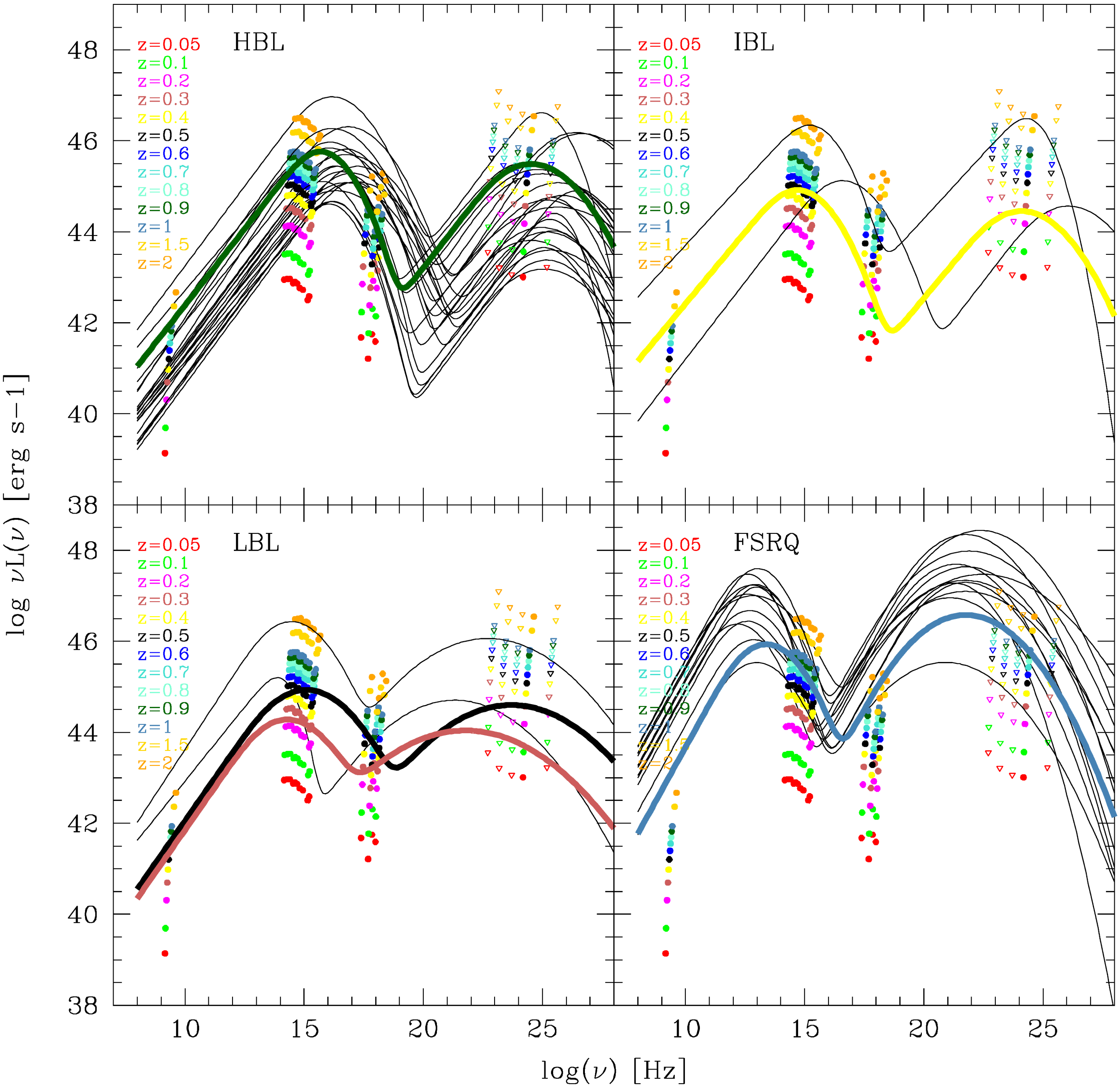

Blazar class	MAD	χ^2_{min}	z
HBL	0.22	0.07	0.9
IBL	0.39	0.27	0.4
LBL	0.1	0.05	0.5
FSRQ	0.24	0.22	1.0

Figure 5.4: Spectral luminosity points of 2FGL J0102.2+0943 for different assumed redshift (from 0.05 to 2.0), compared to the *blazar* SED templates. The latter are built from archive data of known *blazars* for the four classes: HBL, IBL, LBL and FSRQ. The written values of MAD and χ^2_{min} written in the table are referred to the best fit SED template of each class (*bold colored line*). The color of the selected SED template indicates the estimated redshift with our tool. For 2FGL J0102.2+0943 the best-guess identification is an LBL at z ∼XXX.

5.2.2 2FGL J0116.6-6153

In the 2FGL catalogue this γ-ray object is cataloged with a detection significance of 5.5σ and *semi major axis* of the error-ellipse of 6'. *Swift*/XRT observed the source for about 3.2 ksec and using the XRT imaging data analysis we found only one X-ray source as possible counterpart (Sez 3.2.2). The broad-band SED, built combining the fluxes of the likely associations (Fig 3.4), has been used to run the *blazar* identification code and the resulted diagnostic plots are displayed in Fig 5.5. The values of the MAD and χ^2_{min} parameters of the best-fitting SED template for each *blazar* class are in the corresponding table. Looking at the minimum value of χ^2_{min}, provided by the *yellow curve* in the LBL panel, the best-guess identification for the UFO 2FGL J0116.6-6153 is an LBL *blazar* with redshift 0.4.

Actually, for this UFO, we are in presence of degenerancy between two *blazar* classes, because we also found that also the best-fitting SED template of the HBL category matches the source luminosity points with redshift 0.7, providing an χ^2_{min} similar to the LBL class one. This probably occurs because XRT observations did not collected a sufficient number of X-ray counts and we cannot have information about the spectral shape in the X-ray band. Furthermore in the 2FGL catalogue, only the data point with highest energy is reported, while for the others there are upper limits. To disentangle the issue, further observations, especially in the X-ray or optical band, are needed to also combine with the HE data points that will be soon released in the third *Fermi* catalogue.

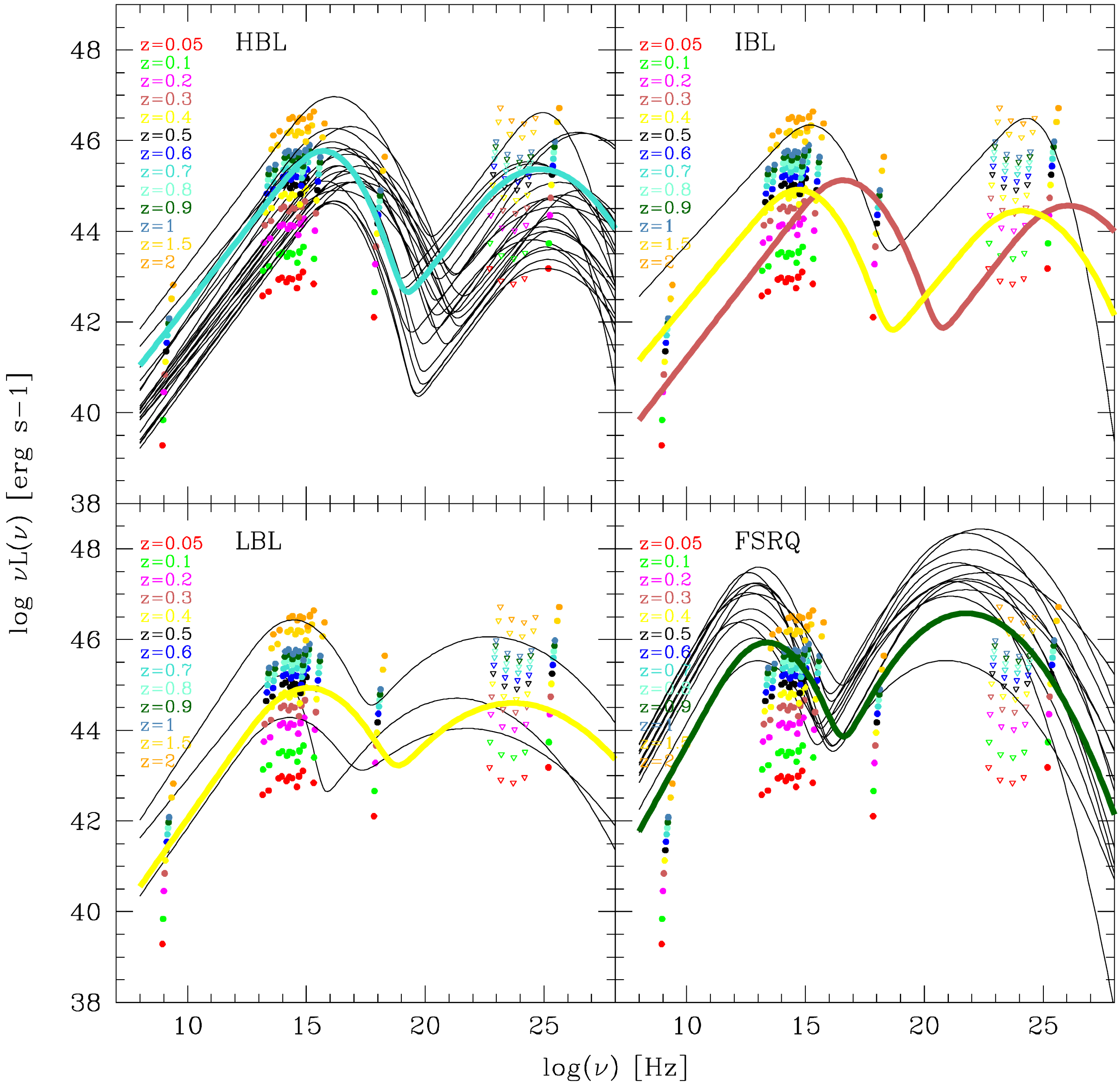

Blazar class	MAD	χ^2_{min}	z
HBL	0.38	0.05	0.7
IBL	0.18 (0.37)	0.19 (0.18)	0.4 (0.3)
LBL	0.16	0.03	0.4
FSRQ	0.20	0.18	0.9

Figure 5.5: Spectral luminosity points of 2FGL J0116.6-6153 for different assumed redshift (from 0.05 to 2.0), compared to the *blazar* SED templates. The latter are built from archive data of known *blazars* for the four classes: HBL, IBL, LBL and FSRQ. The written values of MAD and χ^2_{min} written in the table are referred to the best fit SED template of each class (*bold colored line*). The color of the selected SED template indicates the estimated redshift with our tool. For 2FGL J0116.6-6153 the best-guess identification is an LBL at z ∼0.4.

5.2.3 2FGL J0129.4+2618

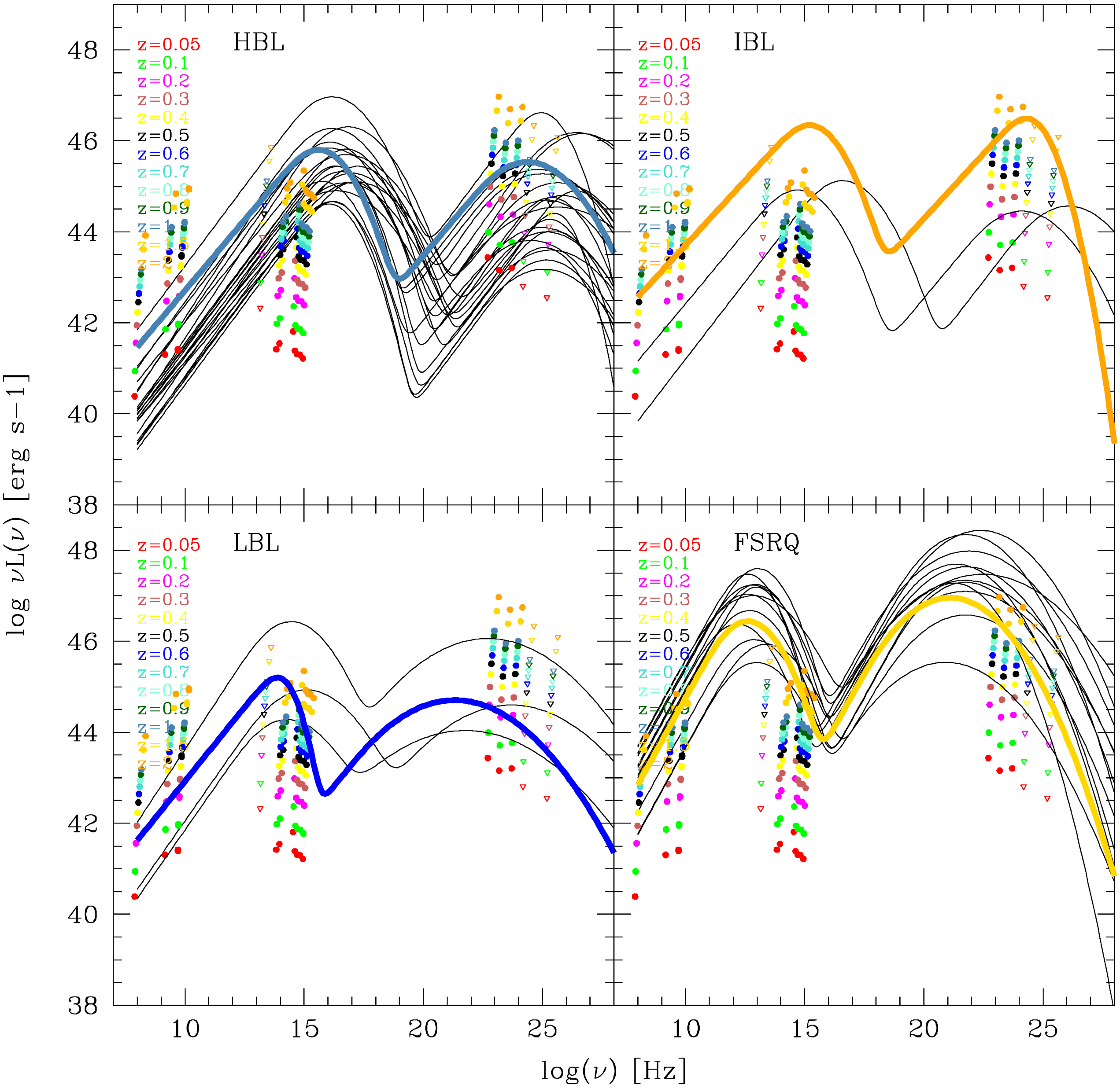

Blazar class	MAD	χ^2_{min}	z
HBL	0.55	1.29	1.0
IBL	0.62	0.95	2.0
LBL	0.08	0.71	0.6
FSRQ	0.28	0.12	1.5

Figure 5.6: Spectral luminosity points of 2FGL J0129.4+2618 for different assumed redshift (from 0.05 to 2.0), compared to the *blazar* SED templates. The latter are built from archive data of known *blazars* for the four classes: HBL, IBL, LBL and FSRQ. The written values of MAD and χ^2_{min} written in the table are referred to the best fit SED template of each class (*bold colored line*). The color of the selected SED template indicates the estimated redshift with our tool. For 2FGL J0129.4+2618 the best-guess identification is an FSRQ at z ∼XXX.

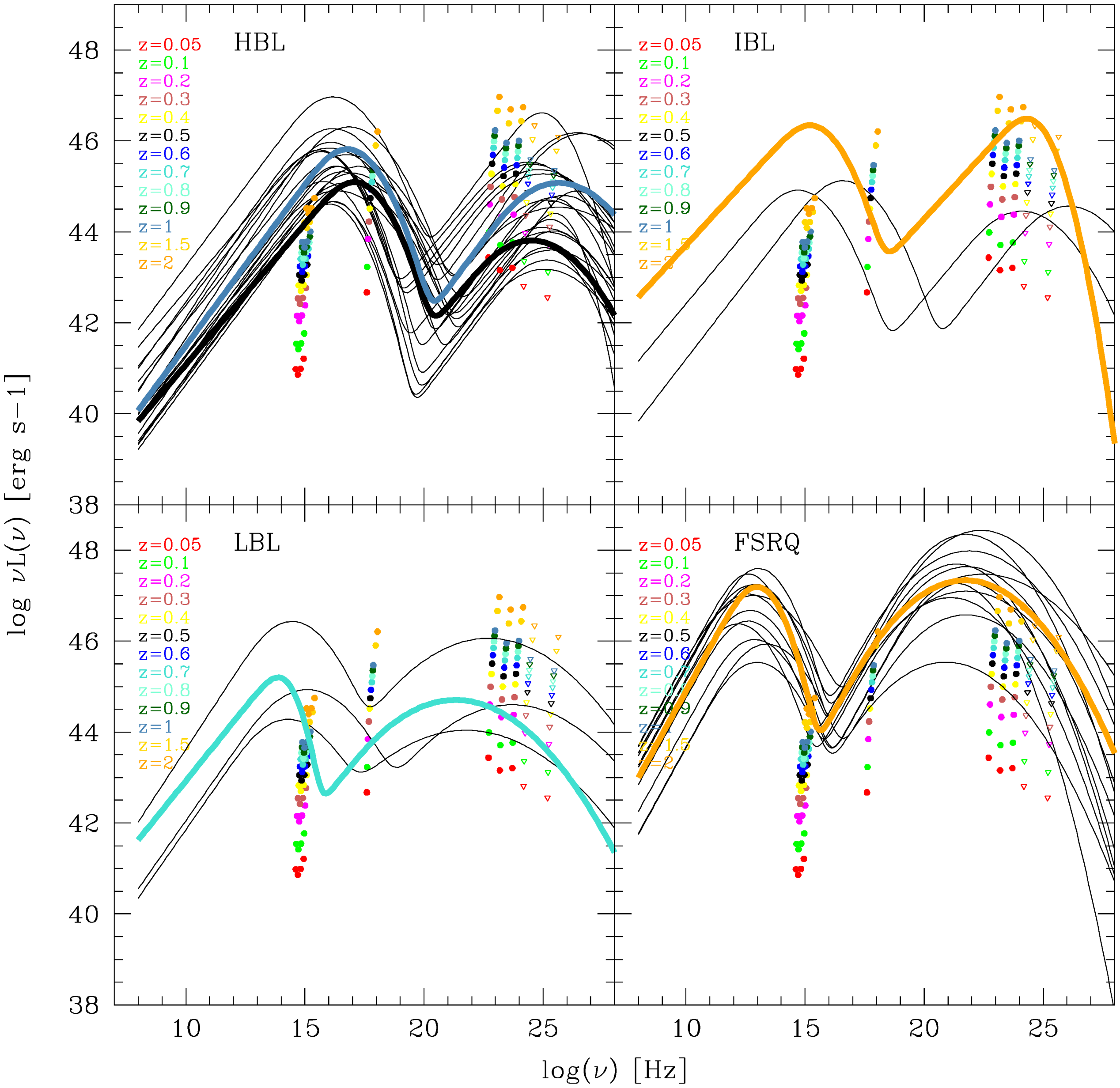

Blazar class	MAD	χ^2_{min}	z
HBL	0.06	0.73	1.0
IBL	0.23	0.94	2.0
LBL	0.09	0.49	0.7
FSRQ	0.05	0.03	2.0

Figure 5.7: Spectral luminosity points of 2FGL J0129.4+2618 for different assumed redshift (from 0.05 to 2.0), compared to the *blazar* SED templates. The latter are built from archive data of known *blazars* for the four classes: HBL, IBL, LBL and FSRQ. The written values of MAD and χ^2_{min} written in the table are referred to the best fit SED template of each class (*bold colored line*). The color of the selected SED template indicates the estimated redshift with our tool. For 2FGL J0129.4+2618 the best-guess identification is an FSRQ at z ∼XXX.

5.2.4 2FGL J0143.6-5844

2FGL J0143.6-5844 is an UFO of the 2FGL catalogue with a detection significance of 14.2σ and a *semi major axis* of 3.6'. There are dedicated *Swift*/XRT observations of this *Fermi* object and through a XRT imaging analysis we found a very bright X-ray source within the UFO *Fermi* error-box. Considering it as the likely X-ray association, we determine the counterpart set as described in Sez 3.2.4. The resulting MWL SED (Fig 3.8) presents a good coverage along the whole electromagnetic spectrum. Starting with these flux data points, through the *blazar* identification tool, we construct the diagnostic plots (shown in Fig 5.8). The corresponding table provides for each *blazar* class the MAD and χ^2_{min} values of the best-fitting SED template. We can see that the SED template with the minimum χ^2_{min} corresponds to an HBL template that fits the source luminosity data with assumed redshift of 0.2. Hence we suggest that the best-guess UFO identification for 2FGL J0143.6-5844 is an HBL at $z \sim 0.2$. In addition, since the source shows a clear hard *Fermi* spectrum and its supposed redshift implies a moderate EBL absorption, 2FGL J0143.6-5844 could be a good target for TeV observations.

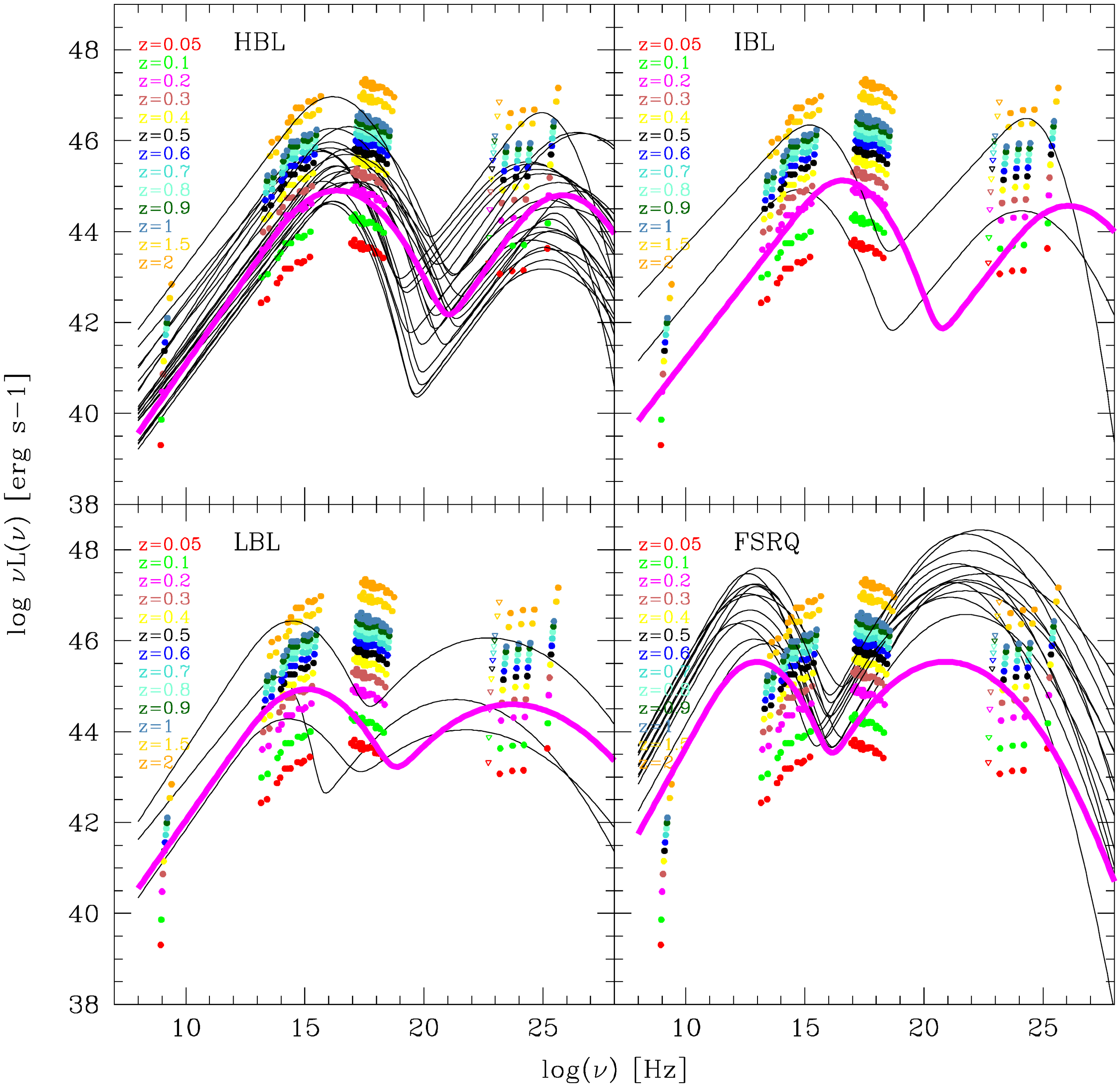

Blazar class	MAD	χ^2_{min}	z
HBL	0.33	0.06	0.2
IBL	0.01	0.09	0.2
LBL	0.36	0.97	0.2
FSRQ	1.87	1.23	0.2

Figure 5.8: Spectral luminosity points of 2FGL J0143.6-5844 for different assumed redshift (from 0.05 to 2.0), compared to the *blazar* SED templates. The latter are built from archive data of known *blazars* for the four classes: HBL, IBL, LBL and FSRQ. The written values of MAD and χ^2_{min} written in the table are referred to the best fit SED template of each class (*bold colored line*). The color of the selected SED template indicates the estimated redshift with our tool. For 2FGL J0143.6-5844 the best-guess identification is an HBL at $z \sim 0.2$.

5.2.5 2FGL J0227.7+2249

2FGL J0227.7+2249 is one of the *Fermi* variable UFO of our selected sample, with a *variability index* of 66.4, a detection significance of 6.5' and *semi major axis* of 7.2'. It was not reported in the 1FGL catalogue. Thanks to imaging analysis of ∼3.7 ksec *Swift*/XRT data collected in 2012, we built the XRT sky map of the UFO error-box region and we found an unique X-ray source, XRT J022744+224837, as possible counterpart for 2FGL J0227.7+2249. In Sec 3.2.5 we report the resulting multiwaveleght SED. The flux data points have been used as input in the *blazar* identification tool and the diagonistic plots are in Fig 5.9. In the corresponding table, for each *blazar* class, we show the MAD and χ^2_{min} of the best-fitting SED template: we can see that the best one, with the minimum χ^2_{min}, belongs to the FSRQ class. However we suppose that the effects of the variability can play an important role for the interpretation of this results. Indeed, despite the LBL best-fitting curve (the *blu curve*, corresponding to the SED template built from the BL Lacertae data) has a greater χ^2_{min}, it provides a better match for the lower energy bump of the SED with respect to the FSRQ.

In addition we highlight that the optical source included in the counterpart set of 2FGL J0227.7+2249, SDSS10 1237670960548807265, is reported in the catalogue as a galaxy with photometic redshift of ∼0.45 ± 0.13, quite in agreement with our estimated redshift found.

We believe that further multiwavelength observations are needed, especially in the X-ray band, in order to have a determination of the overall spectrum shape. An optical spectroscopy study can allow us to estimate the redshift of the source and confirm its nature.

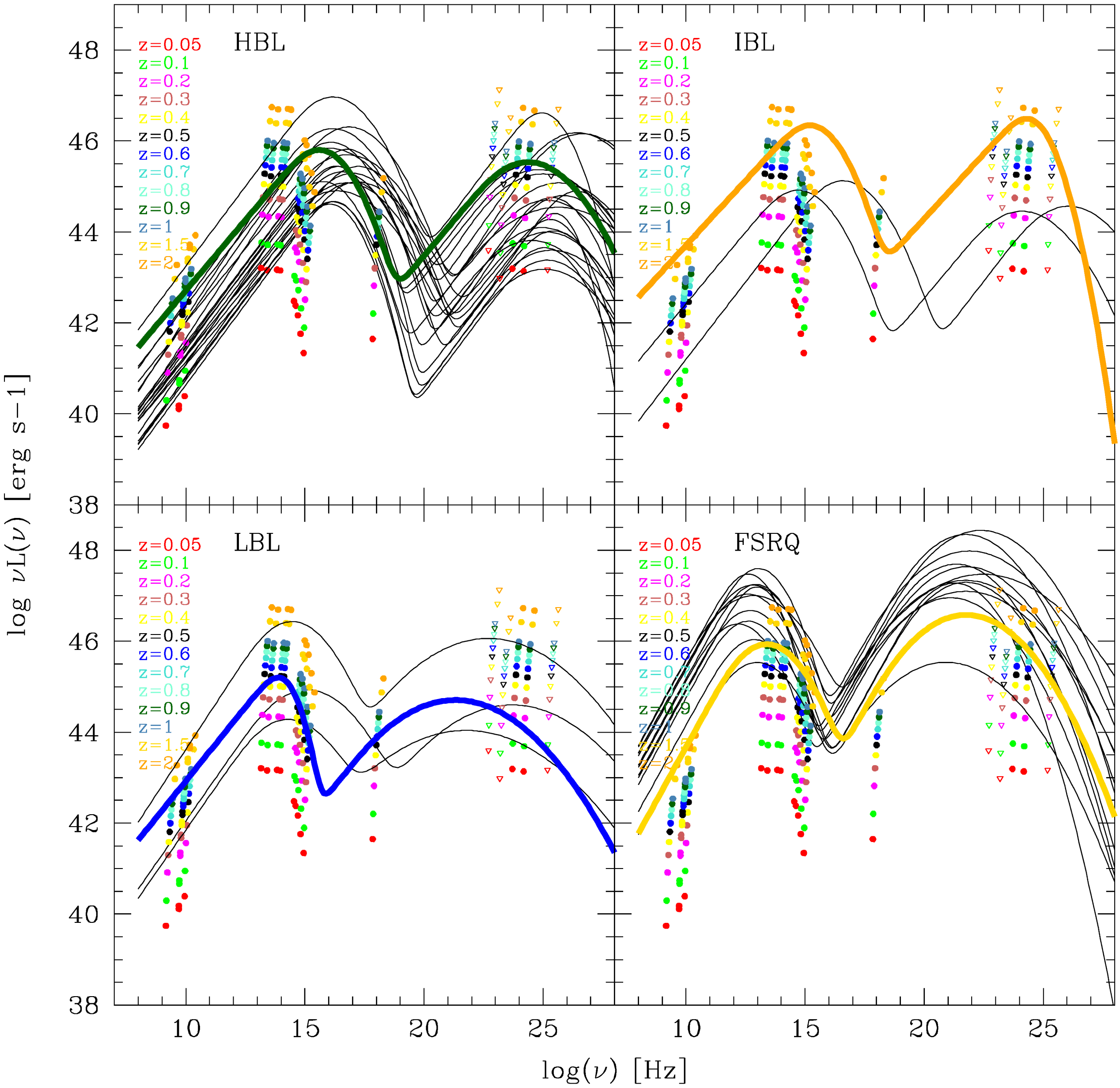

Blazar class	MAD	χ^2_{min}	z
HBL	0.55	0.44	0.9
IBL	0.80	0.42	2.0
LBL	0.04	0.24	0.6
FSRQ	0.28	0.14	1.5

Figure 5.9: Spectral luminosity points of 2FGL J0227.7+2249 for different assumed redshift (from 0.05 to 2.0), compared to the *blazar* SED templates. The latter are built from archive data of known *blazars* for the four classes: HBL, IBL, LBL and FSRQ. The written values of MAD and χ^2_{min} written in the table are referred to the best fit SED template of each class (*bold colored line*). The color of the selected SED template indicates the estimated redshift with our tool. For 2FGL J0227.7+2249 the best-guess identification is an LBL at z ∼0.6.

5.2.6 2FGL J0338.2+1306

In Sec 3.2.6 we performed the selection of the MWL counterpart set for 2FGL J0338.2+1306 and Fig 3.12 is the corresponding MWL SED. This source is a 2FGL object catalogued with detection significance of 5.8σ in the *Fermi* energy band. Its associated SED spans down to the radio frequencies and dedicated *Swift*/XRT observations allowed to investigate its X-ray spectrum. The SED data points were used to run the *blazar* identification tool and the output plots are in Fig 5.11. The best-fitting SED template, with minimum χ^2_{min}, belongs to the HBL class, but in this case we have two likely solutions. We consider the MAD parameter to guide our choice and finally we suggest as best-fitting SED template the *brown curve* that corresponds to an HBL template, which describes the luminosity data points with redshift 0.3. Looking at the rising HE spectrum and from feasibility study (Fig 5.10), we proposed this object as good target for the VHE observations of the Cycle 9 (2014) with the MAGIC telescope. The proposal was accepted but, so far, only 4 hours were peformed of the 19 requested to have detection at least 5σ detection.

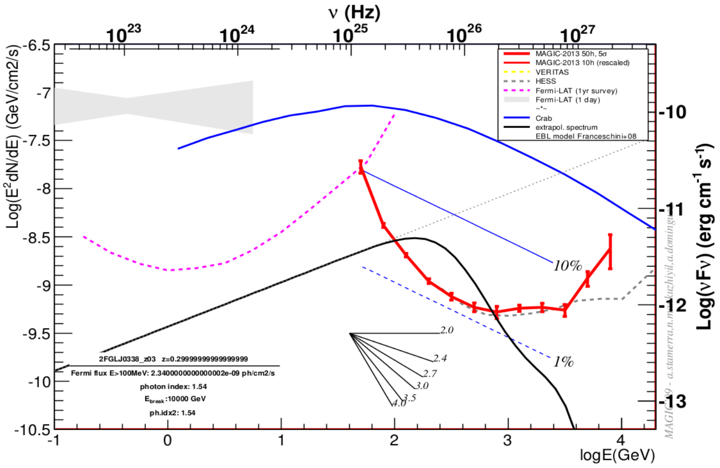

Figure 5.10: Study of the 2FGL J0338.2+1306 visibility at 5σ with the MAGIC telescope for 50 hours of observations: the black curve is the 2FGL J0338.2+1306 *Fermi* spectrum extrapolated up to VHE regime applying the Franceschini model (Franceschini+2008) for the EBL absoption. The red curve is the MAGIC sensitivity. The blue curve is the CrabNebula spectrum.

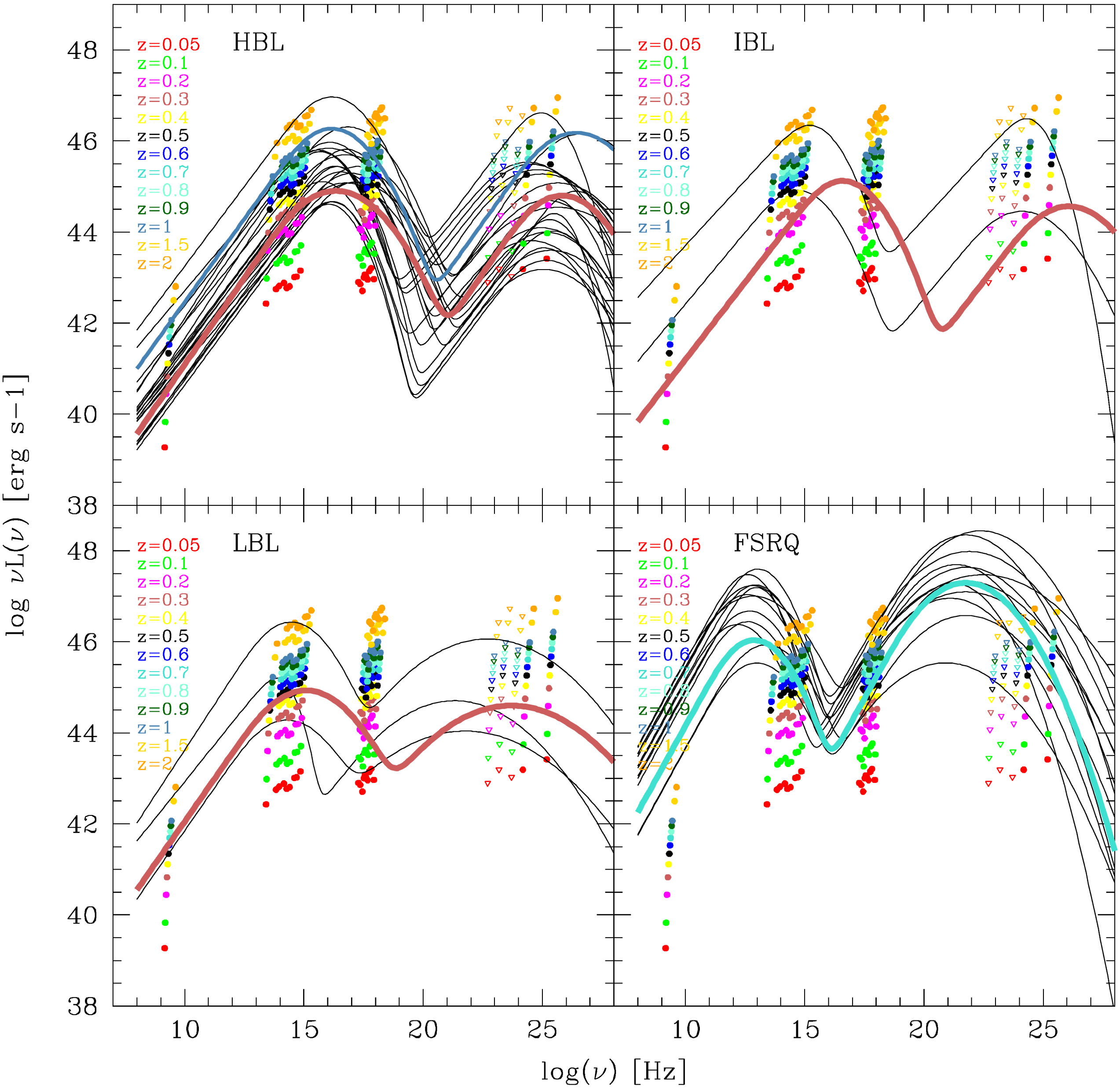

Blazar class	MAD	χ^2_{min}	z
HBL	0.25 (0.96)	0.05 (0.05)	0.3 (1.0)
IBL	0.09	0.145	0.3
LBL	0.02	0.35	0.3
FSRQ	0.44	0.43	0.7

Figure 5.11: Spectral luminosity points of 2FGL J0338.2+1306 for different assumed redshift (from 0.05 to 2.0), compared to the *blazar* SED templates. The latter are built from archive data of known *blazars* for the four classes: HBL, IBL, LBL and FSRQ. The written values of MAD and χ^2_{min} written in the table are referred to the best fit SED template of each class (*bold colored line*). The color of the selected SED template indicates the estimated redshift with our tool. For 2FGL J0338.2+1306 the best-guess identification is an HBL at $z \sim 0.3$.

5.2.7 2FGL J0458.4+0654

2FGL J0458.4+0654 is an UFO reported in the 2FGL catalogue with a detection significance of 5.5σ and a *semi major axis* of 9'. In Sec 3.2.7 we suggested a set of likely counterparts for this UFO and the corresponding MWL SED is displayed in Fig 3.15. It shows a particular feature, as in the IR-Optical band there is a strong bump compatible with the emission of an high mass star. Moreover we note that the X-ray source exhibits a strong variability, during the three *Swift*/XRT observations performed in 2012 with the X-ray flux doubled on on timescales of days. We interpret all these characteristics as due to emission of a Galactic source and we superimpose the MWL data points of the diagnostic plot for the identification of microquasars. In Fig 5.12 we can see that the 2FGL J0458.4+0654 counterpart luminosity points, related to a distance of 3.5 kpc, are located on the region delineated by known microquasars.

Therefore we suggest that our best-guess identification for 2FGL J0458.4+0654 is a microquasar at 3.5 kpc and we encourage to perform further multiwavelegth observations to confirm this identification. This could be a very important result since only four microquasars are reported in the 2FGL catalogue.

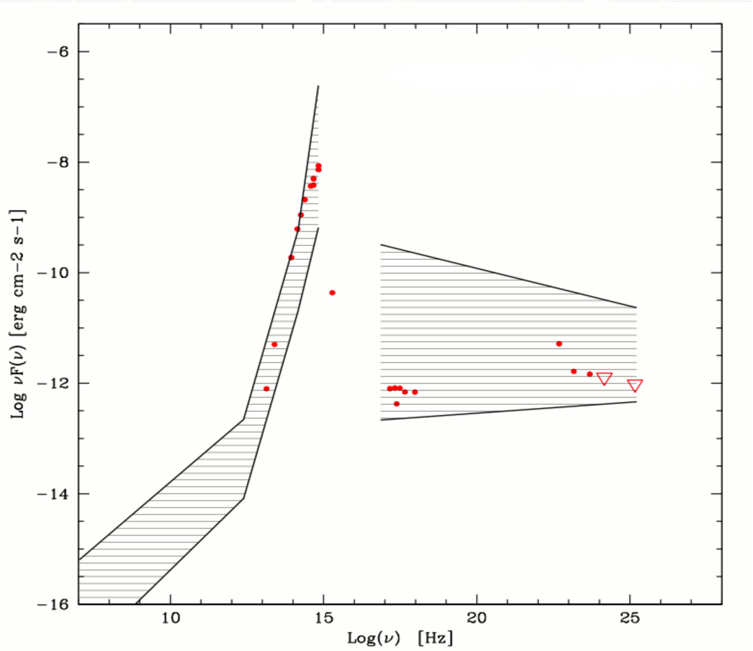

Figure 5.12: Spectral luminosity points of 2FGL J0458.4+0654 for a distance of XX kpc, compared to the region of the Log(νFν)/Log(ν) plot delineated by known microquasars

5.2.8 2FGL J1038.2-2423

2FGL J1038.2-2423 is a γ-ray emitter reported in the 2FGL with 5.9σ of detection. In Sec 3.2.8 we selected two possible X-ray counterparts for this UFO and for both of them we determined the MWL counterpart set. Through our *blazar* identification tool, we estimate the probability that the broad-band SED associated to every set could have a *blazar* origin and, in that case, to lean towards only one solution.

The first set is associated to the X-ray source XRT J103754-242546 and the built diagnostic plots, with the corresponding table, are shown in Fig 5.13. Among the four *blazar* class, the best-fitting SED template is in the FSRQ class with a χ^2_{min} of 0.28 (*steel blue curve*), that fits the luminosity data points corresponding to a redshift of 1.0.

The second X-ray counterpart proposed is XRT J103748-242841 and the output plots and table resulted are in Fig 5.14. In this case we do not find a plausible solution because no SED template is able to describe the spectral shape in every energy band. Indeed, looking at the HBL class plot we can see that the coloured SED template (*turquoise curve*) reproduces the trend IR-Optical data, but its spectral shape is reversed while describing the X-ray band. Viceversa in the FSRQ class plot, the SED template with minimum χ^2_{min} (*dark green curve*) is in agreement with the high energy parte of the SED (from X-ray to HE band), but not elsewhere.

Hence our tool permits to discern among the two counterpart set, in favour of the first source XRT J103754-242546 that can be considered the most likely counterpart for 2FGL J1038.2-2423, with a *blazar* origin belonging to the FSRQ class, with $z \sim 1.0$.

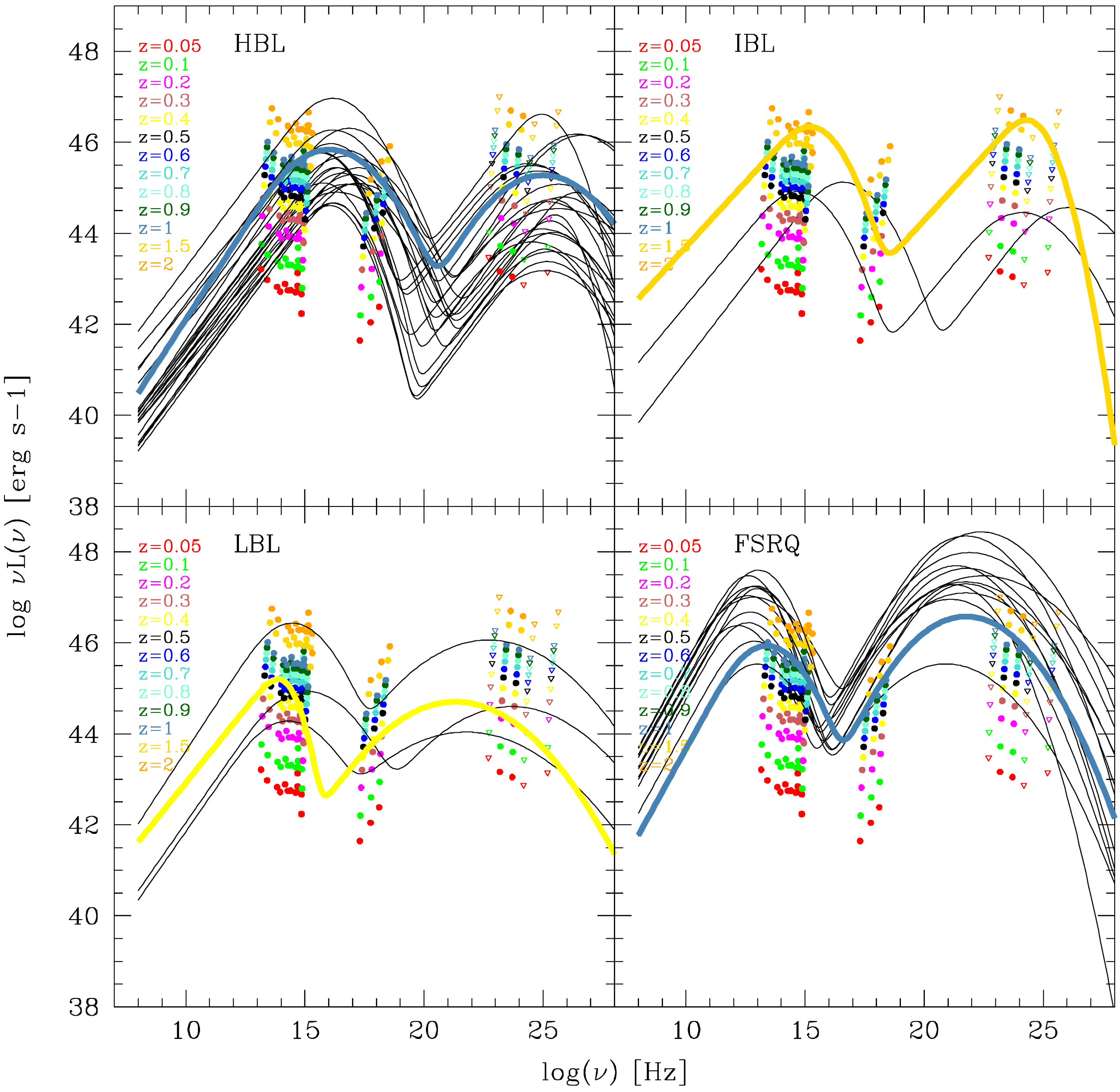

Blazar class	MAD	χ^2_{min}	z
HBL	0.64	0.28	1.0
IBL	0.86	0.46	1.5
LBL	0.25	0.12	0.4
FSRQ	0.25	0.04	1.0

Figure 5.13: Spectral luminosity points of XRT J103754-242546, the first X-ray counterpart candidate for 2FGL J1038.2-2423, for different assumed redshift (from 0.05 to 2.0), compared to the *blazar* SED templates. The latter are built from archive data of known *blazars* for the four classes: HBL, IBL, LBL and FSRQ. The written values of MAD and χ^2_{min} written in the table are referred to the best fit SED template of each class (*bold colored line*). The color of the selected SED template indicates the estimated redshift with our tool. For the XRT J103754-242546 counterpart set the best-guess identification is a FSRQ at $z \sim$1.0.

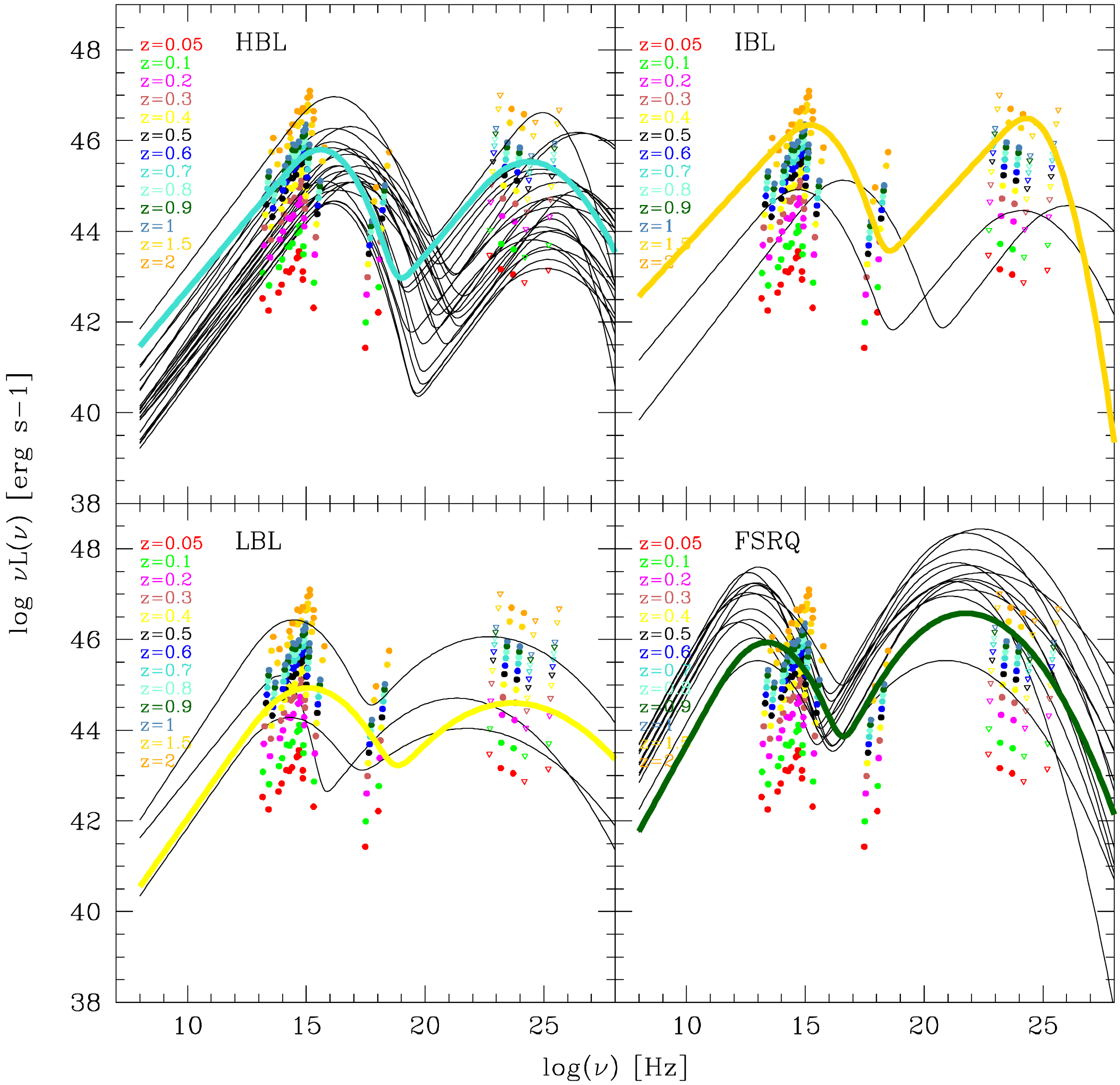

Blazar class	MAD	χ^2_{min}	z
HBL	0.44	0.15	0.7
IBL	0.85	0.24	1.5
LBL	0.12	0.12	0.4
FSRQ	0.21	0.25	0.9

Figure 5.14: Spectral luminosity points of XRT J103748-242841, the second X-ray counterpart candidate for 2FGL J1038.2-2423, for different assumed redshift (from 0.05 to 2.0), compared to the *blazar* SED templates. The latter are built from archive data of known *blazars* for the four classes: HBL, IBL, LBL and FSRQ. The written values of MAD and χ^2_{min} written in the table are referred to the best fit SED template of each class (*bold colored line*). The color of the selected SED template indicates the estimated redshift with our tool. For the XRT J103748-242841 there is not a clear *blazar* SED template fitting the luminosity data points.

5.2.9 2FGL J1410.4+7411

In the second Fermi catalog 2FGL J1410.4+7411 has a 9.8σ significance and a *semi major axis* of 4.8'. Through our association procedure, no counterpart has been found for this sources3.2.9. This object will be discussed below in the Sec 8.2 where we discuss about the possibility to have DM candidates among our sample of UFOs.

In addition, 2FGL J1410.4+7411 has been proposed as good target to perform DM searches with the MAGIC telescope and it was observed in 2012 for 15 hours. The details about the MAGIC observations are in Sec **??**.

5.2.10 2FGL J1511.8-0513

2FGL J1511.8-0513 is present in the *Fermi* catalogue with a detection significance of 7.8σ and a *semi major axis* of 4.8'. Two X-ray counterparts have been proposed in the Sec 3.2.10, although the sources exhibit a different brightness in the X-ray band- Both of their corresponding multifrequency SEDs, shown in Fig 3.21-*right* and Fig 3.22-*right*, have been used in our *blazar* identification tool.

The diagnostic plots for the first counterpart set, corresponding to the X-ray source XRT J151148-051348, are in Fig 5.15. As shown in table, the best-fitting SED template can be described by a HBL class with redshift z =0.4 (*yellow curve and points*).

The second proposed X-ray counterpart is XRT J151159-051526. Running the *blazar* identification tool, we obtain the results displayed in Fig 5.16. We find that the best-fitting template belongs to the class of the FSRQs (*steel blue curve* with χ^2_{min}=0.19), but the agreement with the IR-Optical data points is no clearly evident. A same discussion can be performed for the best-fitting SED template of the LBL class (*brown curve*), where the value of the χ^2_{min} is very similar to the previous one of the FSQR category, but with a mismatch for the HE energies. In addition, we note that XRT J151159-051526 is a very faint X-ray source and its determined broad-band SED does not has a good coverage in wavelength as the case of the first association. Moreover no radio counterpart was found, although the emission in this energy band is a strong hint of a *blazar* origin.

In the light of these considerations, we suggest XRT J151148-051348, and its spatially coincident sources, as the most likely counterparts for 2FGL J1511.8-0513, identifying this UFO as an HBL object wiht z =0.4.

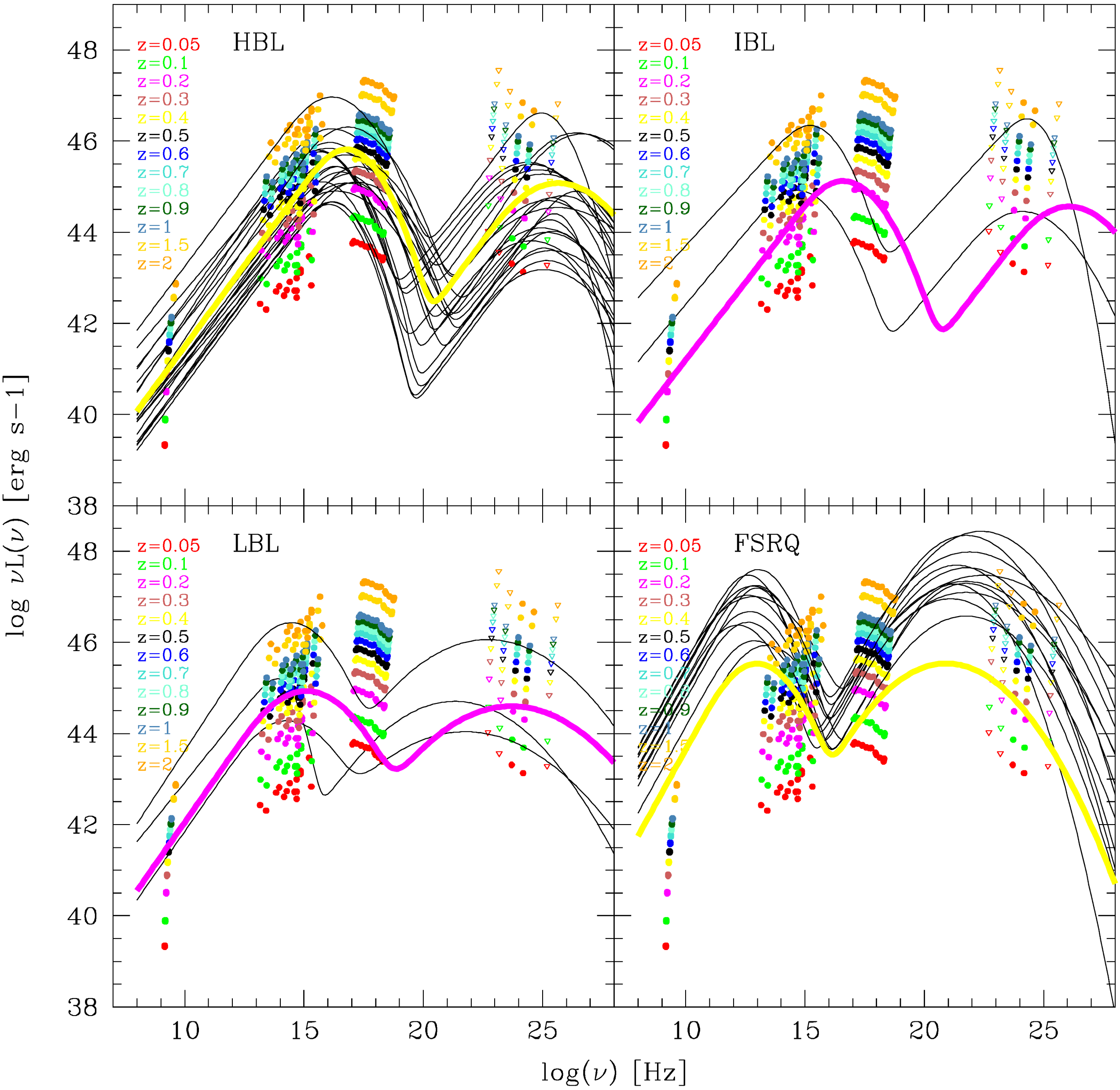

Blazar class	MAD	χ^2_{min}	z
HBL	0.39	0.09	0.4
IBL	0.49	0.14	0.2
LBL	0.36	1.3	0.2
FSRQ	1.19	1.4	0.4

Figure 5.15: Spectral luminosity points of XRT J151148-051348, the first X-ray counterpart candidate for 2FGL J1511.8-0513, for different assumed redshift (from 0.05 to 2.0), compared to the *blazar* SED templates. The latter are built from archive data of known *blazars* for the four classes: HBL, IBL, LBL and FSRQ. The written values of MAD and χ^2_{min} written in the table are referred to the best fit SED template of each class (*bold colored line*). The color of the selected SED template indicates the estimated redshift with our tool. For the XRT J151148-051348 counterpart set the best-guess identification is an HBL at z ∼0.4.

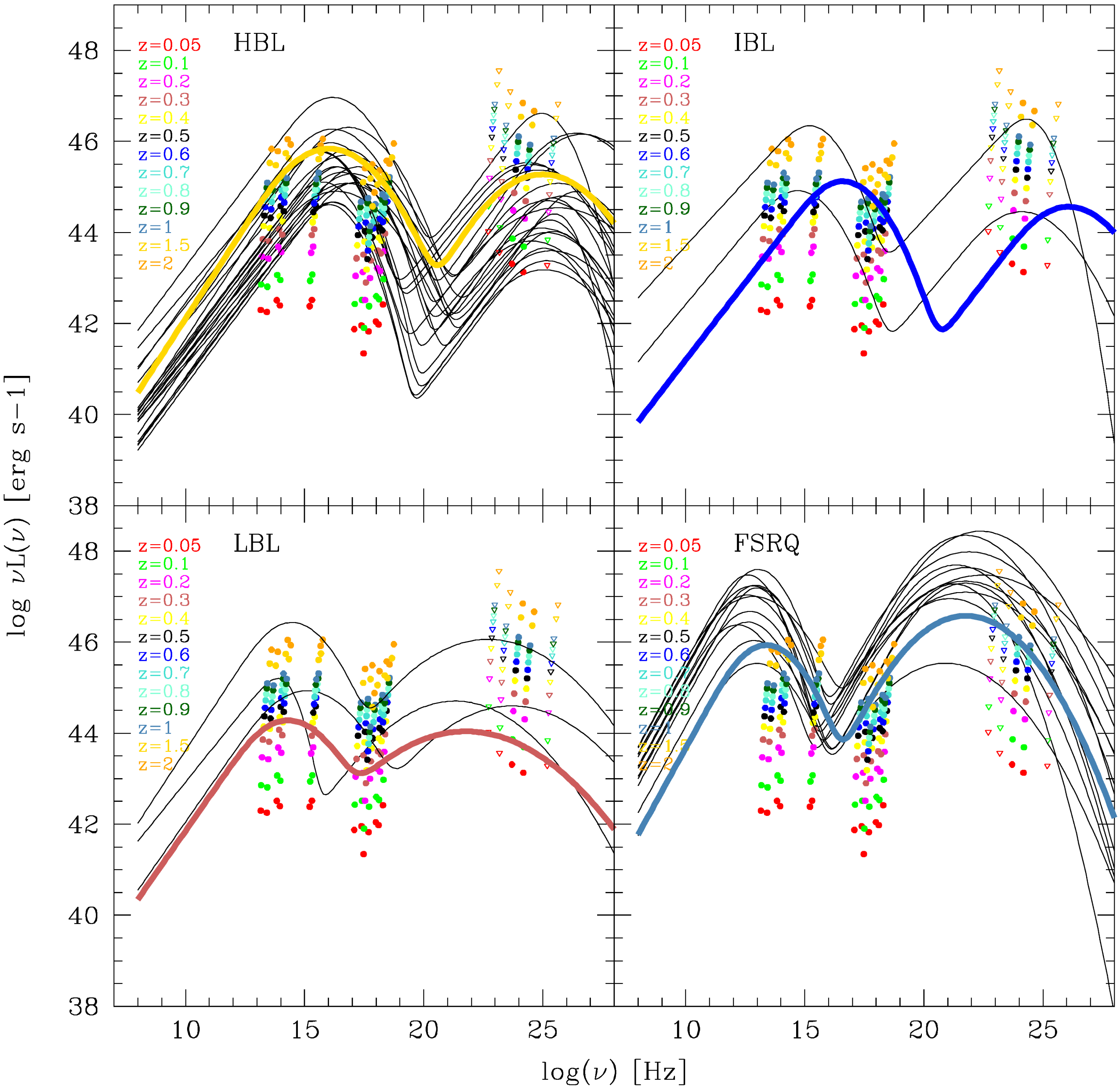

Blazar class	MAD	χ^2_{min}	z
HBL	0.75	0.31	1.5
IBL	0.15	0.66	0.6
LBL	0.48	0.20	0.3
FSRQ	0.67	0.19	1.0

Figure 5.16: Spectral luminosity points of XRT J151159-051526, the second X-ray counterpart candidate for 2FGL J1511.8-0513, for different assumed redshift (from 0.05 to 2.0), compared to the *blazar* SED templates. The latter are built from archive data of known *blazars* for the four classes: HBL, IBL, LBL and FSRQ. The written values of MAD and χ^2_{min} written in the table are referred to the best fit SED template of each class (*bold colored line*). The color of the selected SED template indicates the estimated redshift with our tool.

5.2.11 2FGL J1544.5-1126

In the second Fermi catalogue 2FGL J1544.5-1126 is reported with a detection significance of 5.79σ and a *semi major axis 95%* of 8.4'. From the *Swift*/XRT observations of the X-ray source 1RXS J154439.4-112820 (that falls in the UFO error-box), we have a deep X-ray image of the region surrounding the UFO position. Moreover we proposed (in the Sec 3.2.11) 1RXS J154439.4-112820 as the likely X-ray counterpart, which is also the brightest X-ray source in the field of view. Applying our association procedure, the resulting multiwavelength SED is displayed in Fig 3.24 and its flux data points have been used to run the *blazar* identification tool. The diagnostic plots are shown in Fig 5.17. The best-fitting SED template is in the HBL class, but we can note that actually any SED template (of every *blazar* class) can match the source luminosity points because the spectral trend is not reproduced in any energy band.

To unveil the nature of this X-ray counterpart that exhibits a peculiar SED, we proposed to perform spectroscopical observation with the NOT[2] optical telescope. Indeed an estimate of the distance of this source and of the spectroscopical behaviour in the optical band will shed light on its origin. The resulting preliminary optical spectrum, in Fig 5.18, confirms the result found by [40] for this source. This object is well accommodated as a galactic source characterised by broad emission lines (Balmer series and helium transitions, EW 20 Ang, FWHM 800 km s^{-1}), and in literature is associated to a galactic Cataclysmic Variable (CV) star. CVs have never been detected in gamma-rays although various models, that describe their emission ([13, 52]), claim that γ-ray photons could be produced in particular kind of CV.

In addition, we would like to discuss about another *Fermi* source, 2FGL J1227.7-4853. This is an unidentified *Fermi* object with $b = 13.8°$ and for this reason out from our UFO sample. Considering the work in Bonnett+2012 it could be associated to the X-ray source XSS J12270-4859 and represents the first Low Mass X-ray binary detected by *Fermi*. Comparing the braod-band SED of XSS J12270-4859 with the SED of our 2FGL J1544.5-1126 counterpart set we can note an appreciable similarity (Fig 5.19).

At the same time, we believe that to confirm the association of 2FGL J1544.5-1126 with 1RXS J154439.4-112820, we should be able to exclude the other X-ray sources (found in the 2FGL J1544.5-1126 error-box) as possible X-ray counterparts. In such a way, we determined

---

[2] *Nordic Optical Telescope* (website:www.not.iac.es)

the association set for these X-ray sources and the close-up images centered on their X-ray position are shown in Fig 3.25. These sources are very faint X-ray sources with a few X-ray counts detected by *Swift*/XRT and for most of them any associations in radio, optical and IR band is found. At this stage, the most probable competitors of 1RXS J154439.4-112820 are the sources 1SXPS J154434.9-112954, 1SXPS J154438.5-112641 and 1SXPS J154504.4-112649, although the weakness of their X-ray emission, the lack of precise positional coincidence between the multiwavelength counterparts and the lack of radio emission for the two latter sources suggest an improbable AGN nature. Further investigations are on-going.

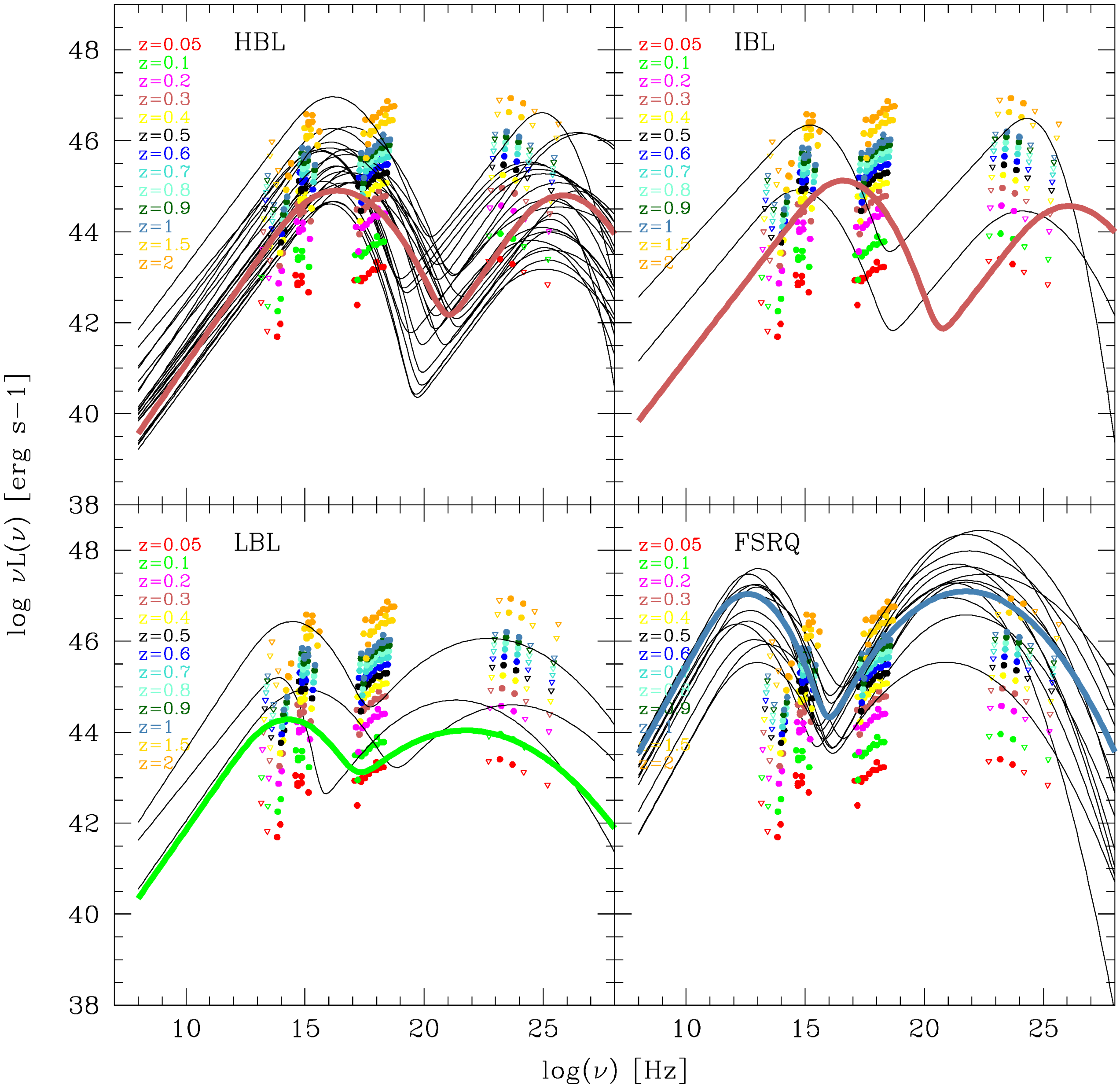

Blazar class	MAD	χ^2_{min}	z
HBL	0.30	0.26	0.3
IBL	0.01	0.33	0.3
LBL	0.91	0.70	0.1
FSRQ	0.04	0.39	1.0

Figure 5.17: Spectral luminosity points of 2FGL J1544.5-1126 for different assumed redshift (from 0.05 to 2.0), compared to the *blazar* SED templates. The latter are built from archive data of known *blazars* for the four classes: HBL, IBL, LBL and FSRQ. The written values of MAD and χ^2_{min} written in the table are referred to the best fit SED template of each class (*bold colored line*). The color of the selected SED template indicates the estimated redshift with our tool.

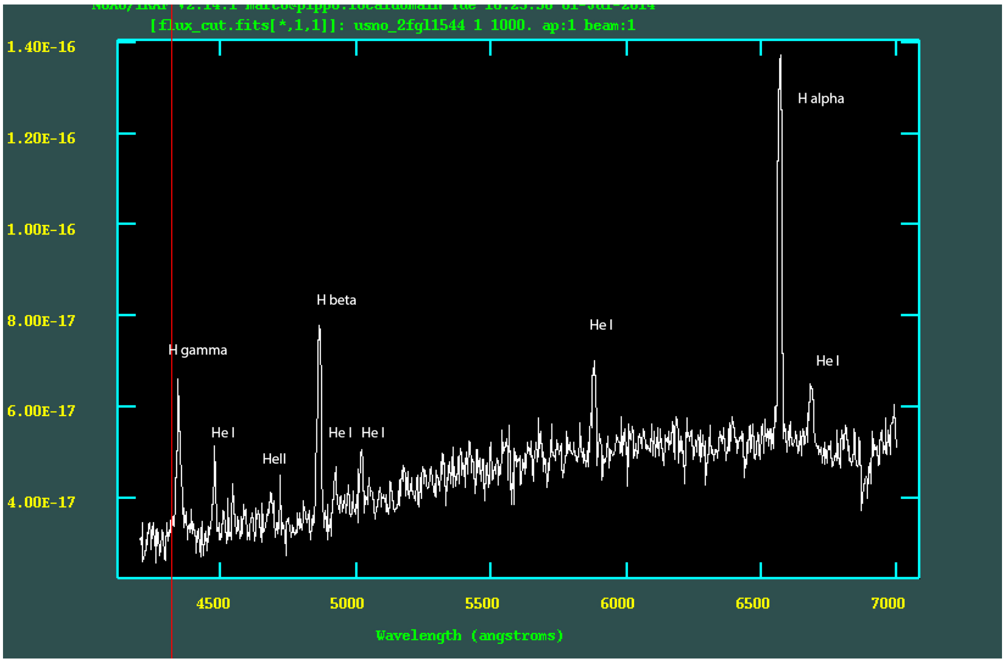

Figure 5.18: NOT spectrum

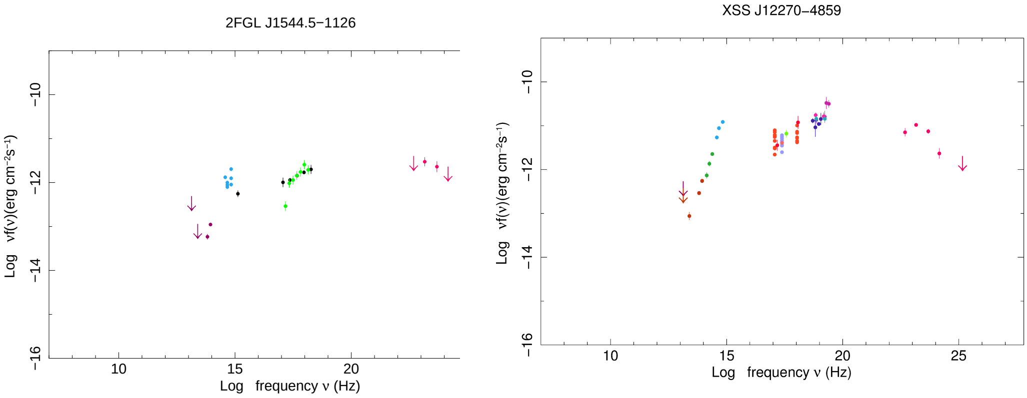

Figure 5.19: Broadband SED (*left*) for the UFO 2FGL J1511.8-0513 created using the SED Builder tool of the ASI ASDC Data Centre and using our proposed MWL association set (see Sec 3.2.11 for details), and the broadband SED (*right*) for XSS J12270-4859. We combine the WISE and 2MASS IR data (violet and green points), the USNOB1.0 optical data (light blue points) with the HE γ-ray data (magenta points) from the 2FGL catalog. The X-ray flux points (light green points) are from the *Swift*-XRT data analysis performed in this work.

5.2.12 2FGL J1614.8+4703

The multi-wavelength counterpart set of 2FGL J1614.8+4703 is described in Sec 3.2.12. We propose the *Swift* source XRT J161541+471110 as possible X-ray counterpart, with some uncertainty because the Fermi errorbox is not fully covered by the XRT imaging. In Fig 3.27-*left* we show the MWL SED built from its counterpart set. Running the *blazar* identification tool we obtain the plots in Fig 5.20 with the table containing the MAD and χ^2_{min} values of the best-fitting SED template for every *blazar* class. We suggest that 2FGL J1614.8+4703 has an LBL object at redshift z=0.2 as likely counterpart, based on the minimim value of χ^2_{min}. The alternative HBL solution is also disfavoured by the very flat shape of the X-ray spectrum, and a similar consideration holds for the IBL solution. For this object, SDSS survey has reported a spectrum with the appearence of an early-type spiral (Sa) of redshift 0.19 (3.27), that may represent the host galaxy of a very faint low-z blazar.

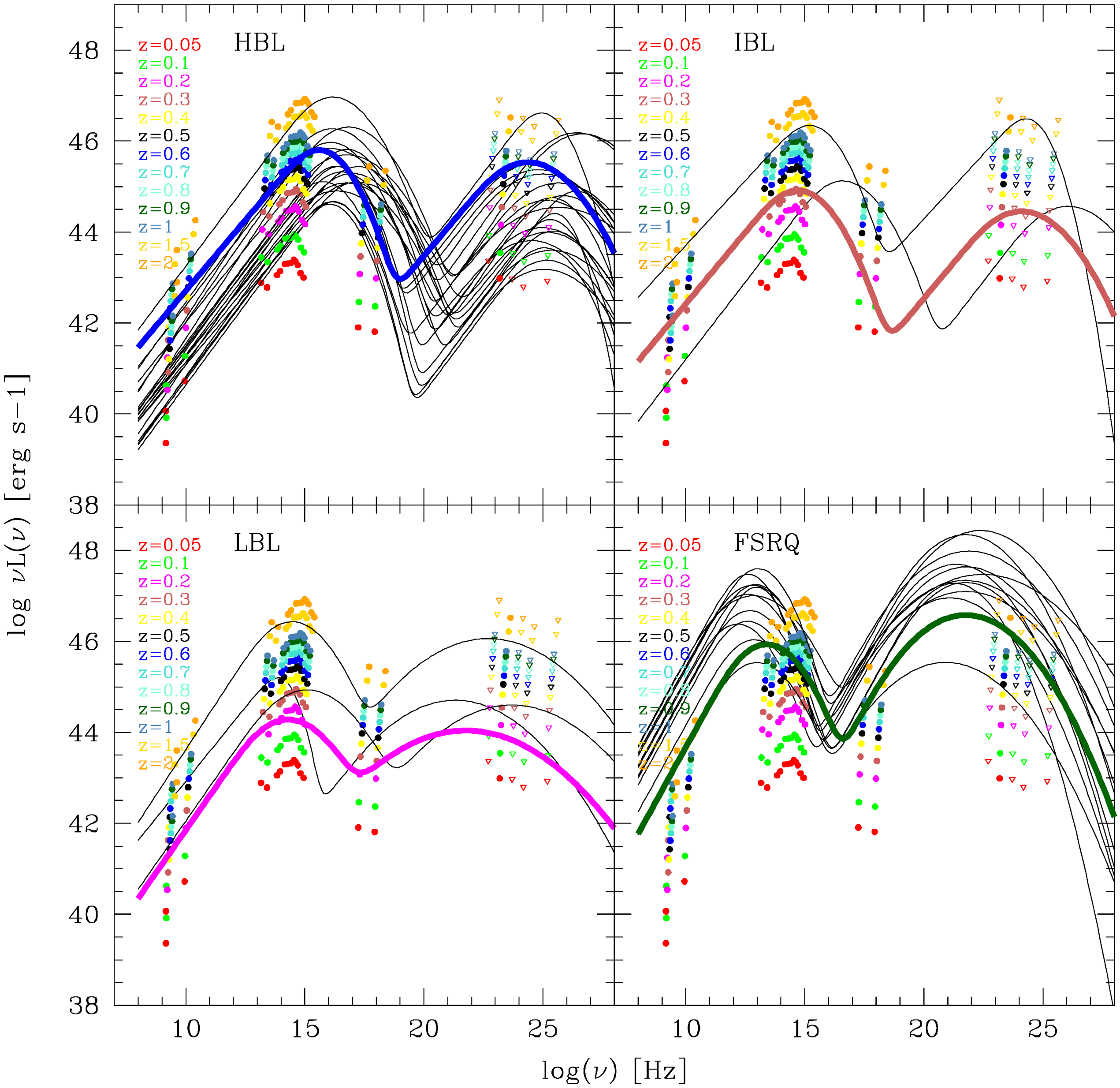

Blazar class	MAD	χ^2_{min}	z
HBL	0.52	0.08	0.6
IBL	0.30	0.14	0.3
LBL	0.65	0.06	0.2
FSRQ	0.37	0.25	0.9

Figure 5.20: Spectral luminosity points of 2FGL J1614.8+4703 for different assumed redshift (from 0.05 to 2.0), compared to the *blazar* SED templates. The latter are built from archive data of known *blazars* for the four classes: HBL, IBL, LBL and FSRQ. The written values of MAD and χ^2_{min} written in the table are referred to the best fit SED template of each class (*bold colored line*). The color of the selected SED template indicates the estimated redshift with our tool. For 2FGL J1614.8+4703 the best-guess identification is an LBL at $z \sim 0.2$.

5.2.13 UFO pulsar candidates

Elenco delle pulsar e relativi plot

5.3 UFO Characterization

Comparison with plots of Fermi colours for the various classes of sources

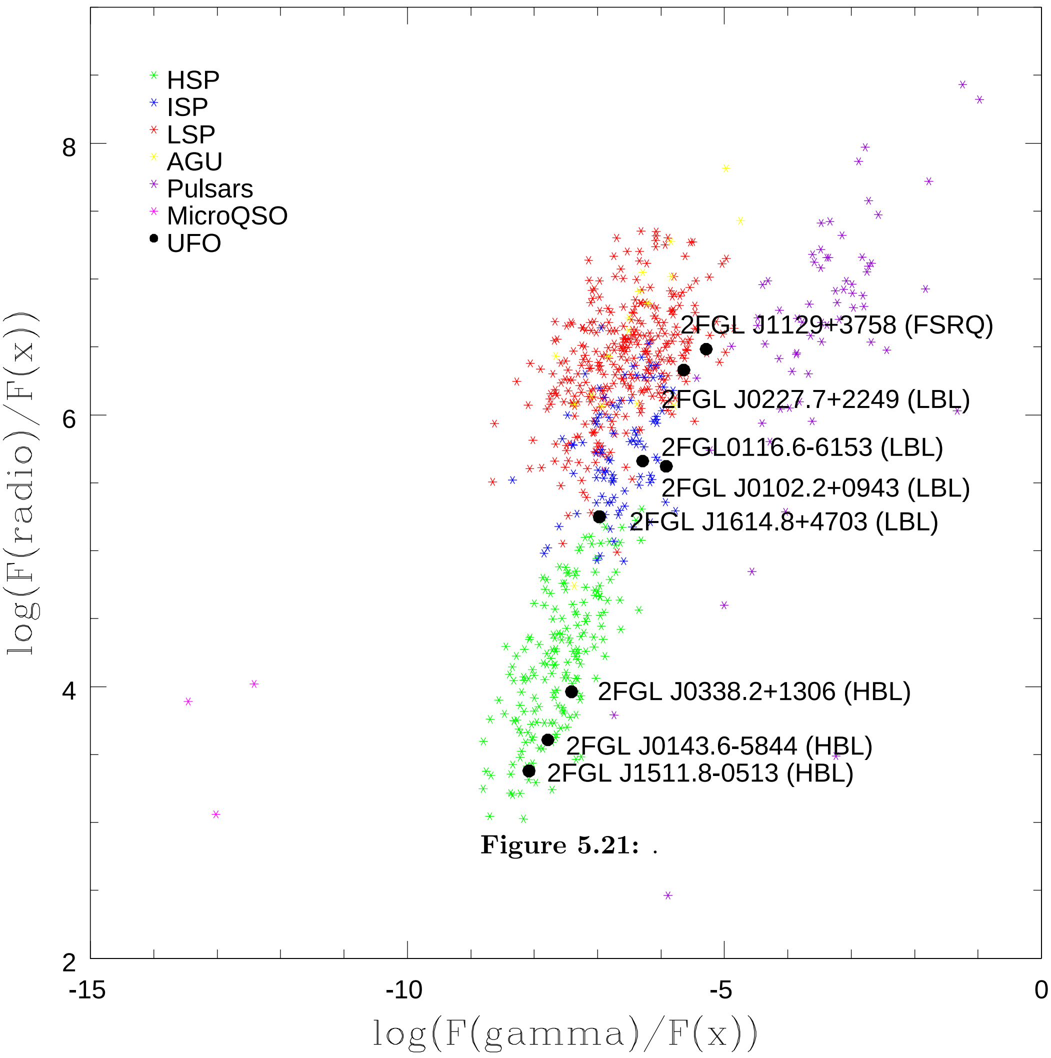

Figure 5.21: .

6

Gamma-ray astronomy with the IACT telescopes: the MAGIC stereo system

6.1 Cherenkov Technique

In Section XXX the experimental ways to perform research in field of high energy and very high energy astrophysics were briefly discussed, distinguishing between the direct and indirect detection in according to the energy of the primary cosmic particle. For energy up to few hundred of GeV the detection can be done in the direct way susing satellite-borne telescopes (Sez XXX), but for higher energies the space satellites present some intrinsic limitations and the detection can be realized only through a indirect procedure with ground-based telescopes.

In this Section we describe the imaging Cherenkov technique that, using the Earth atmosphere as absorbing material of a giant calorimeter, permits the energy and the incoming direction reconstruction of the primary γ-ray photons through the study of the secondary products generated in cosmic particle-induced atmospheric shower. These secondary particle cascades show different morphological features, related to the nature of the primary particle, and can emit UV and optical photons due to Cherenkov effect originating a rapid flash of light.

6.1.1 Interaction of cosmic particles with the atmosphere

Because of the Earth atmosphere opacity, the cosmic rays cannot be directly detectable on the ground, but they interact with atmospheric nuclei producing extended cascades of secondary particles, so-called *Extensive Air Shower* (EAS), that can be studied by ground-based detector. Depending on the nature of the primary particle, there are two types of cascades (Fig6.1) and thanks to their morphological difference they can be distinguished and classified as *electromagnetic* and *hadronic* showers (generated by γ photons and cosmic protons or nuclei respectively). A such discrimination is the basis of the Imaging Cherenkov technique and it will be important to recognize the hadronic events that, as we shall see, constitute the main and undesired background.

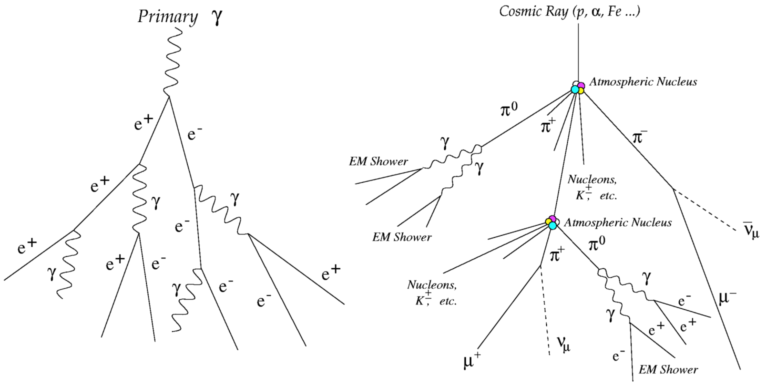

Figure 6.1: Development scheme for an electromagnetic (*left*) and an hadronic (*right*) shower.

Electromagnetic showers

When a γ-ray of high energy E_0 enters into Earth atmosphere, it interacts electromagnetically with the atmospheric nuclei and, after a typical distance X_o called *radiation length*, produces an initial electron-positron pair:

$$\gamma(\gamma) \rightarrow e^+e^- \tag{6.1}$$

Afterwards, via Bremsstrahlung, the electron (and the positron) with energy $E_0/2$ emit new photons of reduced energy $E_0/4$:

$$e^{\pm}(\gamma) \rightarrow e^{\pm}(\gamma) \tag{6.2}$$

These new secondary photons can again produce a new pair of electron/positron, leading to the development of an extensive shower. Hence, the two physics processes involved are the pair-production and Bremsstrahlung emission and following the simple Rybicki & Lightman (1979) treatment, sketching in Fig 6.2, where the radiation length is the same for the both processes involved, we have that after every distance X_o, the number of particles in the shower is doubled and their energy is halved. Therefore after a distance of nX_o, the cascade contains 2^n particles of averaged energy $E_0/2^n$.

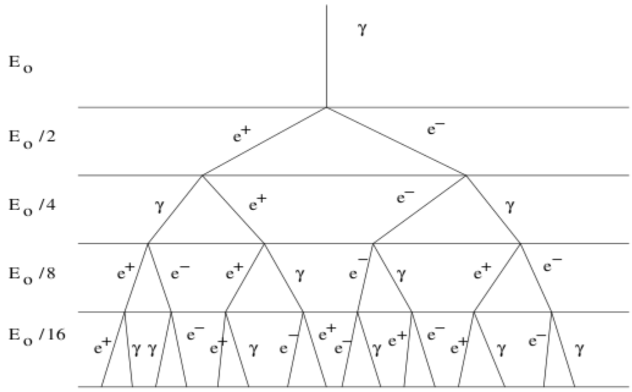

Figure 6.2: Sketch of the simple modeled development of an electromagnetic cascade.

The shower reaches its maximum development when the particle energy reaches the critical energy value E_c that in the air is ∼83 MeV (Longair+1992). Below this energy other processes, as the ionization losses, the photoelectric absorption and the Compton scattering, dominate and the shower cannot grows anymore, waning over time. The maximum number of produced particle is reached when $\frac{E_0}{2^{n_{max}}} = E_c$ at a distance of $X_{max} = X_0 \ln(E_0/E_c)$.

As said before, this is a simplified description of the EAS phenomena, but other more comprehensive models have been suggested, as the one proposed by Greisen and Rossi (1974) where the longitudinal evolution is function of the primary energy, of the atmospheric depth t and of the *age parameter (s)* related to the level of the shower development, following this formula:

$$N_{e^{\pm}}(t) = \frac{0.31}{\sqrt{ln(E_0/E_c)}} e^{t(1-1.5lns)} \tag{6.3}$$

$$s = \frac{3t}{t + 2\ln(E_0/E_c)} \tag{6.4}$$

where

$s < 1$ before of the maximum shower development

$s = 1$ at the maximum development

$s > 1$ after the maximum development

For primary γ-rays with energies between 30 GeV to $\sim$1 TeV, at the maximum development, given for s=1 and t_{max}=$ln(E_0/E_c)$, the shower maximum ranging from 12 km to 8 km, and for this reason the IACT system focus at $\sim$10 Km of altitude.

Hadronic showers

If the primary particle has an hadronic origin, as for example protons or atomic nuclei that are the most component of the cosmic rays, the cascade development is not driven by QED processes, but by strong interactions that generate larger and broader shapes of the shower with respect to the electromagnetic ones.

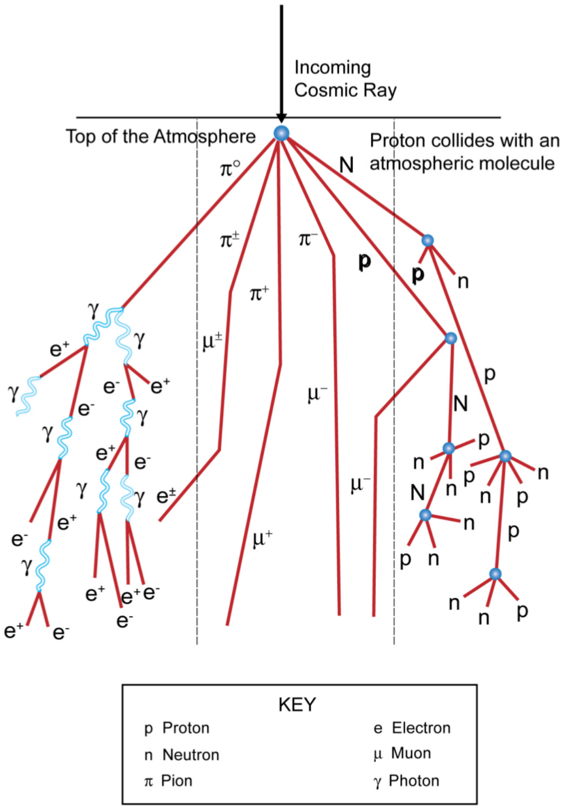

Figure 6.3: Illustration of an hadronic-induced shower and possible interactions involved.

A hadronic shower consists of three components (Fig6.3):

- *The hadronic core component* that is composed of nucleons and mesons that decay into muons and neutrinos:

$$K^{\pm} \rightarrow \mu^{\pm} + \nu_{\mu}(\overline{\nu_{\mu}}) \tag{6.5}$$

$$K^{\pm} \rightarrow \pi^{\pm} + \pi^{0} \tag{6.6}$$

$$\pi^{\pm} \rightarrow \mu^{\pm} + \nu_{\mu}(\overline{\nu_{\mu}}) \tag{6.7}$$

About 90% of secondary particles produced are pions (1/3 neutral and 2/3 charged pions).

- *The muonic component* due to the meson decays. Since the μ mean lifetime is relatively long, they have a high probability to penetrate the atmosphere and to reach ground. Nevertheless a few muons producted can lose energy via ionization or decaying into neutrinos and electrons:

$$\mu^{\pm} \rightarrow e^{\pm}\nu\overline{\nu} \tag{6.8}$$

- *The electromagnetic component* due to immediate decay of the neutral pions

$$\pi^{0} \rightarrow \gamma\gamma \tag{6.9}$$

into two energetic photons which in turn can induce electromagnetic showers indistinguishable from the primary γ-ray-induced ones and hence they consistite the main and isotropic source of background for the IACT detectors.

The most simple description of a hadronic EAS is provided by the *Superposition model*[35TESI-DM]: it assume that a shower induced by a nucleus with A nucleons and primary energy E_0 is equivalent to the superposition of A showers with energy $E_i = E_0/A$, and the maximum development is achived for radiation length of:

$$X_{max} \propto ln\Big(\frac{E_0}{AE_c}\Big) \cdot \xi_N \tag{6.10}$$

where $\xi_N \sim 100$ g cm^{-2} is the air absorption length.

Hence, the heavier nuclei penetrate much less the atmosphere creating showers with a wider lateral distribution (up to a few hundred meters). Through MC simulation it is possible to study the morphology and the temporal evolution of showers generated by different kinds of particles. In Fig6.4, the MC simulations of an hadronic (*left*) and electromagnetic (*right*) air shower, performed by the `CORSIKA` software : we can see that the hadronic shower is less concentrated and has a broader shape with respect the e.m. cascade.

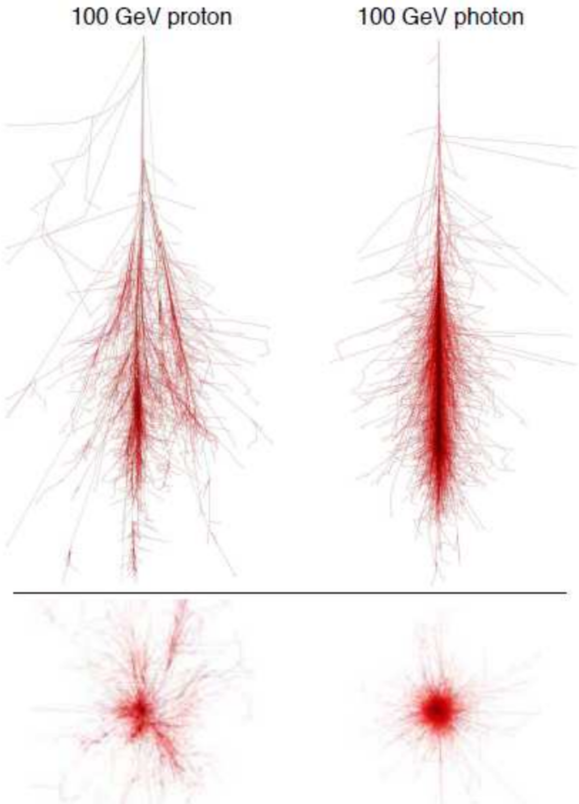

Figure 6.4: MC simulation of an hadronic (*left*) and electromagnetic (*right*) air shower generated by a 100 GeV primary particle, with their corresponding light pool on the ground for the two kinds of showers, performed with the `CORSIKA` software.

6.1.2 Cherenkov light from a EAS

If the secondary particles generated in a EAS have enough energy, they can emit radiation by means of the Cherenkov effect. This radiation can be detected by ground-based telescopes, allowing to infer the energy of the primary particle. Cherenkov light is emitted when in a medium of dielectric constant ϵ and refractive index $n = \sqrt{\epsilon}$, charged particles travell with a speed $v = \beta c$ greater than the phase velocity of the light in the medium or c/n. This effect is due to Coulomb interactions, indeed when a charged particle travels through air, it polarizes the molecules encountered along its trajectory and creates electrical dipoles. If $v < c/n$ the dipole orientation changes and follows the charged particle, instead if $v > c/n$, the reaction of the dipoles is delayed producing a shock wavefront in the electromagnetic field along a conical surface. The lost energy of the superluminal particle results in a light flash called Cherenkov radiation.

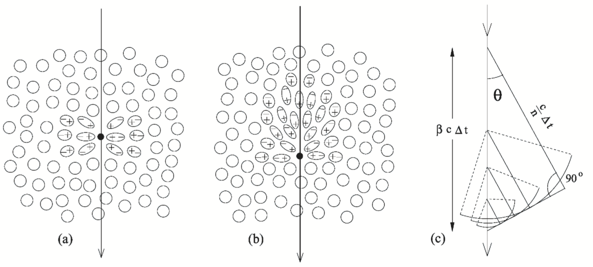

Figure 6.5: *Left*:Polarisation of a dielectric medium due to moving charged particle: (a) when the particle is in non-relativistic regime ($v < c/n$), the polarisation is simmetric in the neighborhoods of its trajectory and no radiation is emitted, instead (b) the effect produced by a travelling particle with $v > c/n$. *Right*:Geometrical description of the Cherenkov angle and of the coherence of the emitted radiation.

From the Fig6.5 and from geometric assumptions, we can see that the Cherenkov radiation is emitted within a cone with aperture angle θ_c:

$$cos\theta_c = \frac{(c/n)t}{(\beta c)t} = \frac{1}{\beta n} \tag{6.11}$$

The minimum value of the particle velocity to have Cherenkov emission is given assuming:

$$\beta = 1/n \quad \Rightarrow \quad E_{th} = \frac{m_e c^2}{\sqrt{1-\beta_{min}^2}} = \frac{m_e c^2}{\sqrt{1-1/n^2}} \tag{6.12}$$

where E_{th} is the energy threshold for the Cherenkov light emission. Instead the Cherenkov angle is maximum when:

$$\beta \sim 1 \quad \Rightarrow \quad \theta_{max} = arccos\frac{1}{n} \tag{6.13}$$

At the level sea, for the Earth atmosphere the reflaction index is $n \sim$1.00029, so θ_{max}=1.3° and E_{th} ~21.3 MeV for electrons, 39.1 GeV for protons and 4.4 GeV for muons.

Considering that the refraction index depens on the altitude h, we can write:

$$n = 1 + \eta_h = 1 + \eta_0 e^{(-h/h_0)} = 1 + 2.9 \cdot 10^{-4} e^{(-h/h_0)} \quad h_0 \approx 7.1 \text{ km} \tag{6.14}$$

For $\eta_h \ll 1$ the maximum Cherenkov angle and the energy thresholds can be espressed as function of the altitude, in according to the following equations:

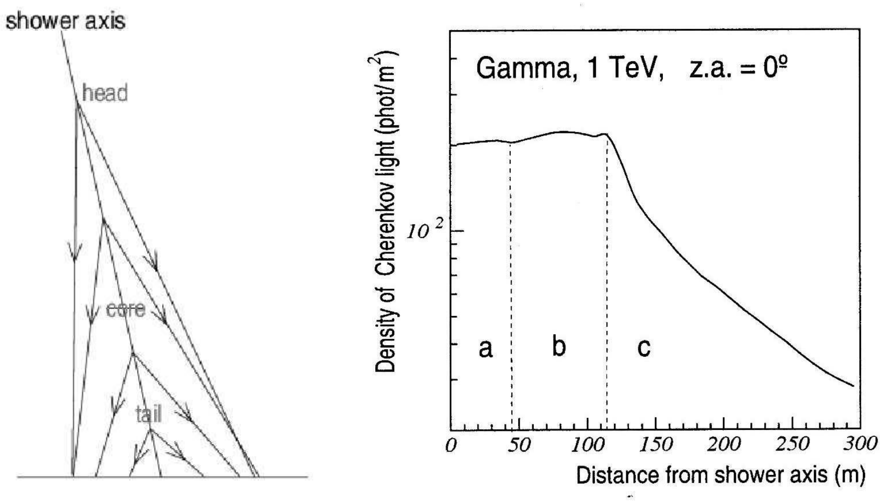

(a) (b)

Figure 6.6: *Left*:Variation of the atmospheric Cherenkov angle at different altitude in a EAS. *Right*: Distirbution of the Cherenkov photon density as function of the radial distance from the shower axis. The region labelled *a* indicates photon of the shower tail, the region *b* from the core and the region *c* from the shower head.

$$E_{th} \simeq \frac{0.511\text{MeV}}{\sqrt{2\eta_h}} = \frac{0.511\text{MeV}}{\sqrt{2\eta_0 e^{(-h/h_0)}}} \tag{6.15}$$

$$\cos\theta_{max}(h) = \frac{1}{1+\eta_h} = 1 - \eta_0 e^{(-h/h_0)} \tag{6.16}$$

We can conclude that the energy threshold to have Cherenkov emission increases with the altitude and viceversa the Cherenkov angle descreases as shown in Fig 6.6.

The Cherenkov light spectrum , or the number of photon emitted per path length x and wavelength λ, emitted by a charge z is given by

$$\frac{dN}{dxd\lambda} = 2\pi\alpha \cdot z^2\Big(\frac{1}{\lambda}\Big) \cdot \Big(1 - \frac{1}{\beta^2 n^2}\Big) \simeq 44e^{(-h/h_0)} \qquad \text{ph/m} \qquad [\text{ph/m}] \tag{6.17}$$

where $\alpha = e^2/\hbar c$ is the fine structure constant and the last term is derived considering that in the Earth atmosphere the Cherenkov radiation spans between 290 nm and 600 nm in the UV-Optical regime.

6.1.3 Imaging Air Cherenkov Technique

The *Imaging Atmospheric Cherenkov Telescopes* are the instruments that perform detection of VHE γ-rays. They exploit the imaging techinque and do not meausere directly the γ-ray flux but detect the optical Cherenkov light emitted by the secondary particles of the EAS (Fig6). The basis idea of the IAC technique is to collect the Cherenkov photons of a atmospheric shower, to analyse the image projected on the camera and to provide an efficient method to reject the background and to determine the γ-ray signal.

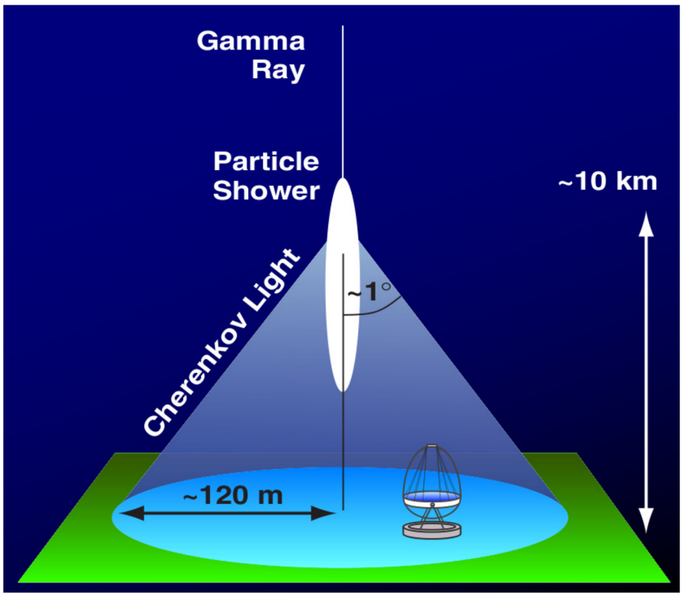

Figure 6.7:

Image formation

The atmospheric showers are characterized by a longitudinal development that can be divided in three principal regions: the *head* composed by the particles of the first interactions, the *core* where the showers present the maximum growth, and finally the *tail* when the showers begin to vanish (see Fig6.6).

Since the Cherenkov cone angle depends on the energy and the emission altitude, the Cherenkov photons are reflected by the mirror with different incidence angles β and focused on different regions of the camera, creating the typical elliptical shape for a shower image (Fig6.8): the photons of the shower head have a β angles smaller than the tail photons and each incidence direction corresponds to a given position on the camera (Fig6.9). For a parabolic reflecting surface it is expressed as:

$$r \sim \sin\beta \cdot f \sim \beta \cdot f \tag{6.18}$$

where f is the focal distance of the telescope mirror and r is the distance between the

Figure 6.8: Image formation of a EAS through the IACT technique. The region A is the shower head, B is the core and C the tail.

position of the light concentration and the central camera pixel.

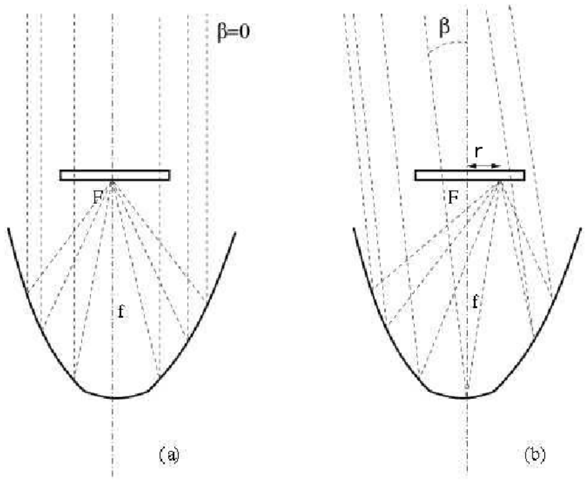

Figure 6.9: Sketch that shows the focusing of the Cherenkov light on the IACT camera.

Background radiation

The formation of Cherenkov light images is affected by various background noises that degrade the quality of the image and hamper the extraction of the gamma signal.

One of the most important is the *Night Sky Background* (NSB) componed mainly by the light of the bright starts, zodiacal light, diffuse light for the galactic plane, airglow, polar light, fluorescence phenomena and artificial light.

Another source of background light is the moon that with its spectrum peak around 500 nm perturbs the Cherenkov light detection.

The main dominant background is given from the showers of hadronic origin, that composed of charged particles, can emit Cherenkov light. Unfortunately for every $\sim 10^4$ hadronic showers there are only few γ-induced cascade, hence the crucial scope of the IACT technique is to provide a method to recognize and then to reject the images of the hadronic component. In Fig6.10......

Figure 6.10: Some example of shower images generated by different primary particles, collected on the MAGIC camera:

Image parameters

In the following the image parameters called source indipendent are described:

- SIZE : The total charge (in phe$^-$) collected in the cleaned images, defined as `size`$= \sum_i^k N_i$, where N_i is the charge in a given pixel i. For a fixed impact parameter and zenith angle, it is roughly proportional to the energy of the primary paricle.
- LENGTH: The RMS of the charge distribution along its major axis or half the length

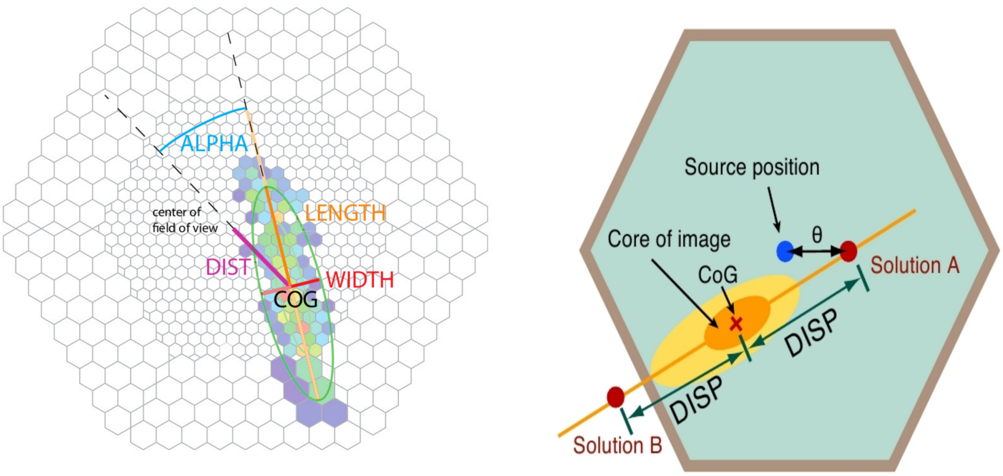

Figure 6.11: *Left*: *Right*: .

of the major image axis. It is related to the longitudinal development of the cascade and also it depends of the particle energy.

- WIDTH: The RMS of the charge distribution along the minor axis of the image or half the width of the minor image axis. It is correlated with the lateral distribution of the shower and together with the `lenght` is an efficient parameter for the γ/hadron discrimination because at fixed value of `size` (and hence of energy) the latters have a wider transversal envelope and are spatially less compact.

- CENTER OF GRAVITY (CoG): the baricentre of the charge distribution of the elliptical image.

- CONC(N): Fraction of the total image charge which is contained in the N brightest pixels. The standard value is N=2. It provides information about the compactness of the shower image and about the shower core. This parameter is expected to be higher for the γ-rays because they tend to be more concentrated.

- M3LONG: Third momentum of the charge distribution along the major axis that measure the asymmetry of the shower image along the longitudianl development. It allows to identify the head and the tail of the shower and discriminate between the two solution for the incoming direction of the primary particle found with the `DISP` methos (see Section XXX), but for lower `size` this parameter is of little utility.

- LEAKAGE: Light fraction contained in the image pixels in the outermost ring of the camera. This parameter estimates the percentage of lost signal and images with high value of `leakage` (>10-20% and likely for events with energies above 2 TeV) are rejected from the analysis chain.
- NUMBER OF ISLANDS: Number of clustered pixels survived after the image cleaning. In general the hadronic shower images tend to show several separated cluster of particles and hence of "islands" on the camera, while the electromagnetic cascade are single connected image.

In addition to these parameters, we can define other two used in the standard MAGIC analysis and based on the time structure of the Cherenkov flashes that improve the rejection of background:

- RMS TIME: The root mean square of the arrival times of all pixels belonging yo the image after the cleaning. It was suggested as a possible background discriminator by Mirzoyan+2006(TG) becuse in general the arrival time distribution of the gamma events are narrower.
- P1GRADIENT It measure the event time profile and its time-evolution of the signal along the major axis of the image.

Hereafter the parameters that depend on the known (or expected) position of the source in the camera:

- DIST: The distance between the CoG of the image from the nominal source position. It permits to evaluate the impact parameter and the distance of the shower maximum of the incoming shower, helping the energy reconstruction.
- ALPHA (α): The angle between the major axis of the image and the line connecting the CoG with the source position in the camera. It is a fundamental parameter for the γ/hadron separation beacuse since the major image axis is the projection of the axis of the shower and the latter points to the source position in the sky, the major image axises displayed on the camera always point in the source position on the camera and hence the `alpha` is expected to be small for the γ-like events. Insted the hadronic

shower images are distribuited isotropically and therefore their `alpha` distribution is rather flat.

- θ^2: θ is the angulaR distance between the real source position and the reconstructed incoming direction of the event. The latter can be estimated by using the DISP parameter (in mono mode) or using the event stereoscopic reconstruction (both described later). The direction distribution for γ-rays should be peak next to the source position, while should be homogeneous for background events. For graphical convenience, θ^2 instead of θ is calculated, as an homogeneous distribution on the sky meads to a constant distribution in θ^2 but to a linearly increasing distribution in θ. The distribution for a γ-ray signal peaks at θ^2=0 deg^2.
- DISP: The distance betwee the center of gravity of the shower image and the estimated source position on the camera plane. It is used in mono data analysis to determine the incoming direction of the primary particle.

6.2 The MAGIC data analysis

The final aim of observations performed with Cherenkov telescopes is to measure the flux of cosmic γ-ray from a given sky position, tipically associated with a astrophysical source. In particular, through the reconstruction of the differential energy spectrum and the lightcurve (the VHE integral flux as function of the time) the study of the physical processes occured in the astrophysical objects is possible. In this Section we provide a description of the analysis pipeline following in order to work out from the raw data the VHE measurements of the celestial object observed from the raw data generated by the MAGIC telescopes. The standard analysis program of the MAGIC collaboration is the MARS (*MAGIC Analysis and Recostruction Software*) package (Moralejo+2009), a constantly evolving software developed in the ROOT[1] environment and written in C++, that permits thanks its executables to carry out the analysis steps descripted below.

6.2.1 Analysis chain and fundamental steps

The MAGIC standard analysis, which permits to extract physical information from the recorded raw data files, has as purposes the rejection of the night sky background (NSB) that

---

[1] for details, see http://root.cern.ch

affects the images of the Cherenkov flash images, the particle identification discriminating the γ-like events from the events generated by hadron particles and finally the determination of the incoming direction and the energy of the primary γ-ray photon.

Here a summary scheme about the main steps of the stero data analysis that will be described in details in the next sections:

- Calibration
- Image Cleaning
- Image reconstruction and parametrization
- Quality check
- Stereoscopic image reconstruction
- Training γ/hadron separation
- Reconstruction of the energy of the primary particle
- Determine of the effective collection area
- Signal search with the estimate of the γ-like event excess
- Construction of the differential spectrum and lightcurve

6.2.2 γ-event MonteCarlo simulations

In particle physics experiment the calibration of the instruments is performed using a controlled incident light beam, but for the Cherenkov telescopes this approach is not possible and MC simulations are used. For this reason the MC simulated γ-ray events represent an fundamental ingredient of the MAGIC analysis chain and are involved mainly for the optimization of the γ/hadron discrimination, for the estimate of the energy of the primary particle event and to calculate the effective collection area, indispensable to derive the spectrum and the lightcurves.

To guarantee a reliable γ/hadron separation, several studies have been dedicated to the MC production in order to achieve a good agreement in parameter distributions between the real and simulated MC γ events. The production can be divide in three steps. Before the atmospheric showers simulation are produced through the CORSIKA[2] package (Heck+1998) using the US standard atmospheric conditions and some specialization for the MAGIC telescopes. At this stage the software takes in account the interactions and decay processes of the different types of particles and provides, in the output files, the location and direction of the Cherenkov photon when reaching the altitude of the MAGIC site for different energy of the primary particle and different zenith angle and orentation respect to the geomagnetic field. In the next step the absorption and scattering of the Cherenkov photons from the shower together with the reflection of these photons on the real MAGIC mirrors, taking account the reflectance and the PSF[3] of the individual telescope dishes, are simulated to determine their location and the arrival times on the camera. At the end the response of the MAGIC camera, trigger system and data acquisition electronics is simulated. The two last steps are done using the two simulation programs `reflector` and `camera` included in the MARS software (more details can be found in Majumdar+2005, Moralejo+2004a, Carmona+2008 and Commuchau+2008).

Finally it is important to note that also hadron MC simulations are produced, but these are not used as a part of the standard analysis because the compatibility with the real hadron events is poor and they are not fondamentali since the background features can be also recovered from real cosmic events which are the majority of the triggered events by the IACT telescopes[4]. For this reason the real datasets of sources that show no signal can be used as OFF sample of hadron events and used to perform the γ/hadron discrimination.

In Fig.6.12 an example of MC simulation for a γ-like events and for an hadronic shower. We can see that at a first glance the purely electromagnetic γ-ray shower is more compact under many considered respects, as explained in the Section XX.

6.2.3 Signal extraction and calibration

The first step of the analysis chain is the extraction and calibration of the Cherenkov light signal in each channel of the camera. Once the raw data are reduces into ROOT files compatible with the MARS software and the relevant informations coming from the telescopes subsystems are available, the signal extraction from the recordered data can be carried out. Each event,

---

[2] COsmic Ray SImulation for KAscade

[3] The optical PSF of the telescope is describe as a 2-D Gaussian function, with σ determined from real observation of star images or from muon ring analysis.

[4] rapporto 1:10^4

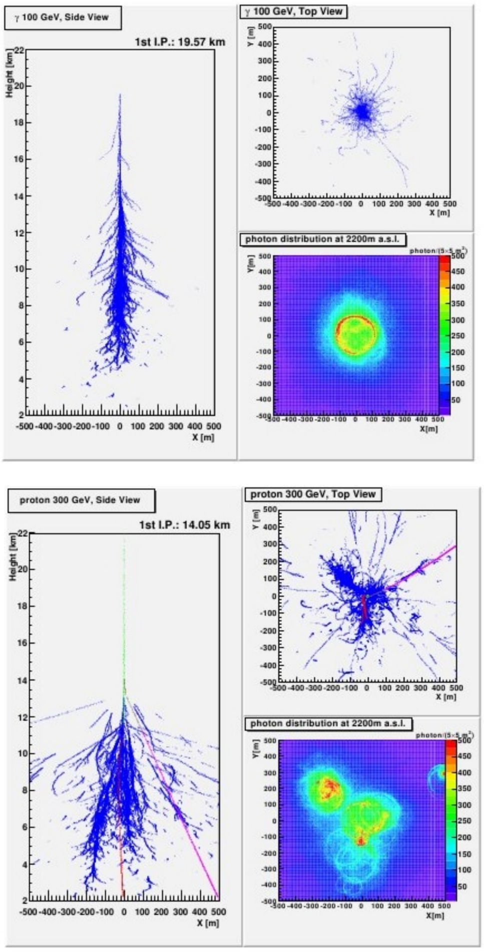

Figure 6.12: Example of simulation of an electromagnetic (*upper panel*) and hadronic (*lower panel*) shower. In both cases, a projection on the vertical and on the horizontal planes of the shower is displayed with the 2-dim map of the Cherenkov light distribution at ground level.

that triggers the Level1 logic of MAGIC, is stored by the Data AcQuisition (DAQ) system and the associated very short signal pulse is digitized with an ultra fast sampling frequency, namely 2 GSample/s. Through the `callisto` (before the upgrade of the readout system) or `sorcerer` executable of MARS the signal, measured in *photo-electrons* (phe), is extracted and reconstructed applying a given extractor algorithm that by means of a cubic spline function permits to evaluate the total intensity (Q) (in FADC unit) and the arrival time of the signal. After the reconstruction of the signal intensity, through the calibration process based on the the *F-Factor* method (Mirzoyan+1997, Gaug+2005), the signal amplitude is converted into number of photo-electrons (phe$^-$) using a proportional relation evaluted thanks to calibration events. The method assumes that the phe$^-$ number in each pixel follows a Poissonian distribution with mean N and standard deviation $\sqrt{N}$ and that the accumulated charge in FADC counts, after pedestal substraction, has a mean value $< Q >$ and RMS σ which is wider than the pure poissonian expectation value mainly due to the electrons multiplication process in PMT dynodes. The relative widths of the distribution can be written as:

$$F\frac{1}{\sqrt{N}} = \frac{\sigma}{Q} \tag{6.19}$$

where, for MAGIC, the averaged *F-Factor* measured in the lab previously to the installation of the photosensors in the camera, is 1.15 for all PMT. Hence the convertion factor can be calculated as:

$$C = \frac{N}{< Q >} = F^2 \frac{< Q >}{\sigma^2} \qquad hence \qquad N = C \times Q \tag{6.20}$$

During the data-taking, since the conversion factor can change due to sensitivity of the electronic chain and temperature variations and hence it has to be constantly updated, special interleaved calibration events are recorded with a rate of 25 Hz.

In case of damaged pixels, so-called *bad pixels*, (usually ∼10-15), that cannot be correctly calibrated due to hardware misfunction and can cause holes in the image, a linear interpolation of their neighboring pixels is calculated and the result is used as signal in order to minimize their impact on the analysis.

6.2.4 Image cleaning

At this stage an image cleaning process is operated to determine which pixels of the camera include signal produced by the Cherenkov light and to reject the diffuse night sky background light that surrounds each shower image. Consequently all information about the other pixels not involved is lost.

This task is performed by a program called `star` of the MARS software and the process is based on two procedures, the *absolute* and *time cleaning*, that combine the signal intensity and the timing information. The so-called *core* and *boundary* pixels are identified through the definition of two thresholds in term of phe$^-$ number (the levels have been adjusted to 8 and 4 phe$^-$ respectively after the 2012 upgrade of the MAGIC system) and through the arrival time of the signal in those pixels. In Fig 6.13 an example of comparison of variuos cleaning levels applyied on the same event.

Recently in addition to this method a new type of image cleaning, named the *sum cleaning*, has been developed by the MAGIC collaboration and it is related to the compactness in time and extension of the Cherenkov images. If the sum of the collected charge in all core pixels is above a certain threshold and within a sharp ($\sim$1ns) time interval, those pixels are considered to belong to the shower image. This procedure has been proved as more efficient, especially for low size events associated to the lower energies, because to allow a better discrimination between the real tails of the Cherenkov images and the NSB fluctuaction and a more accurate reconstruction of the image parameters.

6.2.5 Quality selection and Shower parametrization

The `star` program of MARS, in addition to perform the image cleaning and to select the pixel belonging to the cleaned shower image, calculates some parameters, originated from those proposed by Hillas and described in Section XXX. As said, this allows to parameterize the shower images with a elliptical shape and extract phyical information from them that will be used in the analysis chain.

Once that these image parameters are estimated for each event recorded, they are used to perform a quality check to obtain a final sample of good quality data, studing as they vary with the atmospherical conditions[5] and applying the so-called *filter cuts* that allow to rejected

---

[5] The goodness of the data sample is strongly influenced by the atmospherical conditions and by the bad weather, as expleined in Section XXX.

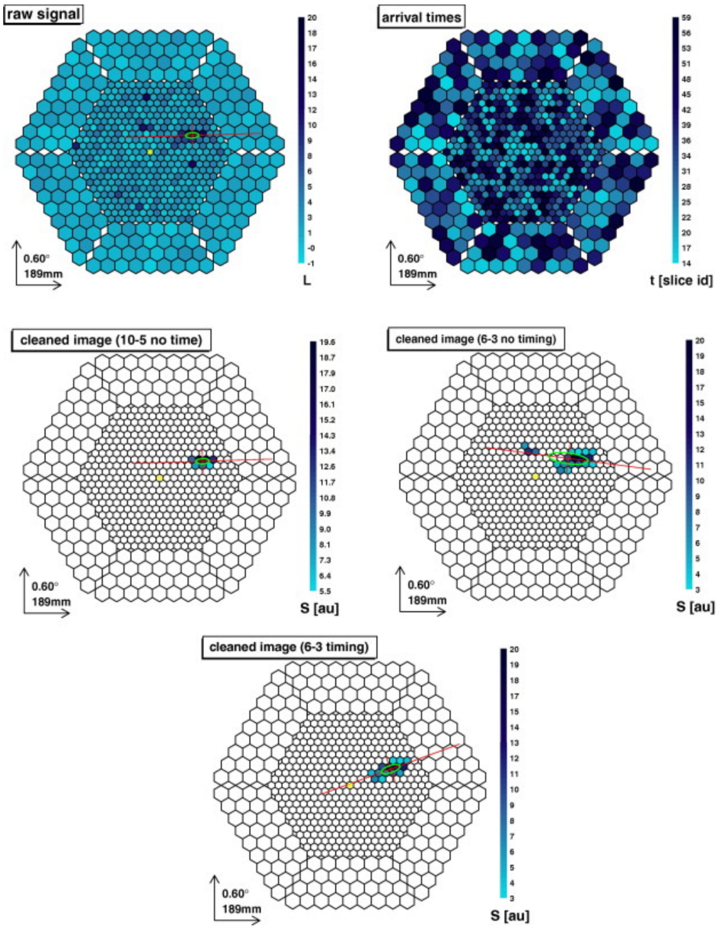

Figure 6.13: Comparison of variuos cleaning levels on the same event, varying the minimum charge values for the core and boundary pixels of the absolute cleaning and applying or not the timing cleaning.

the majority of the background events that are produced by all kinf of non-Cherenkov light and consist in accidental events survived to the image cleaning. The filter cuts generally applied are:

- *Spark cuts*:
- *Car flash cuts*:
- *Leakage cuts*:
- *Island cuts*:
- *Core pixels cuts*:

So far, the previous analysis steps are applied to the data collected from one single telescope, but at this stage the data can be analyzed and the event reconstructed in different ways depending on whether they are collected in mono or stereo mode. In the fist case the DISP method is used to determine the arrival direction of each primary particle, while for stero observations new stereoscopic parameters are defined to making possible the image reconstruction.

DISP method

This method allows the reconstruction of the origin of a γ-ray event for mono observations performed by a single Cherenkov telescopes (Fomin+1994, Lessard+2001). The DISP parameter defined as the distance between the CoG and the estimated source position assumed to lie along the direction of the major image axis (Fig**??**), is thought as function of other Hillas parameters previous described:

$$DISP = a(\texttt{size}) + b(\texttt{size}) \times \frac{\texttt{width}}{\texttt{length}} \tag{6.21}$$

where a and b are second-order polynomials found fitting MC simulated γ-ray showers (Domingo-Santamaria+2005).

Unfortunately an important degeneracy occurs because for each event two candidate arrival directions can be determined. To solve this problem the `M3LONG` and the timing information can be used as the head of the image should be imaged after the tail.

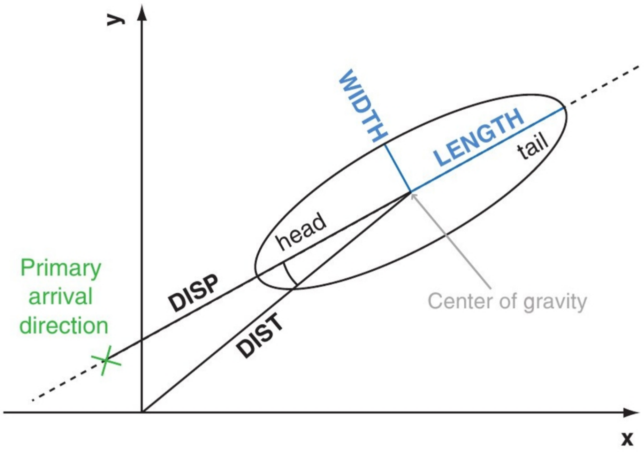

Figure 6.14: Illustration of the DISP method used for the reconstruction of the γ-ray arrival direction.

Stereoscopic parameters

On the other hand when stero observations are performed, we have two sets of data sample, one for each telescopes, cointaining two differnt views of the same cleaned showers. Using the executable `superstar`, we can merge all necessary information of the two data sets into a single file with the aim to identify the matching pairs of images belonging to the same event and to have a 3-D view of the shower. The stereoscopic reconstruction is made possible defining some basic stereoscopic image parameters that give us information about the primary incoming direction, the ground impact point with respect to the two telescopes and the height of the shower maximum. These new parameters are defined using only the main axis and centroid position of both telecope images and provide a strong improvement of the performance of the telescopes (Kohnle+1996TAC). The most important for our analysis are:

- SHOWER AXIS:
- IMPACT:
- MAX-HEIGHT:
- CHERENKOV RADIUS AND PHOTON DENSITY:

6.2.6 γ/hadron separation and Random Forest method

At this stage of the analysis chain, the images of events likely to be due to Cherenkov flashes are selected and cleaned by accidental and night sky background light. Nevertheless the signal is still dominated by undesired noise that mainly consists of images generated by cosmic hadronic particles. The fraction of gamma rays is dominated by background events in the ratio ∼1 : 1000 event for the strong gamma-ray emitters as the Crab Nebula. To extract the gamma-ray signal an suppression of hadron images is mandatory minimizing the loss of γ-ray events, in particular at the lower energies. This crucial aim is performed through the γ/hadron separation process based on the construction of an additional classification parameters, called `hadronness`, combining the image shape information, the stereo parameters, and the timing of the shower. Many approaches can be exploited but the algortihm used in this work and in the MAGIC collaboration is the so-called *Random Forest* (RF) method (Breiman+2001). It is a flexible multivariate classification method based on the construction of a *decisional tree* (Albert+2008ac), a cascade of testes in the multidimensional space of the discriminating parameters used for the classification, and is composed of a training and a test phase. In the training phase, performed by the executable `coach`, specific matrices are created inserting as input files a sample of MC simulated γ-ray events[6] and an hadronic sample[7] usually selected from real datasets. In order to train the RF algorithm, 11 parameters are used and hereunder the most important quantity estimated for the MAGIC analysis:

RF method for the Hadronness

As said before, a first matrix is related to the classification parameter `hadronness`, an real number between 0 to 1 that represents the probability that the images is associated to an hadronic event (`hadronness`=1) or a γ-ray event (`hadronness`=0). The rejection of the hadronic background is therefore performend making a simple cut on this parameter. In Fig 6.15 the hadronness distribution of γ-like events is compared to that of real (hadron-dominated) events for different bins of Size (parameter related to the energy): as expected, while the former peaked at low values of hadronness, the latter at values close to 1 and moreover we can see that at the lower energies the degeneracy in the image shapes for the two types of events is such that the γ/hadron separation is not very efficient, with respect to the case of higher energy.

---

[6] The request for the γ-ray sample are: to have been genereated for the actual telescope configuration, to have the correct optical PSF of the observations, to have been simulated with the same observation mode, calibrated and cleaned with same procedure of the data analyzed.

[7] The hadronic sample should have the same obsevational conditions (zenith angle, weather conditions, trigger rates and telescope perfomance) of the analyzed data and a small contamination from real γ-ray events

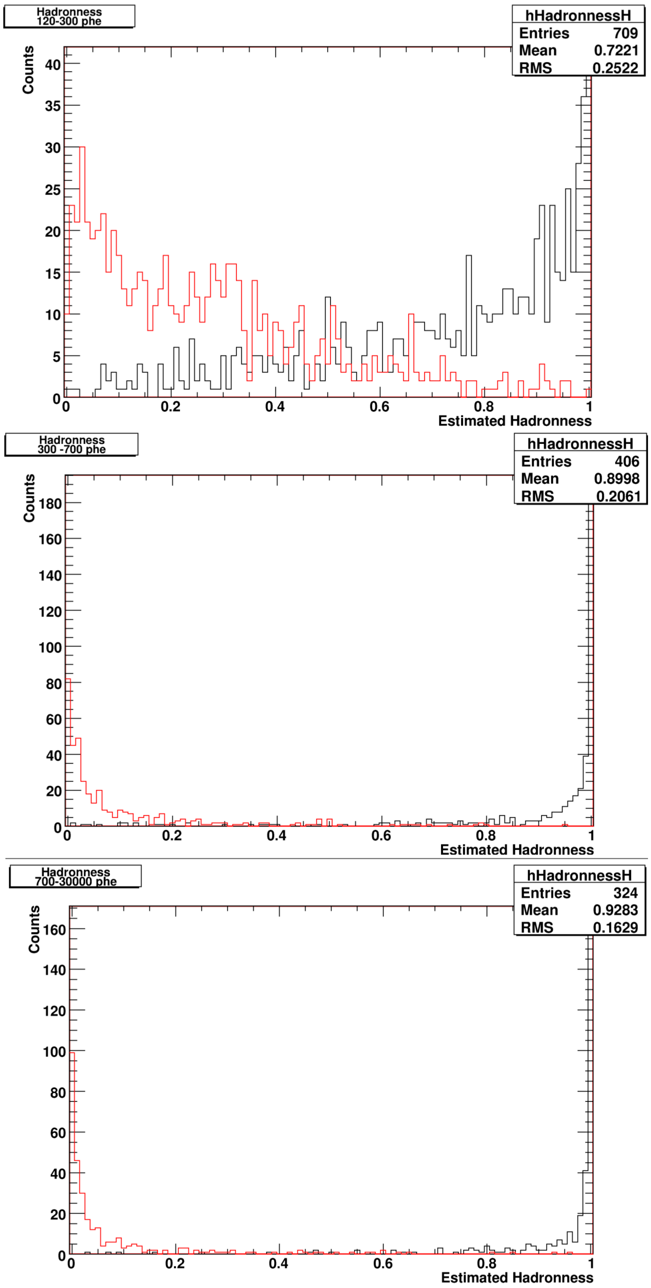

Figure 6.15: Hadronness distribution measured with the RF algorithm in different size bins. The red curve is the distribution of the MC simulated γ-ray sample while the black one is for real hadron-like dataset.

RF method for the DISP

Unlike the case of mono observations where the classical Width over Length parametrization is used, for stereo mode observations a new more performing procedure based on the RF algorithm (called RF DISP method) has been recently introduced in the MAGIC analysis software for the calculation of the Disp parameter. It allows to train the RF algorithm to select the data correctly into given bins of the true distance of the shower center from the source position in the camera using simulated γ-ray data. The improvement in the reconstruction of the arrival direction, and consequently in the angular resolution (about of 25% at 300 GeV and 45% at 1 TeV (Saito and Sitarek, 2009), and sensitivity is achieved thanks to using, beside the standard Hillas parameters, of the Time Gradient parameter that is correlated with the impact parameter of the shower.

RF method for the energy estimation

Even if the RF method is created for discrete classification, it can be extended to the estimation of continuous quantity (Albert+2008c) as for the energy reconstruction of the shower image that permits to convert the number of collected photo-electrons into energy units. As input file a sample of MC simulation files is used for the RF training and the energy matrices, containing the parameter *Estimated Energy*, are created.

With the advent of the MAGIC stereo system this procedure is not used anymore and the reconstruction of the energy is performed using the *energy Lookup Tables* (LUTs) created with the macro `create_Energy_table.C`

After the creation of the multidimensional matrices with the classification method, in the *test* phase the program `melibea` applies these matrices on the real data sample and on another indipendent sample of MC γ-ray events in order to assign the reconstructed energy and the hadronness values to each event. This latter MC sample is mainly used to test the classification performance.

Finally the γ/hadron separation is done applying a hadronness cut to the real data sample producing a final data set which contain real γ-ray signal and the survived hadron event that the RF algorithm recognized as γ-like events.

6.2.7 The energy Reconstruction

As said in the previous paragraph, the energy reconstruction is performed with a simple macro that, using the MC γ-ray simulated events and their three-dimensional shower parameters, generates the LUTs. The idea is that since the most of the Cherenkov light produced by a γ-ray is contained in a light pool or radius, the mean photon density in the light pool from a single charged particle of the γ-ray shower can be calculated from the total power of emitted light by such particle at a given height in the atmosphere. Thus using a simple atmospheric model the amount of light produced by a single particle can be computed for a given zenith angle and `MaxHeight`.

This way is simpler than the RF method and provides a better energy reconstruction, especially at low energies, in terms of energy resolution and energy threshold. This former quantity is a measure for the evaluation of the energy reconstruction and is determined as the standard deviation of a Gaussian fit tothe relative difference between the estimated energy and the true energy:

$$\frac{\Delta E}{E} = \frac{(E_{est} - E_{true})}{E_{true}} \tag{6.22}$$

The energy resolution for MAGIC is $\sim$XXX% (perfPaper+) above 100 GeV and it is shown that in general for the IACT telescopes, the reconstructed energy is overestimated at lower energies and viceversa understimated at higher energies.

The energy threshold E_{th} of the analysis is another parameter for evaluating the goodness of the observations and the analysis chain. It is defined as the maximum in the reconstructed energy distribution of the MC simulation sample, used as test, after applying of a given set of image parameter and hadronness cuts (an example of this distribution are in Fig 7.5). The E_{th} value obtained does not mean that the telescope cannot detect events below, but only that the effective collecting area is considerably reduced.

6.2.8 The signal search

After the hadronic background suppression, the next step is the search for the γ-ray signal though two different techniques, related to the different image parameter used, and denoted as `alpha` and θ^2 plot. Both methods are based on the comparison of the `alpha` or θ^2 parameter distribution for a given studied real dataset and for a background events dataset, respectively called *On* and *Off* sample[8]. This latter can be a data sample taken through dedicated observations of a sky region without γ-ray sources (if the telescope operates in ON-OFF mode) or extracted from the analysed dataset itself in case of wobble observations. Since the γ-like events are expected to be reconstructed close to the source position in the camera and hence to show a peak in the distribution at small values of `alpha` or θ^2, while the *Off* distribution is quite flat, the VHE signal can be evaluated counting within a established signal region the number of excess N_{excess} defined simply as:

$$N_{excess} = N_{On} - N_{bkg} \tag{6.23}$$

where N_{On} is the events number, within the signal region, associated to the studied γ-ray emitter and N_{bkg} the events from the background sky region.

In general the θ^2 tecnique is mainly used for stereoscopic observations and also in the standard MAGIC analysis is implemented. In the MAGIC analysis three different set of image parameter and signal region cuts are used to sample different energy ranges. They have been optimized on simulated γ-ray shower requesting that a given fraction of them are not discarded or to maximize the signal significance of some well-known bright VHE sources (as the Crab Nebula) in the analysis.

- *Low Energy (LE)* option:
- *Full Range (FR)* option:
- *High Energy (HE)* option:

The last step of the signal extraction is to estimate the statistical significance S of the found excess as real photon contribution from the γ-ray emitter and to reject the hypothesis of simple fluctuation in the background measurement. The significance is strictly related to the statistics that descrive the events themselves. If the source is observed for a time t_{on} and t_{off} is the pff-source (background) observation time, it is possible write $N_{excess} = N_{On} - N_{bkg} = N_{On} - \alpha N_{off}$ where $\alpha = (t_{on}/t_{off})$ and $N_{bkg} = \alpha N_{off}$ indicates the number of background events detected during the ON-source observation. Assuming a Poissonian statistics, the

---

[8] *Off* sample is choosen and subjected to the same analysis chain, in order to evaluate the number of γ-like hadronic events survived to the γ/hadron separation.

standard deviation of the event distribution is $\sigma^2(N_{excess}) = \sigma^2(N_{on}) + \sigma^2(\alpha N_{bkg}) = \sigma^2(N_{on}) + \alpha^2\sigma^2(N_{off})$, which provide the simple formula for the signal significance:

$$S = \frac{N_{excess}}{\sigma N_{excess}} = \frac{N_{on} - \alpha N_{off}}{\sqrt{N_{on} - \alpha^2 N_{off}}} \tag{6.24}$$

An more accurate formula tested by Li&Ma+1983 is usally used in the MAGIC collaboration and in the other IACT experiments:

$$S = \sqrt{2}\big[N_{on} \ln\big(\frac{1+k}{k} \cdot \frac{N_{on}}{N_{on} + N_{off}}\big) + N_{off} \cdot \ln\big((1+k) \cdot \frac{N_{off}}{N_{on} + N_{off}}\big)\big]^{1/2} \tag{6.25}$$

In the γ-astronomy a source is considered detected if the signal has a detection significance above 5σ or a probability that the excess events are compatible with a background fluctuation less than 0.00001%.

6.2.9 Instrument sensitivity

To evaluate the capability of a IACT system to detect weak γ-ray sources the *sensibility* is used which is defined as the minimum integral flux above a given threshold that can be detected at the 5σ level in 50 hrs of obervation. It can be expressed in units of the Crab Nebula flux (C.U.) above the same threshold.

The sensitivity can be written as:

$$Sensitivity(t) = \frac{N_{excess}}{\sqrt{N_{bkg}}}\sqrt{\frac{T}{t}} \tag{6.26}$$

where T is the normalization time of 50 hrs and t the observed time.

In Fig6.16 the MAGIC stereo integral and differential sensitivity for a Crab-like spectrum (with slope Γ=2.6).

6.2.10 The spectrum calculation

The last step of the data analysis is to compute the VHE differential and integral spectrum in order to characterize the VHE γ-ray emission of the studied object. In the MAGIC analysis chain this aim is performed by dedicated executables of MARS calles `fluxlc` and `flute` (this latter is more recent and from 2013 used as official program in the MAGIC collaboration).

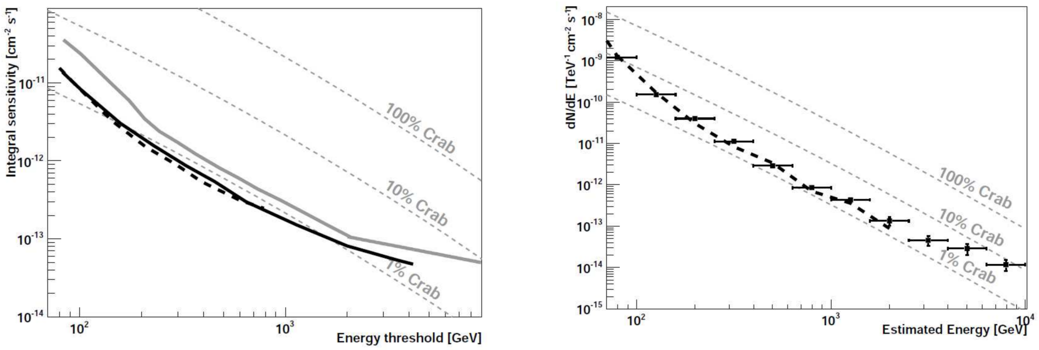

Figure 6.16: *Left*: *Right*: .

The differential spectrum is defined as:

$$\frac{dF}{dE}(E) = \frac{dN_{\gamma}}{dE dA_{eff} dt_{eff}} [ph cm^{-2} s^{-1} TeV^{-1}] \tag{6.27}$$

where in the second member:

- N_{γ} is the number of excess event evaluated from the `alpha` or θ^2 distribution in a finite reconstructed energy bin and applying bin optimized cuts in `hadronness` and `alpha` or θ^2, manually choosen by the analyzer.

- A_{eff} is the instrument effective collection area that rapresent the geometrical area around the IACT system within a γ-ray could produce a trigger and hence the area in which a air shower can be observed. It is wider than the telescope reflecting surface and depends on the primary γ-ray energy, the weather conditions and the zenith angle of observations. The effective area in each zenith angle and energy bin is computed from MC simulations comparing the simulated MC event number with the number of γ-ray events survived to all analysis cuts:

  $$A_{eff}(E, ZA) = A_{geo} \frac{N_{\gamma,surv}}{N_{\gamma,sim}} m^2 \tag{6.28}$$

  with A_{geo} the instrumental geometrical area.

- t_{eff} is the effective time of the observations. It is related to the total observation time T and corrected for all effects that alter the performance of the telescope with respect to an ideal detector (i.e. the dead times).

As said before, the differential spectrum is calculated in reconstructed energy bins which number and maximum size may differ from the different sources in according to the energy resolution, the source intensity of the γ-ray emitter and usually requiring a significance of the excess event in each bin of 1.5σ. The calculation in bins of true energy (that may differ from the reconstructed energy) is performed by the *unfolding* procedure. This procedure corrects the effects introduced on the spectrum determination by the finite energy resolution of the detector mostly at the edge of the observable energy band, and it is performed in the MARS software, through the executable `CombUnfold.C`, following various methods proposed by Bertero+1988, Tikhonov+1979 and Schmelling+1994. In the MAGIC collaboration, the unfolding results are accepted only if the results from different method are consistent.

In order to study the variability in the VHE emission for a given γ-ray source, the integral flux and the lightcurve are investigated. The lightcurve is simply the determination of integral flux above a given energy (usually above the energy threshold of the analysis chain) as a function of the time:

$$F(E > E_{th}, t) = \int_{E>E_{th}}^{\inf} \frac{dN_{\gamma}(t)}{dE dA_{eff}(t) dt_{eff}(t)} dE \tag{6.29}$$

In practice the lightcurve is performed inside time bins of width Δt around the time t, and the timing binning is choosen in according to the number of observation night, to have reasonably detection significance and small error bars on the integral fluxes.

In case there is not the adequate number of excess events to find VHE signal (with negative or zero significance), the *Upper limits* on the differential or integral source flux can be estimated. The calculation is based on the excess event number observed, on the background counts, on the collection area of the IACT system and finally on a theoretical hypothesis of the spectral shape of the studied source, following the Rolke method (Rolke+2005) and discussed in detail in Albert+2007e.

7

Study of Fermi sources with the MAGIC telescopes and MWL observations

7.1 The HBL *blazar* PG 1553+113

7.1.1 The PG 1553+113 overview

PG 1553+113 is a BL Lacertae object discovered and classified through an optical survey (Green+1986). It is located at (RA,DEC)=(15 55 43.04, 11 11 24.4) in the constellation of Serpens Caput of the Norther hemisphere. As its featureless spectrum its distance remains unknown but several works (Aharonian+2006, Mazin+2007, Prandini+2010) suggest upper limit of z <0.7. Based on the Lyα forest method, the most recent estimate is z ~0.40 by Danforth+2010.

Like all BL Lacs, PG 1553+113 shows the typical double-peaked shape SED (in νFν representation) parameterised with four characteristic slopes spanning from the radio to the VHE regime. At the radio frequencies between 4.8 and 14.5 GHz the source shows a mean flux variable on timescales of months (Perlman+2005, Osterman+2006) and the VLBA observations revealed a resolved jet of at least 20 pc (Rector+2003). Regarding the optical range, PG 1553+113 is a bright source in V-band and it is continually monitored in optical R-band on nightly basis by the Tuorla Observatory Blazar Monitoring Program [1]. It shows a modest varibility within a factor of 4 (Aleksic+2012). Also in the X-ray energies, the source is

---

[1] http://users.utu.fi/kani/1m/

bright and has been observed by many X-ray observatories as *Einstein*, *ROSAT*, *BeppoSAX*, *XRTE*, *XMM-Newton*, *Suzaku* and *Swift*. From 2005 to 2009 its X-ray lightcurve exhibits a pronounced variability (Aleksic+2012) but no evidence of spectral hardening or changes in the measured spectral proprieties was found. This indicates that the X-ray component of its MWL SED is due to synchrotron emission and confirms the hypothesis of a synchrotron peak located between the UV and X-ray bands (Fig 7.1). Moreover the position of the synchrotron peak and the high value of the ratio of its radio flux to its X-ray flux classify PG 1553+113 as one high peaked BL Lac.

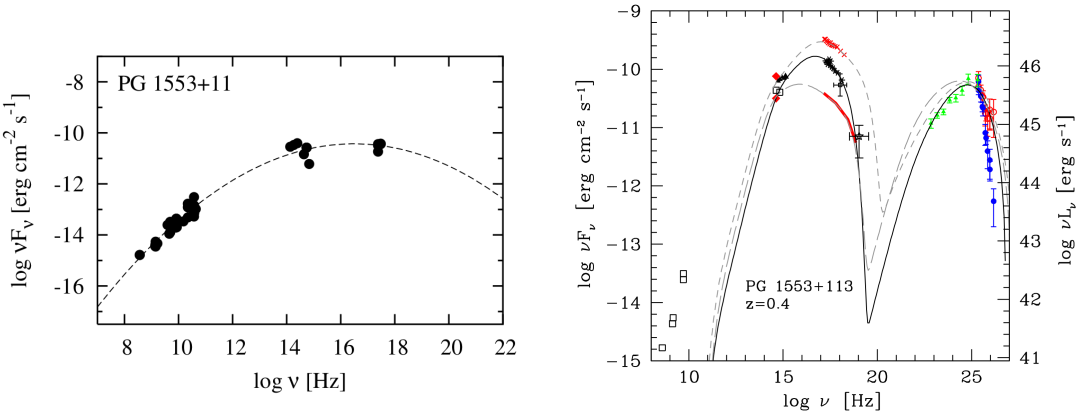

Figure 7.1: *Left*: Spectral Energy Distribution of PG 1553+113 from Nieppola+2006. Through a parabolic fit, the synchrotron peak is located at 0.4 keV. *Right*: MWL SEDs of PG 1553+113 taken from (Aleksic+2012). The average SED is modeled with a one-zone SSC model .

Nevertheless it was not detected by the *EGRET* satellite in the HE gamma-ray regime, PG 1553+113 was observed by *Fermi* and inserted in the *Fermi* LAT bright AGN source list and cataloged in the second Fermi catalog as 2FGL J1555.7+1111 with a detection significance of 69σ. In the *Fermi* collaboration paper (Abdo+2010), dedicated to the first year of PG 1553+113 observations, it is presented that, during the monitoring period, the source shows a stable behavior with a steady HE spectrum in normalization, slope and integral flux above 200 MeV. This seems in contrast with what was found in Aleksic+2012 where the HE lightcurve above 1 GeV shows a modest variability, but probably this discrepancy is apparent and due to the different choice of the energy threshold that permits to sample different part of the IC bump.

In 2005 PG 1553+113 was observed by H.E.S.S. (Aharonian+2006) and confirmed by MAGIC (Albert+2007) as VHE emitter with a flux level of 10.0±0.2×10^{-11} cm^{-2} s^{-1} above

120 GeV. Ever since the source was constantly monitored by MAGIC and the results of the first five observational years are summarized in Aleksic+2012. A quite moderate yearly variability for E>150 GeV, from 4% to 11% C.U. was found, with a maximum flux level in 2009 of 3.70×10^{-11} ph cm^{-2} s^{-1}. Every year the differential spectrum estimated was well fitted by a power law with a very soft spectral index spanning from 3.6 to 4.3, constant within the errors. This stability in the HE and VHE regime was in strong contrast with the typical behavior observed in the other TeV BL Lacs, indicating PG 1553+113 as an extragalactic TeV standard candle.

The situation changed when, during the MAGIC monitoring program, in early 2012 the source was found in an high state (compatible with the flux level of the previous high states detected in 2008) and, in April of the same year, it exhibited its first and unique VHE flare. The PG 1553+113 flux above 150 GeV doubled with respect to the pre-flare period (Atel2012) and the differential spectrum was measured from 70 to 620 GeV, allowing for the first time a more detailed study of the EBL effects (Aleksic+2014inprep) on a distant blazar. Moreover, triggered by the MAGIC observations, a wide multi-wavelength campaign was carried out (Gamma2012, Aleksic+2014inprep). A clear variability (Fig 7.2-*left*) was also found in the X-ray bands with a mean flux of $(1.17\pm0.06)\times10^{-11}$ erg cm^{-2} s^{-1} during the pre-flare high state period and $(4.20\pm0.14)\times10^{-11}$ erg cm^{-2} s^{-1} during the flare episode. While at the lower IR and optical frequencies a similar evolution was seen, no variability was detected in the HE regime exhibiting a constant flux in the course of time.

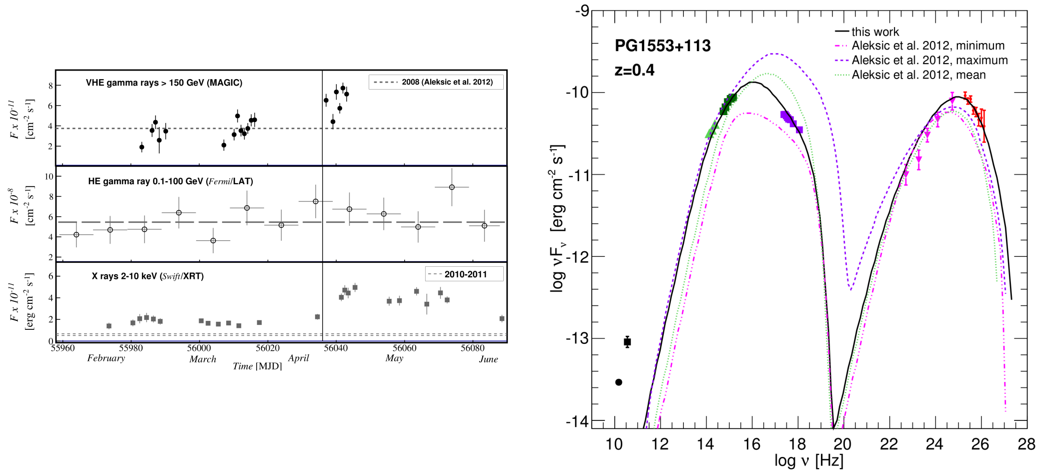

Figure 7.2: *Left*: *Right*: .

This fact is reflected on the broadband SED behavior described with the one-zone SSC model (Maraschi+1993). In Fig 7.2-*right* the best fits for the previous and the flare states are displayed and the highest amplitude flux changes are indeed found at the VHE and X-ray energies.

PG 1553+113 was again observed by MAGIC in 2013, one year after the flare event, in the framework of a new and wide multiwavelength campaign and the results are presented in this Section. Firstly we explain the motivation and the data taking strategy for these observations. Then the MAGIC analysis is described and the VHE differential spectrum and the lightcurve displayed. The last part of the section is dedicated to the instruments involved in the 2013 observational campaign and to the MWL results.

7.1.2 Observational strategy and motivation

The main scientific goal of the 2013 multiwavelength campaign for PG 1553+113, planned accordingly to the MAGIC observations, is the study of the overall SED with unprecedent precision thanks to the upgraded MAGIC system and the continuous monitoring of the state of its activity in the different part of the electromagnetic spectrum.

The γ-ray telescopes (the ground-based TeV MAGIC telescope and the *Fermi* satellite) worked in conjunction with the X-ray and UV space observatories and with the telescopes included in the Whole Earth Blazar Consortium (WEBT), a network of instruments located at different longitudes all around the world that provides continuous optical, NIR and radio observations and permits to obtain high-temporal-density, high-precision and uninterrupted optical light curve during all the campaign period.

In this way using the full power of both upgraded MAGIC telescope combined with Fermi observations it is possible to resolve the high energy bump and subsequently, coupling the γ-ray part of the SED with the simultaneous observations of the synchrotron bump, it allows us to have a more precise estimate of the blazar model parameters and to understand their role in the model.

Last but not least, being a distant extragalactic source (with uncertain redshift, but with strong evidence for high values of the redshift), observations of PG 1553+113 offer the possibility of EBL studies and thanks to the long monitoring to study the same effect in a different activity state.

As said before, the MWL campaign was planned according to the MAGIC observations. The latter were carried out from April to June 2013 and, every month, four data taking nights were scheduled. Simultaneously one *Swift*/XRT/UVOT pointing of about 1200 sec was coupled to the first and the last MAGIC observation of each month. Since the *Fermi* satellite performs an all-sky survey every 3 hours, the HE data were available for the entire campaign and instead, regarding the lower frequencies, the WEBT instruments began to take data from April 2013 continuing over the MAGIC time coverage[2].

The observations carried out during the 2013 campaign were the first ones after the unique VHE flare of PG 1553+113 in April 2012 and permits to estimate the flux level and to understand how the source changed after the flare episode, and to provide a long-term monitoring started ten years after the discovery of this source at the VHE energies.

7.1.3 Dataset and Quality Check

MAGIC observations of PG 1553+113 are carried out in April, May and June 2013 for a total of nearly 14 hours. The data are collected in wobble mode (with duration of 15 minutes), during the dark time and at low zenith angles (ZA<35°) in order to reach the lowest possible energy threshold and to achieve a good match with the Fermi energy band. This aim was also favoured thanks to the new setup of the MAGIC telescopes after the series of upgrades involving the M1 camera and trigger system and the readout system of both telescopes (Performance+2014 inprep). PG 1553+113 was scheduled for a time slot of one hour every night (hence four wobble positions were observed at each pointing), and the data are not effected by serious problems, except for a bug in the AMC system of M2. This could cause a worsening of the PSF but dedicated studies shown no abnormality in the M2 PSF.

A day-by-day quality check based on the hardware problems, bad atmospheric conditions and event rates is applied to select a good quality sample, removing the runs affected by rate spikes (probably due to car flashes on the cameras) and with very low rates. Finally, about 12 hours of good quality data survived and in Table 7.1 we show the whole dataset with the main information for each night.

The event rate distributions for the M1 and M2 selected data after the quality check and the zenith angle distribution, spanning from 17° to $\sim 35°$ (only M1, but the same for M2)

---

[2] For completeness, data collected from instruments involved in the WEBT program taken before April 2013 and after the MAGIC observational period are available

Date	MJD	Obs. Time [min]	Zd [°]	Note
08/04/2013	56390	78	17-21	-
09/04/2013	56391	55	17-20	-
10/04/2013	56392	77	17-19	-
11/04/2013	56393	38	22-30	-
08/05/2013	56420	77	17-25	High clouds, Rate a little bit unstable
09/05/2013	56421	76	17-25	High clouds, Rate a little bit unstable.
10/05/2013	56422	75	17-23	Clouds, Very low rate, Data rejected
11/05/2013	56423	79	17-24	Clouds at the beginning of the night
09/06/2013	56452	80	17-22	M2 AMC bug
10/06/2013	56453	78	17-22	.
11/06/2013	56454	57	17-19	M2 AMC bug
12/06/2013	56455	157	17-32	M2 AMC bug

Table 7.1: PG 1553+113 MAGIC dataset of the 2013 observations. From left to right: Date of the nights observations (first column), time of observation in minutes before the quality check (second column), zenith angle range in degree (third column). In the last column indicates if particular conditions or problems occurred during the night.

are shown in Fig 7.3 and Fig 7.4 respectively.

7.1.4 The signal detection

In order to extract γ-ray signal from the PG 1553+113 data sample, dedicated RFs has been produced to perform the γ/hadron separation (for details see Section XX). A specific sample of MC simulations has been chosen to simulate the new performances of the telescopes, after the upgrades of 2011 and 2012, the wobble observation mode and to cover the whole zenith angle range spanned by the real dataset. As *Off training* data sample, we select about 3 hours of real data of very weak sources in the VHE band, hence dominated by hadron-like events. The *Off* data were taken in the same period of the PG 1553+113 observations to have similar hardware condition of the detector.

Through the standard MAGIC analysis, the signal extraction is based on the analysis of the distribution of the squared angular distance θ^2 related to the incoming direction of the primary cosmic ray. Since the data are taken in wobble mode, the background is evaluated from the data themselves and, since for all four wobble positions we have equal time coverage, we can use 3 off wobble positions for the background estimation.

In our analysis we decide to use two different cuts set of the data parameters to sample different energy ranges referred to as *Low Energy (LE)* and *Full Range (FR)* regime[3] and the same cuts have been applied on the simulated MC data to estimate the energy threshold of

---

[3] For details see Section XXX.

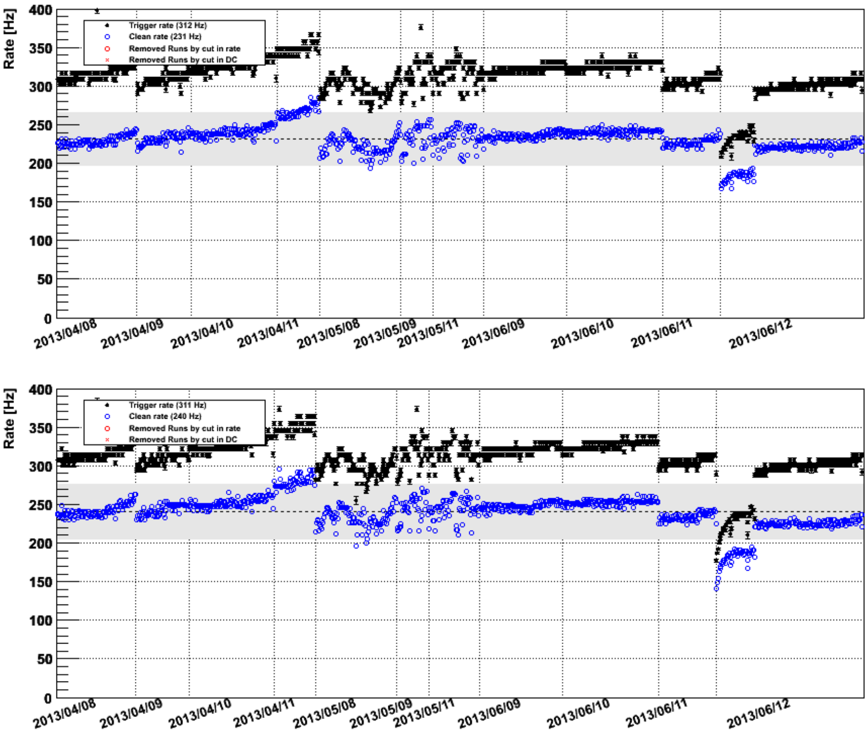

Figure 7.3: PG 1553 event rate distribution for M1 (*upper panel*) and M2 (*lower panel*) of the selected 2013 MAGIC data after the daily quality check.

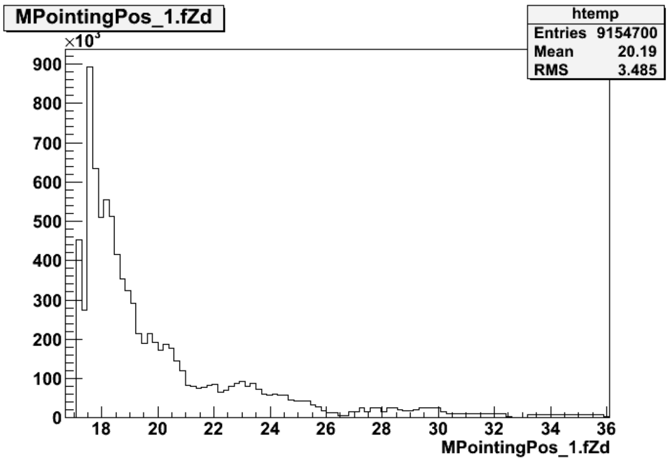

Figure 7.4: PG 1553+113 zenith angle distribution

the analysis chain which depends strongly on the Size and Hadronness cuts, finding E_{th} ~96 GeV and E_{th} ~163 GeV for the LE and FR option respectively (Fig 7.5).

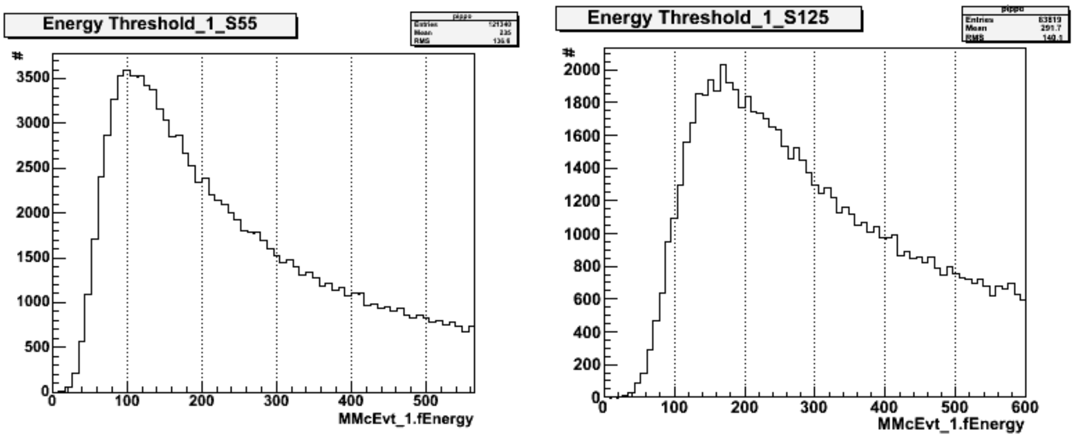

Figure 7.5: Energy thresholds of PG 1553+113 estimated from dedicated MC data applying *Low energy* (left) and *Full range* (right) setting cuts for the 2013 analysis.

In Fig 7.6 the θ^2-plots for PG 1553+113 resulting from our analysis. We can see that also in 2013 the source is well detected exhibiting, in 12.31 hours of effective observational time, a signal significance of 37.75σ in LE regime and 13.25σ in FR. The results and the statistics of the signal search for the two energy range are summarized in Tab 7.2.

Cut setting	Eff.Time [hr]	N_{exc}	N_{bkg}	Significance σ
LE	12.31	2025	2120	32.75
FR	12.31	193	91	13.25

Table 7.2: PG 1553+113 signal study for the 2013 MAGIC observations. From left to right: Period of observation considered (first column), effective time of observation in hours (second column), number of excess events and background events detected (third and fourth column) and the significance of detection (last column).

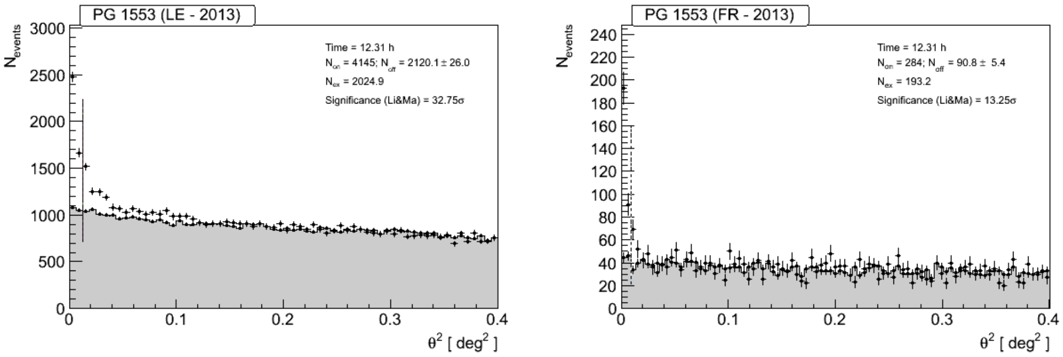

Figure 7.6: PG 1553+113 θ^2 plots from the 2013 data analysis obtained for LE *letf* and FR *right* cut setting and 3 Off wobble positions for the background estimation.

7.1.5 Differential Spectrum

In this Section we present the study of the VHE differential spectrum of PG 1553+113 from 2013 MAGIC data. To determine the differential spectrum , we study the emission in intervals of reconstructed energy and for every energy bin we perform a signal search through the θ^2 technique to estimate the event excess number. Dynamical cuts on the hadronness and the θ^2 parameters were applied, based on the cut efficiency in such way that a certain percentage of the simulated γ-ray MC events survive. At the later stage, with the unfolding algorithm, we correct the analysis from the effects of the finite energy resolution and we deabsorbe the observed spectral points using an appropriate extragalactic background light model.

For PG 1553+113 dataset we use 45 energy bins spanning from 80 to 500 GeV, applying the following loose cuts:

`Size > 50 phe`

`Hadronness cut efficiency = 90%`

θ^2 `cut efficiency = 70%`

`minimal hadronness = 0.07`

`minimal` θ^2 `= 0.02 deg`^{2}

For each energy bin considered the cuts applied, the excess events, the significance and the observed differential spectrum, before the unfolding correction, are displayed in Table 7.3.

The unfolded observed spectrum performed with the Tikhonov model (Tiknonov&Arsenin+1977) is showing in Fig7.7 with the corresponding flux values in Table. It can be fitted with a quite steep power law function:

$$\frac{dF}{dE} = f_o(\frac{E}{200GeV})^{\Gamma} \tag{7.1}$$

with a photon index of 3.5± 0.08 and a normalization flux f_0=(2.25±0.12)×10^{-10} TeV^{-1}cm^{-2}s^{-1} at 200 GeV. In the same figure the EBL-corrected spectrum, using the Franceschini model (Franceschini+2008) for a redshift of 0.40 (as used by Aleksic+2014inprep).

7.1.6 The lightcurve and integral flux

In order to investigate the VHE variability of PG 1553+113, we estimate the integral flux above 150 GeV as function of time. During the monitoring between 2005 and 2009, the source

Mean Energy [GeV]	`hadronness` cut	θ^2 cut	N_{ex}	Significance σ	Flux ph cm^{-2} s^{-1} TeV^{-1}
73	0.47	0.06	669±78	8.7	$(5.7\pm0.7)\times10^{-9}$
90	0.37	0.05	709±60	12.3	$(3.3\pm0.3)\times 10^{-9}$
110	0.34	0.04	603±45	14.3	$(1.8\pm0.5)\times 10^{-9}$
135	0.35	0.03	416±34	13.5	$(8.9\pm0.8)\times10^{-10}$
166	0.36	0.03	407±29	16.0	$(6.0\pm0.5)\times10^{-10}$
203	0.35	0.02	247±21	13.6	$(3.0\pm0.3)\times10^{-10}$
250	0.34	0.02	138±17	9.0	$(1.1\pm0.1)\times 10^{-10}$
306	0.33	0.02	61±13	5.1	$(3.6\pm0.8)\times 10^{-11}$
375	0.31	0.02	43±10	4.5	$(1.8\pm0.5)\times10^{-11}$
461	0.29	0.01	19±7	3.1	$(6.4\pm2.3)\times10^{-12}$
566	0.26	0.01	18±6	3.7	$(4.6\pm1.5)\times10^{-12}$

Table 7.3: 2013 differential spectrum of PG 1553+113: Mean energy of the bin (first column), `hadronness` and θ^2 cuts (second and third column), number of excess events (four column), significance (five column) and mean photon flux before the unfolding (last column).

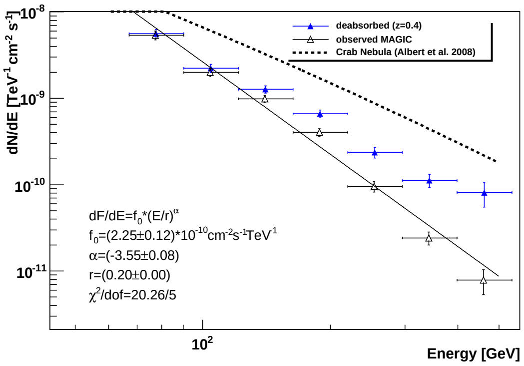

Mean Energy [GeV]	Flux_{obs} [cm^{-2} s^{-1} TeV^{-1}]	Flux_{deabs} [cm^{-2} s^{-1} TeV^{-1}]
77	$(5.4\pm0.6)\times10^{-9}$	$(5.6\pm0.6)\times10^{-9}$
104	$(2.0\pm0.2)\times10^{-9}$	$(2.2\pm0.2)\times10^{-9}$
140	$(9.9\pm0.9)\times10^{-10}$	$(1.3\pm0.1)\times10^{-9}$
189	$(4.0\pm0.4)\times10^{-10}$	$(6.6\pm0.7)\times10^{-10}$
254	$(9.5\pm1.3)\times10^{-11}$	$(2.4\pm0.3)\times10^{-10}$
342	$(2.4\pm0.4)\times10^{-11}$	$(1.1\pm0.2)\times10^{-10}$
461	$(7.9\pm2.5)\times10^{-12}$	$(8.1\pm2.6)\times10^{-11}$

Figure 7.7: Unfolded differential observed *(grey points)* and absorption-corrected *(blue points)* spectrum for PG1553+113 for 2013 MAGIC data.

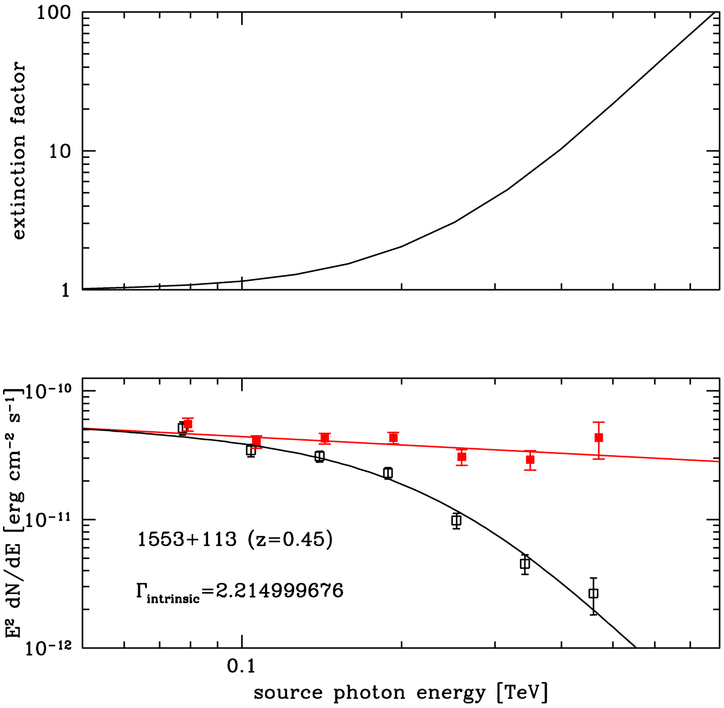

Figure 7.8: .

showed a modest variability on yearly timescale with variations within a factor of three and ranging from 4% to 11% of the Crab Nebula flux (Aleksic+2012) and in 2012 its first VHE flare was detected showing the highest flux in this energy band.

The 2013 campaign was also planned to investigate the flux level after one year from its flare when the source became again visible at the MAGIC latitude. The Fig 7.9 displays the lightcurve with a daily binning (red points) and monthly binning (blue points) and in Tab 7.4 we report the integral flux values resulting from the timing analysis.

7.1.7 Multiwavelength view of PG 1553+113 from the 2013 campaign

In 2013 PG 1553+113 was the object of an intensive multiwavelength campaign in order to sample the whole broad-band SED, after its unique flare in VHE band, and to investigate the evolution of the lightcurves from radio to the γ-ray frequencies.

The main goal of a multiwavelength campaigns is to achieve an extended coverage of the spectrum for a given source. In this way more informations can be extracted and a physical model can be developed to explain the data. In this sense it is crucial to have a temporal coincidence in the MWL observation and to collect the most possible simultaneous data. This

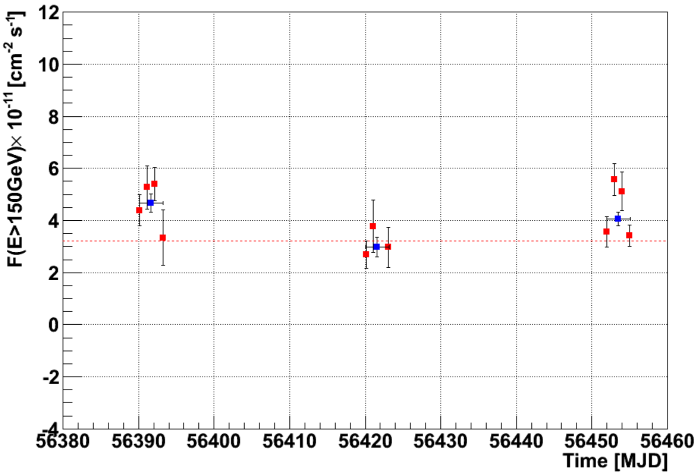

Figure 7.9: PG 1553+113 lightcurve

Night (MJD)	Eff. Time [sec]	F(>150 GeV) [10^{-11} ph cm^{-2} s^{-1}
56390	4255	4.4±0.6
56391	2832	5.3±0.8
56392	4373	5.4±0.7
56393	1941	3.3±1.0
56420	4555	2.7±0.5
56421	1612	3.8±1.0
56423	2590	3.0±0.8
56451	4322	3.6±0.6
56452	5001	5.6±0.6
56453	3081	5.1±0.7
56454	8172	3.4±0.4

Table 7.4: 2013 MAGIC lightcurve of PG 1553+113:

permits to avoid possible bias in the observed SED due to the pronounced flux variability that characterize the blazar activity. Indeed different flux levels of the source can cause spectral changes in the spectrum as an hardening/softening in the rising and falling parts of the SED or a shift of the peak frequencies.In addition correlations between the fluxes at different energy bands are studied and predicted through theoretical models, hence only simultaneous observations can be useful to test them.

In this section the MWL simultaneous data of PG 1555+113 collected by all instruments involved in the 2013 campaign, and with the collaboration of the WEBT consortium, are reported.

Fermi/LAT observations

Thanks to the all-sky survey mode operated by the *Fermi* satellite, HE data from 20 MeV up to 300 GeV are available for the entire period of the 2013 MWL campaign. The data were downloaded by the public database[4] and analyzed with the standard analysis Science Tool software available in the *Fermi* Science Support Center, including the Galactic diffuse and the isotropic component. As instrument response functions (IRF) the version `PXSOURCE_VX` was used. From the data we selected photons within a region of interest (ROI) of 10° of radius centered in the PG 1553+113 position and collected from the beginning of the *Fermi* data acquisition (4th August 2008) and for the lightcurve and covering the MWL campaign period for the SED. To minimize the background effect of the photons coming from the Earth-limb a zenith-angle cut (<100°) is applied. To derive the spectral flux in each time bin the unbinned (binned?) algorithm `gtlike` (Abdo+2009E.P.) was used including a model that takes account of the isotropic background (isop7v6source.txt), the Galactic diffuse background (gal2yearp7v6v0.fits) and the emissions of all sources, located within the ROI, parametrized by a power law spectrum. The resulted *Fermi* lightcurve and SED are displayed in Fig7.11-(*Second Panel*) and in Fig7.13 (*black points*) respectively.

X-ray and UVOT data from *Swift*/XRT/UVOT

For the MWL campaign of PG 1553+113, *Swift* observations were requested to sample the X-ray and UV-Optical band using the on-board instruments XRT detector (covering the 0.2 - 10 keV band) and the UVOT telescope (covering the 180 - 600 nm wavelength range with

---

[4] http://fermi.gsfc.nasa.gov

V, B, U, UVW1, UVM2, and UVW2 filters).

The XRT observations, in photon counting (PC) and windowed timing (mode, were maily performed during the MAGIC observational period with snapshots of about 1200 sec, for a total of 8.0 ksec. [The UVOT data were taken in *filter of the day* mode....].

The *Swift*/XRT data were processed using the FTOOLS task `xrtpipeline` (v0.13.01) distribuited within the HEASoft package of the HEASARC. Events with grades 012 were selected for the data and we used the response matrices of 2013 included in the Swift CALDB. The XRT signal was extracted within a region of 20 pixels (∼47 arcsec), while the background was estimated from a circular off-source region of 20 pixel radius. To take in account of the pile-up affect, only for observations with count rates higher than 0.6 cps,the signal was extracted excising part of the core of the source. For the spectral analysis we used the XSPEC software (v12.8.2). The spectra were extracted from the corresponding event files in the 0.3 - 10 KeV energy range and re-binned using GRPPHA to ensure a minimum of 20 counts per bin and to have a reliable χ^2 minimization fitting. We adopted a power law model absorbed for Galactic extinction with an hydrogen-equivalent column density of $n\mathrm{H}=2.6\times10^{20}$ cm^{-2} (Kaberla+2005).

Regarding to the UVOT data, the source counts were extracted from a XX arcsec-sized circular region centered on the source position, while the background was estimated from a nearby larger source-free region of radius of equal size. This data were processed with the program `uvotmaghist` of the HEASOFT package. In addition the observed magnitudes have been corrected for Galactic extinction (WEBT+inprep).

The results of the XRT and UVOT lightcurves are reported in the third and fourth panel of Fig 7.11. The SED data points are displayed in the Fig 7.13.

WEBT observations: optical, IR and Radio data

The optical, IR and radio data, described in this section, are provided by the WEBT campaign of PG 1553+113, triggered by the 2013 MWL campaign, in turn organized around the MAGIC observations. After the approval for the PG 1553+113 campaign and the call for the recruitment, the observatories listed in Tab7.5 took part in the MWL campaign, for a total of 19 optical, 2 IR and 3 radio telescopes involved.

All data were sent to the Campaign Manager Claudia M. Raiteri from Osservatorio As-

Observatory	Country	Bands
	Optical	
Abastumani	Georgia	R
Belogradchik	Bulgaria	$BVRI$
AstroCamp	Spain	R
Crimean	Ukraine	$BVRI$
Michael Adrian	Germany	$BVRI$
Mt. Maidanak	Uzbekistan	$BVRI$
New Mexico Skies	USA	R
Plana	Bulgaria	$BVRI$
Rozhen[1]	Bulgaria	$BVRI$
San Pedro Martir	Mexico	R
Siding Spring	Australia	R
Skinakas	Greece	$BVRI$
St. Petersburg	Russia	$BVRI$
Teide	Spain	R
Tijarafe	Spain	R
Valle d'Aosta	Italy	$BVRI$
Vidojevica	Serbia	$BVRI$
	Near-infrared	
Campo Imperatore	Italy	JHK
Teide	Spain	$JHKs$
	Radio	
Medicina	Italy	8 GHz
Metsähovi	Finland	37 GHz
Noto	Italy	43 GHz

[1] three telescopes

Table 7.5: The optical, near-IR, and radio observatories participating in the 2013 WEBT campaign of PG 1553+113.

trofisico di Torino (Italy). She was assigned to the data collection and of the data reduction and calibration using the reference stars displayed in the finding chart of Fig7.10 centered on PG 1553+113. The photometry of Stars 3 and 4 has been derived from the Sloan Digital Sky Survey, using *ugriz* to UBVRI transformations by Chonis+ Gaskell2008(AJ, 135, 264). For the calibration of Stars 1 and 2, their SDSS photometry cannot be used because of saturation and a dedicated calibration procedure was developed. Details are in WEBT+2014inprep.

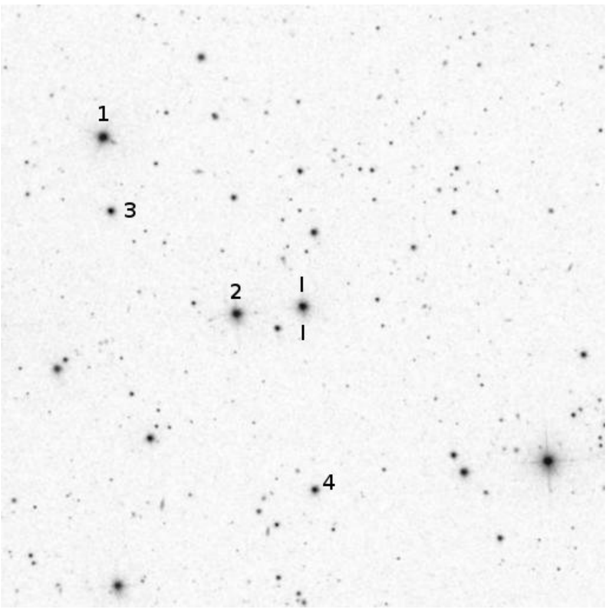

Figure 7.10:

The lightcurves and the SED points in optical (R-band), IR and radio regime are shown in Fig 7.11 and in Fig 7.13.

The MWL Lightcurve and SED modeling

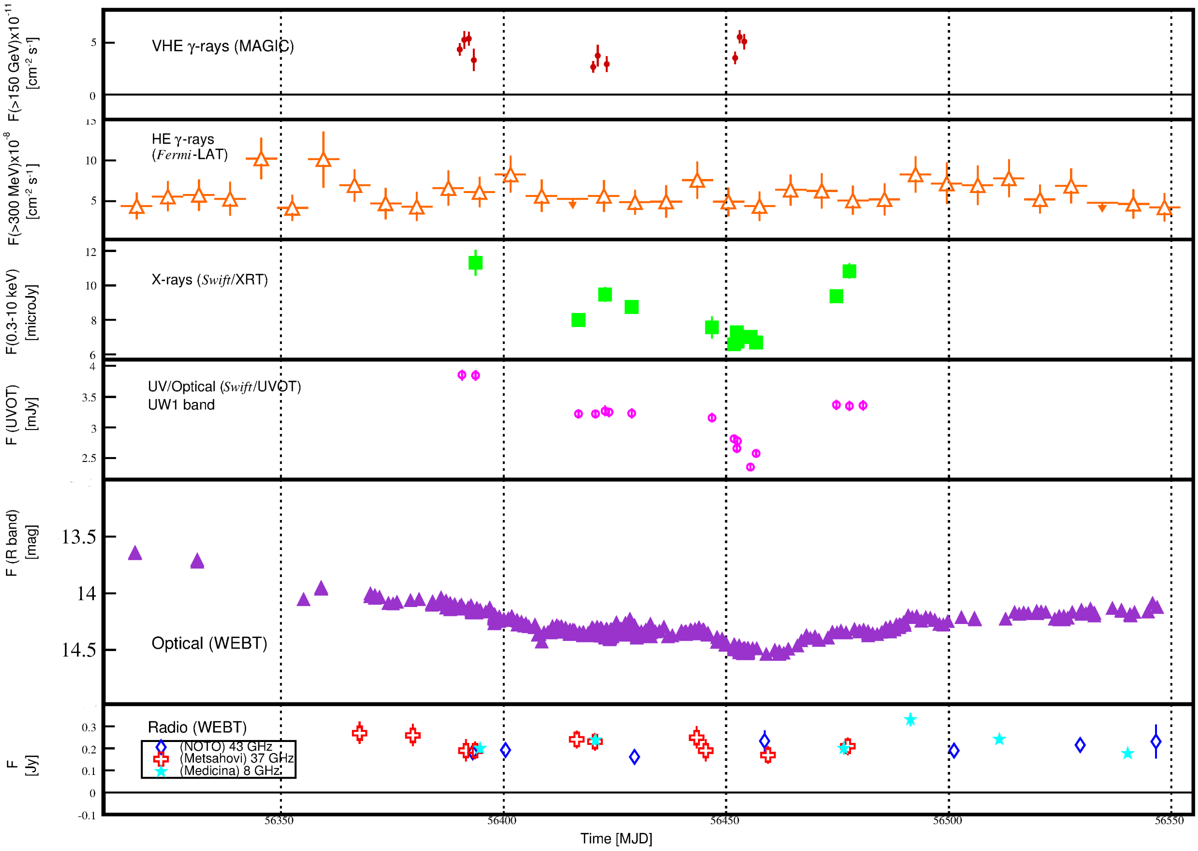

Figure 7.11: 2013 Multiwavelength lightvurve of PG 1553+113

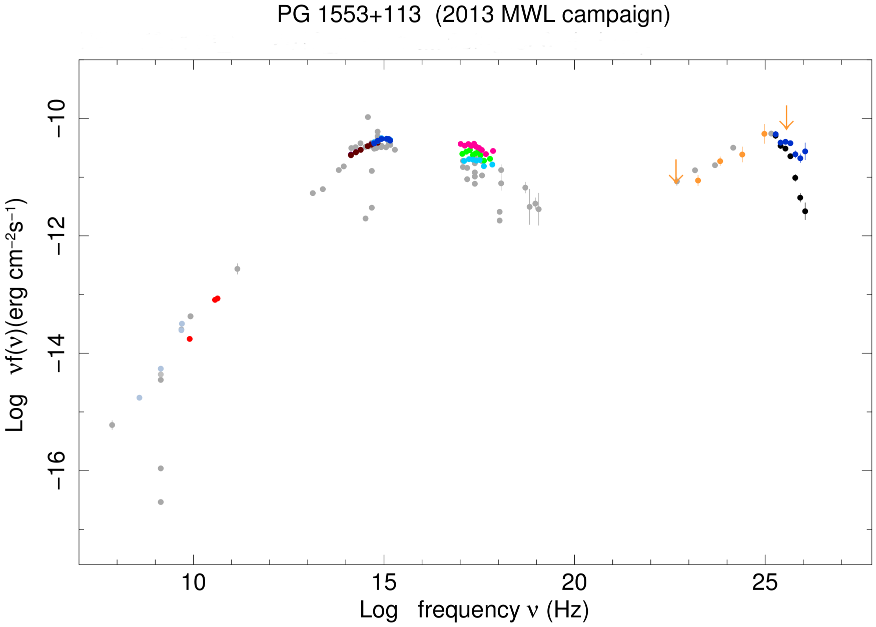

Figure 7.12: 2013 Multiwavelenght SED of PG 1553+113.

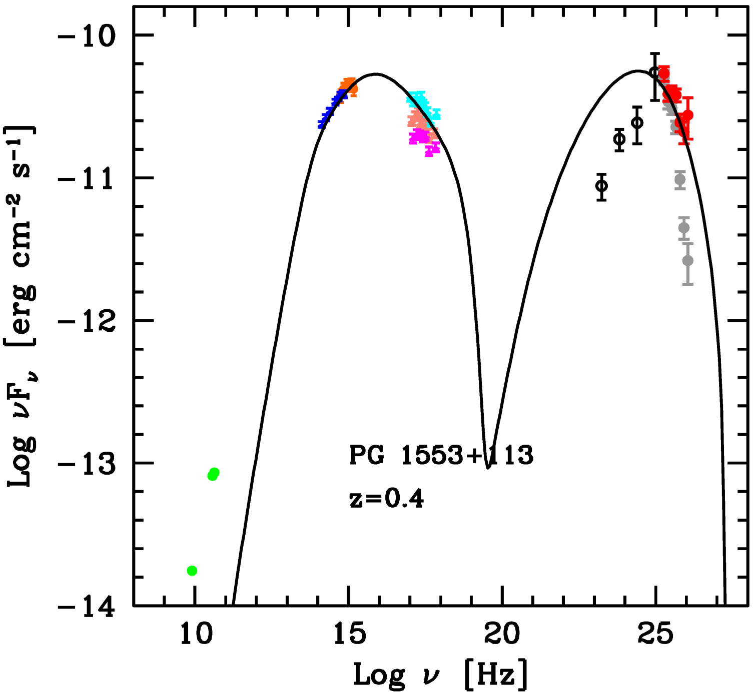

Figure 7.13: 2013 Multiwavelenght SED of PG 1553+113. The average SED is modeled with a one-zone SSC model (continuous black line).

7.2 The HBL *blazar* 1ES 1011+496

7.2.1 The 1ES 1011+496 overview

1ES 1011+496 is a high frequency peaked BL Lac (HBL) object located at (RA,DEC)=(10 15 04.14, 49 26 00.70) and with a relatively high redshift of z=0.212±0.002 inferred thanks to a follow-up optical spectroscopy, Fig 7.14, obtained with the Multi Mirror Telescope (Albert+2007).

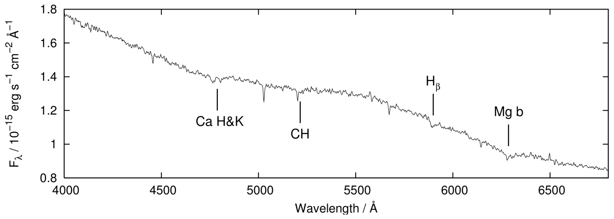

Figure 7.14: Optical spectrum of 1ES 1011+496 obtained with the Multi Mirror Telescope. Absorption lines of the host galaxy (Ca H&K, CH G, H_β and Mg b) are visible and indicate a redshift z=0.212±0.002 (Albert+2007).

From its discovery in the radio and X-ray bands (Hales+1990, McGilchrist+1990), 1ES 1011+496 was monitored by several instruments in different bands of the electromagnetic spectrum. In the radio regime, the source showed a moderate variability with a flux density varying between 0.38 Jy and 0.47 Jy at 1.4 GHz (Nakagawa+2005) and a value of 0.56±0.12 Jy at 37 GHz provided by the Metsähovi radio telescope (Nieppola+2007). The X-ray observations were carried out by the *Einstein* observatory (Elvis+1992), by the *ROSAT* satellite and, more recently, by the *Swift*/XRT telescope that is constantly monitoring the source since 2005[5]. Most of observations shows a steep spectrum, indicating the dominance of synchrotron emission in the X-ray regime, except during the 2008 *Swift*/XRT observations where the source was in a rather high flux state showing a flat spectrum. Moreover 1ES 1011+496 has shown a strong variability in the X-ray band of about a factor of 20 for the integral flux between 2 and 10 keV (low state: $F_{2-10keV}$=0.36×10^{-11} erg cm^{-2} s^{-1} [Massaro+2008], high state: $F_{2-10keV}$=6.67×10^{-11} erg cm^{-2} s^{-1} [Giommi+2012]).

Regarding the optical frequencies, since 2003 this object is regularly monitored in the R-band by the Tuorla Observatory Blazar Monitoring Program[6], showing a sensible and frequent variability that increases up to a factor of 2-3 during the flares respect to its lowest states (see Fig 7.15).

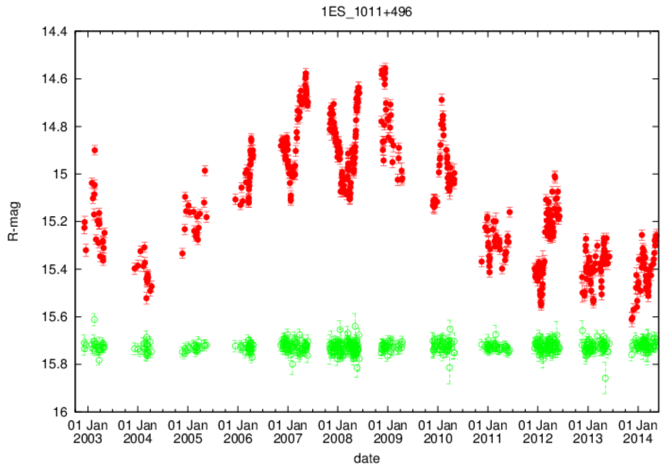

Figure 7.15: Optical R-band light curve of 1ES 1011+496 (red points) and of a control star (green points) performed by the Tuorla Observatory Blazar Monitoring Program taken from http://users.utu.fi/kani/1m/1ES_1011+496.html. The data presented are one-hour averages.

In the HE range (at MeV-GeV energies), it has been done a first attempt to associate 1ES 1011+496 with the EGRET source 3EG J1009+4855 (), but this association was not further confirmed (). 1ES 1011+496 was clearly detected by *Fermi*/LAT and included in all

---

[5] http://www.swift.psu.edu/monitoring/source.php?source=1ES1011+496

[6] http://users.utu.fi/kani/1m/

released Fermi-LAT catalogues. However only in the second (2FGL) one, where the source is called 2FGL J1015.1+4925, it is characterized as significantly variable. In the Table **??** the parameters that characterize the 1ES 1011+496 spectrum and the fluxes are listed for the different Fermi catalogues.

Catalogue	Spectrum Type	Spectral index	Flux density	Photon Flux$_{1-100GeV}$	Variability Index
0FGL	-	-	-	-	-
1FGL	Power Law	1.93±0.04	-	$(8.7\pm0.6)\times10^{-9}$	-
2FGL	LogParabola	1.72±0.04	1.01×10^{-11}	$(7.8\pm0.33)\times10^{-9}$	48.05

Table 7.6:

Moreover, due to its spectral features, 1ES 1011+496 was included in the Costamante and Ghisellini catalogue (Costamante+2002) of TeV candidate BL Lac object. In 2007, during a large optical outburst of the source, MAGIC detected it as a VHE emitter (Albert+2007a) with a 6.2σ detection in 18.7 hours of effective exposure time. The differential spectrum from ∼120 GeV to ∼750 GeV was modelled with a simple power law with a spectral index of -4±0.5 and an integrated flux above 200 GeV of $(1.58\pm0.32)\times10^{-11}$ photons cm^{-2} s^{-1}.

In order to constrain the whole broadband SED, 1ES 1011+496 has been target of three MWL campaigns guided by the MAGIC observations. The first one has been carried out in 2008 (Aleksic+2014inPrep?) where the source was variable in the X-ray and optical bands but stable at the flux level of the discovery in the VHE regime. The second and third campaigns have been done in 2011-2012. The results of two latter campaigns are presented in the next sections of this chapter.

Thanks to the observed hard Fermi spectrum and the ratio between the X-ray and radio fluxes, initially 1ES 1011-496 was classified as an HBL object. This is evident looking the low energy part of the SED taken from (Nieppola+2006) and shown in Fig 7.16 where the synchrotron peak is located at 5.5×10^{16} Hz (corresponding to 0.23 keV). However recent works (Bottcher+2010, Aleksic+2014inPrep?) suggest an IBL or an extreme-IBL classification when the source is in a low and medium state, due to the shift of the synchrotron peak (see Fig 7.17-*Left* and Fig 7.17-*Right*) towards lower frequencies and the deviation of the spectrum from a simple power law at the Fermi energies.

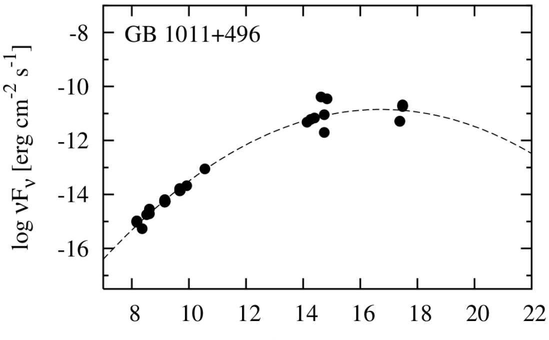

Figure 7.16: SED of 1ES 1011+496 from (Nieppola+2006): the synchotron peak estimated from a parabolic fit is at 0.23 keV (corresponding to 5.5×10^{16} Hz).

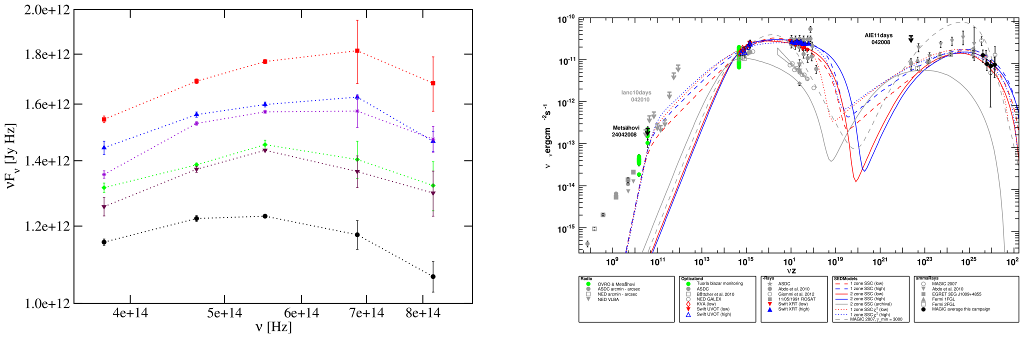

Figure 7.17: *Left*:UBVRI SEDs of 1ES 1011+496 taken from (Bottcher+2010): the νF$_\nu$ peak is located between the B and V band and a positive correlation seems to appear between νF$_\nu$ and the peak frequency. *Right*: MWL SEDs of 1ES 1011+496 taken from (Aleksic+2014).

7.2.2 Dataset and Quality Check

After the discovery of 1ES 1011+496 in 2007, MAGIC observed the source in Spring 2008 during a multiwavelength campaign showing a clear signal of 7σ of significance in $\sim$15 hours of good quality data. With the beginning of the operational phase of the Fermi satellite and of the MAGIC stereo system, the object was proposed as target for VHE MAGIC observations of the 2011 data taking cycle. Indeed only simultaneous MAGIC stereo and Fermi observations of the source can provide important constraints on the SED models parameters (especially about the estimate of the IC peak), thanks to the energy overlap in the peak region. Despite the good quality data collected, only a hint of detection was obtained and for this reason the observations of 1ES 1011+496 were re-proposed for the next cycle of 2012 in order to detect at least 5σ of significance.

The data sets of the two years of observations were analyzed separately because they were collected in two different periods characterized by changes in the hardware setting of the readout system for both telescopes. Also the 2012 dataset was divided in three sub-periods because the observations were performed during the commissioning phase and some hardware problems occurred.

Finally, it is important to note that both the MAGIC observational sets were taken in the framework of two MWL campaign centered around the MAGIC observations and involved the Fermi satellite for the HE band, the *Swift*/XRT/UVOT telescopes for the X-ray and UV frequencies, the KVA telescope for the optical R-band and the OVRO and Metsähovi telescopes in the radio regime.

2011

During the 2011 cycle, 1ES 1011+496 was observed for 11 nights from February to April for a total of 13 hours of data taken in wobble mode. After a severe daily quality check based on event rate of each telescopes, on the value of the DC in the cameras[7] (Britzger+2009) and where the run with rate spikes (probablu due to car flashes) or with very low rate (during the wobbling), about 10 hours of good quality data survived. In Fig 7.19 and Fig 7.18 the zenith angle distribution and the event rate distributions for each telescopes are shown. As summarized in Tab 7.7 the first two nights were affected by moderate moon and this caused a lowering of the rate for both telescopes.

---

[7] This cut reduces the effect of the moon light on the quality of data.

Date	MJD	Obs. Time [min]	Zd [°]	Note
24/02/2011	55616	143	27-40	Moon conditions
25/02/2011	55617	97	28-41	Moon conditions
28/02/2011	55620	90	27-40	-
01/03/2011	55621	39	24-41	-
02/03/2011	55622	61	31-40	-
03/03/2011	55623	64	30-37	-
27/03/2011	55647	62	30-39	-
28/03/2011	55648	68	30-41	-
30/03/2011	55650	46	33-41	-
03/04/2011	55654	61	31-40	-
09/04/2011	55660	60	30-39	-

Table 7.7: 1ES 1011+496 dataset of the 2011 observations. From left to right: Date of the nights observations (first column), observation time in minutes (second column) before the quality check, zenith angle range in degree (third column). In the last column indicates if particular conditions or problems occurred during the night.

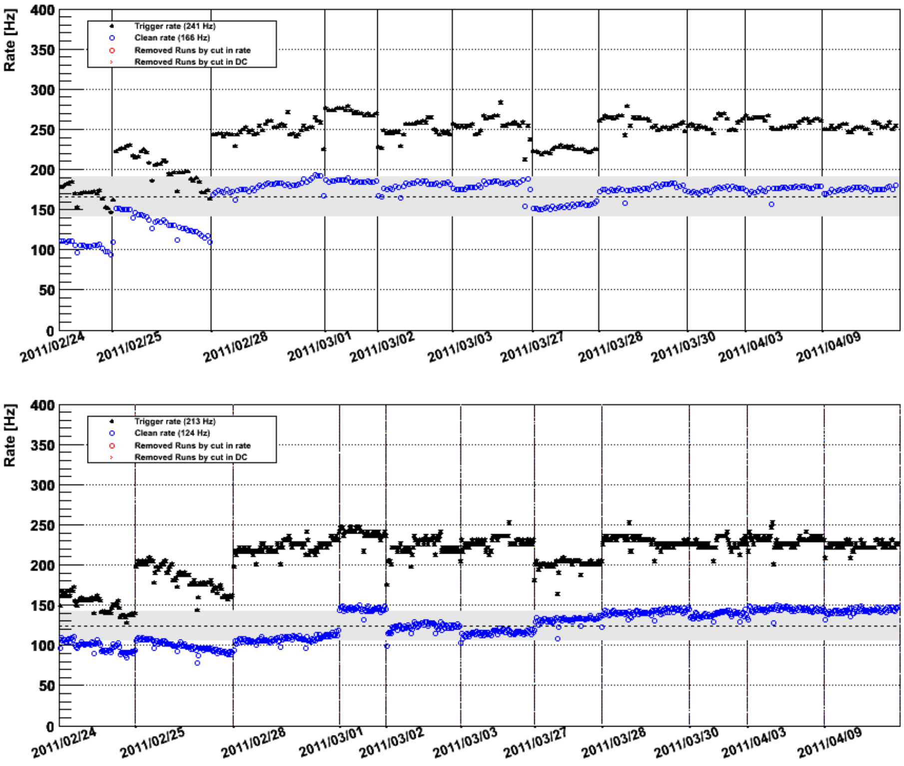

Figure 7.18: 1ES 1011+496 event rate distribution for M1 (*upper panel*) and M2 (*lower panel*) of the selected 2011 MAGIC data after the daily quality check.

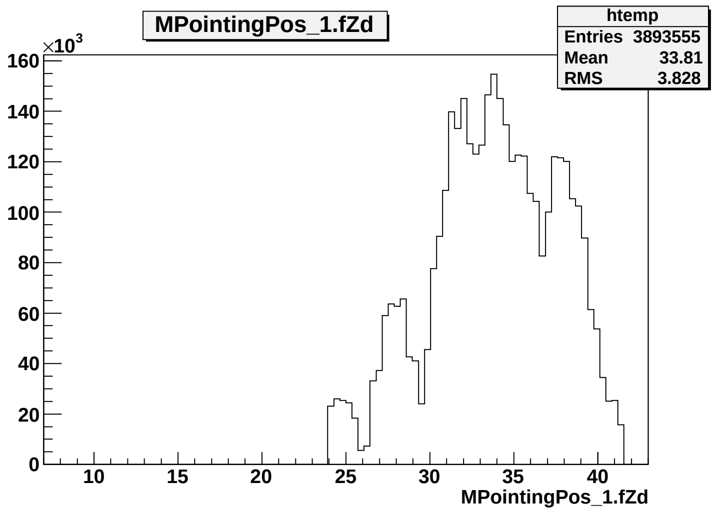

Figure 7.19: 1ES 1011+496 zenith angle distribution

2012

The 2012 MAGIC data of 1ES 1011+496 were collected from late January to mid May 2012 for a total of about 33 hours of observations for 33 nights. This observational cycle was affected by the commissioning of the MAGIC stereo system after the upgrade of the readout system[8] and moreover some hardware problems occurred: some pixels (part of the trigger area) in the M1 camera were dead due to several broken receiver boards and a bug of the AMC system of M1 caused a degradation of PSF. The hardware problems influence the whole MAGIC analysis chain and consequently during the 2012 analysis, dedicated MC simulations were created.

The 2012 data set was divided in three different periods in according to the hardware problems involved and hence for each period a different MC file set was used:

- **Period 1** (22/01/2012 - 25/02/2012)
    - The trigger pattern information were missing
    - The data were contaminated by calibration pulses: they were removed during the data analysis applying a cut on the `Conc` parameter
    - 24 pixels of the inner camera region of M1 were dead creating ´holes` in the trigger area

---

[8] During January 2012 the readout system was upgrated replacing the DRS-2 chip to the latest version DSR-4.

  - Worse PSF of M1

- **Period 2** (26/02/2012 - 01/03/2012): Worse PSF of M1
- **Period 3** (18/03/2012 - 19/05/2012): No technical problems

As for data of the previous year, a daily quality check based on the event rate was performed and in the Tab 7.8 the main information for every observational night are summarized. Moreover in Fig 7.20 the event rate distribution for M1 (*upper*) and M2 data (*lower*) after the quality check and the zenith angle distribution in Fig 7.21.

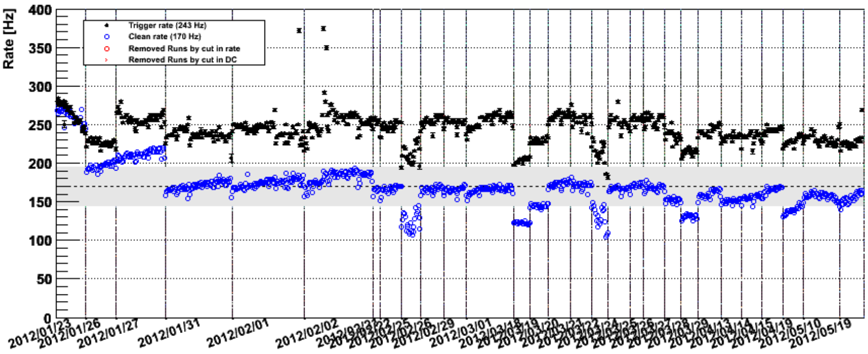

Figure 7.20: 1ES 1011+496 event rate distribution for M1 of the selected 2012 MAGIC data after the daily quality check.

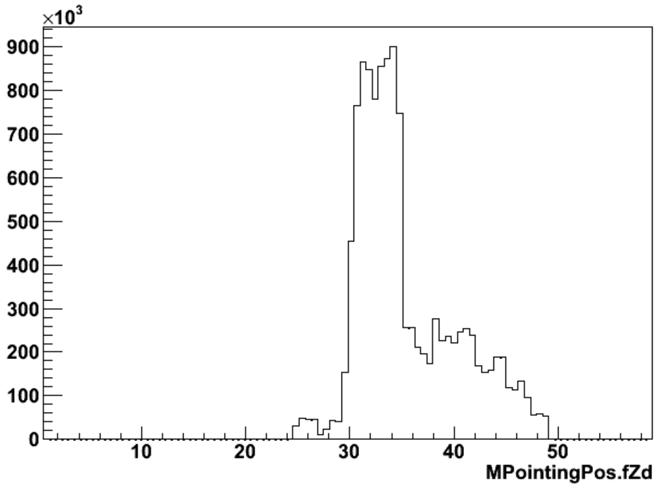

Figure 7.21: 1ES 1011+496 zenith angle distribution of the whole 2012 MAGIC data set.

7.2.3 Signal plots and Skymap

The signal extraction is performed analyzing the distribution of the squared angular distance θ^2. The following standard cuts on the parameters of the data events, `Size > 55 phe` and

Period	Date	MJD	Obs. Time [min]	Zd [°]	Note
	22/01/2012	55948	78	29-39	M2 data missing
	23/01/2012	55949	73	32-43	Very high rate, but data used
	26/01/2012	55952	56	31-42	
	27/01/2012	55953	96	29-45	
	30/01/2012	55956	65	30-40	High Cloudiness, data rejected
	31/01/2012	55957	-	-	
Period 1	01/02/2012	55958	115	29-49	
	02/02/2012	55959	107	31-49	
	21/02/2012	55978	-	-	
	22/02/2012	55979	-	-	
	25/02/2012	55982	35	29-35	High Cloudiness, data rejected
	26/02/2012	55983	35	29-35	
Period 2	29/02/2012	55986	33	30-35	
	01/03/2012	55987	69	24-34	
	18/03/2012	56004	31	29-35	
	19/03/2012	56005	33	30-34	High humidity
	20/03/2012	56006	33	29-35	
	22/03/2012	56008	29	30-35	
	23/03/2012	56009	9	33-35	High Cloudiness, data rejected
	24/03/2012	56010	33	29-34	
	25/03/2012	56011	21	31-34	
	26/03/2012	56012	30	30-34	
Period 3	27/03/2012	56013	27	30-35	High Humidity
	28/03/2012	56014	28	30-35	
	29/03/2012	56015	38	29-34	
	13/04/2012	56030	34	30-34	
	14/04/2012	56031	33	30-34	
	15/04/2012	56032	34	30-35	
	16/04/2012	56033	32	30-34	Problem with the M2 AMC, data rejected
	19/04/2012	56036	35	30-34	Calima
	10/05/2012	56057	65	36-44	
	19/05/2012	56058	69	33-44	

Table 7.8: 1ES 1011+496 dataset of the 2012 observations. From left to right: Period of observation (first column), date of the nights observations (second column), observation time in minutes (third column), zenith angle range in degree (four column). In the last column indicates if particular conditions or problems occurred during the night.

`Hadronness < 0.28`, provided by the MAGIC software analysis and referred to as *low energy* range[9], are applied for the two sets of data. This cut setting does not provide any reconstructed energy cut and lead to an *true* energy threshold[10] of ∼110 GeV and of ∼ 120 GeV for the 2011 (Fig 7.22) and for the three periods of 2012 (Fig 7.23) analysis respectively.

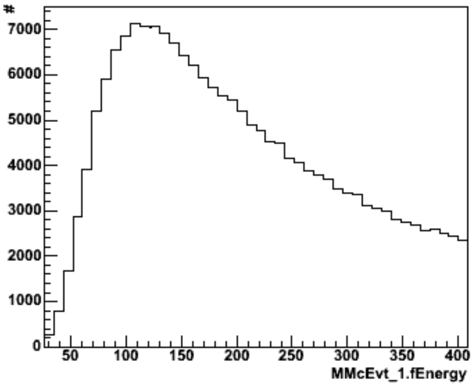

Figure 7.22: Energy thresholds of 1ES 1011+496 estimated dedicated MC data applying *Low energy* setting cuts for the 2011 analysis.

Since all data were taken in wobble mode, the background is extracted from the data themselves. Because for the 2011 observation we have data taken in only two wobble positions and for the 2012 data the times of observation in all four wobble positions are unequal, finally we use only one Off region, located at 180° with respect to the reconstructed position of the source in the camera, to estimate the background level for the whole dataset.

For the 2011 analysis, as mentioned in the previous section, we have only a hint of detection of 3.45σ with an event excess ∼206 γ-like events and a background level of ∼ 1677 events (Fig 7.24).

In Fig 7.26, we display the signal detection plots resulting from the analysis of 2012 data for each period considered. In Table 7.9 we summarize the results obtained for the subsample considered.

Since considering the whole 2012 data set of 1ES 1011+496 we have an homogeneity in the time coverage of the four wobble position, we can use 3 Off position to estimate the level of the background. The detection plot is shown in Fig 7.26 with a detection significance of 12.58σ.

Finally we perform a stacked detection plot joining the 2011 and 2012 data (Fig 7.27).

---

[9] for details see the Section XXX

[10] mettere la differenza tra vera e ricostruita

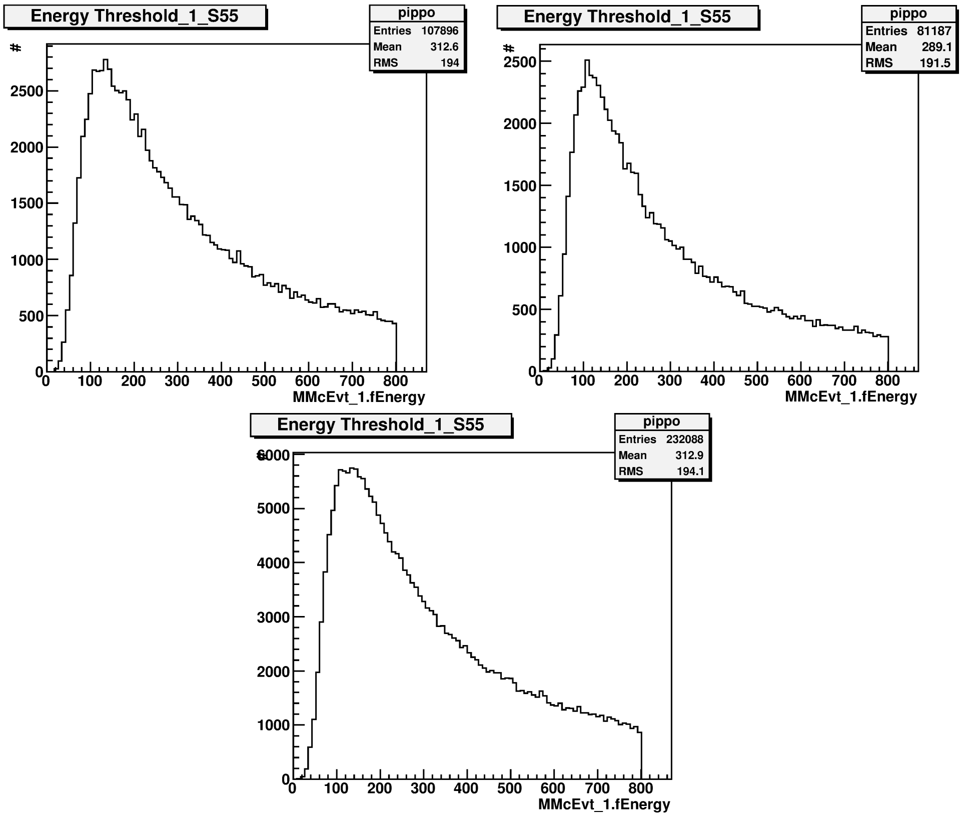

Figure 7.23: Energy thresholds of 1ES 1011+496 estimated dedicated MC data applying *Low energy* setting cuts for the three periods of the 2012 analysis.

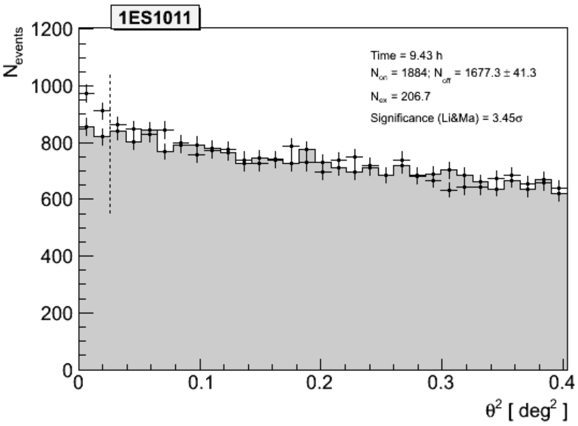

Figure 7.24: Signal detection plot built from the 2011 1ES1011+496 data sample. The cuts applied are `Size>55 phe`, `Hadronness<0.28`. The vertical dashed line defined the signal region on the plot.

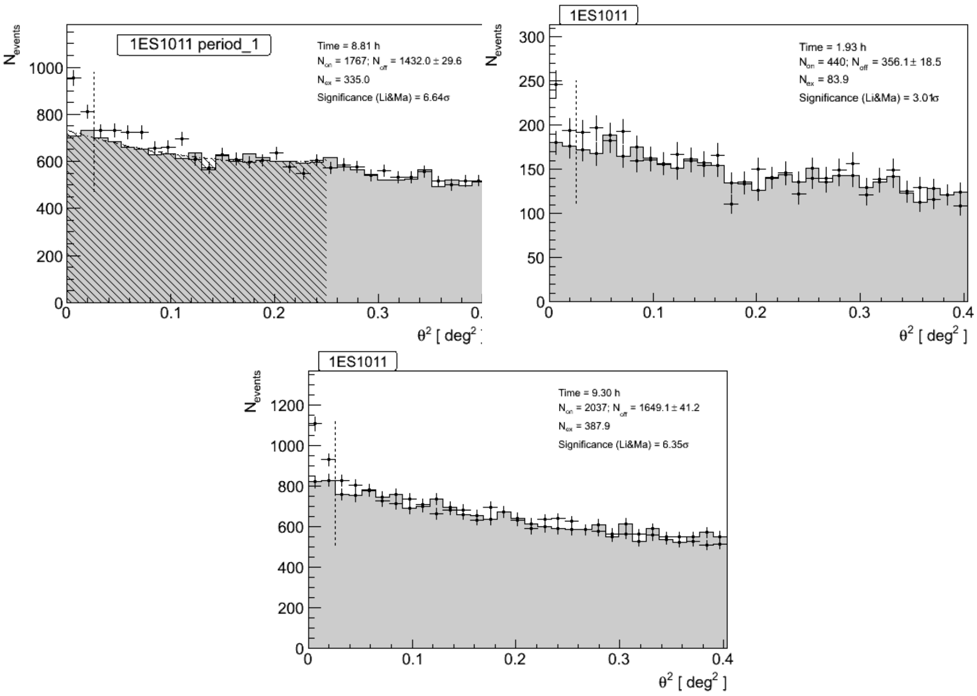

Figure 7.25: Signal detection plot of 1ES 1011+496 during the first period (*left*), the second period (*middle*) and the third period (*right*).

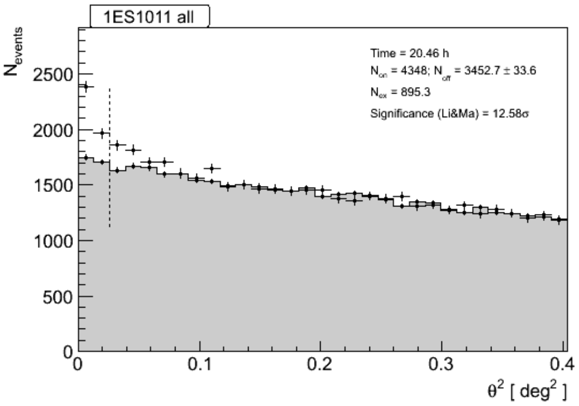

Figure 7.26: Signal detection plot of 1ES 1011+496 using the whole data set collected in 2012.

In Tab (**??**) we summarize the results obtained for all 1ES 1011+496 sub-sample considered and we conclude that despite of the only hint of detection in 2011, the source was strongly detected in 2012, confirming the its VHE emitter nature.

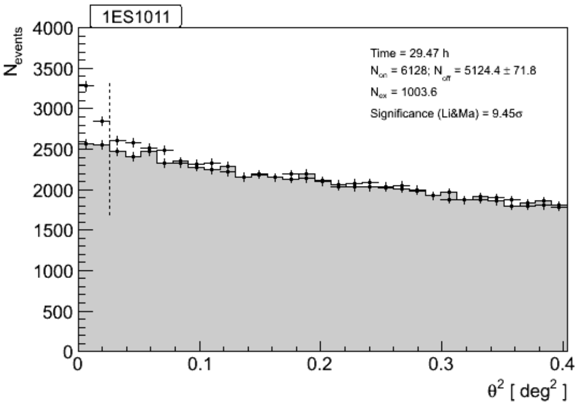

Figure 7.27: Overall signal detection plot of 1ES 1011+496 stacking the data of the 2011 and 2012 MAGIC observations.

Sub-sample	Eff.Time [hr]	N_{exc}	Significance σ
2011	9.43	206.7	3.45
2012 Period 1	8.81	335.0	6.64
2012 Period 2	1.93	83.9	3.01
2012 Period 3	9.30	387.9	6.35
2012	20.46	895.3	12.58
2011+2012	29.47	1003.6	9.45

Table 7.9: 1ES 1011+496 signal study for the 2011-2012 MAGIC observations. From left to right: Period of observation considered (first column), effective time of observation in hours (second column), number of excess events detected (third column) and the significance of detection (last column).

7.2.4 Differential spectrum

In this Section, we present the results of the differential spectra obtained in 2011 and in the three periods of 2012. For each dataset the spectrum is determined performing the signal search with the θ^2 analysis in bins of estimated energy and applying the following cuts:

Size > 50 phe

Hadronness cut efficiency = 90%

θ^2 cut efficiency = 70%

minimal hadronness = 0.07

`minimal` θ^2 `= 0.02 deg`^{2}

The three periods of 2012 were analyzed separately, using dedicated MC simulations for each of them, and further they have been stacked to one data sample to have a single spectrum and to compare it with the 2011 spectrum. Furthermore in order to correct the effect of the limited energy resolution on the spectrum determination, an unfolding procedure is applied on the 2011 and 2012 stacked spectra.

2011

For the 2011 spectrum we use 20 energy bins in logarithmic scale between 5 GeV to 50 TeV and in Tab 7.10 we report the hadronness and the θ^2 cuts, the number of excess events, the significance and the mean flux measured by Eqn**??** for every energy bin considered in our analysis.

The differential spectrum of 1ES 1011+496 unfolded for the finite energy resolution is computed through the Tikhonov method (Tikhonov+1977) and displayed in Fig 7.28. The spectrum in the energy range 95-660 GeV can be fitted by a simple power law with spectral photon index Γ=3.38 ± 0.33 and normalization factor f_0 at 200 GeV of $(6.81\pm1.10)\times10^{-11}$ cm^{-2} s^{-1} TeV^{-1}. In the same plot we show also the differential spectrum absorption-corrected (*blue filled triangle*) using the EBL model by Franceschini+2008 for a redshift z=0.202. The value of the data points are listed in the table on the right.

Mean Energy [GeV]	`hadronness` cut	θ^2 cut	N$_{ex}$	Significance σ	Flux ph cm^{-2} s^{-1} TeV^{-1}
102.419	0.402	0.045	91 +/- 50.4678	1.8033	-
162.324	0.31225	0.03	122 +/- 41.3521	2.95152	$(2.2\pm0.8)\times10^{-10}$
257.266	0.30875	0.02	50 +/- 22.7596	2.19859	$(3.6\pm1.7)\times10^{-11}$
407.739	0.2915	0.015	20 +/- 13.1909	1.51787	-
646.223	0.244	0.01	8 +/- 6.78233	1.18254	-

Table 7.10: 2011 differential spectrum of 1ES 1011+496: Mean energy of the bin (first column), `hadronness` and θ^2 cuts (second and third column), number of excess events (four column), significance (five column) and mean photon flux before the unfolding (last column).

2012

As said, the 2012 data set was divided in three different periods due to some hardware problems that affected the performance of the telescopes and consequently three different MC simulations were used for the analysis.

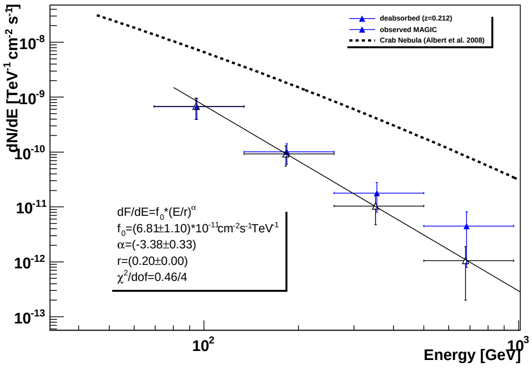

Mean Energy [GeV]	Flux$_{obs}$ [cm^{-2}s^{-1}TeV^{-1}]	Flux$_{deabs}$ [cm^{-2}s^{-1}TeV^{-1}]
95	$(6.8\pm2.8)\times10^{-10}$	$(6.7\pm2.8)\times10^{-10}$
181	$(9.3\pm3.8)\times10^{-11}$	$(1.0\pm0.4)\times10^{-10}$
351	$(1.0\pm0.6)\times10^{-11}$	$(1.8\pm1.0)\times10^{-11}$
678	$(1.0\pm0.8)\times10^{-12}$	$(4.5\pm3.7)\times10^{-12}$

Figure 7.28: Unfolded differential observed *(grey points)* and absorption-corrected *(blue points)* spectrum for 1ES 1011+496 for 2011 MAGIC data.

The θ^2 technique with 36 bins of energy and the same cuts of the 2011 analysis on the `hadronness` and θ^2 parameters were used to estimated the fluxes. The results are shown in Tab 7.11 for each period.

During the period 1 and 3 we have higher significance of detection for energies between ~120 and ~400 GeV. Probably due to the short exposure time the same behavior is not shown for the period 2, where we have a lower number of excess events for each energy bin and only a hint of detection.

Through the unfolding procedure the stacked differential spectrum was built joining the three 2012 datasets of 1ES 1011+496 and in Fig 7.29 the observed and deabsorbed spectra are shown. Also in this case the spectrum is fitted by a simple power law showing a normalization factor of $(1.05\pm0.05)\times10^{-10}$ cm^{-2} s^{-1} TeV^{-1} and spectral index *Gamma*= 3.45 for the observed spectrum.

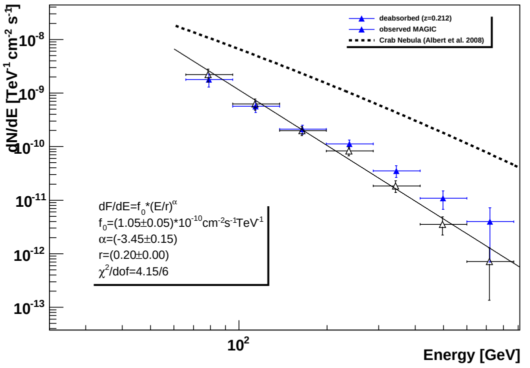

Mean Energy [GeV]	Flux$_{obs}$ [cm^{-2}s^{-1}TeV^{-1}]	Flux$_{deabs}$ [cm^{-2}s^{-1}TeV^{-1}]
79	$(2.2\pm0.6)\times10^{-9}$	$(1.8\pm0.4)\times10^{-9}$
114	$(6.3\pm1.4)\times10^{-10}$	$(5.7\pm1.3)\times10^{-10}$
164	$(2.0\pm0.4)\times10^{-10}$	$(2.1\pm0.4)\times10^{-10}$
237	$(8.3\pm1.6)\times10^{-11}$	$(1.1\pm0.2)\times10^{-10}$
343	$(1.8\pm0.5)\times10^{-11}$	$(3.5\pm0.9)\times10^{-11}$
496	$(3.5\pm1.3)\times10^{-12}$	$(1.1\pm0.4)\times10^{-11}$
717	$(7.1\pm5.8)\times10^{-13}$	$(4.0\pm3.2)\times10^{-12}$

Figure 7.29: Unfolded differential observed *(grey points)* and absorption-corrected *(blue points)* spectrum for 1ES 1011+496 for 2012 MAGIC data.

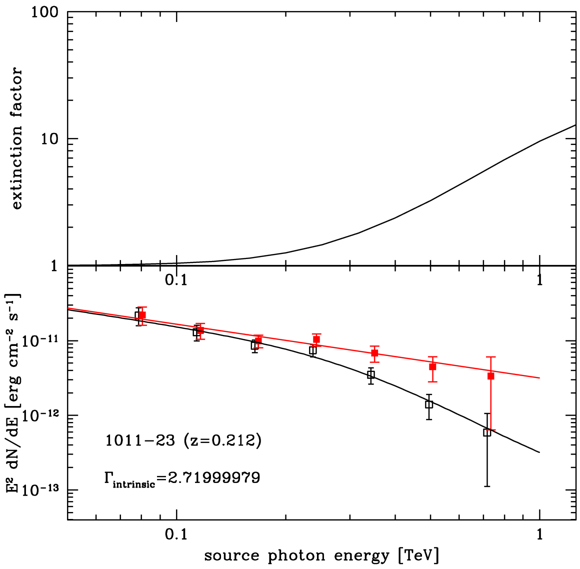

Figure 7.30: .

7.2.5 The VHE Light Curve

In this Section we investigate the temporal VHE emission of 1ES 1011+496 and the night-averaged integral flux above a conservative threshold of 150 GeV is calculated for each observational night of 2011 and 2012 datasets. The same cuts on the `hadronness` and θ^2 parameters, used to estimated the differential fluxes, were applied for the data sample of both observational cycles.

The VHE daily-binned light curve for the 2011 and 2012 observations is shown in Fig **??**with a mean flux level of $(2.1\pm0.3)\times10^{-11}$ cm^{-2} in 2011 and of $(1.8\pm0.2)\times10^{-11}$ cm^{-2} for the 2012 observations. The mean flux level estimated over the entire observational period is $(1.9\pm0.2)\times10^{-11}$ cm^{-2} and is in good agreement with the hypothesis of non-variable emission and constant flux, excluding a flare activity of the source.

7.2.6 Multiwavelength data of 1ES 1011+496 from the 2011-2012 observational campaign

In this section the multiwavelength data provided from different instruments ([54]) during the 2011 and 2012 campaigns and the results are reported. The campaigns were centered around the VHE MAGIC observations and involved the *Fermi*/LAT satellite for the HE regime, the *Swift*/XRT/UVOT telescopes for the X-ray and UV bands, the KVA telescope for the R-band of the optical regime and for the radio frequencies the OVRO and Metsähovi telescopes.

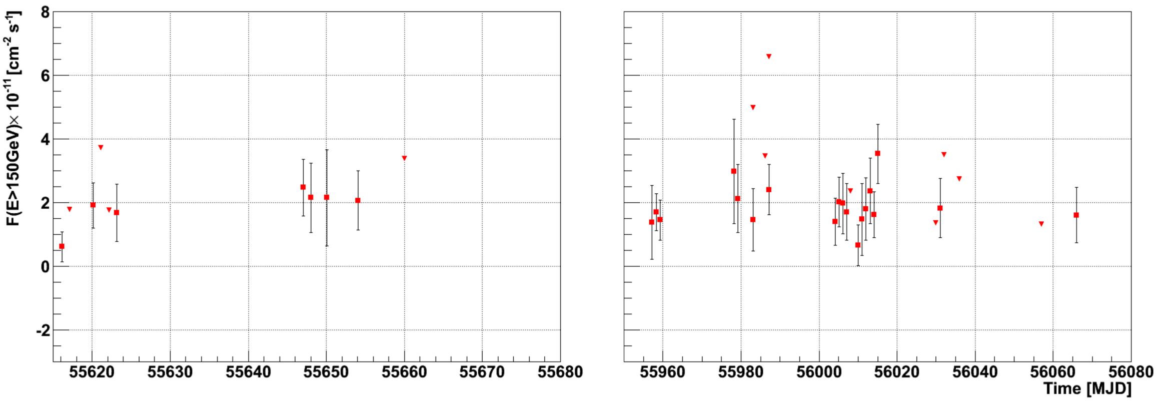

Figure 7.31: MAGIC daily-binned light curve of the integral VHE flux from 1ES 1011+496.

The multiwavelength lightcurves and SED modeling

In Fig 7.32 and Fig 7.33 the multiwavelength lightcurves with daily bins (except for the HE band) of 1ES 1011+496 are displayed. The mean fluxes of the different energy bands considered and for the two years separately are summarized in Table **??**. In the both figures, the MAGIC lightcurves at energies above 150 GeV, as described in Section 6.5.5, are displayed in the upper panel and show a stable emission in the both years. In the second panel we show the *Fermi*/LAT lightcurves above 300 MeV computed in bins of 7 days for the 2011 data and of 3 days for 2012. The data are compatible with the hypothesis of a constant flux and a mean flux over the whole period of $(2.7\pm0.2)\times10^{-8}$ ph cm^{-2} s^{-1}. In the third and fourth panel of Fig 7.33 the daily-binned *Swift* data are shown. We have only 2012 data, since during the 2011 campaign we have not coverage in the UV and X-ray frequencies. The 0.3-10 keV X-ray shows moderate variability and a decreasing trend, with a mean flux of $(4.7\pm0.1)\times10^{--12}$ erg cm^{-2} s^{-1}. The same behavior for the optical U and UV bands where a stable emission is improbable and decreasing in the course of time, while the integral flux seems rather constant in V and B bandsThe R-band flux monitored by KVA telescope is shown in the third panel and in the fifth panel of Fig 7.32 and Fig 7.33 respectively, exhibiting a steady emission in 2011 with a mean flux of XX and a variability with a gradually enhancement in 2012 up to values around 2.7 mJy. No evidence of variability for 1ES 1011+496 is in the radio frequencies. The radio lighcurves provided by the OVRO and Metsähovi telescopes at 37 and 15 GHz are shown in the last panels.

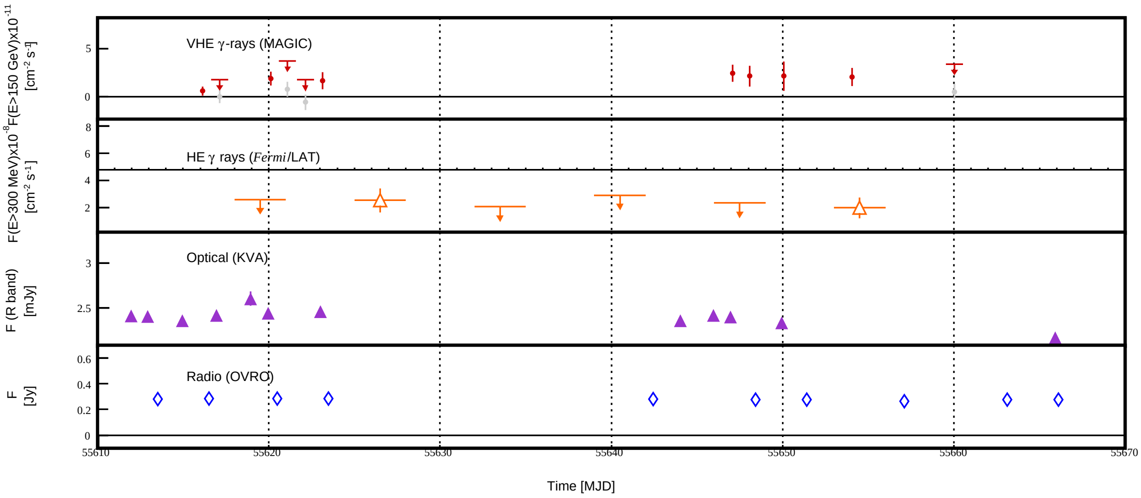

Figure 7.32: 2011 Multiwavelength lightcurve of 1ES 1011+496.

Period 1

Mean Energy [GeV]	`hadronness` cut	θ^2 cut	N$_{ex}$	Significance σ	Flux ph cm^{-2} s^{-1} TeV^{-1}
123.425	0.41875	0.035	71±35	2.03581	(5.5±2.7)× 10^{-10}
159.409	0.38075	0.025	94±29	3.23513	(3.2±0.99) × 10^{-10}
205.885	0.37	0.02	43 +/- 21.5174	1.99982	-
265.911	0.3705	0.02	89±18	5.04894	(9.7±1.9) × 10^{-11}
343.437	0.3745	0.015	23 +/- 12.2882	1.87536	17
443.566	0.322	0.01	26 +/- 8.24621	3.19355	1.11607e-11 +-3.54565e-12
572.887	0.29475	0.01	2 +/- 6.78233	0.29493	19
739.913	0.29025	0.015	2 +/- 4.89898	0.408485	20

Period 2

Mean Energy [GeV]	`hadronness` cut	θ^2 cut	N$_{ex}$	Significance σ	Flux ph cm^{-2} s^{-1} TeV^{-1}
123.425	0.396	0.03	25 +/- 16.7033	1.49772	13
159.409	0.3995	0.025	4 +/- 12.5698	0.31824	(14±0.8) × 10^{-10}
205.885	0.362	0.02	9 +/- 8.544	1.05471	(15±1.7) × 10^{-11}
265.911	0.38	0.015	20 +/- 6.78233	2.99879	8.4529e-11 +-2.87276e-11
343.437	0.34375	0.015	1 +/- 5.19615	0.192472	17
443.566	0.34025	0.01	3 +/- 4.3589	0.68969	18
572.887	0.3285	0.01	6 +/- 3.74166	1.6299	19

Period 3

Mean Energy [GeV]	`hadronness` cut	θ^2 cut	N$_{ex}$	Significance σ	Flux ph cm^{-2} s^{-1} TeV^{-1}
123.425		0.03	162 +/- 36.7696	4.41112	7.2018e-10 +-1.63965e-10
159.409		0.025	127 +/- 26.9258	4.72886	2.79061e-10 +-5.93385e-11(±) × 10^{-10}
205.885		0.02	73 +/- 19.5192	3.7515	9.64806e-11 +-2.58421e-11(- ±) × 10^{-11}
265.911		0.015	67 +/- 13.0767	5.19309	5.57817e-11 +-1.0921e-11
343.437		0.015	32 +/- 11.225	2.86648	1.74786e-11 +-6.13694e-12
443.566		0.01	14 +/- 7.34847	1.09161	-
572.887		0.01	8 +/- 5.65685	1.42175	-
739.913		0.01	5 +/- 5.74456	0.872067	-

Table 7.11: 2012 differential spectrum of 1ES 1011+496 for the three different period considered: Mean energy of the bin (first column), `hadronness` and θ^2 cuts (second and third column), number of excess events (four column), significance (five column) and mean photon flux before the unfolding (last column).

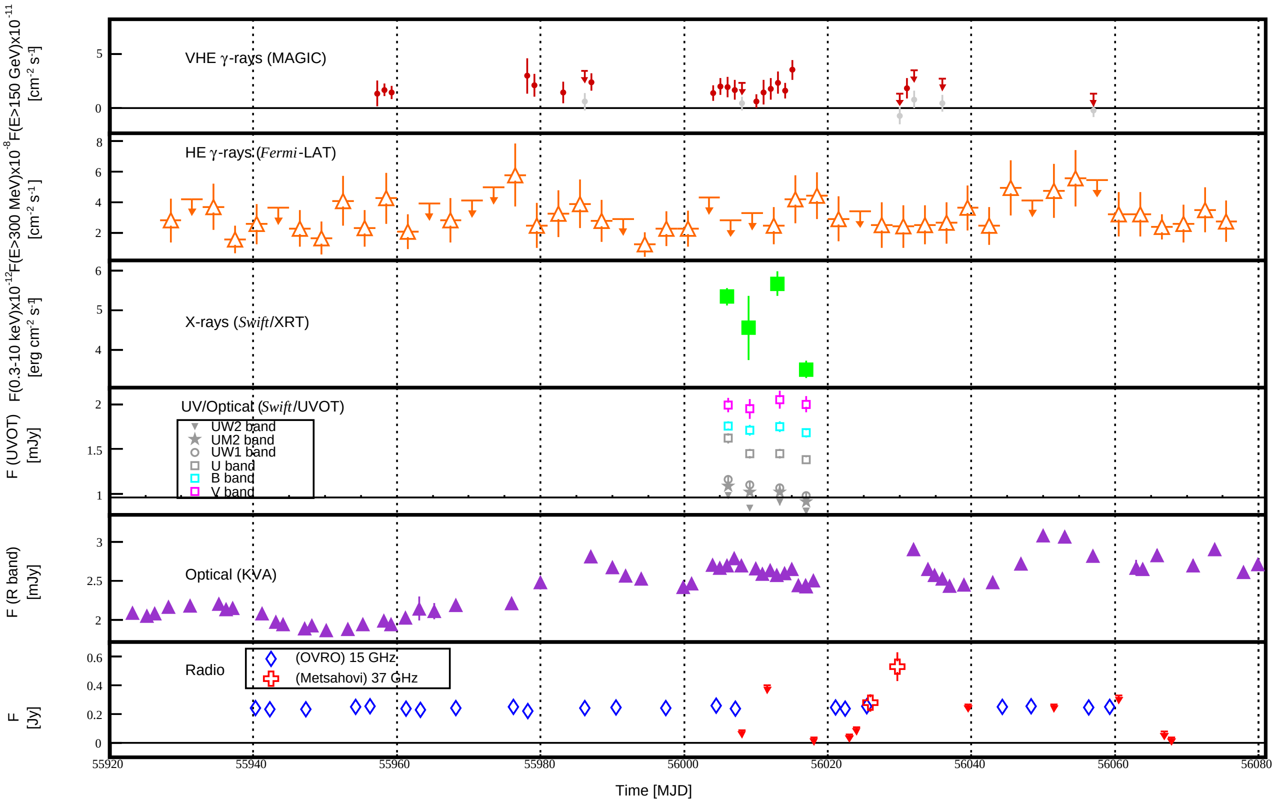

Figure 7.33: 2012 Multiwavelength lightcurve of 1ES 1011+496.

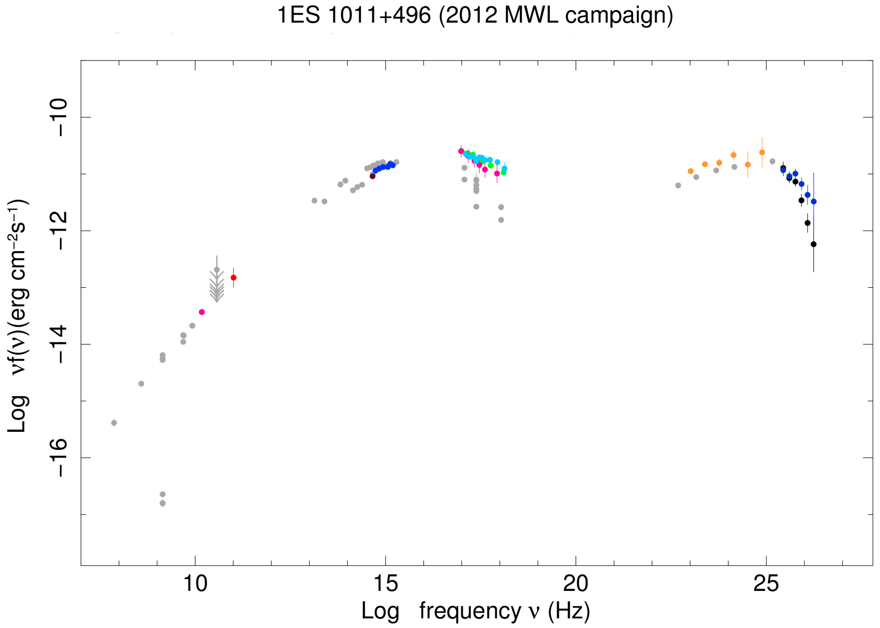

Figure 7.34: 2012 Multiwavelength SED of 1ES 1011+496.

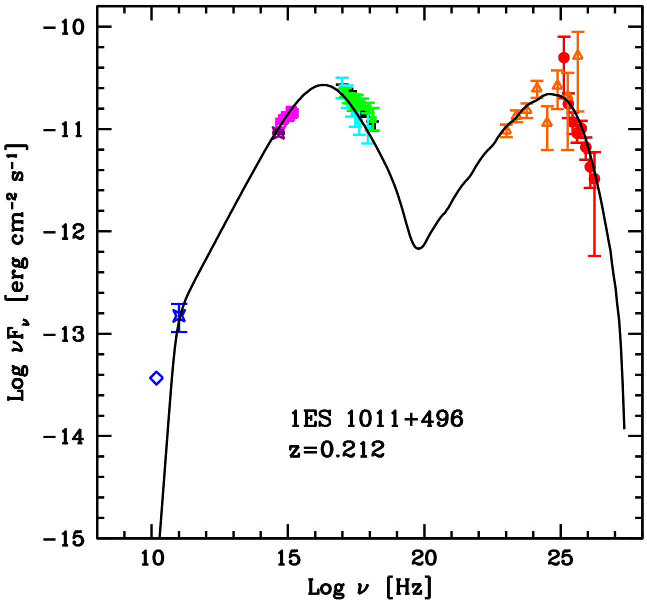

Figure 7.35: 2012 Multiwavelength SED of 1ES 1011+496. The average SED is modeled wiht one-zone SSC model (continuous black line).

8

UFO Dark Matter candidates

8.1 Introduction to the DM and Gamma-ray emission from DM annihilation

Dark Matter is one of the fundamental unsolved question in modern Cosmology. Several observational evidences suggest that about 23% of the Universe is composed of new type of non-baryonic matter, the so-called Dark Matter, and the remaining 4% is in baryons.

The most popular dark matter candidates are weakly interactive massive particles (WIMPs). They are supposed to be massive, stable or with a lifetime greater than age of the Universe (with a cross section $\sigma < 10^{-33}$ cm^2), electrically neutral, weak-interacting only through its gravitational field and *cold* that is to say being a non-relativistic particle at every cosmological epoch.

In Particle Physics there are many theories, beyond the Standard Model that provide particles with suitable characteristics for being good candidates of DM. Among the huge plethora of WIMP particles, we can have as DM candidate the *neutrino*, that being *hot* DM candidate, is not actually compatible with the herarchic scenario of the cosmic structure formation, and the *axion*, a particle introduced in the framework of the CP violation and detectable only through a possible oscillation into photons. However the best motivated ones are related to the Super Symmetrical and Extra Dimensional extensions of the Standard Model of particle physics [][]. In according to these theories, the lighest particle of their particle mass spectrum (the *Neutralino* χ for the Supersymmetric model, and the *Kaluka-Klein particle* for the Ultra Dimensional model) is expected being a Majorana particle[1] with a low cross section, and hence good candidate to be considered as a self-annihilating DM particles. They can annihilate, through different channels, into Standard Model particles, namely quarks, leptons and W bosons. The hadronization of such particles results in a continuum emission of gamma-rays. In addition, a direct annihilation in γ-ray photons with a peculiar sharp line spectrum dependent on the neutralino mass is also supposed [].

The typical annihilation γ-ray spectrum is predicted to be continuous, constant, universal, and characterized by some spectral features, like a spectral hardening and cut-off depending on the mass of the DM particle.

The expected γ-ray flux by DM annihilation astrophysical objects, as function of the nergy threshold E_0 and the integration region $\Delta\Omega$ within the signal is integrated, can be factorized in two terms:

$$\Phi(> E_0, \Delta\Omega) = \Phi^{PP}(> E_0) J(\Delta\Omega). \tag{8.1}$$

The first term is the so-called particle physics factor Φ^{PP}, that depends on the features of the DM particle, and can be written as:

$$\Phi^{PP}(> E_0) = \frac{1}{4\pi} \frac{< \sigma_{ann} v >}{2m_\chi^2} \int_{E_0}^{m_\chi} \sum_{i=1}^{n} B^i \frac{dN_\gamma^i}{dE} dE, \tag{8.2}$$

where $< \sigma_{ann} v >$ is the velocity averaged annihilation cross-section and B^i is the particular branching ratio for the i$-th$ annihilation channel.

The second term $J(\Delta\Omega)$ is the astrophysical factor

$$J(\Delta\Omega) = \int_{\Delta\Omega} \int_{los} \rho^2(r(s, \Omega)) ds d\Omega. \tag{8.3}$$

given by the line-of-sight integral over the DM density squared within a solid angle $\Delta\Omega$ and depends on the density profile of the DM halo of the source.

As illustred in Fig 8.1, the shape of the DM annihilation spectrum and the cut-off at $E = m_{DM}$ depends on the annihilation channel considered and on the DM particle mass. Recently it was pointed out that the Internal Bremsstrahlung (IB) process [17tesimia] may

---

[1] A Majorana particle is a fermion that is its own antiparticle.

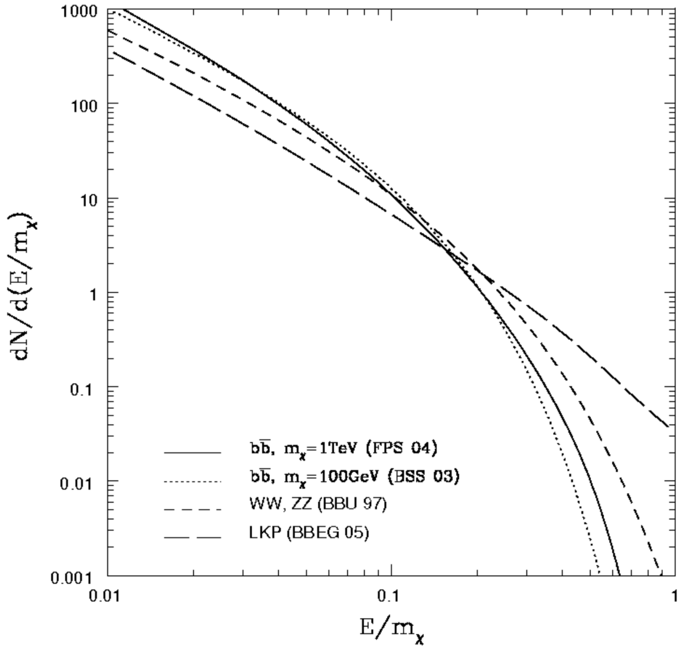

Figure 8.1: *Left. Right*

boost the gamma-ray yield of the neutralino self-annihilation by up to three or four orders of magnitude.

8.1.1 The best DM object candidates

There are three approaches to perform DM search: the direct production in collider experiment, the direct detection through scattering off ordinary matter and finally the indirect detection based on the search for secondary particles, as γ-ray photons among others, producted by annihilation or decay of DM particles.

Focusing on the indirect detection, we can take into account that photons do not suffer neither deflection nor energy losses in the local universe and can give spectral and spatial information at the same time. Moreover the expected DM annihilation γ-ray spectrum is supposed to be universal, so the detection of several gamma-ray sources with no counterpart at other wavelenghts, all of them sharing identical spectra, would provide an clue about the existence of DM.

Since the DM annihilation spectrum is through proportional to the square of the DM density, the best search targets for DM indirect are those astrophysical objects where high DM concentration is expected. Different types of objects are considered as good targets, both of galactic and extragalactic origin, as:

- *The Galactic Center*:

The highest concentration of DM in our galaxy is in the Galactic Center (GC), indeed the γ-ray emission produced by DM from the center of the Milky Way is predicted to be about 100 times brighter than any other known object emission. Despite this, the GC is a very crowded region and it is difficult to detect the DM signal because of the presence of astrophysical γ-ray sources (i.e pulsars and SNRs) closely at the center of the Milky Way.

However several studies work in this direction [Cembranos+2012] considering the possibility to explain the γ-ray flux from the central part of our Galaxy as partially produced by annihilation of DM particles with mass heavier than 10 TeV (Fig 8.2).

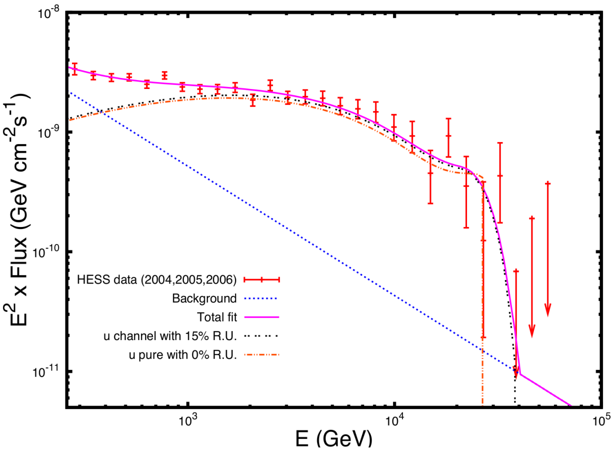

Figure 8.2: *Left. Right*

- *The Dwarf Spheroidal Satellite Galaxies of the Milky Way*:

The Dwarf Spheroidal Satellite Galaxies (sDphs) of the Milky Way are believed to be interesting candidates for indirect DM search thanks to their relative proximity from the Earth, to their high masstolight ratio (with values within tens and thousands of $M_\odot/L_\odot$, and to the expected absence of conventional gamma-ray sources inside them [3, 4]. [2].

---

[2] [3] M. Sanchez-Conde et al., AIP Conf. Proc. 1166 (2009) 191-196——[4] G. Gilmore et al. , Astrophys.J. 663 (2007) 948-959

So far, around two dozen dSphs have been identified. Most of them have been discovered by the SDSS and thanks to kinematics studies their density profile, mass and the masstolight ratio are estimated. In Table 8.1 some dSph are listed and it is possible to note by their values of (M/L) that they consist of a high percentage of DM.

dSph	**Distanza [kpc]**	**Luminosità** $(10^3 L_\odot)$	**rapporto M/L**
Carina	101	430	40
Draco	82	260	320
Fornax	138	15500	10
Sculptor	79	2200	7
Sextans	86	500	90
UMi	66	290	580
Coma Berenices	44	2.6	450
UMaII	32	2.8	1100
Willman 1	38	0.9	700
Segue 1	23	0.3	1200

Table 8.1: Lista di alcune dSph della Via Lattea che grazie al loro rapporto M/L e alla loro distanza risultano buoni target per la ricerca indiretta di materia oscura.

Several dSph have been observed with the HE and VHE instruments, as Draco, Willman 1 and Segue 1. The latter, discovered in 2006 and located at 28 kpc from the Galactic Center, is the most DM dominated dSph known so far. It was observed by MAGIC for a total of 29.4 hours in mono mode and for XX hours. Its DM halo was modeled by the Einasto radial profile. No significant gamma-ray emission was found above 100 GeV. A scan was performed over a reasonable portion of the SUSY parameter space, and the flux upper limit and upper limit on the averaged cross section $< \sigma v >$ for each point was computed 8.3[][]

- *The Galaxy Clusters*:

Galaxy clusters are the largest gravitationally bounded systems of the Universe with total masses M∼10141015 M_{odot}, composed of galaxies, gas and DM. The latter is about 80% of the whole mass. Despite they are farther than the other potential DM objects, galaxy clusters are good DM candidate because they have a huge quantity of DM with very large M/L ratios. In addition they could have considerable overdensities or substructures in the DM distribution that could provide a boost in their expected γ-ray flux. As the GC, the DM search from this kind of sources is challenging due to the complexity to discriminate the DM annihilation contribution from the γ-ray emission of canonical astrophysical objects.

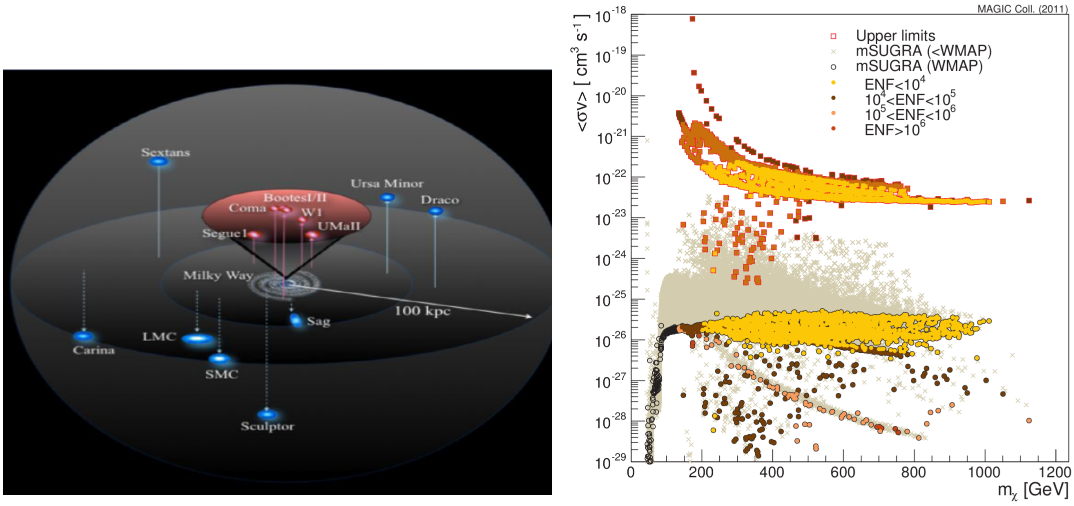

Figure 8.3: *Left. Right*

- *DM clumps within the DM Halo of the Milky Way*

  Dfferent numerical simulations ()(), based on the models of hierarchical structure formation in a ΛCDM cosmology, suggest that DM halos of the galaxies are not smooth but host substructures or clumps, the so-called *sub-halos*, containing overdensities of DM with masses ranging from $10^{-3}M_{\odot}$ to $10^{10}M_{\odot}$. These exotic objects are invisible to conventional telescopes but could be detectable in the γ-ray energy band if the dark matter particles are annihilating particles according to the theories beyond the standard model of particle physics. In the next section we deal about the possibility to detect them through the continuous all-sky observations performed by the *Fermi* satellite.

8.2 DM Subhaols candidates in the 2FGL catalog

Different studies (2) (3) (4) suggest the existence of these exotic objects and provide the number of sources detectable by Fermi satellite as a function of the properties of DM particle (mass, annihilation cross section and channel) and of subhalo (size and extension).

In the light of this, the detection of several gamma-ray sources, with no counterpart at the other wavelenghts, all of them sharing identical spectra, would provide an clue about the existence of DM.

In order to select possible DM subhalo candidates among the 2FGL unassociated sources, the following selection criteria can be applied

9

Conclusion and Perspectives

This PhD Thesis was focused on two parallel tasks, deeply related one with the other and related to the field of the γ-ray astronomy. The first one is an all-sky search for DM signals at the γ-ray energies adopted the Second Catalogue of the Fermi Gamma Ray Observatory (2FGL) as the main dataset for searches of DM objects candidates, but also new classes of extragalactic and Galactic sources or unexpected high-energy phenomena. The second line of investigation is in the field of the VHE astrophysics providing a detailed multiwavelength study of the differential energy spectrum and temporal integral flux variability for two HBL *blazars*, included in the 2FGL catalogue.

- **Multiwavelength study of the UFOs and search for DM candidates**

  Several observational evidence suggest that about 24% of the entire energy budget of the Universe is composed of non-baryonic matter, the so-called Dark Matter (DM). The most popular DM particles candidates are the weakly interacting massive particles (WIMPs) that are supposed to be massive, cold, stable, neutral and with no-strong or electromagnetic interactions. Among the huge plethora of WIMP candidates, the best motivated ones are related to the Super Symmetrical and Extra Dimensional extensions of the Standard Model of particle physics.

  Therefore, DM is one of the most intriguing and challenging question of modern cosmology. Its nature is still unknown, but it has been suggested that γ-ray radiation can be also related to annihilation/decay processes of DM particles expected in several celestial objects with high DM density. Among them, the Galactic Center, the Galaxy cluster, the Dwarf Spheroidal Galaxy Satellite of the Milky Way and, the last but not least, the clumps of DM overdensities (the so-called DM sub-halos) within the DM halo of our Galaxy, suggested by several simulations in the framework of the hierarchical structure formation models, with a roughly isotropic distribution in the sky and detectable only in γ-ray band.

Beyond the important collider or on underground experiments, the search of γ-rays signal from space by DM annihilation/decay would provide a smoking gun for its identification.

In this sense, the 2FGL catalogue, and in particular the large population of the Unidentified Fermi objects, sources without counterparts at the other wavelength or with an ambiguous identification, is the ideal dataset to searches of DM object candidates and new classes of extragalactic and galactic γ-ray sources.

Despite the searching for counterparts of these new high energy sources is a primary objective of the Fermi survey work, it is made difficult by the large *Fermi* error-boxes (of the order of a few arcmin). This uncertaintly in their locations means that a positional correlation with a known object is usually not enought to identify a UFO and a multiwavelength approach, using X-ray, optical and radio data of likely counterparts must be used in order to understand their nature.

In this PhD thesis we define a association procedure to search likely multiwavelength counterparts for this kind of objects, based on the use of X-ray *Swift*/XRT data available, with the aim to build their broad-band SED (Chapter 3). Subsequently through new developed algorithms, able to characterize the SED of the various γ-ray emitters, we provide a classification for several UFOs throwing light on their nature and, in case, excluding an association with a canonical astrophysical objects. This gives us a chance to find new types of extragalactic and/or exotic sources, as dark matter objects.

For the *blazar* identification we build a code based on the adoption of several built *blazar* SED templates (described in the Sec 4.3 and Sec 5.1.1) choosing the one that models the data maximizing the likelihood. In case of microquasar objects, we use a dedicated diagnostic plot 5.1.3 to investigate the affinity between the SED data points of a microquasar candidate UFO with the multiwavelength datasets of well-known microquasars.

In this work we select 183 UFOs of high Galactic latitude (with $|b| > 20^{circ}$ to avoid the confusion effects in the Galactic plane) and for each of them we apply the identification procedure explained before. We obtain a reasonable classification as AGGN objects for about 50 UFOs, belonging to all of the four *blazar* classes considered and with redshift ranging to 0.2 to 1.5. For about 15 UFOs we suggest a Galactic origin, as microquasar and pulsars. They could be finding of great interest, given the small number of such objects in the 2FGL catalogue. However further investigations, thanks to observations performed in X-ray and optical bands, are ongoing. For another ten sources, although Swift/XRT data are avalaible, no X-ray sources has been found within the Fermi error-box, and, less than deeper observations, they could be considered as the best candidates to perform DM searches. Finally for the remaining UFOs we cannot to provide a clear identification since we found multiple sets of associations. In order to disantagle this issue, further observations are needed.

- **Multiwavelength Characterization of the two HBL *blazars* PG 1553+113 and 1ES 1011+496**

  Our second part of this PhD work was in the field of (VHE) observations with ground-base Cherenkov telescopes, in particular with the MAGIC telescope, one of the largest IACT stereo system and situated on the Canarian island La Palma. It was dedicated to the detailed analysis of the VHE radiation emitted by two *Fermi* sources, PG 1553+113 and 1ES 1011+496. These objects are two extragalactic γ-ray emitter, included in th 2FGL catalogue and classify as HBL *blazar* with redshift unknown and 0.212 respectively. For both source, VHE observations were carried out with the upgraded stereoscopic MAGIC system in 2011-2012 for 1ES 1011+496, and in 2013 for PG 1553+113. We have measured the differential energy spectrum and studied the temporal evolution of the integral flux detected. Both sources revealed a modest variability in the VHE γrays, and a steep observed spectrum of power law index $\sim$3.5 The MAGIC observations were planned in a framework of intense and wide multiwavelength campaigns in

2011 and 2012 for 1ES 1011+496, and in 2013 with the collaboration of the WEBT consortium for PG 1553+113, with a good temporal and energy coverage that allowed a good sampling of the broad-band SEDs and of the lightcurves.

PG 1553+113 shown a clear variability (but excluding flare episodes) in the optical, UV and X-ray bands, with a minimun level well correlated in each regime in the May 2013. At the radio frequencies and in the HE and VHE regime, no activity is exhibited. For 1ES 1011+496, beside its clear variability in the optical R band, the source shown modest activity in the other energy bands. Starting from the simultaneous data collected in the multiwavelength campaigns, the broad-band SED were built for both sources and a clear two bump structure is exhibited and reproduced by a current *blazar* SSC model.

Bibliography

[1] A. A. Abdo. Fermi LAT Observations of LS I +61°303: First Detection of an Orbital Modulation in GeV Gamma Rays. *ApJ*, 701:L123–L128, August 2009.

[2] A. A. Abdo. Fermi/LAT observations of LS 5039. *ApJ*, 706:L56–L61, November 2009.

[3] A. A. Abdo. Fermi-LAT first source catalog (1FGL) (Abdo+, 2010). *VizieR Online Data Catalog*, 218:80405, July 2010.

[4] M. Ackermann. The Second Catalog of Active Galactic Nuclei Detected by the Fermi Large Area Telescope. *ApJ*, 743:171, December 2011.

[5] M. Ackermann. The Fermi Large Area Telescope on Orbit: Event Classification, Instrument Response Functions, and Calibration. *ApJS*, 203:4, November 2012.

[6] C. P. Ahn, R. Alexandroff, C. Allende Prieto, F. Anders, S. F. Anderson, T. Anderton, B. H. Andrews, É. Aubourg, S. Bailey, F. A. Bastien, and et al. The Tenth Data Release of the Sloan Digital Sky Survey: First Spectroscopic Data from the SDSS-III Apache Point Observatory Galactic Evolution Experiment. *ApJS*, 211:17, April 2014.

[7] C. P. Ahn, R. Alexandroff, C. Allende Prieto, S. F. Anderson, T. Anderton, B. H. Andrews, É. Aubourg, S. Bailey, E. Balbinot, R. Barnes, and et al. The Ninth Data Release of the Sloan Digital Sky Survey: First Spectroscopic Data from the SDSS-III Baryon Oscillation Spectroscopic Survey. *ApJS*, 203:21, December 2012.

[8] Aleksić. Phase-resolved energy spectra of the Crab pulsar in the range of 50-400 GeV measured with the MAGIC telescopes. *A&A*, 540:A69, April 2012.

[9] Amsler. *Physic review Letters B*, 2012.

[10] K. A. Arnaud. Xspec: The first ten years. *Astronomical Data Analysis Software and Systems V, A.S.P. Conference Series*, 101, 1996.

[11] W. B. Atwood, A. A. Abdo, M. Ackermann, W. Althouse, B. Anderson, M. Axelsson, L. Baldini, J. Ballet, D. L. Band, G. Barbiellini, and et al. The Large Area Telescope on the Fermi Gamma-Ray Space Telescope Mission. *ApJ*, 697:1071–1102, June 2009.

[12] V. Beckmann and C.R. Shrader. *Active Galactic Nuclei.* (Wiley-VCH Verlag GmbH), 2012.

[13] W. Bednarek and J. Pabich. X-rays and γ-rays from cataclysmic variables: the example case of intermediate polar V1223 Sgr. *MNRAS*, 411:1701–1706, March 2011.

[14] M. C. Begelman, R. D. Blandford, and M. J. Rees. Theory of extragalactic radio sources. *Reviews of Modern Physics*, 56:255–351, April 1984.

[15] G. Bertone, D. Hooper, and J. Silk. Particle dark matter: evidence, candidates and constraints. *Phys. Rep.*, 405:279–390, January 2005.

[16] C. C. Cheung, P. Jean, S. N. Shore, and Fermi Large Area Telescope Collaboration. Fermi-LAT Gamma-ray Observations of Nova Centauri 2013. *The Astronomer's Telegram*, 5649:1, December 2013.

[17] R. H. D. Corbet, C. C. Cheung, M. Kerr, R. Dubois, D. Donato, G. A. Caliandro, M. J. Coe, P. G. Edwards, M. D. Filipovic, J. L. Payne, and J. Stevens. 1FGL J1018.6-5856: a New Gamma-ray Binary. *The Astronomer's Telegram*, 3221:1, March 2011.

[18] L. Costamante and G. Ghisellini. TeV candidate BL Lac objects. *A&A*, 384:56–71, March 2002.

[19] L. Costamante, G. Ghisellini, P. Giommi, G. Tagliaferri, A. Celotti, M. Chiaberge, G. Fossati, L. Maraschi, F. Tavecchio, A. Treves, and A. Wolter. Extreme synchrotron BL Lac objects. Stretching the blazar sequence. *A&A*, 371:512–526, May 2001.

[20] R. M. Cutri and et al. AllWISE Data Release (Cutri+ 2013). *VizieR Online Data Catalog*, 2328:0, November 2013.

[21] C. W. Danforth, B. A. Keeney, J. T. Stocke, J. M. Shull, and Y. Yao. Hubble/COS Observations of the Lyα Forest Toward the BL Lac Object 1ES 1553+113. *ApJ*, 720:976–986, September 2010.

[22] J.K. Daugherty and A.K. Harding. Electromagnetic cascades in pulsars. *Astrophysical Journal*, 252:337, 1982.

[23] J.K. Daugherty and A.K. Harding. Gamma-ray pulsars: Emission from extended polar cap cascades. *Astrophysical Journal*, 458:278, 1996.

[24] V. D'Elia, M. Perri, S. Puccetti, M. Capalbi, P. Giommi, D. N. Burrows, S. Campana, G. Tagliaferri, G. Cusumano, P. Evans, N. Gehrels, J. Kennea, A. Moretti, J. A. Nousek, J. P. Osborne, P. Romano, and G. Stratta. The seven year Swift-XRT point source catalog (1SWXRT). *A&A*, 551:A142, March 2013.

[25] D. Donato, G. Ghisellini, G. Tagliaferri, and G. Fossati. Hard X-ray properties of blazars. *A&A*, 375:739–751, September 2001.

[26] P. A. Evans, A. P. Beardmore, K. L. Page, J. P. Osborne, P. T. O'Brien, R. Willingale, R. L. C. Starling, D. N. Burrows, O. Godet, L. Vetere, J. Racusin, M. R. Goad, K. Wiersema, L. Angelini, M. Capalbi, G. Chincarini, N. Gehrels, J. A. Kennea, R. Margutti, D. C. Morris, C. J. Mountford, C. Pagani, M. Perri, P. Romano, and N. Tanvir. Methods and results of an automatic analysis of a complete sample of Swift-XRT observations of GRBs. *MNRAS*, 397:1177–1201, August 2009.

[27] P. A. Evans, J. P. Osborne, A. P. Beardmore, K. L. Page, R. Willingale, C. J. Mountford, C. Pagani, D. N. Burrows, J. A. Kennea, M. Perri, G. Tagliaferri, and N. Gehrels. 1SXPS: A Deep Swift X-Ray Telescope Point Source Catalog with Light Curves and Spectra. *ApJS*, 210:8, January 2014.

[28] G. Fossati, L. Maraschi, A. Celotti, A. Comastri, and G. Ghisellini. A unifying view of the spectral energy distributions of blazars. *MNRAS*, 299:433–448, September 1998.

[29] N. Gehrels, G. Chincarini, P. Giommi, K. O. Mason, J. A. Nousek, A. A. Wells, N. E. White, S. D. Barthelmy, D. N. Burrows, L. R. Cominsky, K. C. Hurley, F. E. Marshall, P. Mészáros, P. W. A. Roming, L. Angelini, L. M. Barbier, T. Belloni, S. Campana,

P. A. Caraveo, M. M. Chester, O. Citterio, T. L. Cline, M. S. Cropper, J. R. Cummings, A. J. Dean, E. D. Feigelson, E. E. Fenimore, D. A. Frail, A. S. Fruchter, G. P. Garmire, K. Gendreau, G. Ghisellini, J. Greiner, J. E. Hill, S. D. Hunsberger, H. A. Krimm, S. R. Kulkarni, P. Kumar, F. Lebrun, N. M. Lloyd-Ronning, C. B. Markwardt, B. J. Mattson, R. F. Mushotzky, J. P. Norris, J. Osborne, B. Paczynski, D. M. Palmer, H.-S. Park, A. M. Parsons, J. Paul, M. J. Rees, C. S. Reynolds, J. E. Rhoads, T. P. Sasseen, B. E. Schaefer, A. T. Short, A. P. Smale, I. A. Smith, L. Stella, G. Tagliaferri, T. Takahashi, M. Tashiro, L. K. Townsley, J. Tueller, M. J. L. Turner, M. Vietri, W. Voges, M. J. Ward, R. Willingale, F. M. Zerbi, and W. W. Zhang. The Swift Gamma-Ray Burst Mission. *ApJ*, 611:1005–1020, August 2004.

[30] N. Gehrels, E. Chipman, and D. Kniffen. The Compton Gamma Ray Observatory. *ApJS*, 92:351–362, June 1994.

[31] G. Ghisellini. Extragalactic relativistic jets. In F. A. Aharonian, W. Hofmann, and F. M. Rieger, editors, *American Institute of Physics Conference Series*, volume 1381 of *American Institute of Physics Conference Series*, pages 180–198, September 2011.

[32] M. R. Goad, L. G. Tyler, A. P. Beardmore, P. A. Evans, S. R. Rosen, J. P. Osborne, R. L. C. Starling, F. E. Marshall, V. Yershov, D. N. Burrows, N. Gehrels, P. W. A. Roming, A. Moretti, M. Capalbi, J. E. Hill, J. Kennea, S. Koch, and D. vanden Berk. Accurate early positions for Swift GRBs: enhancing X-ray positions with UVOT astrometry. *A&A*, 476:1401–1409, December 2007.

[33] J. E. Grove and W. N. Johnson. The calorimeter of the Fermi Large Area Telescope. In *Society of Photo-Optical Instrumentation Engineers (SPIE) Conference Series*, volume 7732 of *Society of Photo-Optical Instrumentation Engineers (SPIE) Conference Series*, July 2010.

[34] H. E. S. S Collaboration, :, D. Berge, F. Aharonian, W. Hofmann, M. Lemoine-Goumard, O. Reimer, G. Rowell, and H. J. Voelk. Primary particle acceleration above 100 TeV in the shell-type Supernova Remnant RX J1713.7–3946 with deep H.E.S.S. observations. *ArXiv e-prints*, October 2007.

[35] K. I. Kellermann. Compact Radio Sources and AGN's. In S. Hayakawa and K. Sato, editors, *Big Bang, Active Galactic Nuclei and Supernovae*, page 239, 1989.

[36] R. W. Klebesadel, I. B. Strong, and R. A. Olson. Observations of Gamma-Ray Bursts of Cosmic Origin. *ApJ*, 182:L85, June 1973.

[37] K. Kohri, Y. Ohira, and K. Ioka. Gamma-ray flare and absorption in the Crab nebula: lovely TeV-PeV astrophysics. *MNRAS*, 424:2249–2254, August 2012.

[38] J.H. Krolik. *Active Galactic Nuclei: from the central black hole to the galactic environment.* Princeton University Press, Princeton, NJ, 1999.

[39] Errando M. *Discovery of very high energy gamma-ray emission from 3C 279 and 3C 66A/B with the MAGIC telescope.* http://wwwmagic.mppmu.mpg.de/publications/theses/index.html, 2009.

[40] N. Masetti, B. Sbarufatti, P. Parisi, E. Jiménez-Bailón, V. Chavushyan, F. P. A. Vogt, V. Sguera, J. B. Stephen, E. Palazzi, L. Bassani, A. Bazzano, M. Fiocchi, G. Galaz, R. Landi, A. Malizia, D. Minniti, L. Morelli, and P. Ubertini. BL Lacertae identifications in a ROSAT-selected sample of Fermi unidentified objects. *A&A*, 559:A58, November 2013.

[41] J. R. Mattox, D. L. Bertsch, J. Chiang, B. L. Dingus, S. W. Digel, J. A. Esposito, J. M. Fierro, R. C. Hartman, S. D. Hunter, G. Kanbach, D. A. Kniffen, Y. C. Lin, D. J. Macomb, H. A. Mayer-Hasselwander, P. F. Michelson, C. von Montigny, R. Mukherjee, P. L. Nolan, P. V. Ramanamurthy, E. Schneid, P. Sreekumar, D. J. Thompson, and T. D. Willis. The Likelihood Analysis of EGRET Data. *ApJ*, 461:396, April 1996.

[42] J. R. Mattox, J. Schachter, L. Molnar, R. C. Hartman, and A. R. Patnaik. The Identification of EGRET Sources with Flat-Spectrum Radio Sources. *ApJ*, 481:95–115, May 1997.

[43] C. Meegan, G. Lichti, P. N. Bhat, E. Bissaldi, M. S. Briggs, V. Connaughton, R. Diehl, G. Fishman, J. Greiner, A. S. Hoover, A. J. van der Horst, A. von Kienlin, R. M. Kippen, C. Kouveliotou, S. McBreen, W. S. Paciesas, R. Preece, H. Steinle, M. S. Wallace, R. B.

Wilson, and C. Wilson-Hodge. THE fermi gamma-ray burst monitor. *ApJ*, 702:791–804, September 2009.

[44] D. G. Monet, S. E. Levine, B. Canzian, H. D. Ables, A. R. Bird, C. C. Dahn, H. H. Guetter, H. C. Harris, A. A. Henden, S. K. Leggett, H. F. Levison, C. B. Luginbuhl, J. Martini, A. K. B. Monet, J. A. Munn, J. R. Pier, A. R. Rhodes, B. Riepe, S. Sell, R. C. Stone, F. J. Vrba, R. L. Walker, G. Westerhout, R. J. Brucato, I. N. Reid, W. Schoening, M. Hartley, M. A. Read, and S. B. Tritton. The USNO-B Catalog. *AJ*, 125:984–993, February 2003.

[45] Longair M.S. High energy astrophysics. *Cambridge University Press*, 1992.

[46] P. L. Nolan, A. A. Abdo, M. Ackermann, M. Ajello, A. Allafort, E. Antolini, W. B. Atwood, M. Axelsson, L. Baldini, J. Ballet, and et al. Fermi Large Area Telescope Second Source Catalog. *ApJS*, 199:31, April 2012.

[47] D. Pacini. *Nuovo Cimento*, V I 3, 1912.

[48] J. M. Paredes, V. Bosch-Ramon, and G. E. Romero. Spectral energy distribution of the γ-ray microquasar LS 5039. *A&A*, 451:259–266, May 2006.

[49] E. Prandini, G. Bonnoli, L. Maraschi, M. Mariotti, and F. Tavecchio. Constraining blazar distances with combined Fermi and TeV data: an empirical approach. *MNRAS*, 405:L76–L80, June 2010.

[50] Robson. *Active Galactic Nuclei.* John Wiley & Sons, 1996.

[51] R. W. Romani. Gamma-Ray Pulsars: Radiation Processes in the Outer Magnetosphere. *ApJ*, 470:469, October 1996.

[52] E. M. Schlegel, P. E. Barrett, O. C. de Jager, G. Chanmugam, S. Hunter, and J. Mattox. Gamma-ray emission from Cataclysmic variables. 1: The Compton EGRET survey. *ApJ*, 439:322–329, January 1995.

[53] R. Schlickeiser. Cosmic ray astrophysics. *(Springer-Verlag, Berlin, Heidelberg, New York)*, 2002.

[54] PhD Thesis Schultz C. Development of new composite mirrors for imaging cherenkov telescopes and observations of the two blazar objects 1es 0806+524 and 1es 1011+496 with magic. 2013.

[55] M. F. Skrutskie, R. M. Cutri, R. Stiening, M. D. Weinberg, S. Schneider, J. M. Carpenter, C. Beichman, R. Capps, T. Chester, J. Elias, J. Huchra, J. Liebert, C. Lonsdale, D. G. Monet, S. Price, P. Seitzer, T. Jarrett, J. D. Kirkpatrick, J. E. Gizis, E. Howard, T. Evans, J. Fowler, L. Fullmer, R. Hurt, R. Light, E. L. Kopan, K. A. Marsh, H. L. McCallon, R. Tam, S. Van Dyk, and S. Wheelock. The Two Micron All Sky Survey (2MASS). *AJ*, 131:1163–1183, February 2006.

[56] D. N. Spergel, R. Bean, O. Doré, M. R. Nolta, C. L. Bennett, J. Dunkley, G. Hinshaw, N. Jarosik, E. Komatsu, L. Page, H. V. Peiris, L. Verde, M. Halpern, R. S. Hill, A. Kogut, M. Limon, S. S. Meyer, N. Odegard, G. S. Tucker, J. L. Weiland, E. Wollack, and E. L. Wright. Three-Year Wilkinson Microwave Anisotropy Probe (WMAP) Observations: Implications for Cosmology. *ApJS*, 170:377–408, June 2007.

[57] J. B. Stephen, L. Bassani, R. Landi, A. Malizia, V. Sguera, A. Bazzano, and N. Masetti. Using the ROSAT catalogue to find counterparts for unidentified objects in the first Fermi/LAT catalogue. *MNRAS*, 408:422–429, October 2010.

[58] M. Tavani, G. Barbiellini, A. Argan, A. Bulgarelli, P. Caraveo, A. Chen, V. Cocco, E. Costa, G. de Paris, E. Del Monte, G. Di Cocco, I. Donnarumma, M. Feroci, M. Fiorini, T. Froysland, F. Fuschino, M. Galli, F. Gianotti, A. Giuliani, Y. Evangelista, C. Labanti, I. Lapshov, F. Lazzarotto, P. Lipari, F. Longo, M. Marisaldi, M. Mastropietro, F. Mauri, S. Mereghetti, E. Morelli, A. Morselli, L. Pacciani, A. Pellizzoni, F. Perotti, P. Picozza, C. Pontoni, G. Porrovecchio, M. Prest, G. Pucella, M. Rapisarda, E. Rossi, A. Rubini, P. Soffitta, M. Trifoglio, A. Trois, E. Vallazza, S. Vercellone, A. Zambra, D. Zanello, P. Giommi, A. Antonelli, and C. Pittori. The AGILE space mission. *Nuclear Instruments and Methods in Physics Research A*, 588:52–62, April 2008.

[59] C. M. Urry and P. Padovani. Unified Schemes for Radio-Loud Active Galactic Nuclei. *PASP*, 107:803, September 1995.

[60] website:. http://tools.asdc.asi.it/sed/.

[61] website:. http://www.batse.msfc.nasa.gov/batse/grb/skymap/.

[62] website:. http://www.physics.utah.edu/ whanlon/spectrum.html.

[63] H.-S. Zechlin, M. V. Fernandes, D. Elsässer, and D. Horns. Dark matter subhaloes as gamma-ray sources and candidates in the first Fermi-LAT catalogue. *A&A*, 538:A93, February 2012.